

NORTHWESTERN UNIVERSITY

The Role of TACC3 in Regulating Microtubule Dynamics During Herpesvirus Infections

A DISSERTATION

SUBMITTED TO THE GRADUATE SCHOOL  
IN PARTIAL FULFILLMENT OF THE REQUIREMENTS

for the degree

DOCTOR OF PHILOSOPHY

Field of Life Sciences

By

Colleen Patricia Furey

EVANSTON, ILLINOIS

December 2021

© Copyright by Colleen Furey 2021

All Rights Reserved

## Abstract

The microtubule (MT) network and associated regulatory proteins play a critical role during viral infection from facilitating viral particle transport towards the nucleus upon entry to later mediating virion assembly and egress. Many of the precise mechanisms by which viruses commandeer the host MT network to propagate infection remain poorly defined. The MT network is largely controlled by a group of proteins known as plus-end tracking proteins or +TIPs which directly or indirectly bind growing MT plus-ends and regulate their dynamic instability. Among the +TIPs, the end-binding (EB) proteins have long been considered the master regulators of the MT network due to their ability to directly bind MT plus-ends and recruit a diverse array of other +TIP partners there. As mediators of MT dynamics and stability, +TIPs can be exploited by viruses to manipulate MT behavior. Indeed, previous work from our lab demonstrated that herpes simplex virus type 1 (HSV-1) hijacks a +TIP complex including EB1 at the cell periphery to initiate viral particle transport on dynamic tyrosinated MTs during early infection in primary normal human dermal fibroblasts (NHDFs). In examining whether HSV-1 utilizes similar mechanisms during infections in other cell types, I found that HSV-1 adopts a different approach to infect the neuronal SK-N-SH cell line, with HSV-1 particles trafficking upon stable de-tyrosinated MTs in an EB-independent manner to the nucleus. To explore the potential contribution of an EB-independent +TIP to HSV-1 infection in SK-N-SHs, I began studying transforming acidic coiled-coil protein 3 (TACC3), an autonomous tip-tracker primarily characterized as a mitotic protein that promotes MT spindle elongation by recruiting the MT polymerase chTOG to spindle plus-ends.

Through my studies, I found that TACC3 plays a role not only in facilitating HSV-1 infection in both NHDFs and SK-N-SHs, but more generally in controlling interphase MT

dynamics. In this work, I show that altering TACC3 levels disrupts the nuclear-cytoplasmic localization of chTOG and thus the balance between dynamic and stable MTs in the cell. Loss of TACC3 results in nuclear sequestration of chTOG, reduced MT growth in the cytoplasm, and accumulation of post-translationally modified stable MTs. In NHDFs, the loss of EB1 and dynamic MTs at the periphery of TACC3-depleted cells inhibits HSV-1 particle transport to the nucleus and subsequently blocks infection. In SK-N-SHs the upregulation of de-tyrosinated MTs in TACC3-depleted cells results in impaired HSV-1 particle transport to the nucleus which I found is due to the biasing of MT-dependent transport towards outward-directing kinesin motors. Together, these findings highlight the previously unappreciated role for TACC3 in regulating interphase MTs and in turn facilitating transport of cellular and viral cargo. To expand upon these findings, I next examined the role of TACC3 in a different herpesvirus infection, human cytomegalovirus (HCMV). Compared to HSV-1, HCMV has a protracted infectious cycle and is characterized by the formation of a viral assembly compartment (AC) which consists of rearranged host secretory machinery and requires precise coordination by the MT network. I found that HCMV specifically upregulates TACC3 late in infection to maintain high levels of chTOG and dynamic MTs in the cytoplasm, which is necessary for recruitment of secretory machinery to the AC and subsequent virion egress. The work presented here provides evidence towards the centrality of TACC3 in MT network regulation. This work also presents an example of a virus targeting TACC3 to promote infection, laying a foundation for future investigations of TACC3 in the context of other viral infections.

## Acknowledgement

I would like to thank my advisor, Dr. Derek Walsh, for his invaluable support and mentorship over my years at Northwestern. I feel incredibly fortunate to have had you in my corner, inspiring and encouraging me along the way. I would also like to thank my thesis committee members, Dr. Mojgan Naghavi, Dr. Richard Longnecker, and Dr. Dileep Varma, for your thoughtful feedback and guidance. A big thank you to my fellow labmates of the Walsh Lab—once again I feel quite lucky to have found my way to this group of scientists. Special thanks to Dr. Dean Procter for showing me how cool microscopes can be.

To my family—To Andrew, thank you for celebrating with me in the good times, ushering me onward in the difficult times, and for hearing so much about TACC3 over the years that you could have your very own PhD. You are my *vie en rose*. To my incredible parents, thank you for your constant prayers, love, and support without which I certainly would not be close to where I am now. I strive everyday to be like you. To my sisters Caitlin and Meghan, thank you for listening to my worries, giving much-needed advice and prayers, and always providing me with distractions in the best sense of the word. To Lita, Daddy G, and my King family, thank you for taking me under your wing when I most needed it and keeping me on my toes. To the rest of my extended Furey, Mayo, and Lydon families, there are far too many of you to thank personally but I love you all endlessly!

Thank you to my gaggle of friends, for giving me life outside the lab, and especially to my Roscoe family because collectively you carried me through years 1 to 5.

And thank you to TS for honestly everything.

## Table of Contents

Abstract.....	3
Acknowledgement.....	5
Table of Contents.....	6
List of Figures.....	7
CHAPTER 1: Introduction.....	11
<i>Herpesviridae</i> .....	11
Herpes simplex virus type 1.....	13
Human cytomegalovirus.....	15
HSV-1 and HCMV: shared significance.....	20
The microtubule network.....	21
Post-translational modifications of tubulin.....	22
Microtubule associated proteins.....	24
chTOG and TACC3.....	27
Viruses and the microtubule network.....	31
Summary and key questions.....	34
CHAPTER 2: Materials and Methods.....	36
CHAPTER 3: TACC3 Regulates Microtubule Plus-End Dynamics and Cargo Transport in Interphase Cells.....	51
Introduction.....	51
Results.....	54
Discussion.....	106
CHAPTER 4: Human Cytomegalovirus Exploits TACC3 to Control Microtubule Dynamics and Late Stages of Infection.....	108
Introduction.....	108
Results.....	111
Discussion.....	147
CHAPTER 5: Discussion.....	151
References.....	160

## List of Figures

Figure 1 Herpesviruses that infect humans.....	12
Figure 2 HSV-1 infection at a glance. ....	14
Figure 3 A comparison of HSV-1 and HCMV infectious cycles. ....	17
Figure 4 Tubulin composition at the plus-end. ....	23
Figure 5 chTOG, TACC3, and EB1 at the microtubule plus-end. ....	28
Figure 6 SK-N-SH cells are a near-pure neuronal cell line.....	55
Figure 7 HSV-1 infection is EB-independent in SK-N-SHs.....	56
Figure 8 Stable MTs mediate HSV-1 infection in SK-N-SHs.....	58
Figure 9 Nocodazole dampens MT dynamics.....	59
Figure 10 Stable MTs persist at low doses of nocodazole .....	60
Figure 11 HSV-1 infection is unaffected by low-dose nocodazole treatment in SK-N-SHs.....	63
Figure 12 Nocodazole treatment does not affect HSV-1 entry.....	64
Figure 13 Nocodazole treatment does not alter actin organization in NHDFs or SK-N-SHs.....	65
Figure 14 TACC3, but not EB1, regulates stable MTs in SK-N-SHs.....	67
Figure 15 Localization of TACC3 in mitotic and interphase human cells.....	68
Figure 16 TACC3 depletion results in an increase in de-tyrosinated MTs in SK-N-SHs.....	71
Figure 17 TACC3 regulates cell diameter in SK-N-SHs.....	72
Figure 18 TACC3 rescue confirms that knockdown phenotypes are not siRNA off-target effects.....	73
Figure 19 TACC3 regulates <i>trans</i> -Golgi organization.....	74
Figure 20. TACC3 depletion does not significantly affect centrosome.....	76

Figure 21 TACC3 does not regulate MT nucleation in interphase cells.....	77
Figure 22 Quantification of MT regrowth in SK-N-SHs.....	78
Figure 23 TACC3 regulates MT plus-end dynamics in SK-N-SHs.....	80
Figure 24 Number of EB1 comets correlates with amount of TACC3 in cell.....	81
Figure 25 TACC3 regulates MT plus-end dynamics in NHDFs.....	82
Figure 26 Live-cell imaging of plus-end dynamics in TACC3-depleted cells.....	83
Figure 27 FLAG-tagged TACC3 forms cytoplasmic aggregates when expressed in cells.....	84
Figure 28 EB1 comets are elongated in cells expressing FLAG-TACC3.....	85
Figure 29 Expression of dominant-negative TACC3 suppresses MT dynamics.....	87
Figure 30 Dominant-negative TACC3 expression upregulates acetylated MTs in NHDFs.....	88
Figure 31 FLAG-TACC3 sequesters chTOG in cytoplasmic aggregates.....	89
Figure 32 TACC3 regulates chTOG localization during interphase.....	90
Figure 33 Confocal microscopy confirms an increase in nuclear chTOG in TACC3-depleted cells.....	91
Figure 34 TACC3 regulates HSV-1 infection in both SK-N-SHs and NHDFs.....	93
Figure 35 TACC3 knockdown slows but does not inhibit HSV-1 entry in SK-N-SHs.....	94
Figure 36 Quantification of fused HSV-1 particles in TACC3-depleted cells.....	95
Figure 37 HSV-1 particles exhibit net anterograde motility during early infection in TACC3- depleted SK-N-SHs.....	97
Figure 38 Kinesin-1 prevents perinuclear accumulation of HSV-1 particles in TACC3-depleted SK-N-SHs.....	98

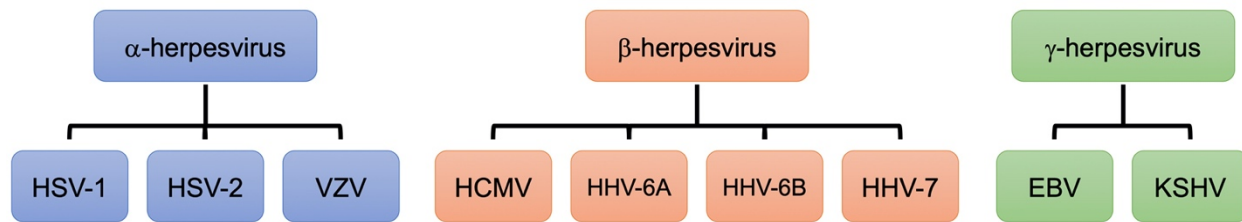
Figure 39 Co-depletion of TACC3 and kinesin-1 rescues retrograde motility of HSV-1 particles in SK-N-SHs.....	100
Figure 40 Kinesin-1 prevents perinuclear accumulation of transferrin in TACC3-depleted SK-N-SHs.....	101
Figure 41 TACC3 and kinesin-1 co-depletion rescues accumulation of transferrin at perinuclear space in SK-N-SHs.....	104
Figure 42 HCMV increases TACC3 expression as infection progresses.....	112
Figure 43 TACC3 levels increase within the cytoplasm during late HCMV infection.....	114
Figure 44 TACC3 immunofluorescence staining is specific.....	115
Figure 45 chTOG accumulates in the cytoplasm as HCMV infection progresses.....	116
Figure 46 chTOG localizes diffusely throughout AC and colocalizes with centrosomal markers during HCMV infection.....	117
Figure 47 RNAi treatment depletes cytoplasmic chTOG but leaves residual chTOG at the AC and centrosome.....	118
Figure 48 RNAi-mediated depletion of TACC3 does not affect establishment of HCMV infection in NHDFs.....	120
Figure 49 TACC3 and chTOG are required for efficient HCMV spread.....	122
Figure 50 TACC3 controls chTOG localization in HCMV-infected cells.....	125
Figure 51 TACC3 and chTOG regulate MT dynamics in HCMV-infected cells.....	128
Figure 52 Model for how TACC3 regulates chTOG localization and enables the AC to increase MT dynamics.....	131
Figure 53 Depletion of TACC3 or chTOG does not eliminate microtubule networks.....	132

Figure 54 Loss of TACC3 or chTOG activity results in increased levels of acetylated MTs....	134
Figure 55 Categorization of changes in acetylated MTs caused by loss of TACC3 or chTOG..	135
Figure 56 TACC3 and chTOG coordinate the organized recruitment of endosomal vesicles to the AC.....	138
Figure 57 Rab7 localization at the AC is disrupted by TACC3 or chTOG depletion.....	140
Figure 58 Rab5 localization at the AC is disrupted by TACC3 or chTOG depletion.....	141
Figure 59 Loss of TACC3 or chTOG results in formation of MVBs which are Rab5-positive..	144
Figure 60 MVBs that form in TACC3- or chTOG-depleted cells are Rab7-positive.....	145
Figure 61 Depletion of TACC3 or chTOG causes defects in virus trafficking. ....	146
Figure 62 Model of HSV-1 infection in TACC3-depleted SK-N-SHs.....	154
Figure 63 A simplified model of TACC3 activity.....	158

## CHAPTER 1: Introduction

### *Herpesviridae*

The family *Herpesviridae* consists of large, enveloped, double-stranded DNA viruses that establish lifelong, latent infection in their hosts [1]. Members of the family *Herpesviridae*, colloquially termed herpesviruses, are further classified into three subfamilies including *Alpha* ( $\alpha$ )-, *Beta* ( $\beta$ )-, and *Gamma* ( $\gamma$ )- *herpesvirinae* [2]. Herpesviruses are ubiquitous pathogens found across animal species in nature [1, 3]. Nine herpesviruses are known to infect humans, including  $\alpha$ -herpesviruses herpes simplex virus type 1 (HSV-1), herpes simplex virus type 2 (HSV-2), and varicella-zoster virus (VZV);  $\beta$ -herpesviruses human cytomegalovirus (HCMV), human herpesvirus 6A, 6B, and 7 (HHV-6A, HHV-6B, HHV-7); and  $\gamma$ -herpesviruses Epstein-Barr virus (EBV) and Kaposi's sarcoma-associated herpesvirus (KSHV) (Figure 1) [1]. Structurally, herpesvirus virions consist of a glycoprotein-studded lipid envelope, an underlying layer of proteins termed the tegument, and an icosahedral capsid containing the linear double-stranded DNA genome [3]. Outside of their shared morphology and use of latency to persist in hosts, herpesviruses diverge from each other in a number of ways, including cell types targeted, length of infectious cycle, and the mechanisms by which the virus undergoes latency. For example, while  $\alpha$ -herpesvirus HSV-1 is characterized by a short infectious cycle and establishment of latency in the trigeminal ganglia,  $\beta$ -herpesvirus HCMV replicates far more slowly and establishes latency in monocytes, dendritic cells, and hematopoietic progenitor cells [1]. As this dissertation will focus



**Figure 1** Herpesviruses that infect humans. Across the *Herpesviridae* subfamilies *Alphaherpesvirinae* (blue), *Betaherpesvirinae* (orange), and *Gammaherpesvirinae* (green), there are nine viruses that infect humans. These viruses are herpes simplex virus type 1 (HSV-1), herpes simplex virus type 2 (HSV-2), varicella-zoster virus (VZV), human cytomegalovirus (HCMV), human herpesvirus 6A, 6B, and 7 (HHV-6A, HHV-6B, and HHV-7), Epstein-Barr virus (EBV), and Kaposi's sarcoma-associated herpesvirus (KSHV). This dissertation will cover HSV-1 and HCMV in particular.

in particular on HSV-1 and HCMV, the following two sections will describe the characteristics of these two herpesviruses in detail.

### **Herpes simplex virus type 1**

HSV-1 is a highly prevalent human pathogen, infecting approximately 67% of the global population [4]. Though HSV-1 most often causes asymptomatic disease or cutaneous lesions in mucosal sites, severe complications including encephalitis or keratitis can occur in immunocompromised individuals who become infected [1, 5]. During primary infection, HSV-1 targets and actively replicates in cells of the mucosal epithelium before entering nerve termini and undergoing latency in sensory neurons (Figure 2) [6]. In order to reach the nucleus in sensory neurons, the virus must traverse relatively long distances through the axon from the nerve termini to the cell body in a retrograde manner [7]. During reactivation, HSV-1 traffics back down the axon in an anterograde manner before disseminating into the mucosal epithelium where the virus again replicates and is shed [6, 7].

HSV-1 enters the cell through plasma membrane fusion or endocytosis [8-10]. The released nucleocapsids are then transported to the nucleus in a retrograde manner by microtubules [1, 7, 11, 12]. At the nuclear membrane, the viral genome is released from the nucleocapsid and imported into the nucleus at nuclear pore complexes [13, 14]. Once the viral genome is in the nucleus a temporal cascade of gene transcription occurs, beginning with transcription of the immediate-early viral genes by the host RNA polymerase II [1, 15]. Sequential transcription of early and late genes follows, which encode proteins required for

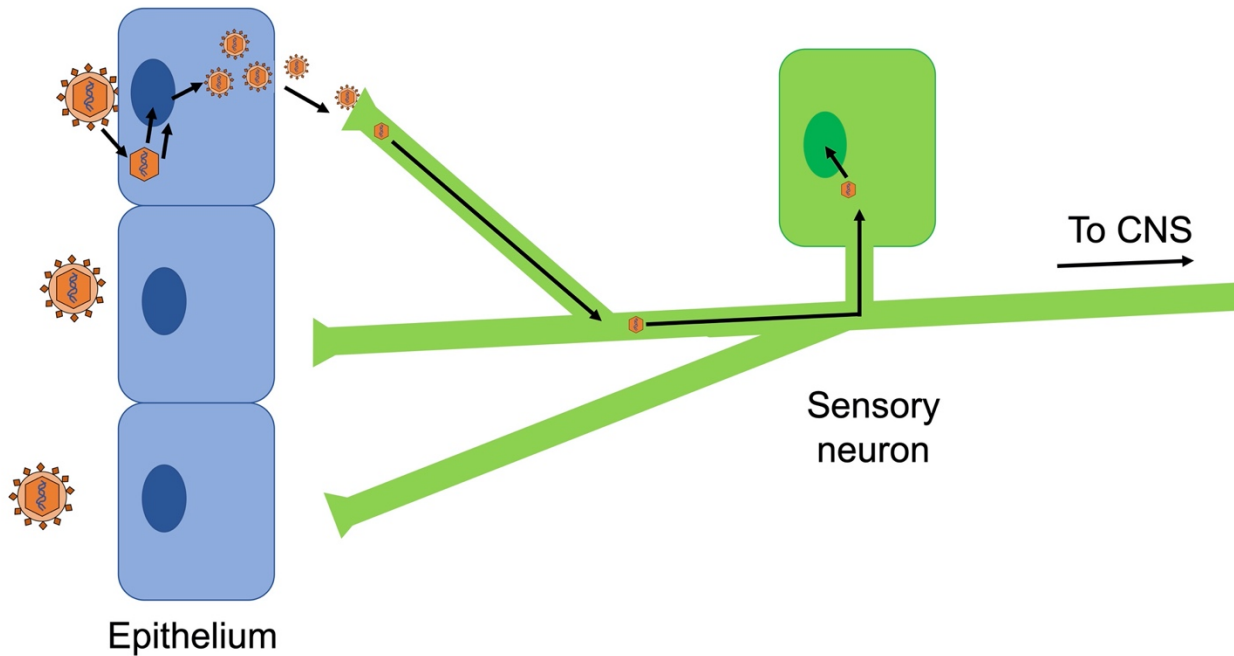


**Figure 2** HSV-1 infection at a glance. Primary HSV-1 (orange) infection occurs at the mucosal epithelium (blue), where the virus actively replicates and produces progeny virions. Virions then invade the axon termini of sensory neurons (green) and travel in a retrograde manner to the cell body where the virus establishes latency. Periodic reactivation results in a reversal of this sequence of events, with the virus emerging from the sensory neuron and traveling in an anterograde manner to axon termini. Virus released from axon termini invade epithelial cells resulting in recurrent infection.

viral genome replication and virion assembly, respectively [16]. As the viral genome is replicated, nascent DNA is packaged into capsids which then egress from the nucleus by budding through the inner and outer nuclear membranes [17, 18]. There are a number of theories regarding how the nucleocapsids obtain their final envelope, with the prevailing theory suggesting that nucleocapsids undergo final envelopment by budding into cytoplasmic membranes derived from either the *trans*-Golgi or the plasma membrane [1, 19-21]. In the case of neuronal infection, there is evidence that nucleocapsids first undergo anterograde transport to nerve termini before associating with tegument proteins and obtaining their final envelope [22]. Regardless of cell type, mature virions egress from the cell by way of the secretory network, with virion exocytosis as the final stage of the infectious cycle [19, 22, 23].

During infection of sensory neurons, HSV-1 latency is characterized by high transcription levels of the latency-associated transcript (LAT) which in part represses lytic gene expression and virus replication, though the precise trigger for latency remains uncertain [24-26]. Periodic reactivation of HSV-1 in neurons occurs both spontaneously and in response to external stimuli, with leaky lytic gene expression leading to robust, disordered expression of immediate-early, early, and late genes and subsequent production of infectious virus [27-30]. Progeny virions are released from axon termini and active replication in epithelial cells follows, resulting in a characteristic lesion in the epithelial tissue. Shedding of virus following reactivation occurs on the order of days [31, 32].

### **Human cytomegalovirus**

HCMV shares a number of properties with HSV-1, including its widespread distribution amongst the human population. Though the vast majority of HCMV infections are asymptomatic, HCMV can cause debilitating disease in immunocompromised individuals such as organ transplant recipients and patients with acquired immunodeficiency syndrome (AIDS) [33, 34]. Perhaps most significantly, HCMV is the leading infectious cause of birth defects including hearing and vision loss, developmental delays, and microcephaly [35, 36]. Transmission occurs through bodily fluids such as saliva and urine, as well as perinatally through transplacental transfer, vaginal birth, or breastfeeding [37].

As with other herpesviruses, HCMV causes lifelong, latent infection punctuated by periodic reactivation. However, in contrast with HSV-1, HCMV has a broad cellular tropism including endothelial cells, epithelial cells, fibroblasts, smooth muscle cells, neurons, monocytes, and neutrophils [1, 38-40]. Latency occurs in monocytes, dendritic cells, and hematopoietic progenitor cells within the bone marrow [34, 41, 42]. The switch from latent to lytic infection is regulated by a number of factors, including differentiation, epigenetic changes, cell cycle stage, and stress response to trauma [1, 34, 41, 42].

The replication cycle of HCMV broadly follows that of HSV-1, with two important distinctions. Firstly, while HSV-1 takes up to 12 hours to complete one infectious cycle, the infectious cycle of HCMV lasts approximately 5-7 days [1, 43, 44]. Secondly, during its protracted infectious cycle HCMV reorganizes the intracellular secretory network into a unique structure termed the assembly compartment (AC) in the space adjacent to the nucleus, which becomes enlarged and kidney-shaped during infection [45-47]. Aside from these differences, the early stages of viral replication remain similar between HSV-1 and HCMV (Figure 3). HCMV virions

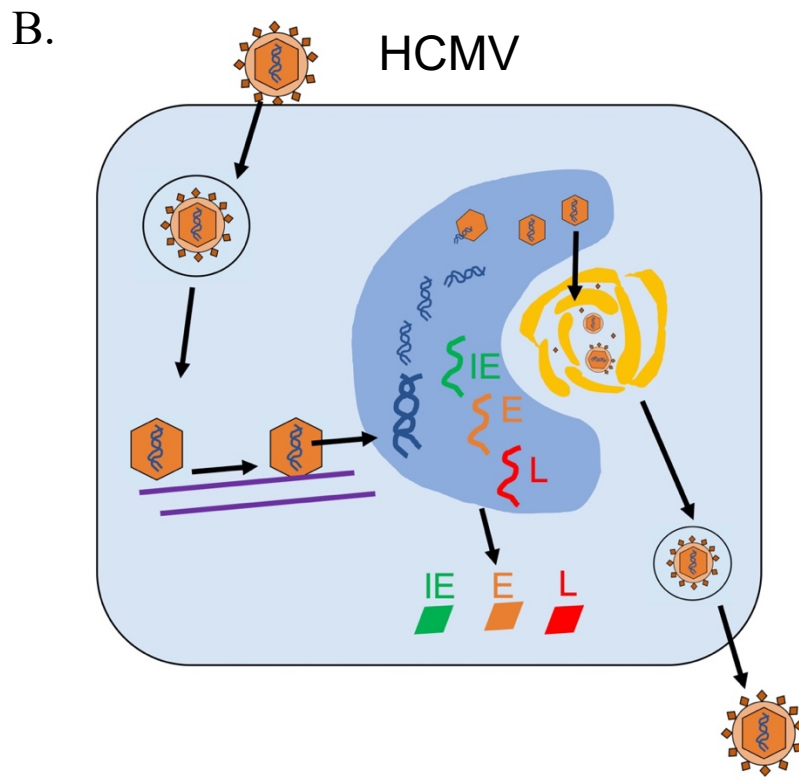
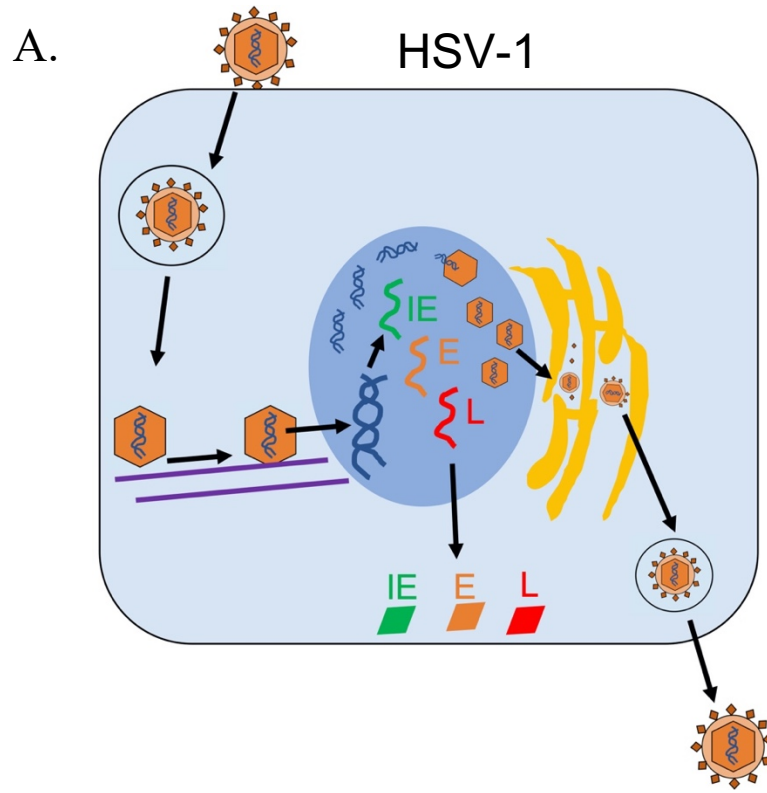


**Figure 3** A comparison of HSV-1 and HCMV infectious cycles. A-B. The early stages of HSV-1 and HCMV infection are largely similar. Following cell entry, viral capsids are released into the cytoplasm and traffic upon microtubules to the nucleus. The viral genome is imported to the nucleus, where a temporal cascade of immediate-early (IE, green), early (E, orange), and late (L, red) genes are transcribed, resulting in production of IE, E, and L proteins in the cytoplasm. The viral genome is replicated and packaged into nucleocapsids. Nucleocapsids egress into the cytoplasm. A. For HSV-1, nucleocapsids gain their tegument and envelope by budding into membranes derived from either the *trans*-Golgi network or the plasma membrane. Virions are released from the cell by exocytosis. B. For HCMV, nucleocapsids are trafficked to the assembly compartment (AC) where they obtain a layer of tegument proteins and undergo final envelopment as the capsids move through the different layers of the AC. Mature virions egress in vesicles for exocytic release.

enter the cell largely through endocytosis followed by envelope fusion with the endosomal membrane, though in fibroblasts virions may enter by direct fusion with the plasma membrane [48-51]. Upon release into the cytoplasm, viral capsids undergo microtubule-dependent, retrograde transport to the nucleus [52]. Similarly to HSV-1, the HCMV viral genome is imported into the nucleus through the nuclear pore complex where a temporal cascade of HCMV gene expression begins. Interestingly, recent reports suggest that genome import for both HSV-1 and HCMV depends upon interaction with stimulator of interferon genes (STING) at the nuclear membrane, highlighting a conserved mechanism between the two herpesviruses [53]. After HCMV genome replication and nucleocapsid packaging, primary envelopment and de-envelopment occur as the capsids translocate through the inner and outer nuclear membrane [1, 54, 55]. Once in the cytoplasm, nucleocapsids gain their tegument and undergo final envelopment as the capsids move through the AC [46, 55, 56]. Mature, enveloped virions egress from the AC to the plasma membrane for exocytic release within vesicles derived from *trans*-Golgi and endosomal membranes [55, 57, 58]. Virion release from the cell peaks between 120 and 168 hours post infection (hpi) [59, 60]. Interestingly, there are some cell-type specific differences in terms of the composition and origination of HCMV virion-containing exocytic vesicles [61]. A recent study found that in fibroblasts the virions egress within vesicles derived from the canonical endocytic pathway, while in endothelial cells the vesicles are derived from the Golgi as well as autophagic and lysosomal pathways [61]. Despite these differences, in all cell types examined the egressing virions are either individually contained within small vesicles or multi-vesicular bodies (MVBs), or contained in bulk within larger vesicles [59, 62-64].

The AC is the site for all virion assembly events during HCMV infection, including tegumentation, envelopment, and maturation. As early as 24 hpi the AC begins to take shape with the Golgi apparatus rearranging from a ribbon-like structure into a cylindrical ring [46, 65-67]. Components of the secretory network then incorporate into organized layers within the AC, which can be visualized by immunofluorescence microscopy using markers of early, late, and recycling endosomes [68]. Interestingly there are some differences across cell types in terms of the presence and localization of these markers in the AC, which may explain why virion egress occurs in different types of exocytic vesicles depending on the cell type [46, 60, 61, 65]. The AC reaches full maturity in terms of size and organization around 72 to 120 hpi [45, 60, 65, 68]. As the AC forms the nucleus undergoes morphological changes as well, becoming enlarged and concave around the AC [69]. At the same time, the virus hijacks the host microtubule (MT) network, discussed in greater detail below, and the AC becomes a MT organizing center [45, 65]. Interactions between nuclear membrane proteins and the MTs that emanate from the AC hold the AC in place within the nuclear pinch [44, 69, 70]. Overall, the structure and organization of the AC are critical to the proper assembly and maturation of HCMV virions prior to their release from the cell.

### **HSV-1 and HCMV: shared significance**

Both HSV-1 and HCMV are widespread herpesvirus infections that can cause severe disease in certain individuals. Understanding the mechanisms by which HSV-1 and HCMV control cellular processes can identify pathways and proteins to target when developing anti-viral therapeutics. At the cellular level, one of the keys to successful establishment and dissemination

of viral infection is effective intracellular trafficking of virions. Replication and spread of HSV-1 and HCMV cannot occur unless the virus is able to reach the host nucleus early in infection and the plasma membrane late in infection. Intracellular virion transport hinges upon the arrangement of specialized filaments that serve as tracks for cargo transport within cells, the host microtubule network. Importantly, microtubules have a number of functions beyond cargo trafficking that make them attractive targets for HSV-1 and HCMV manipulation during infection.

### **The microtubule network**

The microtubule (MT) network is an integral component of the cytoskeleton, responsible for facilitating cellular division, maintaining cellular shape and motility, regulating transport of organelles and cargo, and dictating the spatial organization of intracellular compartments [71]. On a molecular level, MTs consist of  $\alpha/\beta$ -tubulin heterodimers arranged head-to-tail in protofilaments that associate laterally to form a hollow cylinder [72, 73]. MTs emanate in a polarized fashion from various microtubule organizing centers (MTOCs) throughout the cell, with the site of MT nucleation at the MTOC termed the minus-end and the distal end of the MT termed the plus-end [74-77]. Though for many years the centrosome was thought to be the single site of MT nucleation within the cell, it is now clear that there are several non-centrosomal sites that control MT nucleation and organization, including the nuclear envelope, plasma membrane, and the Golgi apparatus [78-80].

Growth and shrinkage of MTs occur primarily at the MT plus-end *in vivo*, though minus-ends grow at a slow rate *in vitro* as well [71, 81-83]. During MT growth, tubulin heterodimers bound to guanosine tri-phosphate (GTP) are added to the MT tip [84-86]. The GTP-tubulin

incorporated into the MT lattice later becomes hydrolyzed into guanosine di-phosphate (GDP), resulting in a MT made up of mostly GDP-tubulin with a stabilizing GTP cap at the growing end [86] (Figure 4). If the MT GTP-tubulin cap is removed or hydrolyzed to GDP-tubulin, the MT undergoes catastrophe whereby tubulin dimers dissociate from the newly destabilized end [87-89]. Catastrophe is reversed by MT regrowth or rescue, although the precise mechanism or trigger for a rescue event remains a topic of debate [90-93]. This interchange between phases of growth, catastrophe, and rescue which characterizes MT behavior is termed dynamic instability [82]. MTs can also exhibit periods of stability absent of growth or shrinkage events [94]. MT plus-end capture at the cell cortex or at other intracellular surfaces can initiate stabilization, as can the binding of various stabilizing proteins [95-99]. In comparison to dynamic MTs which are actively undergoing polymerization or depolymerization, stable MTs are more resistant to drug-induced or cold-induced depolymerization and naturally exhibit longer half-lives in the cytoplasm [100, 101].

### **Post-translational modifications of tubulin**

Both  $\alpha$ - and  $\beta$ -tubulin can be post-translationally modified while in soluble dimer form or while incorporated into a MT. The first post-translational modification (PTM) identified on a MT was detyrosination, the removal of the final tyrosine residue from the C-terminal tail of  $\alpha$ -tubulin [102]. Tubulin detyrosination occurs over time on filaments in the cytoplasm, causing long-lived stable MTs to become enriched in detyrosinated tubulin [100-104]. While this PTM does not alone confer stability upon MTs, detyrosination decreases the activity of depolymerizing kinesin-13 proteins which in turn makes the MT more resistant to catastrophe [105-107]. Detyrosination is reversed when tubulin dimers dissociate from the MT into the cytoplasm where tubulin tyrosine

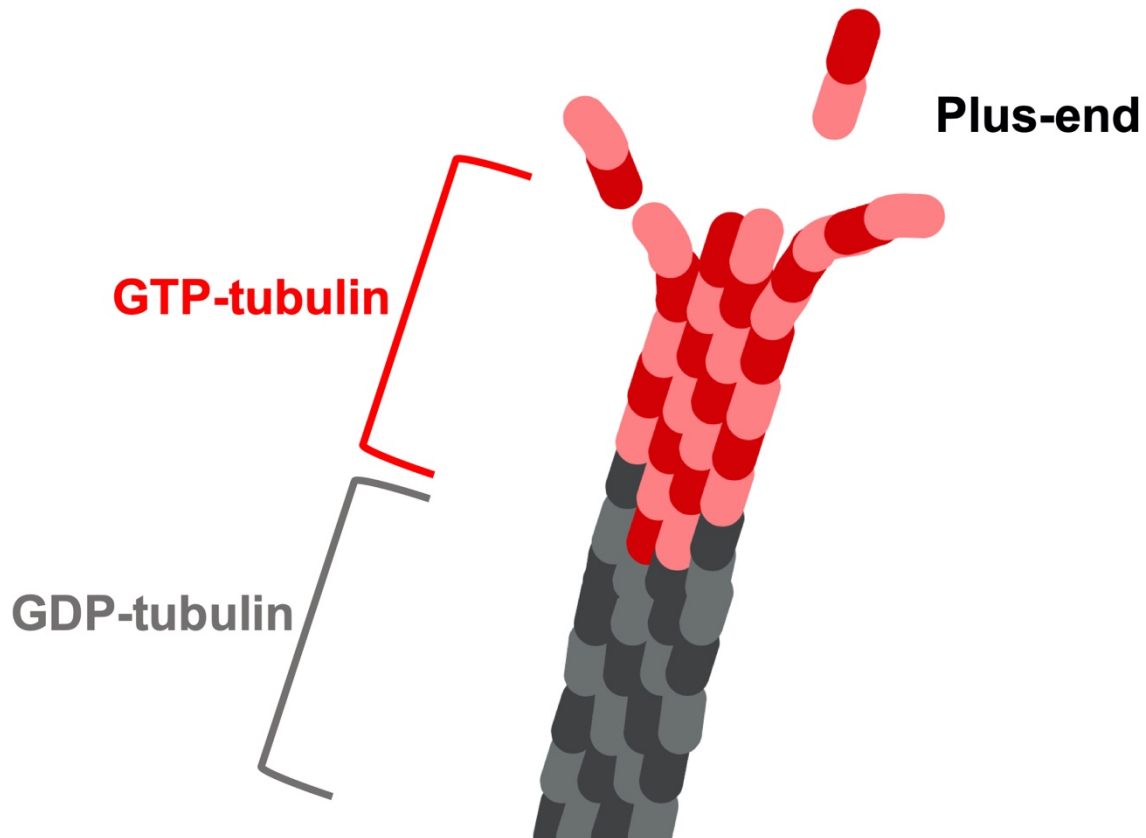


**Figure 4** Tubulin composition at the plus-end. GTP-bound tubulin dimers (pink/red) are added to the microtubule at the plus-end. As the microtubule grows, GTP-tubulin in the lattice is hydrolyzed to GDP-tubulin (grey/black) while new GTP-bound tubulin dimers are added to the plus-end, resulting in a microtubule composed of primarily GDP-tubulin with a GTP-tubulin plus-end cap. The GTP-tubulin cap has a curved structure that differentiates the plus-end from the straight lattice.

ligase rapidly adds a terminal tyrosine back onto  $\alpha$ -tubulin [103, 106]. As a result, soluble tubulin dimers being actively incorporated into dynamic MTs are almost entirely tyrosinated. Another PTM that occurs on polymerized tubulin is acetylation, which occurs on a lysine residue of  $\alpha$ -tubulin within the MT lumen. Although previously associated with MT stability, acetylation has recently been shown to specifically increase MT mechanical strength and resistance against breakage, rather than contribute to overall longevity of the MT [108, 109]. Neurons in particular contain a high number of diverse tubulin PTMs, including the removal of the penultimate glutamate following detyrosination (creating  $\Delta 2$ -tubulin), polyglutamylation, and polyamination [102]. These PTMs contribute to the specialization of neuronal MTs, which span unusually long distances and vary between highly stabilized in axons to dynamic in growth cones [110]. Tubulin PTMs can have both direct and indirect effects on MT functionality, as PTMs may alter the local MT conformation or binding affinities of interacting proteins. However, these effects are at times difficult to attribute to a single PTM due to the heterogenous and often overlapping distribution of PTMs along a MT *in vivo* [102, 106]. As such, the most extensively characterized tubulin PTMs remain detyrosination and acetylation, both of which have been examined using *in vitro* reconstitution experiments to confirm *in vivo* studies [102, 107-109, 111].

### **Microtubule associated proteins**

The MT network is largely influenced by microtubule-associated proteins (MAPs) which can be further classified based upon localization along the MT. Certain factors display minus-end specificity and are critical for MT nucleation and anchoring to cellular surfaces [112]. The protein complex which binds the exposed  $\alpha$ -tubulin at the minus-end of nascent microtubules is termed

the  $\gamma$ -tubulin ring complex ( $\gamma$ -TURC) and its components are highly conserved across eukaryotic organisms. The mammalian  $\gamma$ -TURC is composed of  $\gamma$ -tubulin and a number of minus-end targeting proteins called  $\gamma$ -tubulin complex component proteins (GCPs) [112-114]. The  $\gamma$ -TURC is recruited, tethered, and organized by several proteins including pericentrin, cyclin dependent kinase 5 regulatory subunit associated protein 2 (CDK5RAP2), A-kinase anchoring protein of 450 kDa (AKAP450), and augmin/HAUS, the latter of which specifically anchors  $\gamma$ -TURC to the sides of pre-existing microtubule lattices [115, 116]. Together these minus-end MAPs form MTOCs throughout the cell which provides spatial organization to MT arrays.

Beyond the minus-end, a second group of MAPs bind along the MT lattice. A number of lattice-binding MAPs are highly expressed in neurons, including the Tau/MAP2/MAP4 family which stabilizes axon microtubules while also regulating microtubule motor activity [117, 118]. The microtubule motor proteins kinesin-1 and cytoplasmic dynein bind and move along the MT lattice as well, driving cargo transport towards the MT plus-end and minus-end respectively. Dynein activity in cells requires the adaptor protein dynactin, which binds both MTs as well as dynein to increase dynein processivity [119]. Interestingly, while kinesin-1 exhibits higher affinities for both detyrosinated and acetylated MTs compared to tyrosinated MTs, detyrosination of MTs reduces binding by the dynein-dynactin complex, enabling these post translationally-modified filaments to act as specialized tracks for anterograde cargo transport [120-125].

A third group of MAPs known as the plus-end tracking proteins (+TIPs) targets the MT plus-end. Given that MT growth and shrinkage occurs predominantly at the plus-end, +TIPs strongly influence MT dynamics and mediate interactions between MTs and the surrounding cellular environment [126]. While a number of +TIPs independently recognize and bind the plus-

end, there are others that must be recruited to the plus-end by binding partners [126-128]. +TIPs that bind autonomously are thought to recognize structural elements unique to the GTP-tubulin cap at the plus-end, as the protofilaments in this region curve outwards rather than remaining straight as they do in the lattice [129, 130]. This enables the proteins to track growing MT ends and dissociate from the MT further down the lattice. The most well-characterized autonomous tip-trackers are members of the end-binding (EB) protein family, consisting of EB1, EB2, and EB3 in mammalian cells [131, 132]. The EB protein family is highly conserved across organisms with homologs found in yeast, *Drosophila*, and plants [133-137]. The EBs are commonly termed the “master regulators” of the +TIP network, as they not only directly bind MTs but also recruit a diverse array of +TIPs to the MT plus-end.

While all three mammalian EBs can accumulate at the plus-end, EB1 and EB3 largely outcompete EB2 for binding, resulting in EB2 localization shifting to the MT lattice [130, 132]. Beyond their similar localization patterns, EB1 and EB3 are partially redundant in function as well, although in some cell types the proteins display more specialized, unique functions [138, 139]. When examined *in vitro*, both EB1 and EB3 induce catastrophe events while also promoting MT growth by stabilizing interactions between lateral protofilaments [132, 140, 141]. Interestingly EB1 and EB3 suppress catastrophe events *in vivo*, suggesting that binding partners largely influence the impact of EBs in cells [126, 132, 142]. One extensively studied EB binding partner is cytoplasmic linker protein 170 (CLIP-170) which localizes diffusely along the MT lattice in the absence of EBs [127, 143]. When concentrated at the plus-end by EBs, CLIP-170 links cargo to MTs and recruits the dynein-dynactin complex for subsequent retrograde cargo trafficking [144-146]. A number of other EB binding partners influence the stability of MTs. When EB1 binds the

tumor suppressor protein adenomatous polyposis coli (APC) at the cell's leading edge, the complex induces MT stabilization and promotes cell migration [95]. On the other hand, EB1 can also recruit the MT destabilizing kinesin protein MCAK to plus-ends which triggers depolymerization [128, 147]. The EBs indeed have a large influence on MT dynamics given the functional diversity of their interacting partners. However, there is an EB-independent complex in humans that forms ahead of the EBs on the plus-end that is comparatively less well understood [148]. This complex is composed of the MT polymerase colonic and hepatic tumor-overexpressed gene (chTOG) and transforming acidic coiled coil protein 3 (TACC3) (Figure 5).

### **chTOG and TACC3**

chTOG is evolutionarily conserved across eukaryotes, with homologs to the human protein found in yeast (Alp14, Dis1, Stu2), plants (MOR1), *Drosophila* (Msps), and *Xenopus* (XMAP215) [149-152]. chTOG was first identified in humans as a gene upregulated in a number of cancers [153]. Subsequent studies determined that chTOG dysregulation leads to mitotic aberrations including defects in chromosomal segregation [154, 155]. In mitotic cells, MTs nucleate from two poles formed by centrosomal duplication and migration to opposing ends of the cell [156]. MTs emanate from the poles to form a bipolar spindle which coordinates chromosomal segregation. During mitosis in *Xenopus*, yeast, and human cells, chTOG localizes to both the spindle poles at the MT minus-end as well as to the spindle MT plus-ends [150, 157-159]. At the plus-end, chTOG acts ahead of EB1 as a MT polymerase by binding tubulin dimers and facilitating their transfer to the growing MT end [148, 160, 161] (Figure 5). At the minus-end, chTOG facilitates MT nucleation likely by promoting nascent MT outgrowth [162-164]. During interphase, chTOG

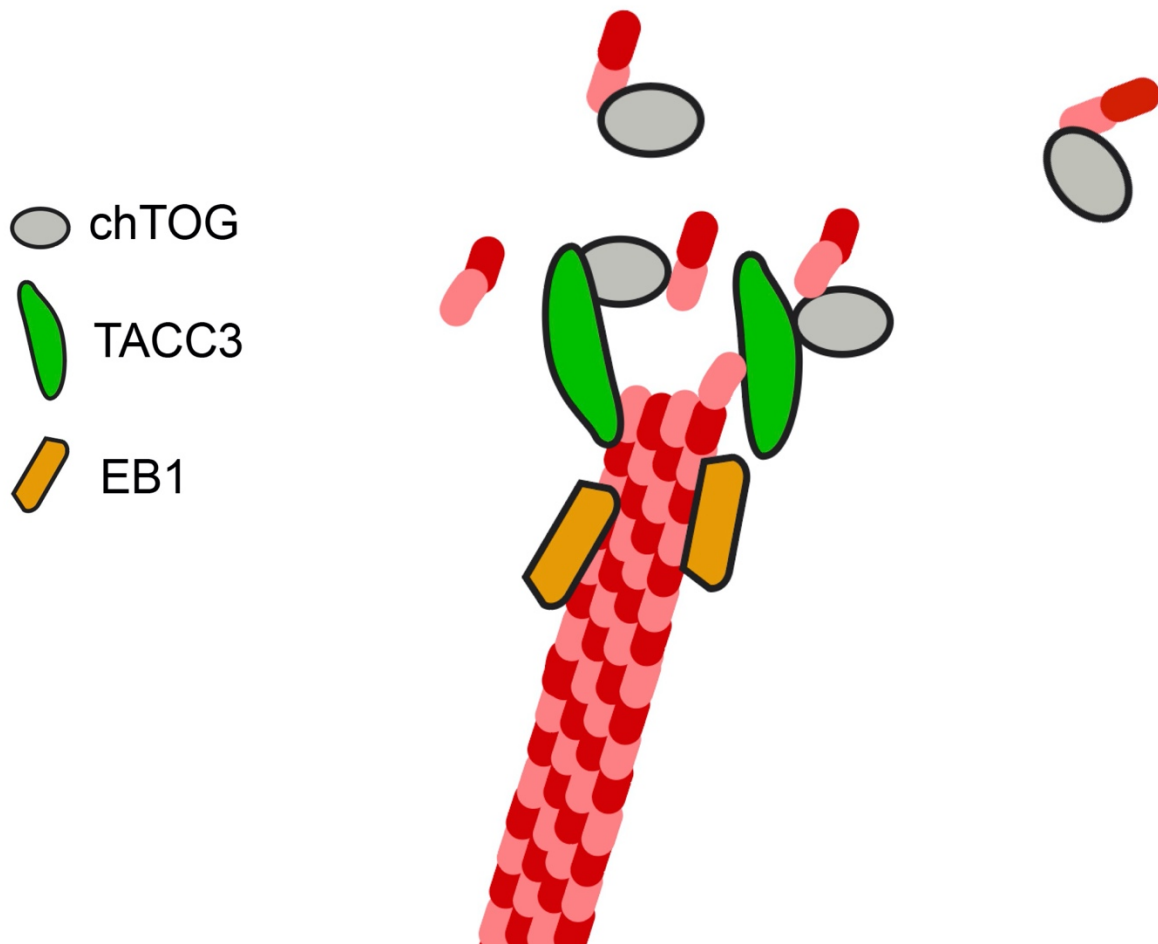


**Figure 5** chTOG, TACC3, and EB1 at the microtubule plus-end. Depicted here is the plus-end of a microtubule. While EB1 (orange) is commonly referred to as the master regulator of microtubule dynamics due to its ability to bind plus-ends and recruit other +TIPs there, the chTOG/TACC3 (grey/green) complex localizes ahead of EB1 on the MT plus-end and acts independently of the EB proteins. chTOG binds tubulin dimers (pink/red) and adds them to the growing MT end. TACC3 increases the efficiency of chTOG binding at the plus-end.

plays similar roles at the MT plus-end [159, 165, 166]. Depletion of chTOG in interphase cells results in reduced MT growth rates along with disrupted organization of the MT array [165, 167, 168]. While chTOG can autonomously bind to MTs and accelerate nucleation and growth rates *in vitro*, chTOG requires members of the transforming acidic coiled-coil (TACC) protein family to efficiently localize to centrosomes and MT plus-ends *in vivo* [154, 160, 169-172].

Similarly to chTOG, TACC proteins are conserved across eukaryotes and have been associated with a number of human cancers [173-176]. While vertebrates such as human, mouse, and *Xenopus* contain three TACC proteins (TACC1, TACC2, and TACC3), less complex organisms such as *Drosophila* and yeast express a single TACC protein [173, 176-178]. The interaction between chTOG and TACC proteins is well-conserved in all species examined [154, 172, 179]. During mitosis, the TACC proteins colocalize with chTOG at the spindle poles, along the spindle lattice, and at the spindle plus-ends [172, 179-181]. Centrosomal localization of TACC proteins is controlled by Aurora-A phosphorylation of the protein's C-terminal domain [176, 182, 183]. Interestingly, Aurora-A phosphorylation is not required for TACC localization at the spindle plus-end, indicating separate pools of TACC are targeted for minus and plus-end activity [181, 183]. Studies in yeast and *Xenopus* demonstrate that the presence of TACC significantly increases chTOG localization at the plus-end (Figure 5) [184, 185]. Depletion of TACC proteins disrupts the recruitment of chTOG to the spindle during mitosis, resulting in disorganized spindle MTs and mitotic defects [154, 172, 179]. Importantly, there are some distinctions between the TACC homologs in regards to their role at the centrosome. While in *Drosophila* TACC is required for efficient chTOG localization at the centrosome and spindle elongation, in HeLa cells depletion of TACC3 affects neither, though it does result in loss of chTOG along spindle MTs [154, 159, 181,

185, 186]. One possible explanation for this discrepancy is that human cells contain more than one TACC protein and thus there may be functional redundancy between the proteins at the centrosome. Of the three human TACC proteins, TACC1 and TACC2 are predicted to have arisen most recently in evolutionary time from gene duplication events of TACC3 [175, 176]. All three TACC proteins contain a conserved coiled-coil domain in the C-terminus, termed the TACC domain, which is sufficient for interactions with both MTs and chTOG [173, 180, 187, 188]. By contrast, the N-termini of human TACCs vary significantly in length and sequence, which may contribute to functional divergence between the proteins [175]. Human TACC proteins also vary in spatial and temporal expression patterns across human tissues, with TACC3 most widely expressed of the three [189].

While the role of TACC proteins during mitosis has been well-established, much less is known about how TACC proteins function during interphase. The vast majority of studies examining TACC proteins during interphase use yeast or *Xenopus* model systems. In fission yeast cells, TACC protein Alp7 colocalizes with interphase MTs and regulates MT growth through its interaction with chTOG homolog Alp14 [190]. As the cells enter interphase, Alp7 facilitates the shuttling of Alp14 from the nucleus to the cytoplasm which is required for efficient MT growth and organization [179, 191]. During interphase in *Xenopus* cells, all three TACC proteins exhibit MT plus-end tracking behavior, colocalizing with chTOG and ahead of EB1 [177, 192, 193]. With some variation depending on cell type examined, overexpression of each *Xenopus* TACC results in increased MT polymerization, indicating a degree of functional overlap between TACC1, TACC2, and TACC3. Interestingly, although human TACC3 tracks MT plus-ends in HeLa cells similarly to its yeast and *Xenopus* homologs, depletion of TACC3 does not alter MT plus-end

growth in this cell type, though these findings are limited to one study [159]. Given the functional variation in TACC proteins between organisms and between cell types, the role of TACC3 in regulating interphase MTs remains uncertain, particularly in human cells.

Due to its upregulation in a number of human cancers including multiple myeloma, breast cancer, and glioblastoma, there is high potential for TACC3 to serve as a therapeutic target in cancer treatment [194-197]. Indeed, recent studies demonstrate that targeting TACC3 with a small molecule inhibitor blocks cell growth in breast cancer cells and reduces glioblastoma and breast cancer tumor growth in mice [197-199]. Given the clinical significance of TACC3 in regards to human cancers, investigating TACC3 behavior during interphase is key to more fully understanding how targeting this protein will impact human cells.

### **Viruses and the microtubule network**

With the MT network so central to facilitating the wide range of cellular processes discussed above, it is perhaps unsurprising that viruses have developed mechanisms to control MTs during infection [200]. Early studies that used harsh MT-depolymerizing drugs like nocodazole successfully demonstrated that disruption of MTs blocks several different virus infections in cells, but failed to achieve a more nuanced understanding of how the viruses engage with and manipulate the MT network during infection [12, 52, 201-204]. Subsequent research has focused on uncovering the mechanistic details behind virus-MT interactions that occur from cell entry to egress.

Viruses gain access to cells by engaging with receptors on the surface of the plasma membrane. Upon binding cellular receptors, viruses can trigger a number of signaling pathways to

rearrange the host cytoskeleton in preparation for entry and subsequent trafficking of viral particles [205]. For instance Kaposi's sarcoma-associated herpesvirus (KSHV) triggers the focal adhesion kinase (FAK) pathway by binding to  $\alpha 3 \beta 1$  integrin receptors at the cell surface, which activates Rho-GTPases and induces MT acetylation [206]. Following cell entry, KSHV capsids then traffic upon acetylated MTs in a dynein-dependent manner towards the nucleus for replication [206, 207]. Viruses can also trigger MT stabilization post-entry within the cytoplasm, as is the case with human immunodeficiency virus type 1 (HIV-1). HIV-1 particles bind a number of +TIPs including Kif4, MAP1, CLASP2, Dia1, and Dia2 to induce MT stabilization prior to particle transport to the nucleus [208-211]. Other viruses depend upon dynamic MTs for intracellular transport, like hepatitis C virus (HCV) which induces MT polymerization early in infection through a direct interaction between the viral core protein and tubulin [212]. In fibroblasts HSV-1 also uses dynamic MTs to facilitate viral particle transport to the nucleus, with incoming HSV-1 particles engaging dynamic MTs through a bridging +TIP complex containing EB1, CLIP-170, and dynactin (DCTN1) [213]. Following MT capture at the periphery, HSV-1 particles undergo dynein-mediated retrograde transport towards the nucleus [214, 215]. Later during infection, HSV-1 induces MT stabilization through the viral kinase Us3 which inactivates glycogen synthase kinase 3 beta (GSK3 $\beta$ ) and enables cytoplasmic linker-associated proteins (CLASPs), downstream of GSK3 $\beta$ , to stabilize MTs at the trans-Golgi network [216]. This MT stabilization pathway plays an essential role in HSV-1 virion egress and viral spread [216].

Viruses also use the MT network to reorganize the intracellular space for optimal replication. In the case of viruses that replicate in the cytoplasm such as HCV and vaccinia virus (VacV), the formation of cytoplasmic replication compartments require a coordinated

rearrangement of host organelles [217, 218]. During HCV infection, the virus upregulates the host protein septin 9 which associates with and stabilizes MTs [219]. Stabilized MTs then recruit lipid droplets, which play a key role in HCV virion assembly, to replication compartments in a dynein-mediated manner [219, 220]. In VacV-infected cells, MTs organize viral mRNA into cytoplasmic aggregates during early infection and facilitate the clustering of mitochondria near these replication sites [221, 222].

The MT network also plays a role in organizing the cell for nuclear-replicating viruses, with HCMV providing a clear example of how involved the MT network can be during different stages of viral infection. As discussed earlier, HCMV infection results in both the alteration of nuclear morphology as well as the rearrangement of the host secretory apparatus to form the viral assembly compartment (AC) [47]. The MT network is intimately involved in both processes and together with MT regulatory proteins provide a mechanical link between the nucleus and the AC during infection [44, 69]. The minus-end directed motor protein dynein is required for maintaining the kidney-bean shape of the nucleus, likely by binding proteins within the nuclear envelope and creating tension as the motor moves on MTs towards the AC [69]. Additionally, dynein and its adaptor protein Bicaudal-D1 (BicD1) are responsible for coordinating retrograde transport of different host and viral proteins to form the AC early in infection [70]. Aside from hijacking motor proteins, HCMV also upregulates all three EB proteins during infection [45]. Interestingly, in contrast to their behavior in uninfected cells EB1 and EB3 exhibit unique localizations and functions in infected cells. While EB1 localizes to MT plus-ends throughout the cytoplasm, EB3 localizes to the AC and promotes nucleation of MTs which become rapidly acetylated [45]. As a result, during mid-stages of infection the AC becomes a hub of acetylated MTs which interact with

the nucleus and maintain the structural integrity of the AC [45]. The AC-derived acetylated MTs then exert mechanical forces which cause the nucleus to rotate around the AC, propagating a polarization of nuclear membrane proteins, including SUN1 and emerin, towards the AC as well as the segregation of viral and host DNA within the nucleus [44, 45]. The MT-driven, dynamic events surrounding the AC are crucial for HCMV replication, egress, and spread, highlighting the precision with which a virus can coordinate the MT network to promote infection.

### **Summary and key questions**

In this dissertation, I address a number of questions regarding how two herpesviruses, HSV-1 and HCMV, interact with the MT network during infection. In the section above, I discuss how viruses have developed precise mechanisms to control MT behavior during infection. In particular, I describe how HSV-1 particles use dynamic MTs to reach the nucleus in fibroblast cells [213]. However, the MT network is organized differently depending on cell type and viruses will encounter these differences in the cytoskeleton upon the cell type being infected. As mentioned earlier, neurons in particular have a unique organization of MTs, with highly stabilized MTs in the axon shaft and dynamic MTs in the axon terminal [110]. Given that HSV-1 infects both neuronal and non-neuronal cells over the course of infection in humans, I begin Chapter 3 by examining how cell type affects the mechanism by which HSV-1 engages MTs to reach the nucleus. In answering this question I determine that while HSV-1 indeed requires different +TIPs and MT subsets to infect neuronal and non-neuronal cells, there is a common requirement for the +TIP TACC3 that underscores a previously unappreciated role of TACC3 in controlling interphase MT dynamics across human cell types. With these studies providing new insight into the role of

TACC3 in human interphase cells both during and outside of HSV-1 infection, extending on this in Chapter 4 I investigate whether HCMV uses TACC3 to facilitate the formation of the AC, a process that depends heavily on coordination of the MT network. I uncover that HCMV specifically upregulates TACC3 in order to enhance MT growth during late stages of infection, which TACC3 does by regulating the cytoplasmic availability of the MT polymerase chTOG. Together these findings raise the possibility that other viruses exploit the TACC3-chTOG complex to manipulate MT behavior, given the central nature of the complex in dictating MT growth. The implications of this work extend beyond the context of viral infection as well, as these findings contribute to our understanding of a clinically important factor involved in human cancer.

## CHAPTER 2: Materials and Methods

### Cell lines

All cells described below were maintained at 37°C and 5% CO<sub>2</sub>.

*For Chapters 3 and 4:* Certified Primary Normal Human Dermal Fibroblasts (NHDFs, Lonza CC-2509) isolated from human male neonatal foreskin were cultured in Dulbecco's Modified Eagle's Medium (DMEM, Fisher Scientific) containing 5% Fetal Bovine Serum (FBS), 1% L-Glutamine, and 1% penicillin-streptomycin. Only low passage NHDFs (less than passage 25) were used for experiments. *For Chapter 4:* For experiments using growth-arrested cells, NHDFs were grown to confluency in the media described above before being washed in PBS and cultured in DMEM supplemented with 0.2% FBS, 2mM L-Glutamine, and 1% penicillin-streptomycin for 72 hours.

*For Chapter 3:* Phoenix-AMPHO (ATCC), Vero, and BSC40 cells (Dr. Ian Mohr, NYU School of Medicine) were cultured in DMEM (Fisher Scientific) containing 5% FBS, 1% L-Glutamine, and 1% penicillin-streptomycin. SK-N-SH cells, originally isolated from a female neuroblastoma patient, were obtained from Dr. Patricia Spear at Northwestern University in Chicago, IL. SK-N-SH cells were maintained in DMEM containing 10% FBS, 1% L-Glutamine, and 1% penicillin-streptomycin. Only low passage SK-N-SHs (less than passage 7) were used for experiments.

### Virus strains

*For Chapter 3:* Wildtype HSV-1 strain F and HSV-1 K26GFP were obtained from Dr. Prashant Desai at John Hopkins University in Baltimore, MD and were propagated on sub-confluent Vero cells in DMEM containing 1% FBS, 1% L-glutamine, and 1% penicillin-streptomycin [216, 223]. Virus was collected once more than 90% cytopathic effect was reached by scraping the cells into the culture medium and lysing the cells through three rounds of freeze-thawing. The virus-containing medium was then spun down by centrifugation to remove cell debris before aliquoting. To titer, the virus was serially diluted and added to sub-confluent Vero cells in a 6-well plate. Cells were fixed 2 days post infection using 10% trichloroacetic acid (TCA) in PBS and plaques were counted using crystal violet staining. Vesicular Stomatitis Virus (VSV) was propagated and titrated on BSC40 cells [224]. Multiplicity of infection (MOI) details for individual experiments involving viral infection are described in Chapter 3.

*For Chapter 4:* HCMV TB40/E strains expressing an eGFP reporter, UL99-eGFP, or UL99-mCherry were previously generated in the lab by Dr. Dean Procter using BAC recombineering (Procter 2018, 2020). TB40/E strains were propagated on NHDFs in DMEM containing 1% FBS, 1% L-glutamine, and 1% penicillin-streptomycin. Media was changed every three days until cells reached greater than 90% cytopathic effect or around 17 days post infection, at which time the virus was collected. Supernatants and cells were harvested, with the cells undergoing three rounds of freeze-thaw to release cell-associated virus. Cellular debris was removed by centrifugation. Virus was titrated by serial dilution on NHDFs followed by plaque counting using phase and fluorescence microscopy. Protocol for low MOI HCMV spread assays is described in detail below. For all other experiments, NHDFs were grown to confluency and infected at an

MOI of 1. Since HCMV infection induces cell cycle arrest, all cells were growth-arrested as described above prior to infection for experiments involving bulk non-single cell analysis by western blot. This eliminates the possibility of uninfected control cells continuing to divide while infected cells undergo cell-cycle arrest.

### **RNA-interference (RNAi)**

*For Chapter 3:* For siRNA transfections in SK-N-SH cells, SK-N-SHs were seeded into a 6-well plate and transfected at 60% confluency the following day with 150 pmol/ml siRNA using RNAiMax (Thermo Fisher Scientific), according to manufacturer's protocol. SK-N-SHs required a second round of 150 pmol/ml siRNA treatment three days after the first, in order to obtain efficient protein depletion. Cells were split into 12-well plates two days after the second siRNA treatment. The following day, cells were infected or processed as described in the main text of Chapter 3. For experiments involving co-depletion by multiple siRNAs, 150 pmol/ml of each siRNA was used, with control non-targeting siRNA added to ensure all samples were treated with equal amounts of siRNA. For siRNA transfections in NHDFs, cells in a 12-well were treated with a single round of 150 pmol/ml siRNA. Three days following siRNA treatment, NHDFs were infected or processed as described in the main text of Chapter 3. siRNAs used in this study were obtained from Thermo Fisher Scientific: control (Cat# AM4635), EB1 (3891), EB2 (21079, 136575), EB3 (19984), CLIP-170 (142517), TACC3 (135672, 3056), KIF5A (s7837), KIF5B (s731), and KIF5C (s7842).

*For Chapter 4:* For siRNA experiments, confluent NHDFs were transfected with 150 pmol/ml siRNA using RNAiMax (Thermo Fisher Scientific) according to manufacturer's protocol. All siRNA transfections occurred at 5 hours post TB40/E infection. siRNAs used in this chapter were obtained from Thermo Fisher Scientific: control (Cat# AM4635), TACC3 (135672, 3056), and chTOG (122705).

### **Plasmids**

*For Chapter 3:* The vector containing GFP-tagged TACC3 (pBRAIN-GFP-TACC3-KDP-shTACC3) was obtained from Stephen Royle via Addgene. Human TACC3 was PCR amplified from pBRAIN-GFP-TACC3-KDP-shTACC3 to generate a FLAG-tagged TACC3 vector, using the following primers that contain AgeI and BamHI restriction sites:

Forward:

5'GCAACCGGTGCCACCATGGACTACAAAGACGATGACGACAAGAGTCTGCAGGTCT  
TAAAC 3'

Reverse:

5'GCAGGATCCTTATCTAGAGATCTTCTC 3'

To generate a vector expressing untagged TACC3, human TACC3 was PCR amplified from pBRAIN-GFP-TACC3-KDP-shTACC3 using the following primers containing NotI and AgeI restriction sites:

Forward:

5'GCAGCGGCCGCGCCACCATGAGTCTGCAGGTCTTAAAC 3'

Reverse:

5'GCAACCGGTTTAGATCTTCTCCATCTTGGA 3'

These PCR products were purified using the QIAquick PCR purification kit, digested with the enzymes listed above, and ligated into the retroviral vector pQCXIP from Clontech. The inserts were confirmed by sequencing at the Northwestern University Sequencing Core. In order to transiently express GFP- or FLAG-tagged TACC3 in SK-N-SHs, cells in a 12-well plate were transfected with 1  $\mu$ g of vector DNA using Lipofectamine 3000 (Thermo Fisher Scientific), according to manufacturer's protocol. After 3 days, the cells were imaged or processed as described in the main text of Chapter 3. For transient expression of GFP- or FLAG-tagged TACC3 in NHDFs, cells from a 10 cm dish were electroporated with 2  $\mu$ g of vector DNA using the human dermal fibroblast protocol provided for Amaxa<sup>TM</sup> 4D-Nucleofector<sup>TM</sup> (Lonza). After 1 day, the cells were imaged or processed as described. Retrovirus expressing untagged or FLAG-tagged TACC3 was produced by transfecting a 10 cm dish of Phoenix-Ampho cells with 10  $\mu$ g of the pQCXIP vectors described above using Lipofectamine 3000. Cell media was changed the following day and retrovirus-containing supernatants were collected and filtered through a 0.45 $\mu$ m filter 2 days post transfection. For transient expression, SK-N-SHs in a 12-well plate were transduced with retrovirus expressing untagged TACC3, FLAG-tagged TACC3, or retrovirus containing an empty pQCXIP control vector. For each well, 0.75  $\mu$ l of 10mg/ml polybrene was included during the transduction to increase infection efficiency. After 5 hours, the cells were washed twice with PBS and fresh media without polybrene was added. For rescue experiments involving both siRNA knockdown and retrovirus transduction, SK-N-SHs were split from a 6-well plate to a 12-well plate one day following the second siRNA treatment, described above. The next day, SK-N-SHs were transduced with the retroviral vectors indicated in the main

text. One day post transduction, the cells were processed or analyzed as described in the main text. To generate retrovirus that expresses eGFP-CLIP170, the retroviral vector pBABE-puro-AA-GFP-CLIP170 [45] was transfected into Phoenix-Ampho cells and supernatants were collected as described above. For stable expression of eGFP-CLIP170 in NHDFs, very low passage (less than passage 6) NHDFs were grown to 50-75% confluency in DMEM containing 5% FBS and 1% L-glutamine in a 6 cm dish. The cells were then transduced with pBABE-puro-AA-GFP-CLIP170 retrovirus supernatant in the presence of 3  $\mu$ l 10mg/ml polybrene. Five hours post transduction, media was replaced with fresh DMEM without polybrene. The following day the media was changed to include 0.8  $\mu$ g/ml puromycin. Following this, the media and puromycin was replaced every other day for about 6 days to select for cells expressing the vector. Cells were then split into 10 cm dishes for use or freezing down, with cells now maintained in DMEM containing 0.16  $\mu$ g/ml puromycin.

*For Chapter 4:* In attempts to rescue TACC3 levels in siRNA-treated NHDFs during HCMV infection, infected NHDFs were treated with siRNA at 5 hours post infection as described above. At 24 hours post infection, NHDFs were transduced with retrovirus expressing either untagged-TACC3 or empty pQCXIP, including 0.75  $\mu$ l polybrene per well. In order to not disrupt infection, media was not changed after transduction. Cells were lysed at 14 days post infection and analyzed by western blot, as described below.

### **Chemicals and nocodazole treatments**

*For Chapter 3:* Bafilomycin A1 (Sigma, B1793) was used at a concentration of 100 nM and actinomycin D (MP Biomedicals) was used at a concentration of 1 µg/ml. For nocodazole dose experiments, cells were treated with DMSO (solvent control) or 10 µM nocodazole for 3 hours prior to infection or incubation with transferrin to depolymerize all microtubules. To selectively depolymerize dynamic microtubules, cells were treated with 500 nM nocodazole for 2 hours prior to infection or incubation with transferrin. The total amount of DMSO was equivalent across all samples. For infections, cells were then infected with HSV-1 at MOI 10 for 5 hours before being lysed and analyzed by western blot, as described below. To visualize incoming virus particles by immunofluorescence, cells were seeded onto coverslips in a 12-well plate prior to nocodazole treatment. In order to image virus particles through VP5 staining, actinomycin D was used as follows to prevent de-novo production of VP5 which would interfere with visualizing the incoming capsids. The cells were treated with 1 µg/ml actinomycin D for 1 hour prior to infection. Cells were then infected at MOI 20 for 4 hours before fixation in ice-cold methanol and staining using the indicated antibodies. Nocodazole washout assays were carried out on NHDFs or SK-N-SHs seeded onto coverslips in a 12-well plate. A day after the cells were seeded, cells were treated with 10 µM nocodazole for 6 hours to ensure the total depolymerization of microtubules prior to washout. After 6 hours of nocodazole treatment, the cells were washed in PBS before fresh media was added. After the times indicated in the main text of Chapter 3, the cells were fixed in ice-cold methanol, stained using antibodies described in the main text, imaged, and processed as detailed below. The ImageJ threshold area function was used to determine total area of microtubule regrowth after nocodazole washout. Thresholds were set to be identical across all images processed.

### **Western blot analysis**

*For Chapters 3 and 4:* For analysis by western blot, cells were lysed in Laemmli buffer consisting of 62.5 mM Tris-HCl at pH 6.8, 2% SDS, 10% glycerol, and 0.7 M  $\beta$ -mercaptoethanol. Lysates were then boiled for 3 minutes and resolved using a 10% SDS-PAGE gel. Gels were transferred at 57 V for 1 hour onto nitrocellulose membranes (GE Healthcare Life Sciences). All of the following incubation steps were done while rocking the membranes. Membranes were blocked for 1 hour at room temperature in 5% non-fat milk diluted in TBS containing 0.1% Tween (TBS-T). The membranes were then washed three times in TBS-T and incubated overnight at 4°C with the indicated primary antibodies diluted in 3% BSA/TBS-T. The following day the blots were washed three times in TBS-T and then incubated for 1 hour at room temperature with the corresponding HRP-conjugated secondary antibodies diluted in 5% non-fat milk/TBS-T. The membranes were washed again three times in TBS-T before incubation with Pierce ECL Western Blotting Substrate (Thermo Fisher Scientific). The membranes were then exposed on x-ray film. For densitometry analysis, scanned films were processed using the ImageJ Gel Analyzer tool and adjusted relative density was calculated using  $\beta$ -actin (Chapter 3) or  $\alpha$ -tubulin (Chapter 4) as loading controls. *For Chapter 4:* Protein levels were quantified relative to mock-infected cells.

### **Fixed and live cell microscopy**

*For Chapters 3 and 4:* For immunofluorescence (IF) experiments, cells were seeded onto No. 1.5 glass coverslips in a 12 well plate. Cells were rinsed in PBS prior to fixation. For fixation, cells were incubated in either ice cold methanol for 7 minutes (all IF experiments in Chapter 3, as

indicated in Chapter 4) or 4% paraformaldehyde (Affymetrix) at room temperature for 20 minutes (as indicated in Chapter 4) before being rinsed three times in PBS. Samples were blocked at 37°C for 30 minutes in PBS containing 0.25% saponin and either 10% fetal bovine serum (FBS) for experiments in Chapter 3 or 10% human serum (HS) for experiments in Chapter 4. After blocking, samples were incubated overnight at 4°C with the indicated primary antibodies diluted in PBS containing 0.025% saponin and 10% FBS (Chapter 3) or 10% HS (Chapter 4). The following day, samples were washed three times for 5 minutes in wash buffer consisting of 0.025% saponin in PBS and samples were then incubated for 1 hour at room temperature with the appropriate Alexa Fluor-conjugated secondary antibodies diluted in PBS containing 0.025% saponin and 10% FBS (Chapter 3) or 10% HS (Chapter 4). Samples were then incubated with 0.03% Hoechst 33342 (Thermo Fisher Scientific, 62249) diluted in wash buffer for 5 minutes, followed by two 5 minute washes in wash buffer. Coverslips were then dipped in deionized water, gently tapped to dry, and mounted on slides using 5  $\mu$ l FluorSave (EMD Millipore, 345789). Slides were imaged by wide field microscopy using a Leica DMI6000B-AFC microscope using a 100x objective (HC PL APO 100 $\times$ /1.44 NA oil), an ORCA-FLASH 4.0 CMOS camera, and MetaMorph software. Images were then processed in ImageJ, with equivalent settings applied across all images in a given dataset.

*For Chapter 3:* For confocal microscopy, cells were imaged using a motorized spinning-disc confocal microscope (Leica DMI 6000B) with Yokogawa CSU-X1 A1 confocal head. Confocal z-stacks were acquired at 0.2 $\mu$ m intervals and maximum intensity Z-projections were created using ImageJ software. For time-lapse microscopy experiments, cells were grown in four-

compartment 35 mm glass bottom dishes (Greiner Bio-One). Cell culture media was changed immediately before imaging to Leibovitz's L-15 Medium without phenol red (Thermo Fisher Scientific) supplemented with 2 mM L-Glutamine and 5% FBS. Cells were imaged at 100x using a Leica DMI6000B-AFC microscope with an environmental chamber at 37°C (InVivo). For time-lapse imaging of viral particles, cells were infected with HSV-1 K26GFP at MOI 100 in Leibovitz's L-15 medium and immediately imaged at 1 second intervals for 4-5 minutes. Virus particle motility was quantified by manual particle tracking in ImageJ, with individual particles tracked for at least 10 seconds and virus particle displacement relative to the nucleus calculated between the first and final frame of the track.

Virus Particle Displacement =

$$\sqrt{(x_{first} - x_{last})^2 + (y_{first} - y_{last})^2}$$

For live-cell analysis of cells expressing GFP-tagged CLIP170 or TACC3, images were acquired at 500 ms intervals for 1 minute. For experiments involving transferrin, cells were incubated with 25 µg/ml Alexa Fluor 647-conjugated transferrin (Thermo Fisher Scientific) for 30 min at 37°C. For subsequent IF analysis, cells were fixed in ice-cold methanol, stained with the antibodies indicated in the main text of Chapter 3, and imaged as described above. For live-cell imaging of transferrin, cell medium was changed to fresh L-15 medium and cells were then imaged at 500 ms intervals for 30 seconds.

*For Chapter 4:* For time-lapse microscopy experiments involving HCMV infection, NHDFs were grown to confluency in four-compartment 35 mm glass-bottom dishes (Cellvis: Cat# D35C4-20-

1.5-N). Cells were then infected with TB40/E-UL99-GFP at MOI 1 and treated with siRNA at 5 hours post infection as described above. At 5 days post infection, cell media was changed to L-15 medium and cells were imaged at 100x using a Leica DMI6000B-AFC microscope with an environmental chamber (InVivo) at 37°C. Images were acquired at 2 second intervals for 4 minutes and time-lapse videos were processed using ImageJ. Total distance travelled per particle was quantified by manual tracking in ImageJ of individual particles for 20 seconds, or 10 frames. The ImageJ manual tracking tool records the distance between tracking points in each frame. Distances were summed across 10 frames per particle and total distance travelled per particle was averaged across 10 particles per cell.

### **Image analysis and quantification**

*For Chapter 3:* For quantification of EB1 comet number in fixed cells, identical thresholds for EB1 staining were applied across all conditions using ImageJ. Individual cells were manually outlined using tyrosinated-tubulin staining and the number of EB1 comets within the outlined cell was determined using the particle analysis tool in ImageJ. For quantification of chTOG levels in the nuclei of fixed cells, the corrected total fluorescence intensity (CTFI) of chTOG staining in the nucleus was averaged across the indicated number of cells. The CTFI of nuclear chTOG was determined by using Hoechst staining to manually outline the nucleus, applying the nuclear outline to corresponding images of chTOG staining, and using ImageJ to obtain the integrated density and area of each outlined region along with the mean grey value of the background. The product of the mean grey value of the background and the area of each region was subtracted from the region's integrated density to give the CTFI.

Corrected Total Fluorescence Intensity =

$$\text{Integrated Density} - (\text{Area} \times \text{mean grey value of background})$$

The above calculation was also used to quantify CTFI of cytoplasmic TACC3 and perinuclear transferrin, using the whole cell area excluding the nucleus and a fixed circular area adjacent to the nucleus, respectively, as the area of interest. The area of TGN staining was quantified using the ImageJ threshold area function, with identical thresholds for TGN46 staining set across all conditions before analysis. For quantification of cell diameter,  $\beta$ -actin or overexposed acetylated-tubulin staining was used to determine cell bounds and a line across the cell perpendicular to the nucleus was measured in ImageJ. Two quantifications were used to analyze HSV-1 infectivity in fixed cells. For the first quantification, cells were infected with HSV-1 at MOI 20 for 4 hours before being fixed and stained for HSV-1 immediate early protein ICP4 and Hoechst. For the second quantification, cells were treated with 1  $\mu$ g/ml actinomycin-D for 1 hour before infection to inhibit de-novo production of HSV-1 capsid protein VP5. Cells were then infected at MOI 20 for 4 hours before being fixed and stained for VP5 and Hoechst. The indicated number of nuclei were then accessed manually for either ICP4 expression or VP5 accumulation at the nucleus, measured relative to the control condition. To analyze HSV-1 cell entry, cells were infected with HSV-1 at MOI 30 for 30 and 60 minutes before being fixed and stained for HSV-1 glycoprotein gB and capsid protein VP5. To have a control for visualizing gB and VP5 in virus prior to cell entry, cells were infected at MOI 30 for 1 hour at 4°C before being fixed and stained as described above. The fraction of viral particles that had entered the cell was calculated by dividing the number of green VP5 particles by the total number of viral particles, including both green VP5 particles and yellow (green VP5 and red gB colocalizing) particles.

*For Chapter 4:* To quantify chTOG levels in the assembly compartment (AC) or in the cytoplasm of fixed cells, the AC area was manually outlined using gB staining while the cytoplasmic area, which excludes the AC and the nucleus, was outlined using gB and Hoechst staining. The AC and cytoplasm outlines were applied to corresponding images of chTOG staining and CTFI was calculated using the equation described above for Chapter 3. The ratio of cytoplasmic chTOG to AC chTOG and vice versa was calculated by dividing the respective CTFI values. CTFI ratios were averaged across 25 cells per condition.

*For Chapters 3 and 4:* To analyze EB1 comet length in fixed cells, the fluorescence intensity of EB1 staining along individual microtubules was quantified using the line-scan function in ImageJ. Prior to analysis, line-scans were normalized and aligned in Excel, as described previously [45].

### **Viral titering and HCMV spread assays**

*For Chapter 4:* To determine the effects of RNAi on virus production during high MOI infection, NHDFs were infected with TB40/E-GFP at MOI 1 and treated with the indicated siRNAs at 5 hours post infection. Seven days post infection the supernatants were collected and diluted in a 1:10 series. The 1:10 dilution series was titrated on confluent NHDFs in 12 well plates, with four technical replicates for each dilution per individual experiment. GFP-positive plaques for the appropriate dilution were counted at 12 days post infection. Plaques were imaged at 10x using a Leica DMI8 S module Infinity TIRF microscope with Leica DFC9000 sCMOS camera and LAS X control software (Leica Microsystems, Leica Application Suite X version 3.4.2.18368). To examine the effects of RNAi on viral spread during low MOI infection, NHDFs were infected with

TB40/E-GFP at MOI 0.001 and treated with the indicated siRNAs at 5 hours post infection. GFP-positive plaques were imaged by fluorescence microscopy at 14 days post infection using the same microscope described above. Plaque areas were quantified using the ImageJ threshold area function with identical thresholds set across all conditions before analysis.

### **Antibodies**

The following antibodies were used for western blotting or IF analysis.

*For Chapter 3:* **Abcam:** ICP4 (ab6514), ICP0 (ab6513), VSV-G (ab50549), Kif5A (ab5628), Kif5B (ab25715), Kif5C (ab5630), de-tyrosinated-tubulin (ab48389); **Cell signaling technologies:** TACC3 *for western* (8069S), Flag *for IF* (15009), **MilliporeSigma:** Flag M2 *for western and 1 IF* (F3165), TACC2 (07-228), EB3 (AB6033); **Santa Cruz Biotechnology, Inc:** CLIP-170 (sc-25613); **Absea:** EB2 (010614A11); **Bethyl:** Pericentrin (IHC-00264); **BioLegend:** chTOG (620401); **Novus Biologicals:** TACC1 (NBP189447); **Bio-Rad:** TGN46 (AHP500GT); **Virusys:** VP5 (HA018). Anti-gB antibody was a gift of Dr. Richard Longnecker (Northwestern University, Chicago, IL). Anti-PABP antibody was a gift from Dr. Simon Morley (University of Sussex, Sussex, England, UK). Anti-tyrosinated-tubulin antibody was a gift from Dr. Gregg Gunderson (Columbia University, New York, NY).

*For Chapter 4:* **Abcam:** TACC3 *for western* (ab134154), HCMV IE1/2 (ab53495); **Invitrogen:** chTOG (PA5-59150), **Virusys:** HCMV UL44 (CA006); **USBiological:** Cytomegalovirus Glycoprotein B (C9100-21N); **Cell signaling technologies:** Rab5 (46449 for dual staining with

Rab7 and 3547 for dual staining with gB), Rab7 (9367). Anti-pp28 was a gift from Dr. Thomas Shenk (Princeton University, Princeton, NJ).

*For Chapters 3 and 4:* **Abcam:** TACC3 for IF (ab134154),  $\alpha$ -tubulin (ab18251),  $\gamma$ -tubulin (ab27074); **Cell signaling technologies:**  $\beta$ -actin (3700); **MilliporeSigma:** Acetylated tubulin (T6793); **Life Technologies:** EB1 (412100).

### **Quantification and statistical analysis**

*For Chapter 3:* GraphPad Prism 7 was used to analyze data and create graphs.

*For Chapters 3 and 4:* Results are shown as mean  $\pm$  standard errors of the mean. Independent sample t-tests were used to assess statistical significance, with p values less than 0.05 considered as significant. Number of biological replicates are indicated in the figure legends.

## **CHAPTER 3: TACC3 Regulates Microtubule Plus-End Dynamics and Cargo Transport in Interphase Cells**

This chapter appeared as the published article: Furey C, Jovasevic V, Walsh D. 2020. *Cell Rep* 30(1):269-283.e6. doi: 10.1016/j.celrep.2019.12.025.

Videos included in the results section can be found in Supplementary Files.

### **Introduction**

The microtubule (MT) network regulates processes ranging from cell division and motility, to cargo transport [126, 225, 226]. Filaments nucleate from a MT Organizing Center (MTOC) and explore the cytosol through phases of polymerization, pause and catastrophe as tubulin heterodimer subunits are either added or removed from their more dynamic plus-end [227, 228]. The MT plus-end transiently contains GTP-bound tubulin before it is hydrolyzed to GDP-tubulin within the filament lattice [228-230]. This GTP-tubulin cap enables the growing MT plus-end to be recognized by members of the end-binding family of proteins, EB1-3 [129, 132, 230]. At the plus-end, EBs can directly suppress catastrophe events leading to enhanced MT growth [132]. EBs also bind and recruit other plus-end tracking proteins (+TIPs) to form functional nodes that control filament growth, stability, spatial organization and interactions with targets such as cortical actin or cellular cargos [126, 128, 140, 231, 232]. While several +TIPs have been identified in recent years, many of which can bind MT filaments independently, most require EB proteins to mediate their specific accumulation at MT plus-ends. For this reason, EBs are widely considered as master regulators of MT function [126].

However, other proteins do operate at the MT plus-end independently of EB proteins yet their functions are less well defined. chTOG (colonic and hepatic tumor-overexpressed gene) is a

microtubule polymerase that binds soluble tubulin dimers and catalyzes their addition to MT plus-ends [160, 161, 233]. chTOG binds MT plus-ends autonomously but its optimal plus-end localization depends upon recruitment by transforming acidic coiled-coil containing (TACC) proteins [184, 185]. Homologs of both chTOG and TACCs are widely-conserved across eukaryotes [149, 176]. Humans express three TACC proteins (TACC1-3) and along with chTOG, TACC's have been extensively studied in the context of mitotic spindle organization during cell division and in cancer [149, 173, 176, 185, 188, 234], although TACC3 is the most widely studied and best characterized family member. By recruiting chTOG, TACC3 functions at the centrosome to regulate MT nucleation, along the MT lattice to stabilize the spindle apparatus, and at the MT plus-end to promote mitotic spindle elongation [154, 172, 180, 181, 185, 186]. However, our understanding of the potential functions of TACC3 in interphase remains limited [165, 235-239]. In yeast, the homolog of TACC3, Alp7 recruits Alp14/TOG to the nucleus during cell division or to the cytoplasm during interphase. The absence of Alp7 results in short spindles during mitosis or defects in MT growth and organization in interphase [179, 184, 190, 191, 240, 241]. Moreover, yeast Alp7 mediates recruitment of Alp14/TOG to MT plus-ends in vitro [184]. Evidence for similar interphase functions of TACC3 are also emerging in higher organisms. TACC3 has been shown to recognize interphase MT plus-ends in *Drosophila* and *Xenopus* embryonic cells, as well as in human HeLa and Rpe1 cells [159, 172, 192]. However, while TACC3 homologs promote interphase MT dynamics in both *Drosophila* and *Xenopus* systems, modulating TACC3 levels has been reported to have no effect in HeLa cells [159, 192, 242, 243]. Thus, the potential role of TACC3 in regulating MT dynamics and its broader functionality during interphase remains poorly understood, particularly in human cells.

As intracellular pathogens, viruses are dependent upon MTs to facilitate their replication [200]. However, the importance of +TIPs during infection has only recently begun to emerge [45, 208, 211, 213, 216]. Of particular relevance to this study, we previously showed that EB1 and the +TIP, Cytoplasmic Linker-associated Protein 170 (CLIP170) are required for herpes simplex virus type 1 (HSV-1) particles to load onto dynamic MTs for subsequent motor-mediated transport to the nucleus in dermal fibroblasts [213]. However, *in vivo* HSV-1 infects a variety of cell types that include epithelial, dermal and neuronal cells [244]. Many cell types contain mixtures of both dynamic and stable MT arrays, but neuronal cells contain a particularly high proportion of stabilized filaments [245-248]. While dynamic MTs have a relatively short half-life, stable MTs are long-lived and therefore accumulate higher levels of several tubulin post-translational modifications [106]. Tubulin PTMs include acetylation at Lysine 40, which resides within the lumen of the filament and confers mechanical strength against breakage [108, 109]. While acetylation can occur quite rapidly another PTM, tubulin detyrosination, appears to occur more gradually and accumulates largely on stable MTs. Tubulin detyrosination occurs on the cytosolic side of the MT filament [249, 250] and alters interactions with motors to favor kinesin-1 activity [121-123]. As such, distinct properties conferred by different tubulin PTMs enable stable MTs to serve as long-lived, specialized tracks for cargo sorting [106].

Here, in examining the role of +TIPs during HSV-1 infection of different human cell types we unexpectedly reveal that EB1 and CLIP170 are required for infection of fibroblasts but not neuronal cells. In neuronal cells, infection was largely mediated by stable, de-tyrosinated MT networks that formed independently of EB1. Stemming from this we find that TACC3 regulates

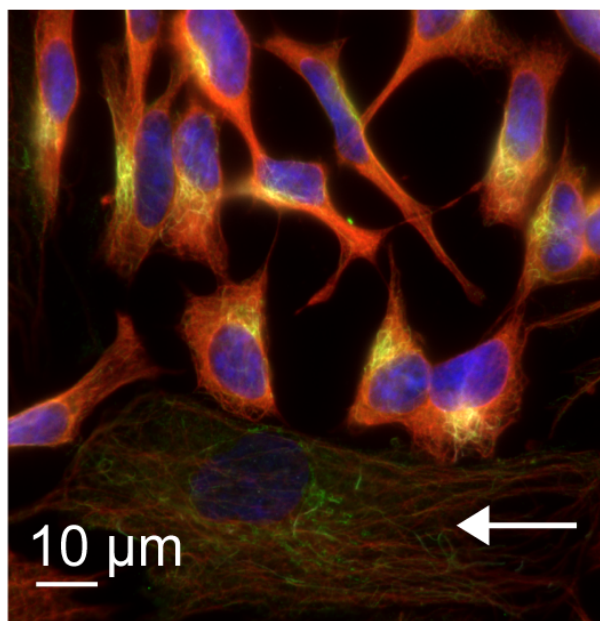
interphase MT dynamics and in neuronal cells, by regulating the organization of de-tyrosinated MT arrays, influences kinesin-1-based sorting of both pathogenic and cellular cargos.

## Results

### **Stable microtubules mediate EB-independent HSV-1 infection in neuronal cells.**

EB1 and CLIP-170 are required for HSV-1 infection in normal human dermal fibroblasts (NHDFs) [213]. This prompted us to test whether these +TIPs also functioned during infection of neuronal cells. To do this, we compared the effects of EB1 or CLIP-170 depletion on infection in NHDFs versus SK-N-SH cells, a human neuroblastoma cell line used to model neuronal infection [251, 252] (Figure 6). Western blot (WB) analysis revealed that while knockdown of either EB1 or CLIP-170 suppressed early infection in NHDFs, as detected by reduced abundance of the viral immediate early Infected Cell Protein 4 (ICP4), depletion of either factor had no effect on infection in SK-N-SHs (Figure 7A). While EB1 is the dominant EB family member in many cell types [126, 132], depletion of the closely related family member, EB3, either alone or in combination with EB1, or depletion of the more distantly related EB2, had no detectable effect on the expression of early viral proteins in SK-N-SHs (Figure 7B-C). Furthermore, Bafilomycin-A1 (BafA) blocked infection of SK-N-SHs by VSV but not HSV-1 (Figure 7D), demonstrating that HSV-1 did not use alternative low-pH fusion (e.g. endocytosis) over its natural route of membrane fusion to enter these cells. This suggested that EB1-mediated dynamic microtubule capture was not a significant mechanism for infection of SK-N-SHs.

A.



B.

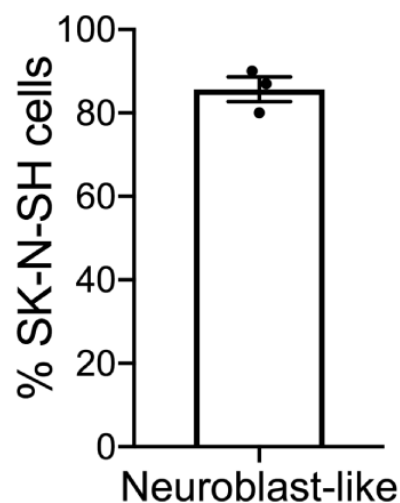


**Figure 6** SK-N-SH cells are a near-pure neuronal cell line. (A) SK-N-SH cells were fixed and stained for tyrosinated tubulin (red), detyrosinated tubulin (grey) and acetylated tubulin (green). Nuclei were stained using Hoechst. Examples of neuroblast-like and epithelial-like cells in the SK-N-SH population are shown. Arrow points to epithelial-like cell that represents the minor subpopulation. (B) The fraction of neuroblast-like cells was quantified. 300 cells were counted over 3 biological replicates. Error bars = SEM. For all IF analyses throughout this manuscript we focus on the predominant neuronal population, while the low levels of epithelial-like cells lacking detyrosinated MTs do not impact WB analyses. Representative image is shown of results derived from 3 independent experiments.

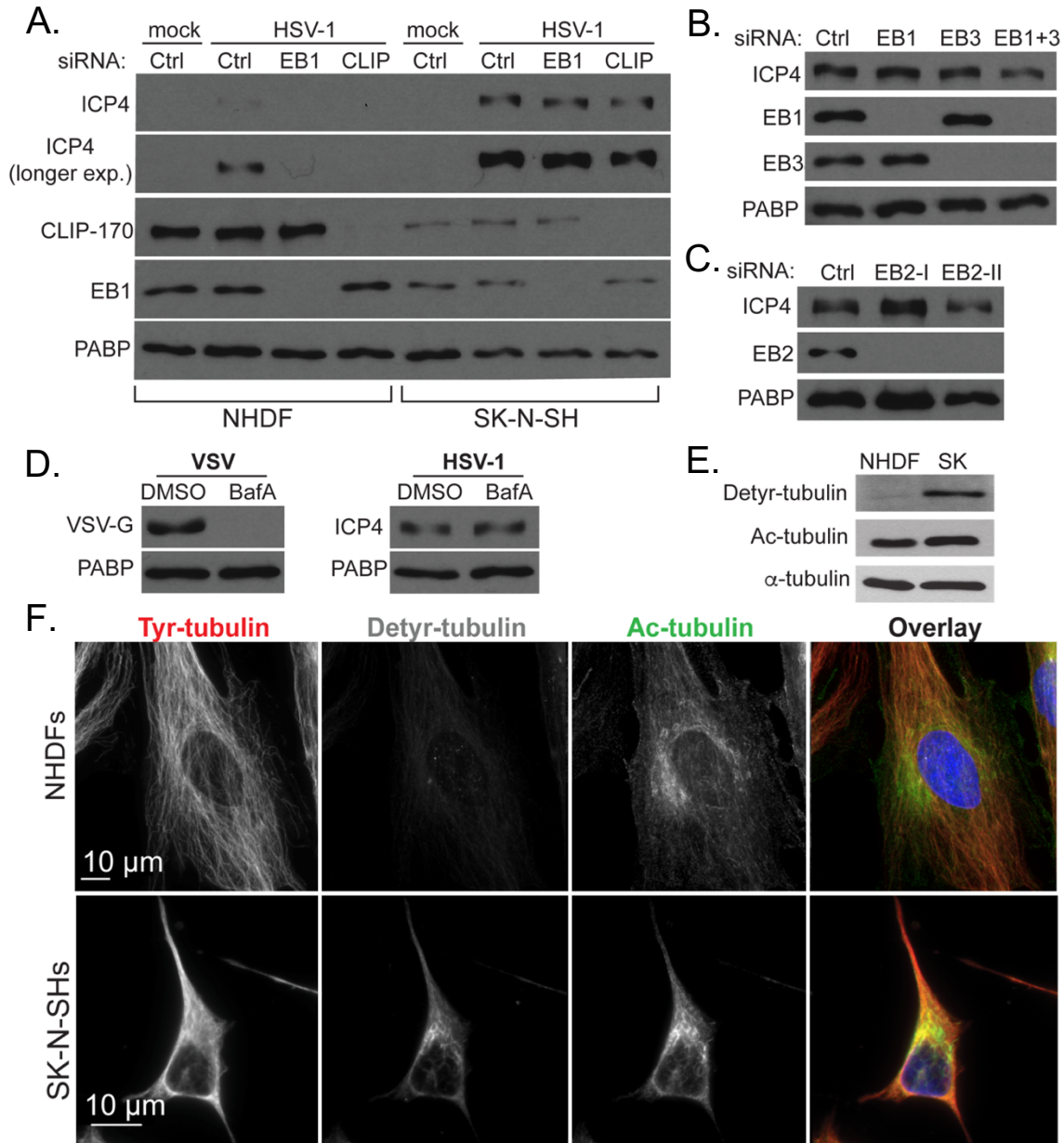


**Figure 7** HSV-1 infection is EB-independent in SK-N-SHs. (A) NHDFs or SK-N-SHs treated with non-targeting (ctrl), EB1, or CLIP-170 (CLIP) siRNA were mock-infected or infected with HSV-1 at MOI 10 for 5h and analyzed by WB. (B-C) SK-N-SHs treated with independent EB2 siRNAs (I or II) were infected as in A. (D) SK-N-SHs were treated with 100nM BafA or DMSO and infected at MOI 10 with VSV for 4h or HSV-1 for 5h. (E) NHDFs or SK-N-SHs analyzed by WB using the indicated antibodies. (F) NHDFs or SK-N-SHs stained for tyrosinated (Tyr), detyrosinated (Detyr) and acetylated (Ac) tubulin. Nuclei were stained with Hoechst. All of the above experiments represent 3 biological replicates. Representative images are shown of results derived from 3 independent experiments. Experiments A-D were performed by Walsh Laboratory member Dr. Vladimir Jovasevic.

We next used WB and immunofluorescence (IF) analysis to compare the nature of MT networks in both cell types. Samples were probed with antibodies against total or tyrosinated  $\alpha$ -tubulin, as well as de-tyrosinated- or acetylated- $\alpha$ -tubulin. Results showed that NHDFs contained both tyrosinated and acetylated MTs, but little-to-no discernible de-tyrosinated tubulin or filaments (Figure 7E-F). By contrast, SK-N-SHs contained a high proportion of acetylated and de-tyrosinated MTs, which extended from a perinuclear region (Figure 7E-F).

To determine if these differences in tubulin PTMs reflect differences in MT stability that influence infection, we treated NHDFs and SK-N-SHs with DMSO solvent control or different doses of the MT depolymerizing agent, nocodazole prior to infection with HSV-1. Low nanomolar concentrations of nocodazole either depolymerize or dampen the growth of dynamic MTs, but do not affect stable filaments; by contrast, higher micromolar concentrations result in the loss of both dynamic and stable MTs [103, 253]. In NHDFs that contain a high proportion of dynamic MTs, several tyrosinated MT filaments persisted in cultures treated with 500nM nocodazole (Figure 8A). However, EB1 no longer formed comet-like staining patterns demonstrating that, despite the persistence of some filaments, MT dynamics were dampened under these conditions (Figure 9A). In SK-N-SHs that contain a mix of tyrosinated and de-tyrosinated filaments, 500nM nocodazole depolymerized tyrosinated MTs and caused a loss of EB1 comet staining, but de-tyrosinated MTs persisted (Figure 8B, Figure 9B, Figure 10). The accumulation of de-tyrosinated tubulin combined with resistance to nanomolar concentrations of nocodazole is a defining characteristic of stable MTs. Finally, treating cells with 10 $\mu$ M nocodazole depolymerized dynamic and stable MTs in both cell types (Figure 8, Figure 10A).

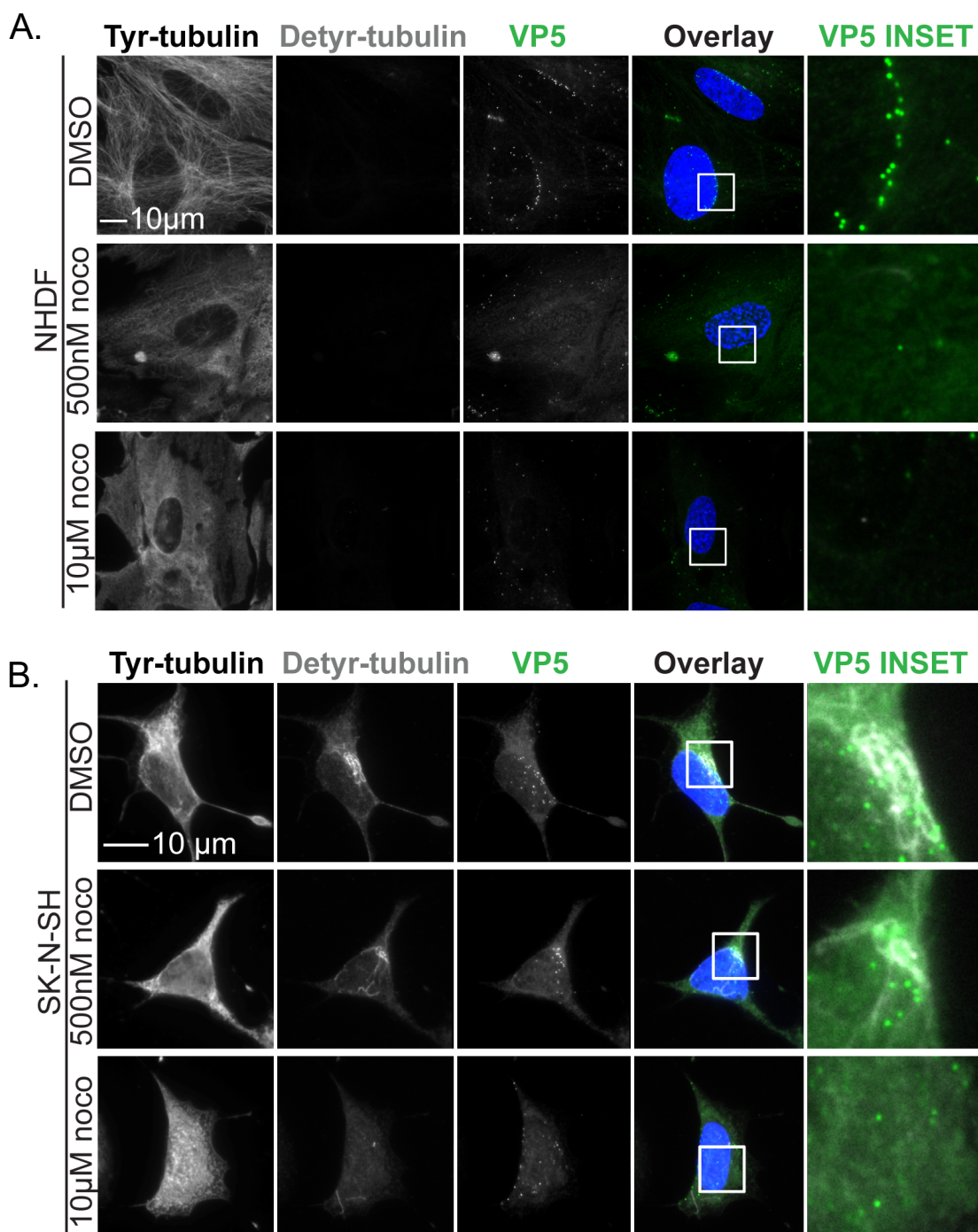


**Figure 8** Stable MTs mediate HSV-1 infection in SK-N-SHs. (A) NHDF or (B) SK-N-SH treated with DMSO for 3 hours (top), 500nM nocodazole for 2 hours (middle), or 10μM nocodazole for 3 hours (bottom). Cells were also treated with 1μg/ml actinomycin D for 1 hour to prevent de-novo production of VP5. Cells were then infected with HSV-1 at MOI 20 for 4 hours, fixed and stained for tyrosinated tubulin (Tyr; not included in overlay), detyrosinated tubulin (Detyr; grey), and HSV-1 capsid protein VP5 (green). Nuclei were stained with Hoechst. Inset shows zoomed view of perinuclear VP5 and detyrosinated tubulin. Representative images are shown of results derived from 2 independent experiments.

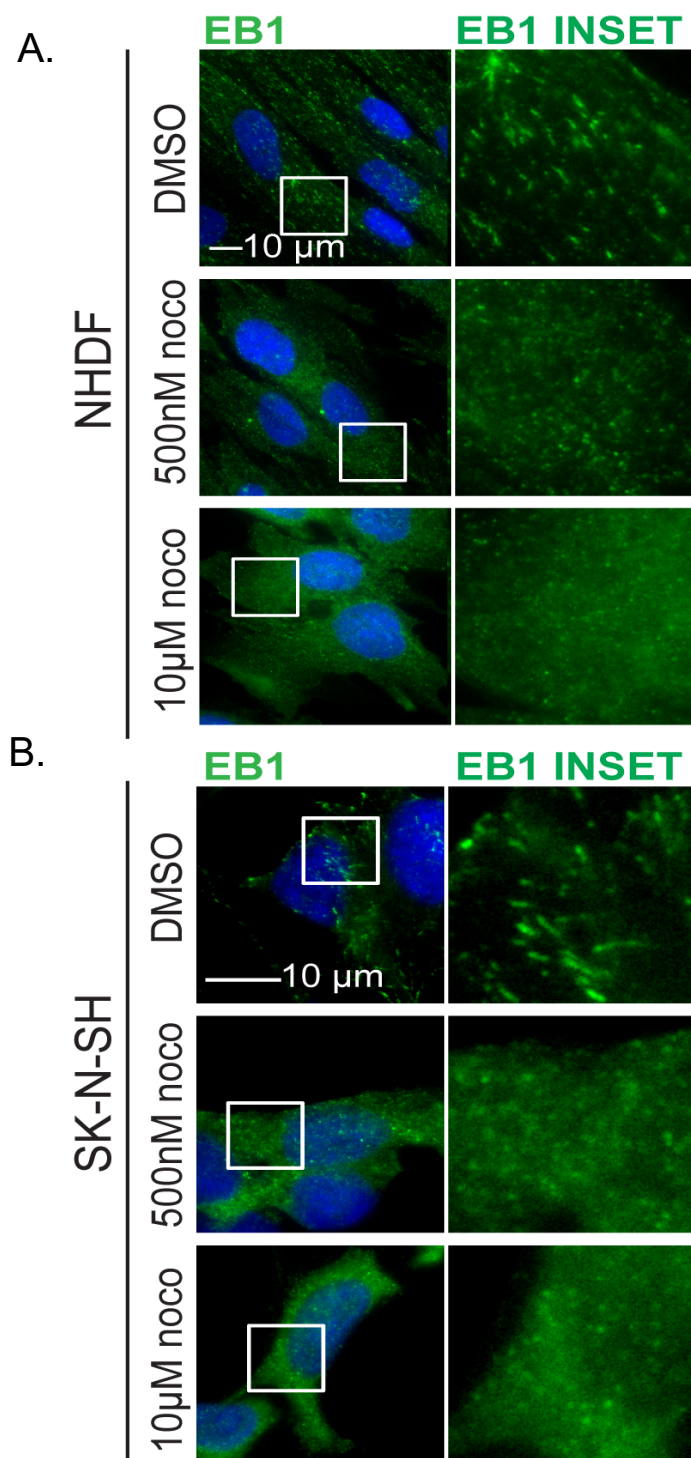


**Figure 9** Nocodazole dampens MT dynamics. (A) NHDFs or (B) SK-N-SHs were treated with DMSO or nocodazole as in Figure 8. Fixed cells were stained for EB1 (green) along with Hoechst. Inset shows zoomed view of EB1 comets. Representative images are shown of results derived from 2 independent experiments.

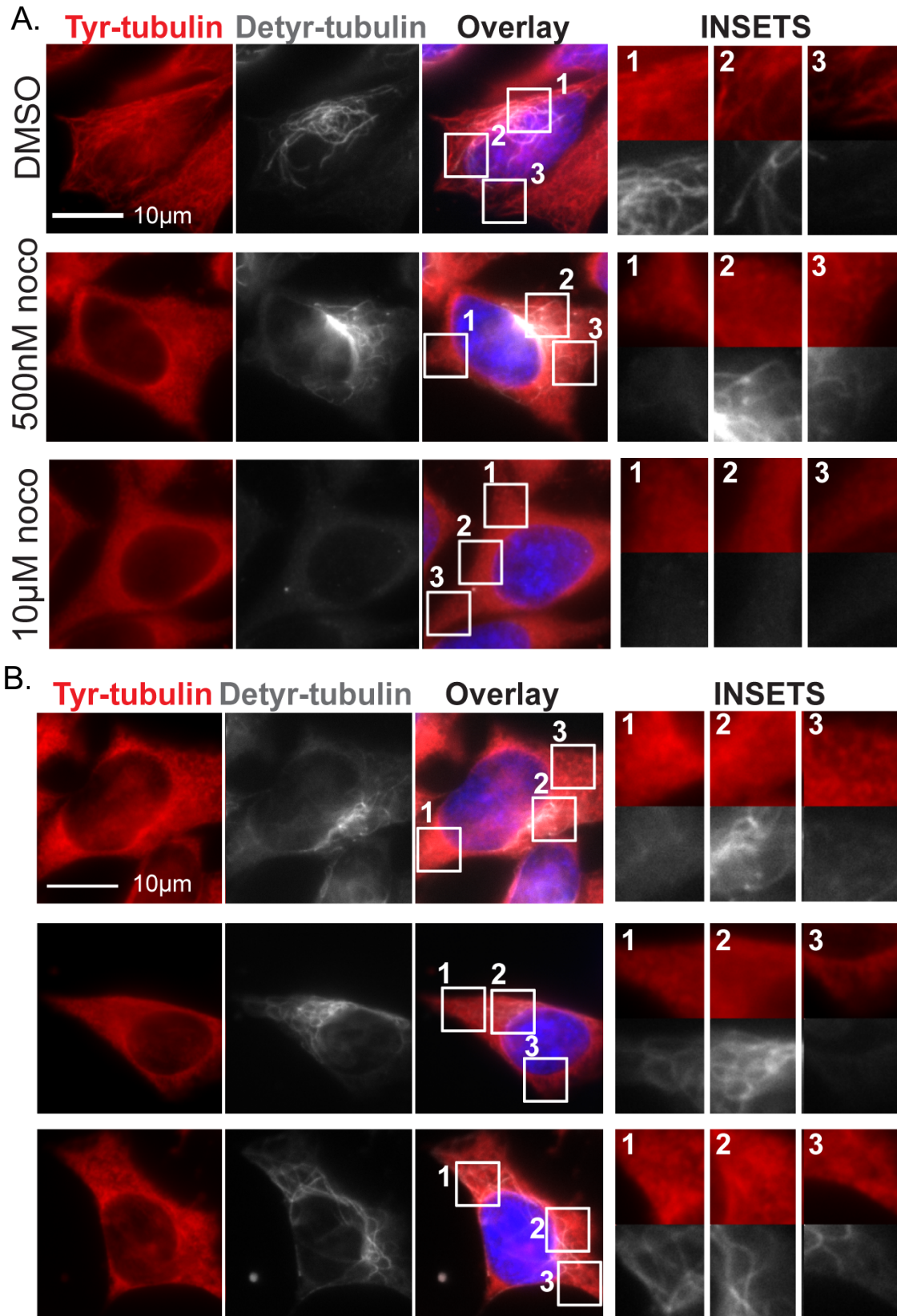


**Figure 10** Stable MTs persist at low doses of nocodazole. (A) SK-N-SHs treated with DMSO or nocodazole as in Figure 8. Fixed cells were stained for tyrosinated (red) and detyrosinated (grey) tubulin, along with Hoechst. Insets show three zoomed and labeled regions within the cell. (B) Additional examples of SK-N-SHs treated with 500 nM nocodazole. Representative images are shown of results derived from 3 independent experiments.

To test effects on virus translocation to the nucleus, we stained samples for the capsid protein, VP5. Staining and quantification showed that while virus particles reached the nuclear periphery in both cell types in DMSO-treated controls, this was impaired in NHDFs treated with 500 nM nocodazole (Figure 8, Figure 11A). By contrast, in SK-N-SHs HSV-1 particles accumulated along perinuclear de-tyrosinated MT networks in both DMSO-treated and 500nM nocodazole-treated samples (Figure 8, Figure 11A). However, 10 $\mu$ M nocodazole depolymerized both dynamic and stable MTs and impaired the nuclear accumulation of HSV-1 in both NHDFs and SK-N-SHs (Figure 8, Figure 11A). WB analysis confirmed these IF-based observations, showing that expression of the HSV-1 immediate early proteins, ICP0 and ICP4 was potently blocked by either high- or low-dose nocodazole in NHDFs, while in SK-N-SHs viral gene expression was relatively resistant to low-dose nocodazole treatment (Figure 11B). This supported the notion that dynamic MTs mediate infection in NHDFs while stable MTs mediate infection in SK-N-SHs.

We next tested whether these effects on HSV-1 infection reflected defects in virus entry by staining nocodazole-treated, HSV-1 infected cells for the viral glycoprotein, gB together with VP5. In this assay, VP5 capsids that do not co-stain for gB represent viral particles that have lost their envelope after fusing into the cytosol, while those that co-stain for both proteins represent unfused particles. Results showed that nocodazole did not block HSV-1 fusion in either cell type, while infections at 4 $^{\circ}$ C validated this assay's ability to detect impairments in virus fusion (Figure 12). Despite differences in actin organization between the two cell types, no gross changes in actin staining were detected in nocodazole-treated SK-N-SHs or NHDFs compared with DMSO controls (Figure 13). As such, while we cannot rule out subtle effects on actin organization or dynamics that might influence infection, there were no striking differences in how nocodazole affected actin

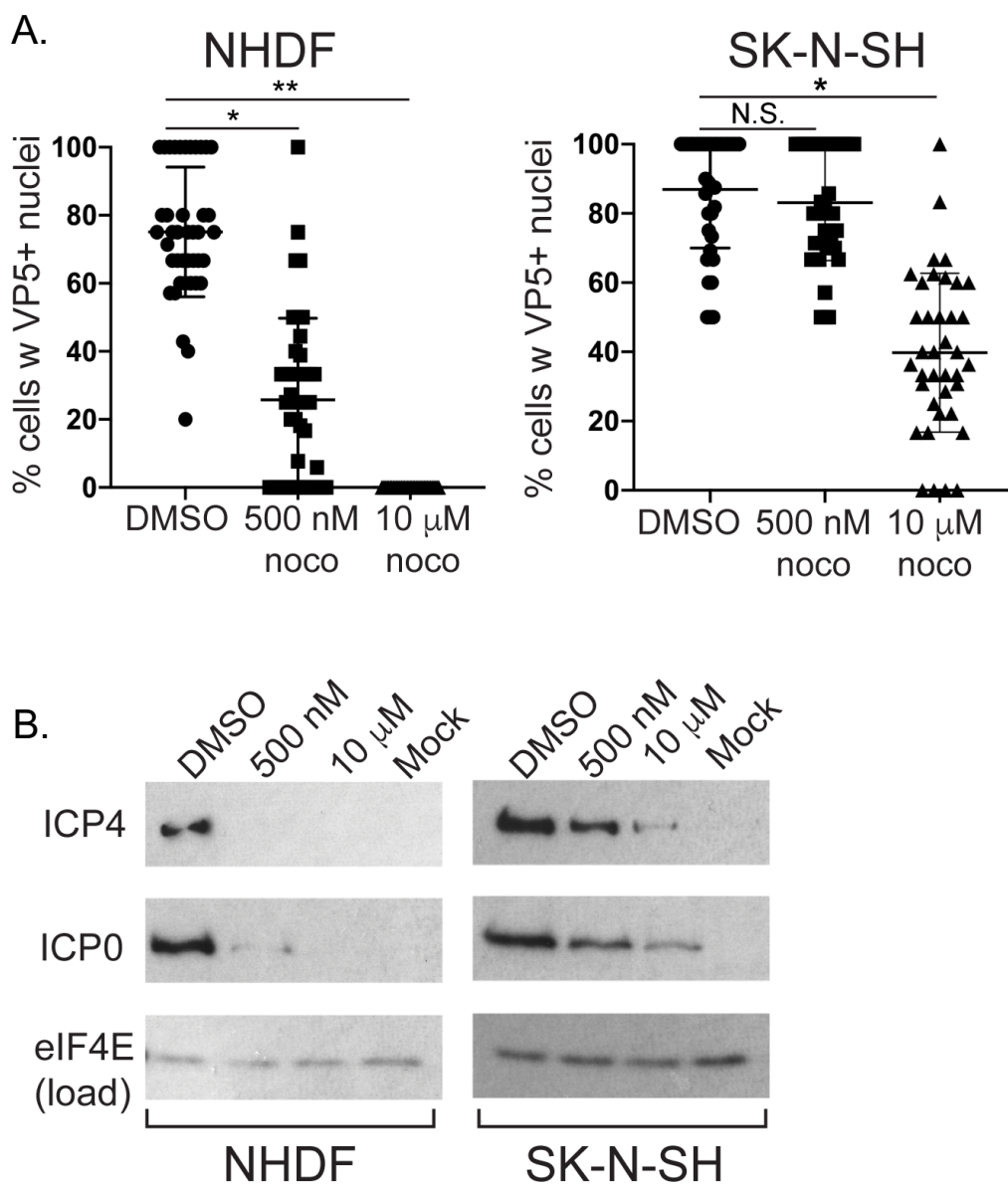


**Figure 11** HSV-1 infection is unaffected by low-dose nocodazole treatment in SK-N-SHs. (A) NHDFs or SK-N-SHs treated with DMSO, 500nM or 10 $\mu$ M nocodazole were infected at MOI 20 with HSV-1 for 4h in the presence of 1 $\mu$ g/ml actinomycin D. Fixed cells were stained for VP5 and with Hoechst.  $\geq 165$  NHDF or  $\geq 190$  SK-N-SH nuclei were assessed for accumulation of VP5 over 2 biological replicates; error bars = SEM; \* $p < 0.05$ , \*\* $p < 0.01$ , N.S. = not significant; unpaired two-tailed t-test. (B) Cells treated as in A. were infected at MOI 10 with HSV-1 for 5h and analyzed by WB for 3 independent experiments.

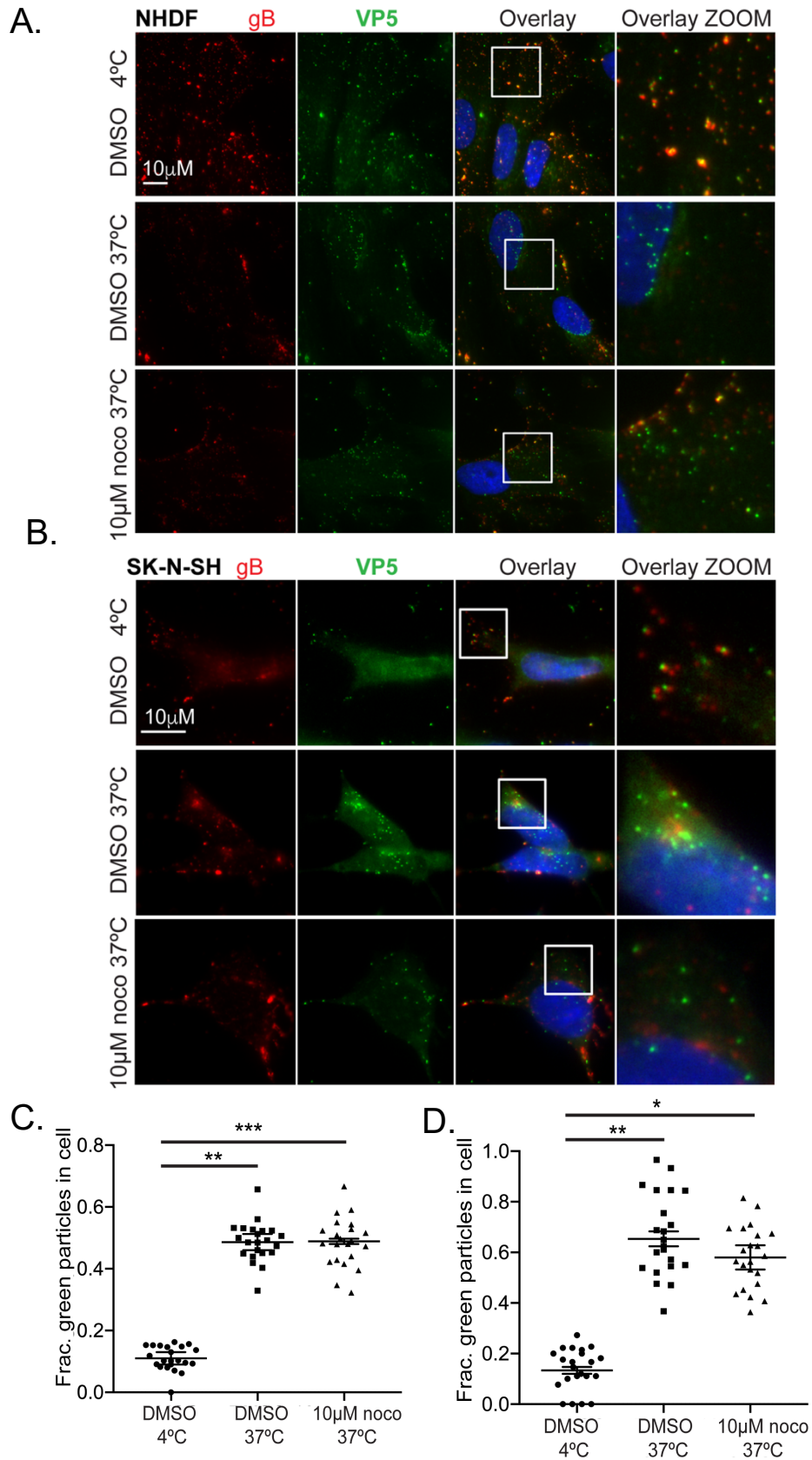


**Figure 12** Nocodazole treatment does not affect HSV-1 entry. (A-D) NHDFS or SK-N-SHs were treated with DMSO or 10 $\mu$ M nocodazole for 3 hours. NHDFS (A, C) or SK-N-SHs (B, D) were then infected with HSV-1 in the presence of actinomycin D, at MOI 20 at 37°C for 4 hours or MOI 30 at 4°C for 1 hour. Fixed cells were stained for gB (red) and VP5 (green) along with Hoechst. Representative images are shown of results derived from 2 independent experiments. (C, D) Average fraction of green particles vs green and yellow particles per cell was quantified. 20 cells per condition and cell type were quantified over 2 biological replicates; error bars = SEM; \* $p < 0.05$ , \*\* $p < 0.01$ , \*\*\* $p < 0.005$ ; unpaired two-tailed t-test.

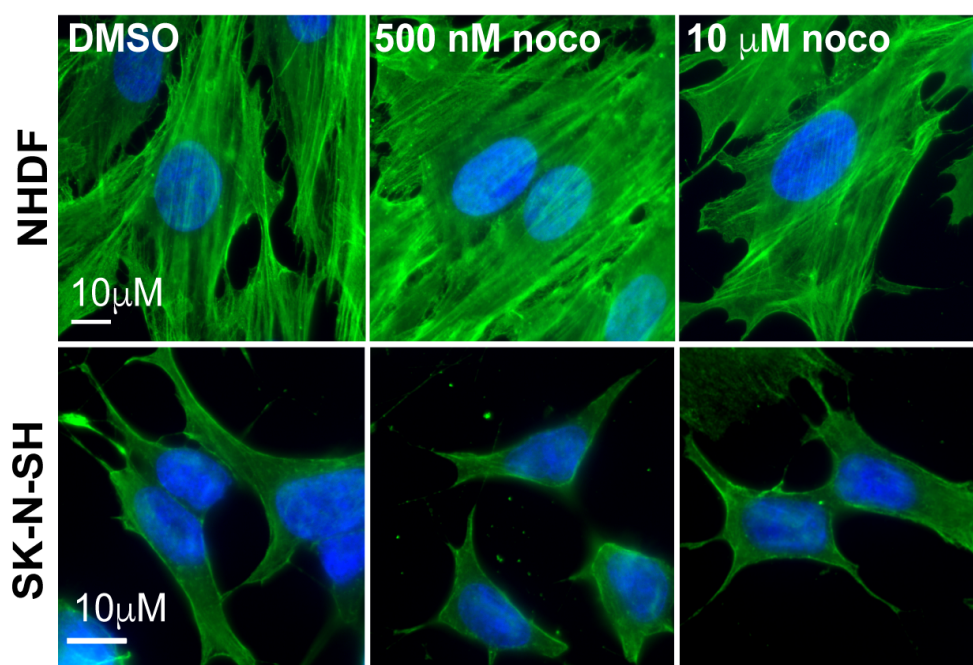


**Figure 13** Nocodazole treatment does not alter actin organization in NHDFs or SK-N-SHs. Cells treated with DMSO or nocodazole as in Figure 8. Drug-treated NHDFs or SK-N-SHs were fixed and stained for  $\beta$ -actin along with Hoechst. Representative images are shown of the predominant phenotype.

organization that might explain the differential sensitivity of infection to this drug between these two cell types. Cumulatively, nocodazole exerted a post-entry effect on viral translocation to the nucleus that correlated with effects on dynamic MTs in NHDFs, or stable MTs in SK-N-SHs. This was also in line with the relative sensitivity of infection to depletion of EB1 in each cell type, shown earlier, further suggesting that EB1 might not play a major role in regulating stable MTs in SK-N-SHs.

### **TACC3 regulates stable MT networks in SK-N-SHs**

To test this, we determined the effects of EB1 depletion on MT networks in SK-N-SHs. While EB1 regulates several aspects of MT plus-end dynamics, potent depletion of EB1 had little effect on the levels or organization of acetylated- or de-tyrosinated-MTs in SK-N-SHs (Figure 14). This prompted us to explore potential contributions from TACC3, based on recent reports that TACC3 can track MT plus-ends independently of EB1 in interphase cells [159, 192]. To do so, we first examined the expression of TACC protein family members and chTOG. WB analysis showed that both cell types express similar levels of chTOG but that SK-N-SHs express higher levels of TACC proteins, in particular TACC3 (Figure 15A). Higher levels of TACC3 in SK-N-SHs was confirmed by measuring relative fluorescence intensity in IF images (Figure 15B-C). Notably, NHDFs and SK-N-SHs contain a significantly smaller fraction of cells undergoing mitosis at any given time than more widely used cell lines (Figure 15D-E). In addition, while TACC3 accumulated along the mitotic spindle in this small fraction of cells (Figure 15D), TACC3 was diffusely cytoplasmic in the larger interphase population of both cell types (Figure 15C). As such, both cell types are relevant to the study of TACC3's functionality in interphase cells, as well as in infection. To test whether TACC3 regulated MT networks we treated SK-N-SHs with either of

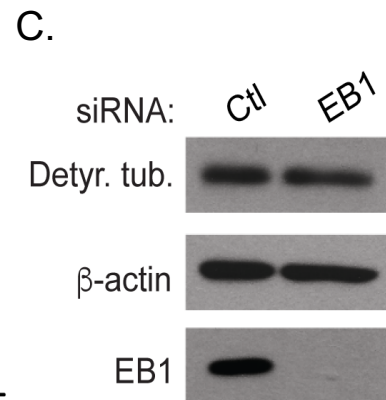
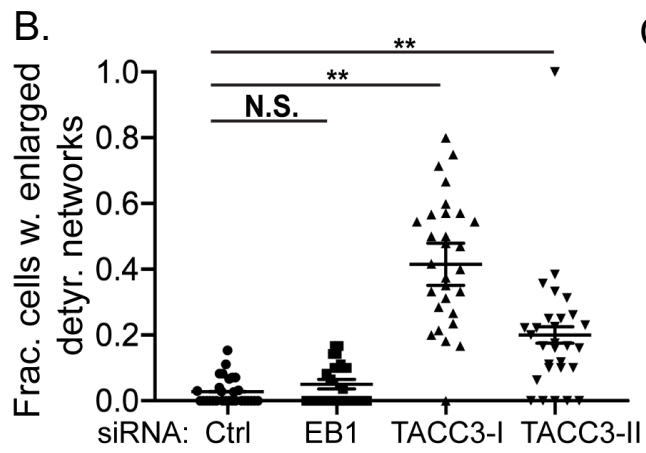
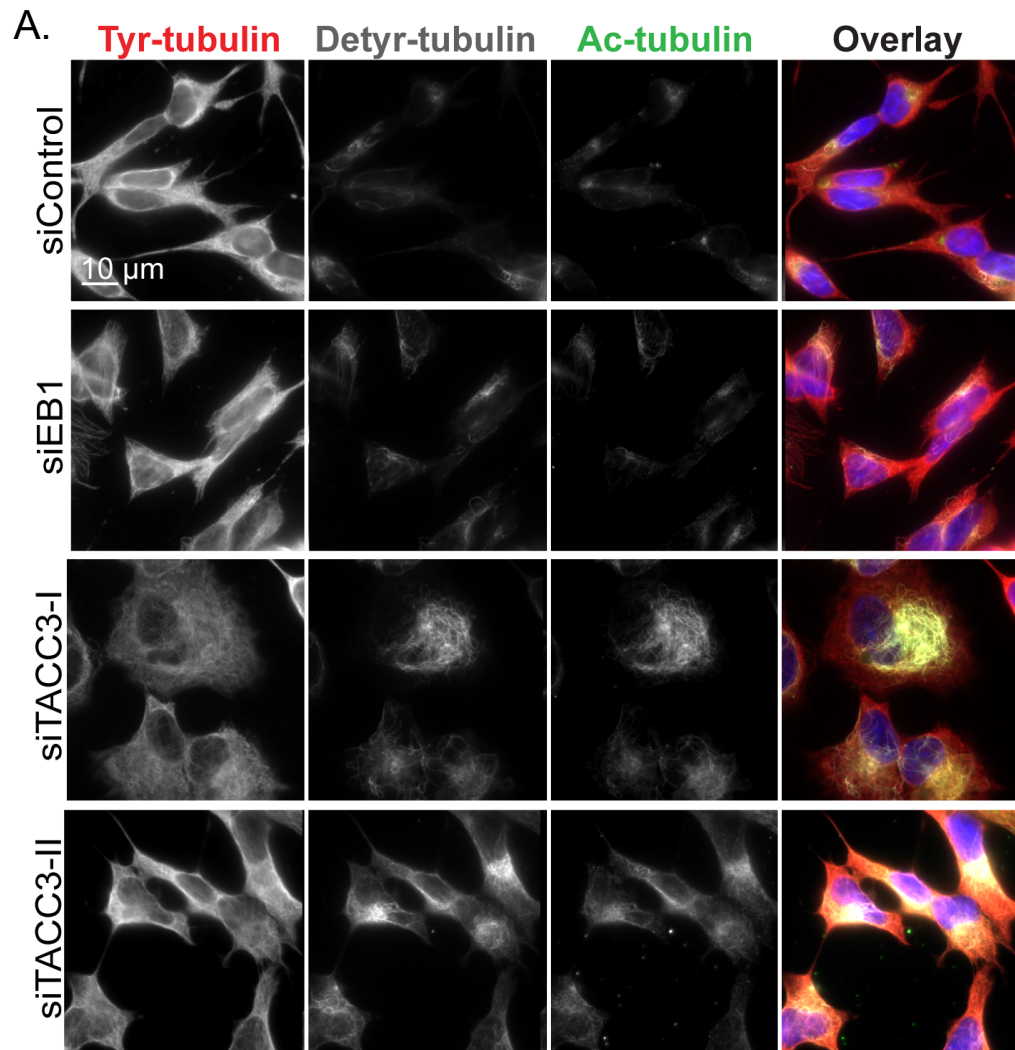


**Figure 14** TACC3, but not EB1, regulates stable MTs in SK-N-SHs. A) SK-N-SHs treated with control, TACC3 (I or II), or EB1 siRNAs were fixed and stained for tyrosinated (Tyr) tubulin (red), detyrosinated (Detyr) tubulin (grey), or acetylated (Ac) tubulin (green). Nuclei were stained with Hoechst. Representative images are shown of results derived from 3 independent experiments. (B) Average fraction of SK-N-SHs treated as in A. with highly enlarged Detyr-MT networks.  $\geq 170$  cells per siRNA over 2 biological replicates; error bars = SEM;  $**p < 0.01$ , N.S. = not significant; unpaired two-tailed t-test. C) SK-N-SHs treated with control or EB1 siRNA were analyzed by WB using the indicated antibodies.

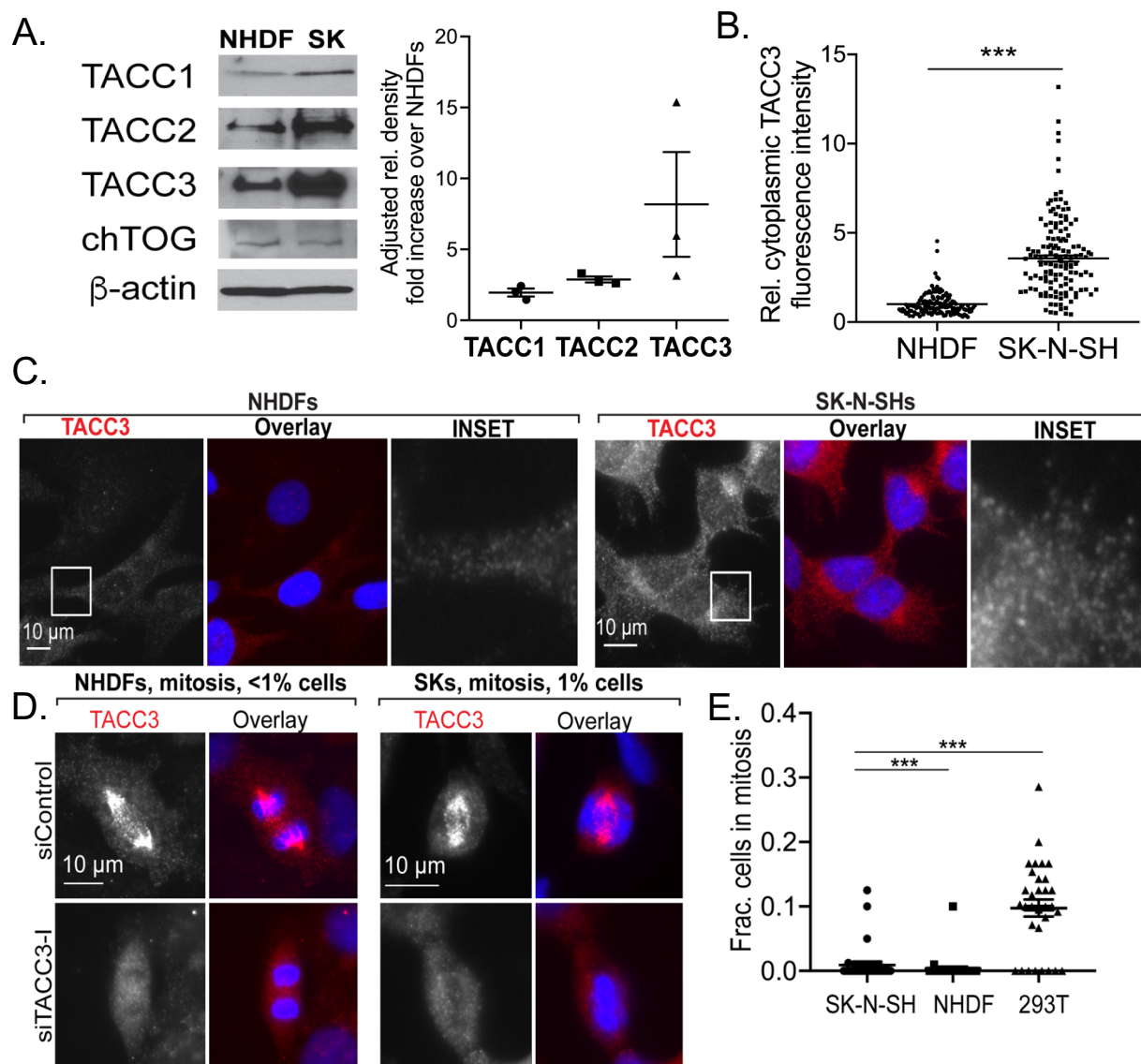


**Figure 15** Localization of TACC3 in mitotic and interphase human cells. (A) NHDF and SK-N-SH cell lysates were analyzed by WB using indicated antibodies. Average adjusted relative densities (AU) of TACC1, TACC2, and TACC3 in SK-N-SHs and NHDFs were quantified across WBs from 3 independent experiments. Shown here are average levels of TACC1, 2, and 3 in SK-N-SHs relative to those in NHDFs, arbitrarily set to a value of 1 for each TACC family member; error bars = SEM; unpaired two-tailed t-test. (B-C) NHDFs or SK-N-SHs were fixed and stained for TACC3, along with Hoechst to detect nuclei. (B) Average corrected total fluorescence intensity of cytoplasmic TACC3 relative to NHDFs.  $\geq 120$  cells per cell type were counted over 3 biological replicates; error bars = SEM; \*\*\* $p < 0.005$ ; unpaired two-tailed t-test. (C) Images of TACC3 localization in interphase cells representative of results derived from 3 independent experiments. Inset shows zoomed view of punctate cytoplasmic TACC3. (D-E) The number of mitotic cells is significantly lower in NHDF and SK-N-SH cultures compared with commonly used transformed cell lines. (D) Fixed cells were stained for TACC3, along with Hoechst to detect nuclei. Shown are examples of NHDF and SK-N-SH cells in mitosis. Use of TACC3 siRNA shows specificity of TACC3 antibody staining. (E) Average fraction of cells in mitosis relative to 293T cells. 300 cells per cell type were counted over 3 biological replicates; error bars = SEM; \*\* $p < 0.01$ ; unpaired two-tailed t-test.

two independent siRNAs, which resulted in different degrees of TACC3 depletion (Figure 16A). The most potent siRNA (TACC3-I) resulted in the accumulation of high levels of acetylated and de-tyrosinated MTs, which appeared disorganized (Figure 14A-B, Figure 16B). Potent depletion of TACC3 also resulted in changes in cell diameter compared with control siRNA-treated SK-N-SHs, which were not observed in EB1-depleted cells (Figure 14A-B, Figure 17A-B). The second, less potent siRNA (siTACC3-II) resulted in intermediate phenotypes (Figure 14A-B, Figure 16, Figure 17A-B), establishing a dose-dependent effect of TACC3 loss on the organization of stable MTs and cell diameter. To confirm that these were not off-target effects we rescued TACC3 expression TACC3-I siRNA-treated SK-N-SHs (Figure 18A). Due to species incompatibility between TACC3 and de-tyrosinated tubulin antibodies, we stained for acetylated tubulin as both modifications arise on stable MTs (Figure 14A). IF imaging and quantification showed that restoring TACC3 expression reversed the effects of TACC3 depletion on acetylated MTs and cell diameter (Figure 18B-D). Finally, we used the Golgi as an additional readout for TACC3's effects, as the Golgi is dependent on MTs to maintain its organization [45, 76]. IF imaging and measurements of the area stained by the trans-Golgi marker, TGN46 revealed that TACC3 depletion resulted in a significant increase in TGN area (Figure 19A-B). Changes in cell diameter and TGN area were not observed in cells depleted of EB1 (Figure 19C) and these phenotypes were reversed by restoring TACC3 expression in TACC3-I siRNA-treated cells (Figure 19A-B). Phenotypes were only partially rescued as we transiently reintroduced TACC3 expression for just the final day of siRNA-treatment.

### **TACC3 regulates chTOG localization and MT plus-end growth in interphase cells**

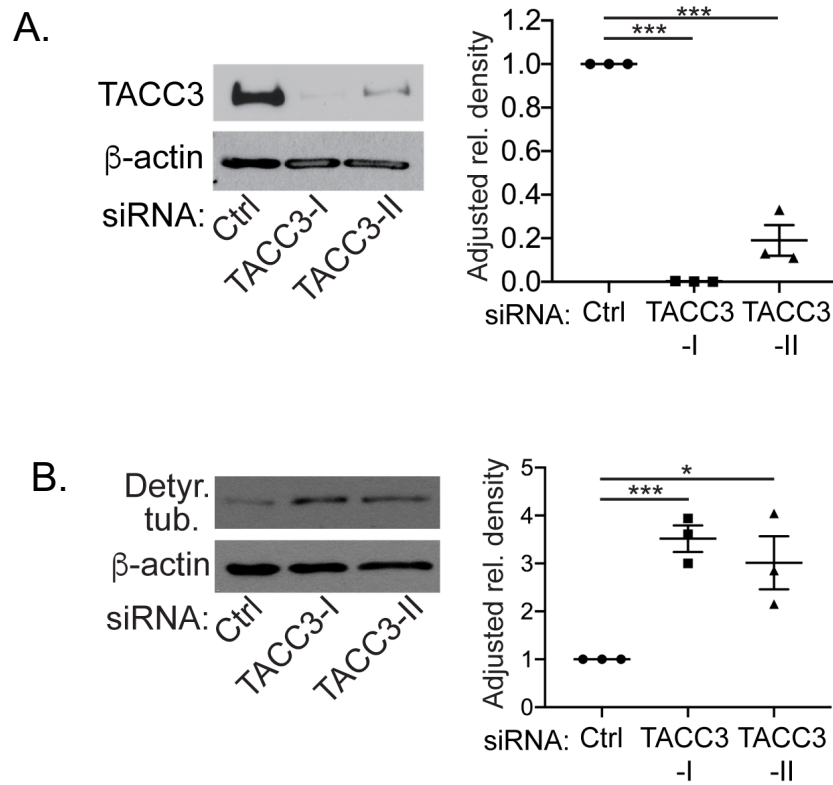
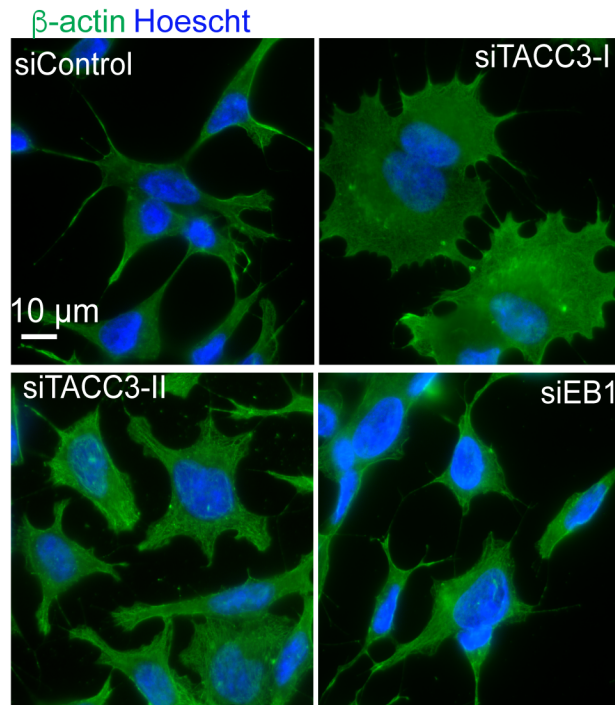


**Figure 16** TACC3 depletion results in an increase in de-tyrosinated MTs in SK-N-SHs. (A) SK-N-SHs were treated with the indicated siRNAs. Average adjusted relative density (AU) of TACC3 was quantified across WBs from 3 independent experiments; error bars = SEM; \*\*\* $p < 0.005$ ; unpaired two-tailed t-test. (B) SK-N-SHs were treated with the indicated siRNAs. Average adjusted relative density (AU) of de-tyrosinated-tubulin was quantified across WBs from 3 independent experiments; error bars = SEM; \* $p < 0.05$ , \*\*\* $p < 0.005$ ; unpaired two-tailed t-test.

A.



B.

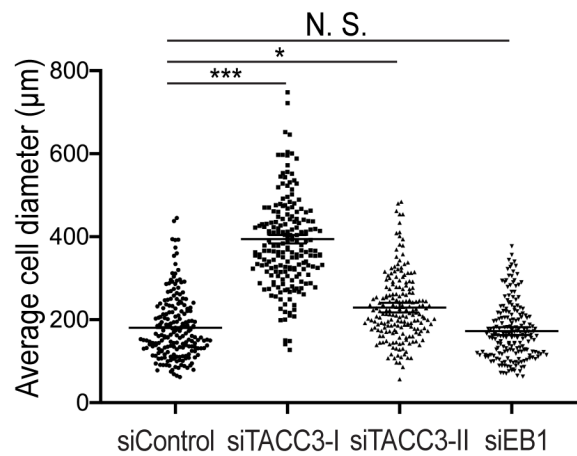


**Figure 17** TACC3 regulates cell diameter in SK-N-SHs. (A) SK-N-SH cells were treated with control, TACC3, or EB1 siRNAs. Fixed cells were stained for  $\beta$ -actin (green) along with Hoechst to detect nuclei. (B) Average cell diameter taken perpendicular to the nucleus in SK-N-SHs treated with indicated siRNAs.  $\geq 195$  cells per siRNA were counted over 3 biological replicates; error bars = SEM; \* $p < 0.05$ , \*\*\* $p < 0.005$ , N.S. = not significant; unpaired two-tailed t-test. Representative images are shown of results derived from 3 independent experiments.

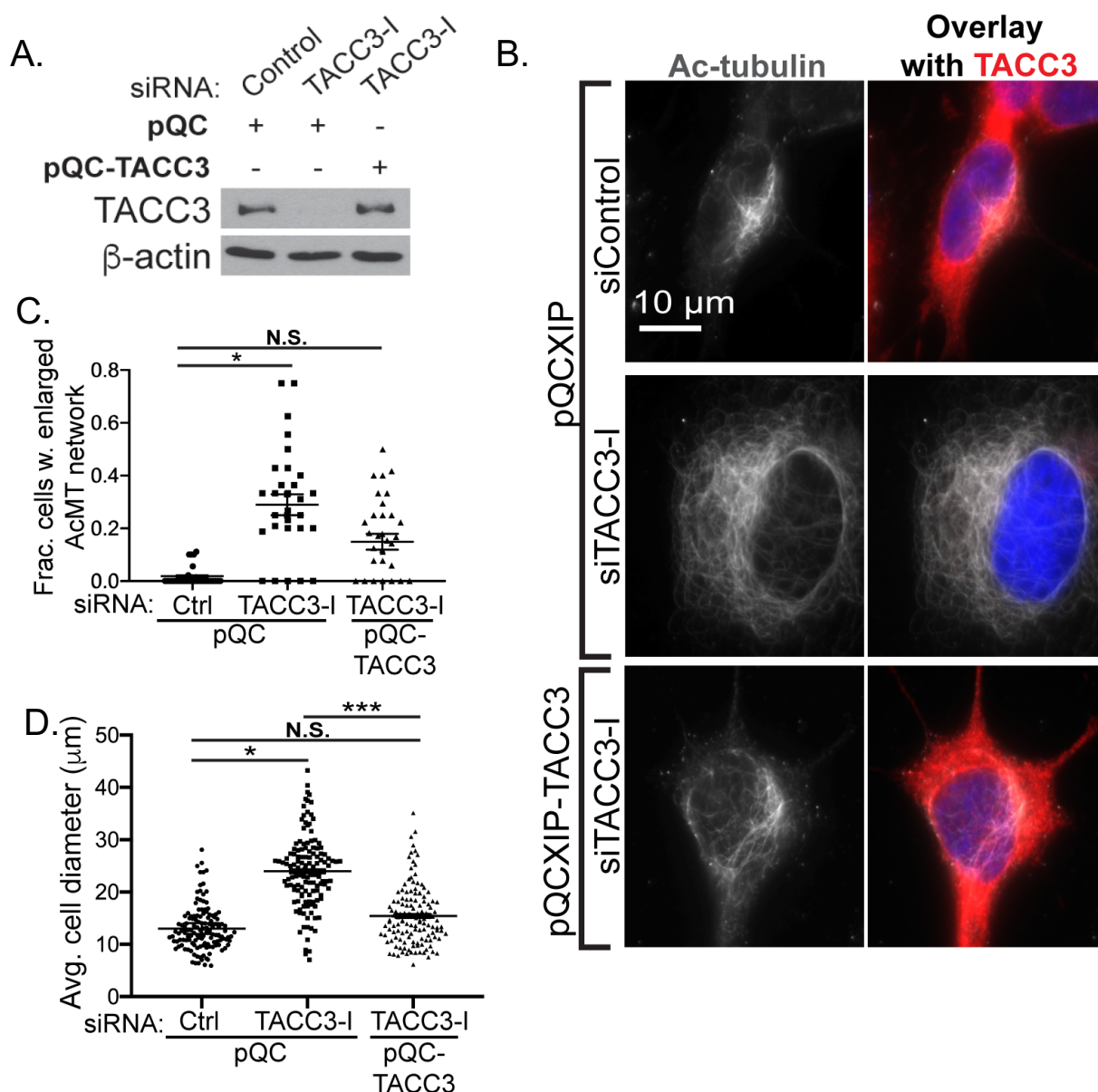


**Figure 18** TACC3 rescue confirms that knockdown phenotypes are not siRNA off-target effects. (A) SK-N-SHs were treated with the indicated siRNAs and then transduced with either pQCXIP (pQC) or pQCXIP-TACC3 (pQC-TACC3) retroviral vectors, and analyzed by WB. Representative of 3 independent experiments. (B) Cells treated as in A. were fixed and stained for TACC3 (red) and acetylated-tubulin (grey). Nuclei were stained using Hoechst. Representative images are shown of results derived from 2 independent experiments. (C) Average fraction of SK-N-SHs with highly enlarged acetylated MT networks.  $\geq 250$  cells per condition over 2 biological replicates; error bars = SEM; \* $p < 0.05$ , N.S. = not significant; unpaired two-tailed t-test. (D) Average cell diameter taken perpendicular to the nucleus.  $\geq 130$  cells per condition over 2 biological replicates; error bars = SEM; \* $p < 0.05$ , \*\*\* $p < 0.005$ , N.S. = not significant; unpaired two-tailed t-test.

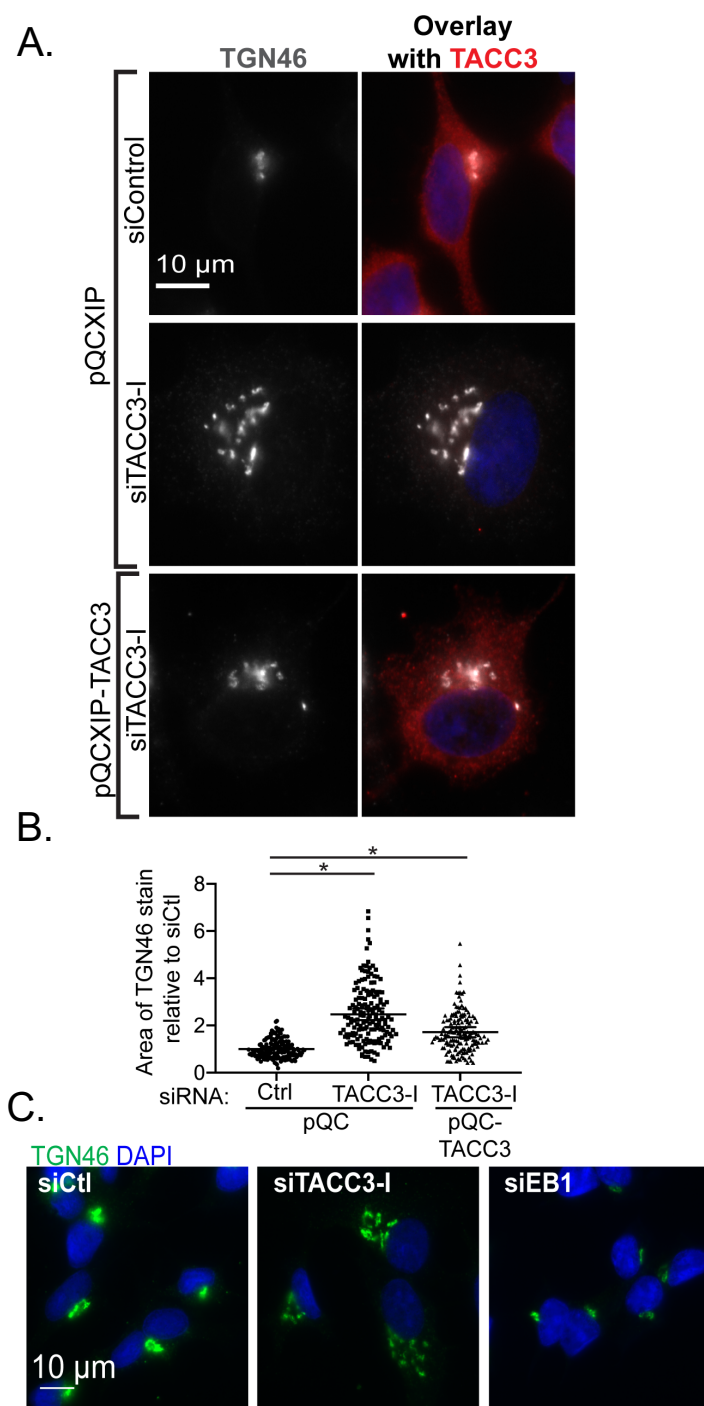


**Figure 19** TACC3 regulates *trans*-Golgi organization. (A) Cells treated as in Figure 18 were fixed and stained for TACC3 (red) and TGN46 (grey). Representative images are shown of results derived from 2 independent experiments. (B) Average area of TGN46 staining in SK-N-SHs treated as in A.  $\geq 160$  cells per condition over 2 biological replicates; error bars = SEM;  $*p < 0.05$ ; unpaired two-tailed t-test. (C) SK-N-SHs treated with indicated siRNAs were fixed and stained for TGN46 (green) along with Hoechst. Representative images are shown of results derived from 3 independent experiments.

We next explored how TACC3 might exert these effects on MT organization, and whether it exhibited cell-specific differences in functionality between SK-N-SHs or NHDFs. Given its established functions at centrosomes and spindle poles during mitosis, we first examined whether TACC3 exerted effects on centrosomes or MT nucleation in interphase cells.

NHDFs or SK-N-SHs were transfected with control or TACC3-I siRNA. Staining for both pericentrin and  $\gamma$ -tubulin, together with measurements of pericentrin fluorescence intensity, showed that TACC3 loss did not grossly affect centrosomes in either cell type, although subtle changes cannot be ruled out (Figure 20). Moreover, tyrosinated tubulin staining suggested that overall MT organization and cell shape was largely unaffected in NHDFs, while SK-N-SHs again exhibited changes in MT organization and morphology upon TACC3 depletion. This provided the first evidence of potential cell-specific differences in TACC3 function.

To test effects on MT nucleation, we examined the repolymerization of MTs in nocodazole washout assays. siRNA-treated cells were incubated with 10 $\mu$ M nocodazole to depolymerize MTs, followed by washout and staining for  $\alpha$ -tubulin. In NHDFs, TACC3 depletion had no significant effect on tubulin levels at centrosomes or the average area of new MTs extending from centrosomes compared with controls (Figure 21A-B). Similar results were observed in SK-N-SHs, although high levels of  $\alpha$ -tubulin throughout the cytosol made it challenging to accurately quantify the area of new MTs (Figure 21C). However, these MTs were also acetylated and quantifying their area showed that, like NHDFs, TACC3 depletion had no significant effect on the formation of new MTs in SK-N-SHs (Figure 22). As TACC3 did not significantly impact MT nucleation, we next tested whether it affected MT plus-end dynamics. As a central plus-end recognition factor, EB1 proteins form a comet-like staining pattern as they track growing MT tips [126]. In SK-N-SHs,

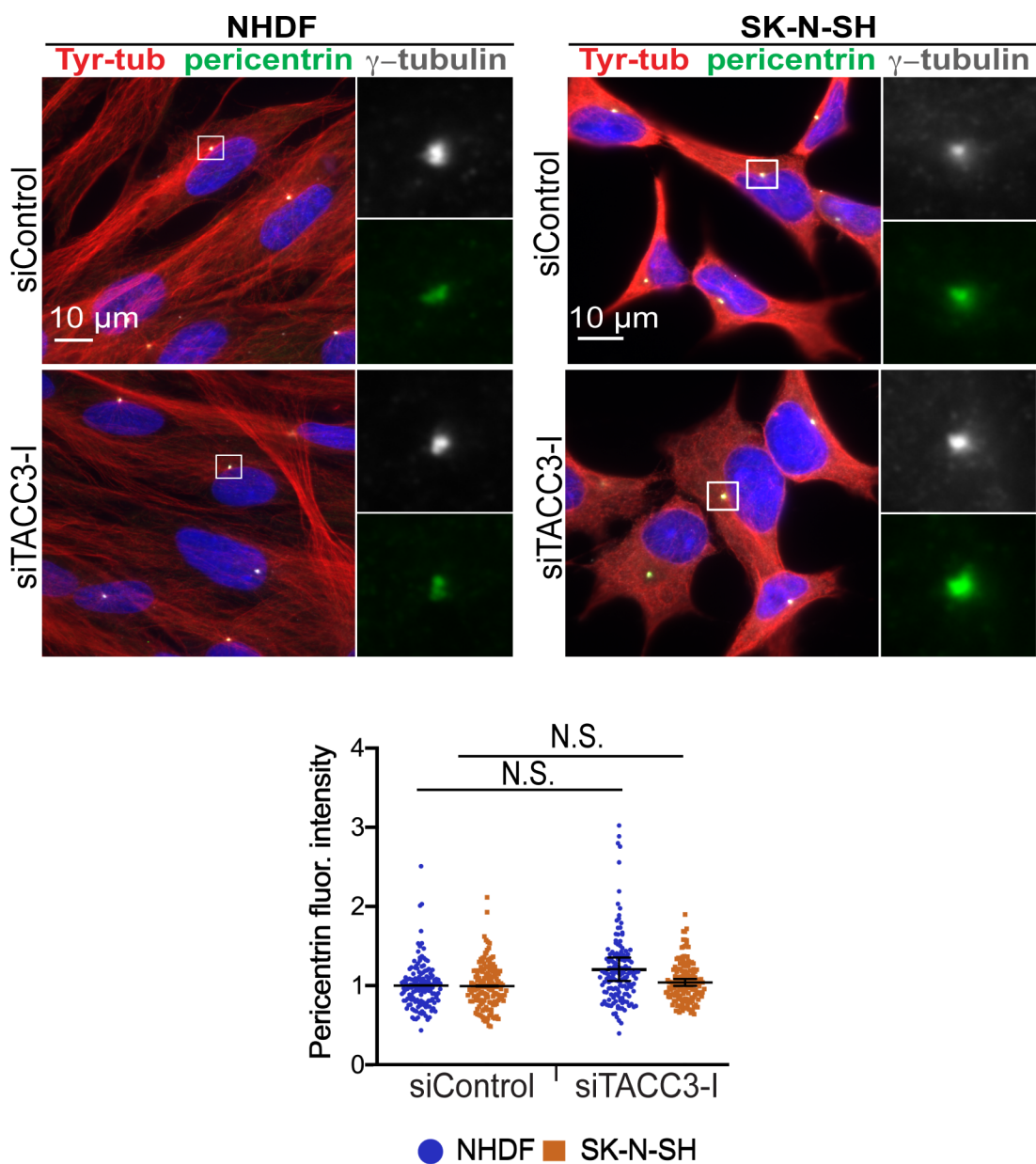


**Figure 20.** TACC3 depletion does not significantly affect centrosome. NHDF or SK-N-SH cells were treated with control or TACC3-I siRNA. (Top) Fixed cells were stained for tyrosinated (Tyr) tubulin (red), pericentrin (green), and gamma-tubulin ( $\gamma$ -tubulin; grey). Inset panels show zoomed view of pericentrin and gamma-tubulin staining. Representative images are shown of results derived from 3 independent experiments. (Bottom) Average corrected total fluorescence intensity of pericentrin in NHDFs and SK-N-SHs treated with indicated siRNAs.  $\geq 150$  cells per siRNA were counted over 3 biological replicates; error bars = SEM; N.S. = not significant; unpaired two-tailed t-test.

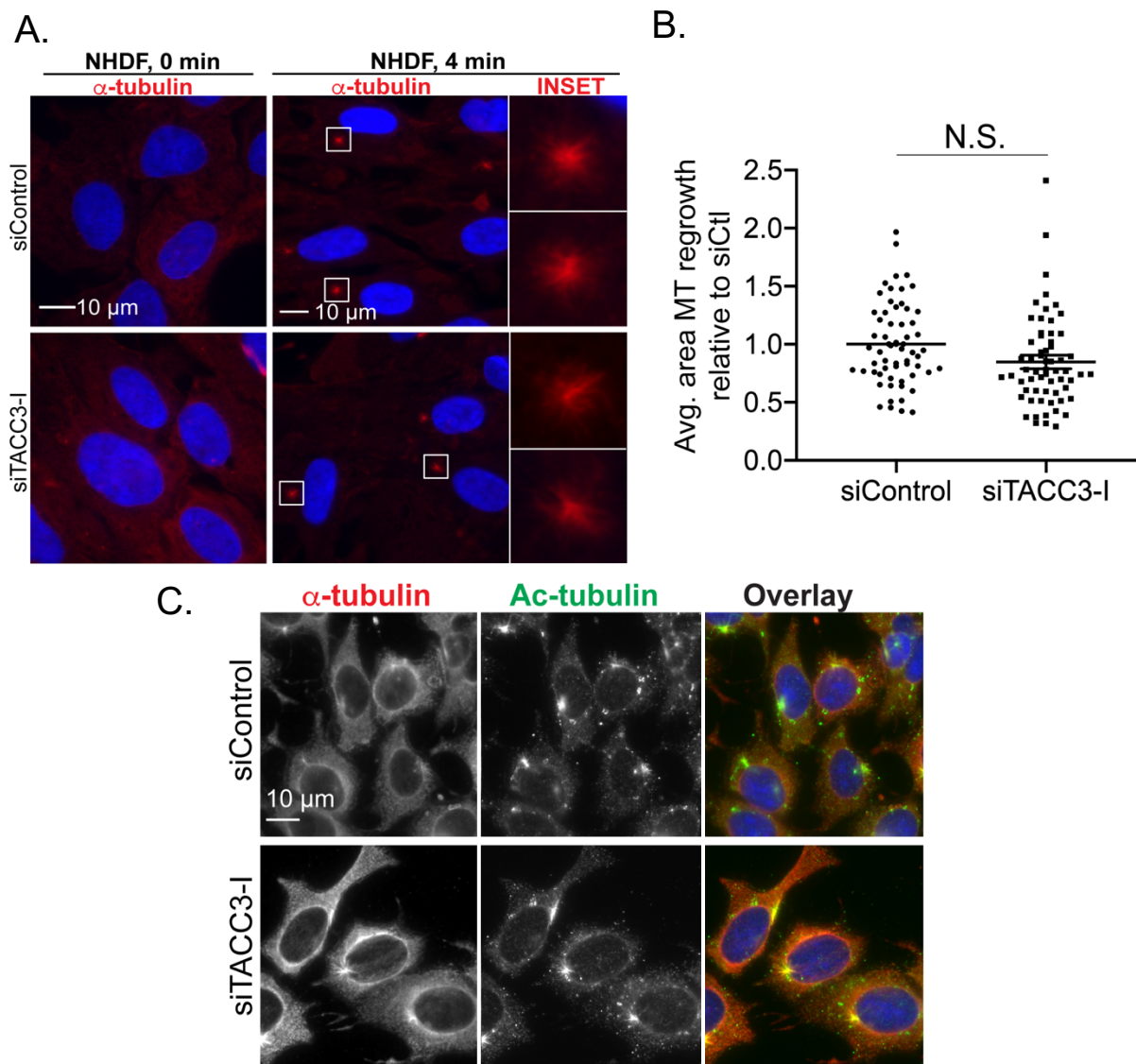


**Figure 21** TACC3 does not regulate MT nucleation in interphase cells. siRNA-treated NHDF or SK-N-SH cells were treated with 10  $\mu$ M nocodazole for 6 hours. Nocodazole-containing medium was then removed, cells were quickly rinsed and replenished with fresh medium without nocodazole. (A) NHDFs were fixed at 0 or 4 min post nocodazole washout and stained for  $\alpha$ -tubulin (red) along with Hoechst. (B) Average area of MT regrowth was calculated for NHDFs 4 min post nocodazole washout. 60 cells were counted per siRNA over 3 biological replicates. error bars = SEM; N.S. = not significant; unpaired two-tailed t-test. (C) SK-N-SHs were fixed at 10 min post nocodazole washout and stained for  $\alpha$ -tubulin (red) and acetylated (Ac) tubulin (green), along with Hoechst. All images shown are representative of results derived from 3 independent experiments.

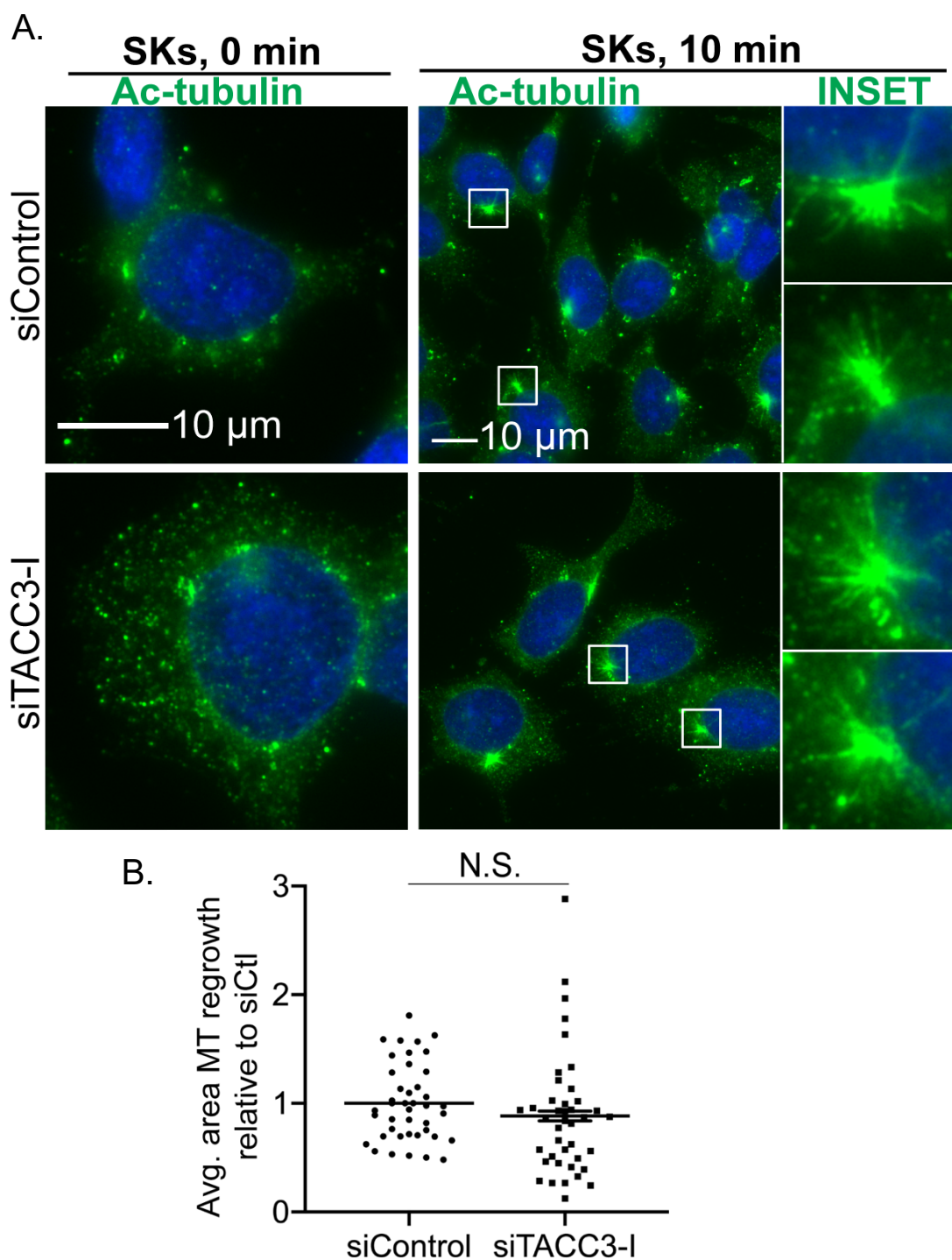


**Figure 22** Quantification of MT regrowth in SK-N-SHs. (A) SK-N-SHs were fixed at 0 or 10 min post nocodazole washout and stained for acetylated (Ac) tubulin (green) along with Hoechst. Representative images are shown of results derived from 3 independent experiments. (B) Average area of MT regrowth was calculated for SKs 10 min post nocodazole washout. 40 cells were counted per siRNA over 3 biological replicates; error bars= SEM; N.S. = not significant; unpaired two-tailed t-test.

TACC3-I and TACC3-II siRNAs revealed a dose-dependent effect of TACC3 depletion on the number of EB1 comets per cell, which also correlated with an increase in de-tyrosinated MTs (Figure 23). Fluorescence intensity comparisons further highlighted the correlation between the degree of TACC3 loss and reductions in EB1 staining across individual cells (Figure 24). Similar effects of TACC3 depletion on EB1 staining were observed in NHDFs (Figure 25), suggesting that TACC3 regulates MT dynamics in both cell types. We further confirmed changes in MT dynamics by performing time-lapse fluorescence microscopy using NDHFs that stably express GFP-CLIP170 [45]. CLIP170 tracks growing MT plus-ends in a manner that is both EB1-dependent and -independent [143], making it ideal to study broader MT behavior. In control siRNA-treated NHDFs, GFP-CLIP170 exhibited typical plus-end tracking behaviors (Figure 26, Video S1). However, TACC3 depletion caused notable changes in CLIP170 behavior. In some instances, GFP-CLIP170 extended down the lattice of MTs that did not appear to grow or shrink. Beyond these, the number of GFP-CLIP170 comets was reduced and comets that formed were slower and more elongated. This demonstrated that TACC3 influenced MT plus-end growth as suggested by EB1 staining. To validate siRNA-based findings, we used a dominant-negative approach. GFP- or Flag-tagged TACC3 forms aggregates that recruit the MT polymerase, chTOG [172, 180]. Based on this, we postulated that tagging might generate a dominant-negative TACC3 that sequesters chTOG. In line with this, expression of untagged TACC3 did not result in the formation of aggregates, while expression of Flag-tagged TACC3 formed aggregates in both SK-N-SHs and NHDFs (Figure 27). In SK-N-SHs, Flag-TACC3 expression resulted in elongation of EB1 comets (Figure 28). However, these effects proved difficult to quantify as this dominant-negative approach was less effective in SK-N-SHs, likely due to their high basal levels of TACC3 expression. Indeed,

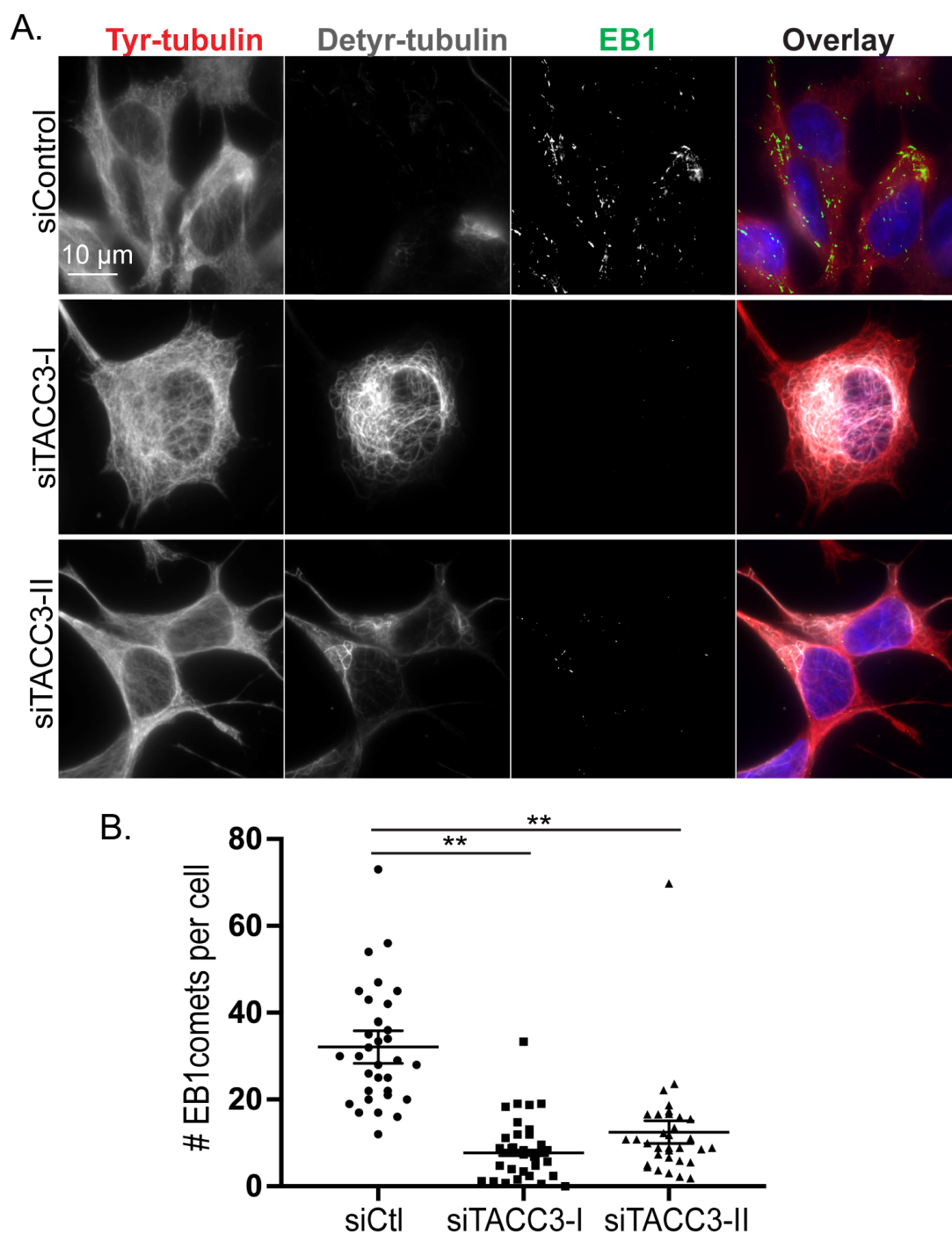


**Figure 23** TACC3 regulates MT plus-end dynamics in SK-N-SHs. (A) SK-N-SHs were treated with siRNAs and then fixed and stained for tyrosinated (Tyr) and de-tyrosinated (Detyr) tubulin, EB1 and Hoechst. Representative images are shown of results derived from 3 independent experiments. (B) Average number of EB1 comets per cell treated as in A. Total number of EB1 comets in 30 cells per siRNA over 3 biological replicates; error bars = SEM; \*\* $p < 0.01$ ; unpaired two-tailed t-test.

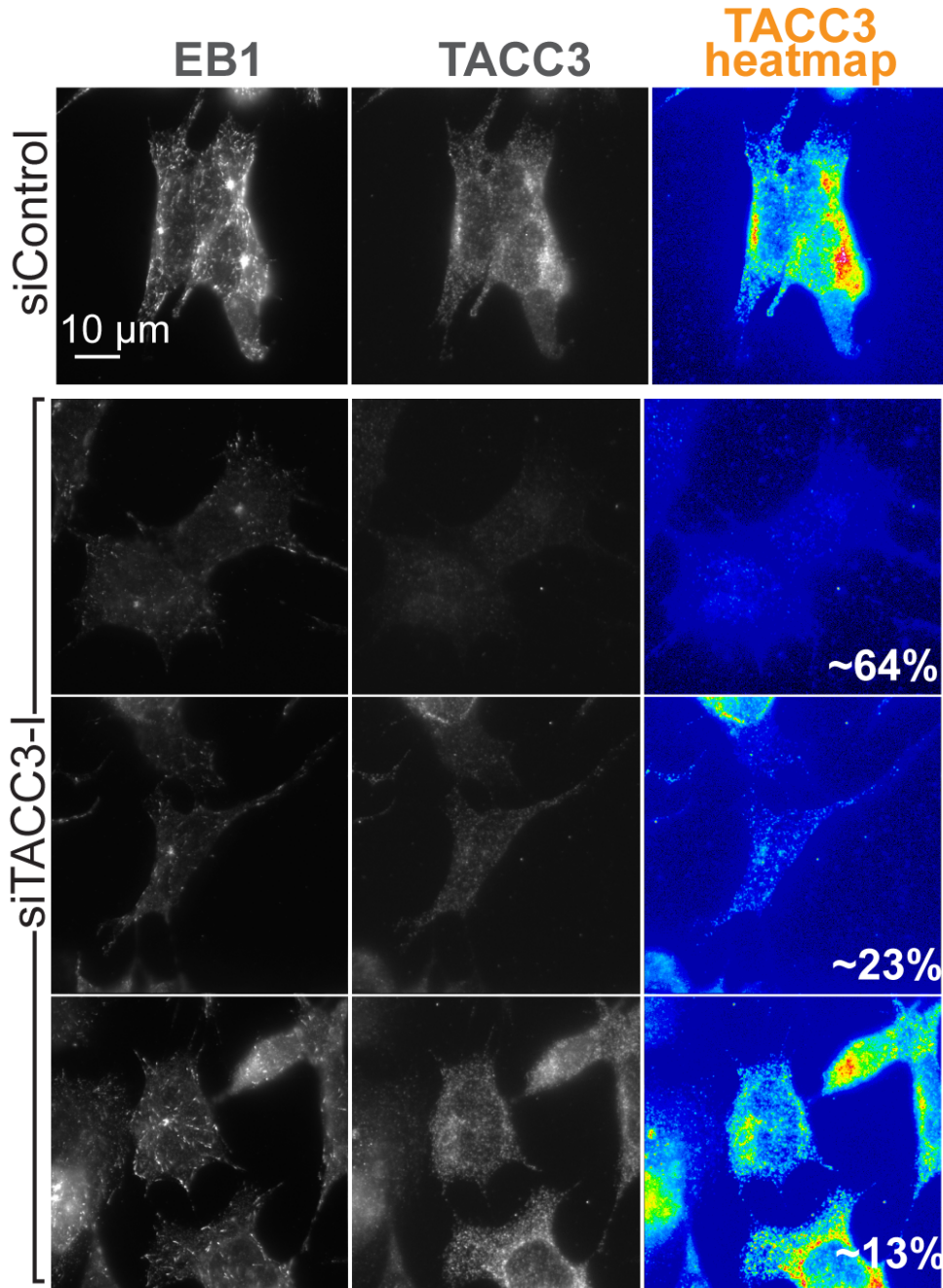


**Figure 24** Number of EB1 comets correlates with amount of TACC3 in cell. SK-N-SH cells were treated with control or TACC3-I siRNA. Cells were stained for EB1 and TACC3. TACC3 color-intensity heatmap is also shown. Three examples of siTACC3-I treated cells are shown which represent the range of TACC3 knockdown within the overall population. The percentage of siTACC3-I cells displaying each level of knockdown was quantified from over 100 cells per condition. Despite variable knockdown, the extent of TACC3 depletion in individual cells correlated with the degree to which EB1 comet staining was affected. Representative images are shown of results derived from 3 independent experiments.

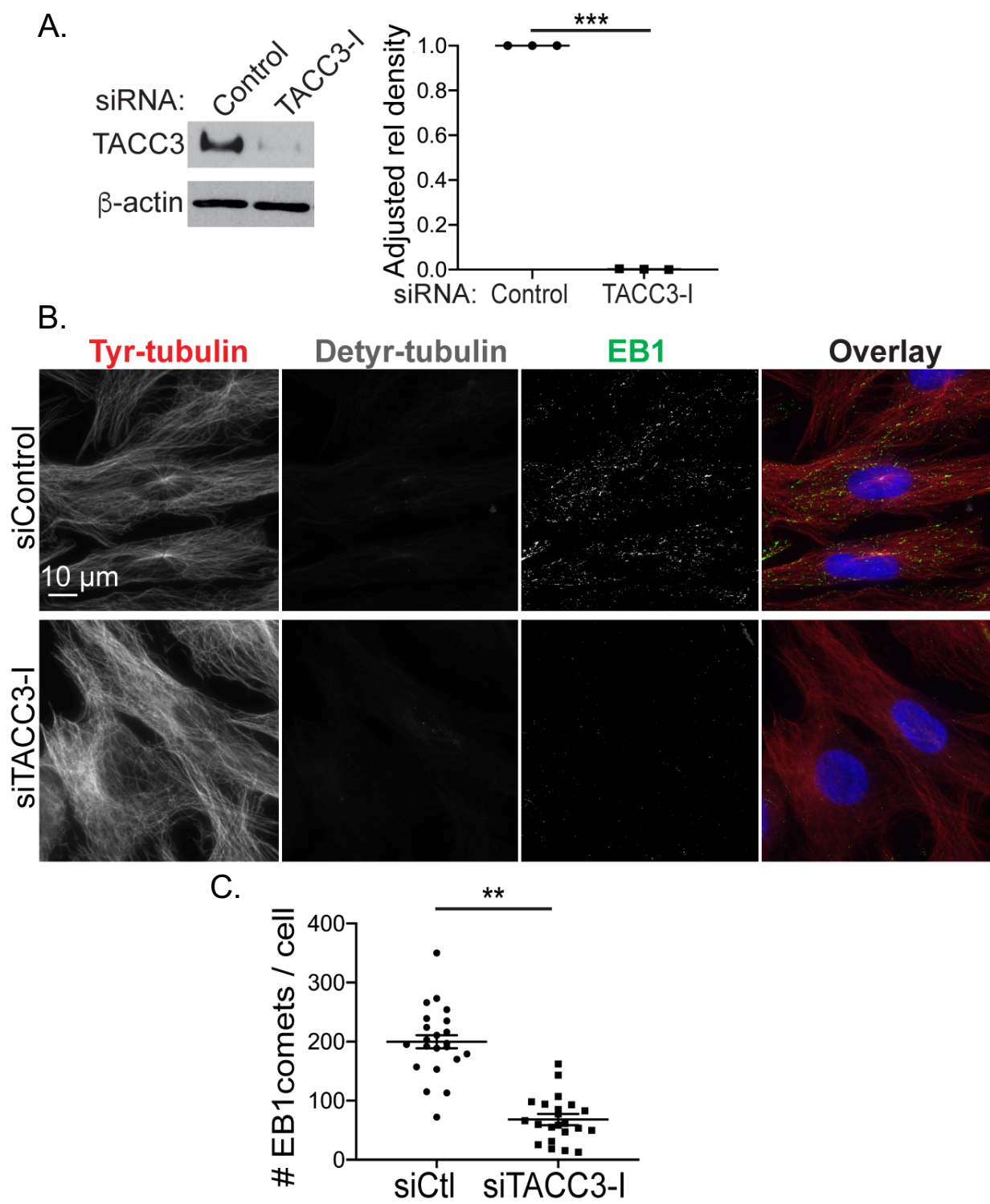


**Figure 25** TACC3 regulates MT plus-end dynamics in NHDFs. (A, left) NHDFs were treated with indicated siRNAs and analyzed by western blot. (A, right) Average adjusted relative density (AU) of TACC3 was quantified across WBs from 3 independent experiments; error bars = SEM; \*\*\* $p < 0.005$ ; unpaired two-tailed t-test. (B) NHDFs treated with control or TACC3 siRNAs were stained for Tyr- (red) and Detyr- (grey) tubulin, along with EB1 (green) and Hoechst. Representative cells are shown. (C) Average number of EB1 comets per cell treated as in B. Total number of EB1 comets were counted in 30 cells per siRNA over 3 biological replicates; error bars = SEM; \*\* $p < 0.01$ ; unpaired two-tailed t-test.

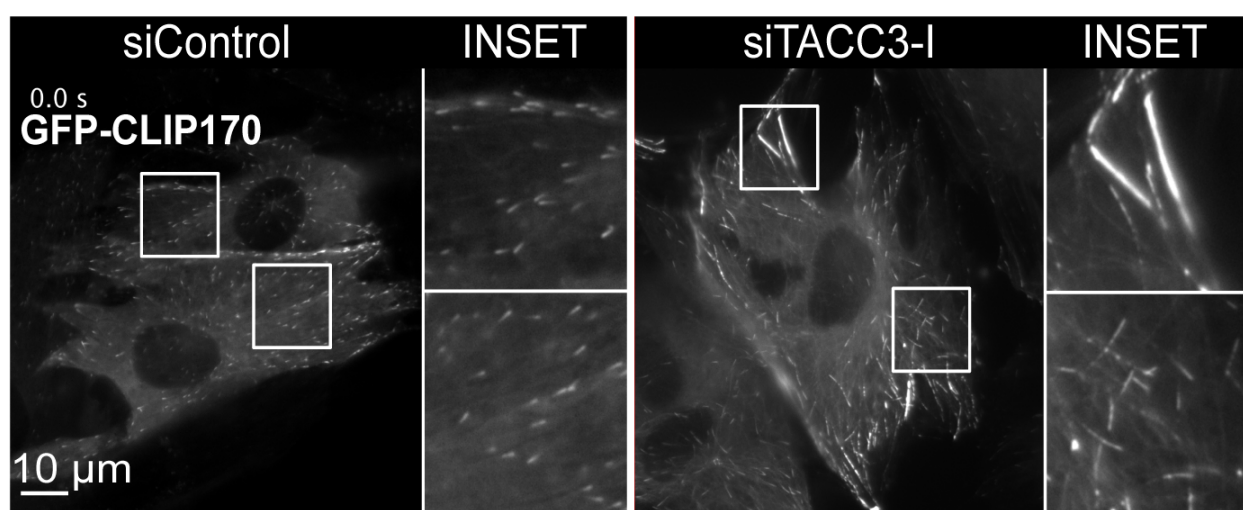


**Figure 26** Live-cell imaging of plus-end dynamics in TACC3-depleted cells. Still image from Video S1 of NHDFs expressing GFP-CLIP-170 treated with control or TACC3-I siRNA. Insets show zoomed view of GFP-CLIP-170 comets. Representative images are shown of results derived from 3 independent experiments.

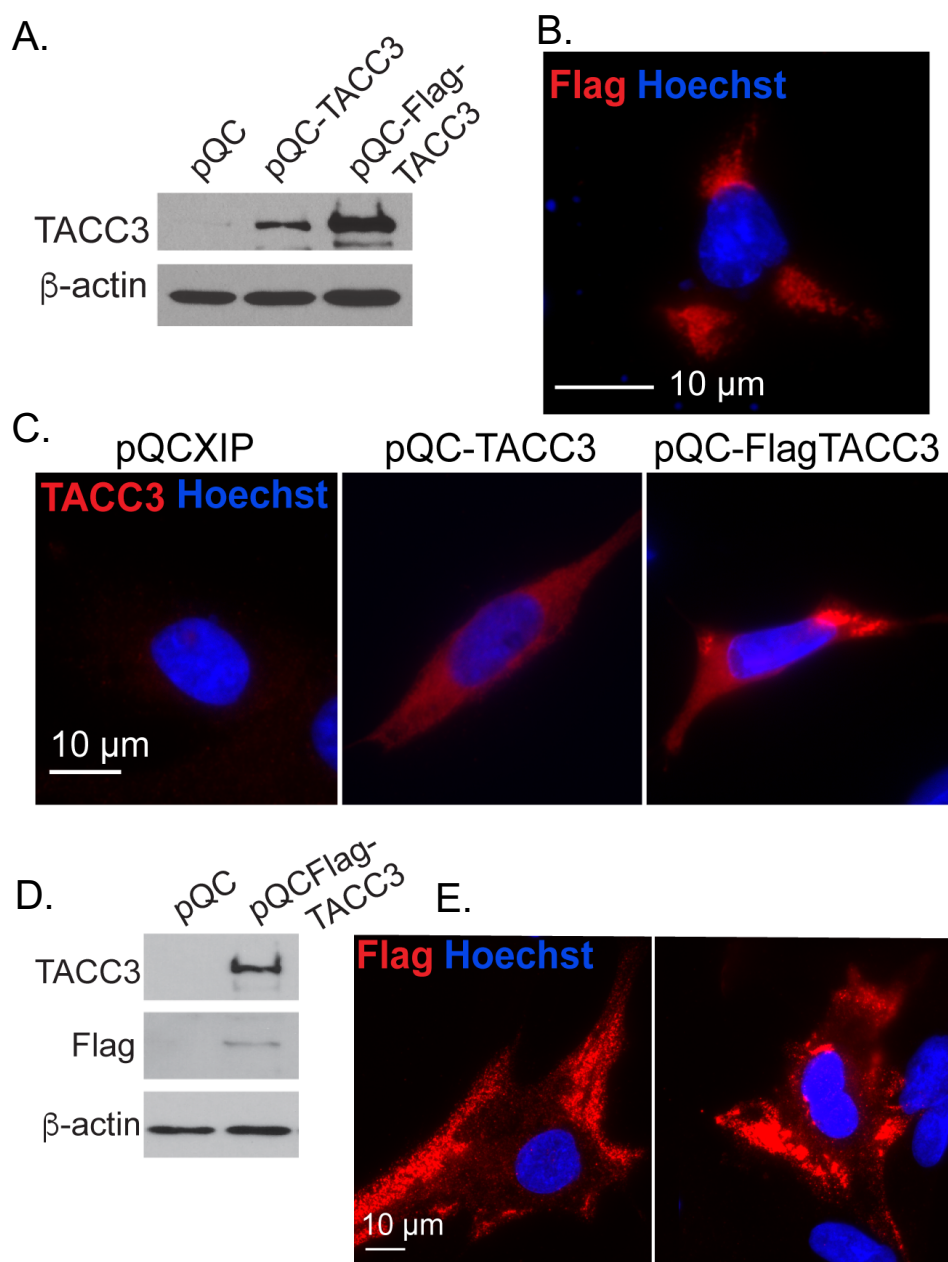


**Figure 27** FLAG-tagged TACC3 forms cytoplasmic aggregates when expressed in cells. (A) SK-N-SHs were transduced with pQCXIP (pQC), pQCXIP-TACC3 (pQCTACC3), or pQCXIP-FLAG-TACC3 (pQCFlagTACC3) retroviral vectors and analyzed by WB. (B) SK-N-SHs transfected with pQCXIP-FLAG-TACC3, fixed and stained for FLAG and with Hoechst. (C) SK-N-SHs transduced as in A. were fixed and stained for TACC3 and Hoechst. (D) NHDFs were electroporated with pQCXIP (pQC) or pQCXIP-FLAG-TACC3 (pQCFlagTACC3). Lysates analyzed by WB with indicated antibodies. (E) NHDFs electroporated with pQCXIP-FLAG-TACC3, fixed and stained for FLAG (red) along with Hoechst. All of the experiments represent  $\geq 3$  replicates unless indicated. Representative images are shown of results derived from 3 independent experiments.

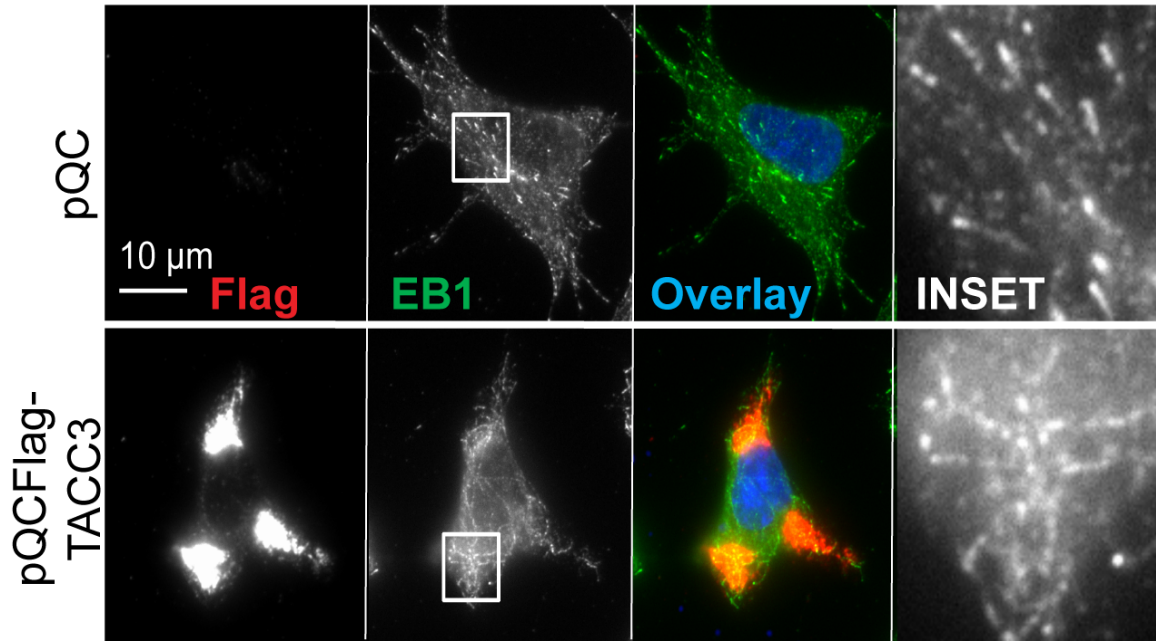


**Figure 28** EB1 comets are elongated in cells expressing FLAG-TACC3. SK-N-SHs were transfected with pQCXIP or pQCXIP-FLAG-TACC3, fixed after 3d and stained for FLAG (red), EB1 (green) and with Hoechst. Zoom shows elongated EB1 staining patterns, indicative of reduced MT polymerization, in cells expressing FLAG-TACC3. Representative images are shown of results derived from 2 independent experiments.

more robust and readily quantifiable effects were observed in NHDFs that express lower levels of endogenous TACC3. Compared with controls, Flag-TACC3 expression resulted in both a decrease in the number of EB1 comets per cell and an increase in the length of EB1 comets, indicative of a reduction in the number and growth rate of dynamic MTs, respectively (Figure 29). Flag-TACC3 expression also caused an increase in acetylated MTs in NHDFs (Figure 30), suggesting an increase in PTMs accumulating on less dynamic MTs. Cumulatively, these data demonstrated that TACC3 regulated MT plus-end dynamics in both cell types. We next confirmed that our Flag-TACC3 dominant-negative did indeed sequester chTOG. To accommodate co-staining, a mouse anti-FLAG antibody that generates more background signal had to be used. Despite this, aggregates of Flag-TACC3 were readily discernible in both cell types and chTOG was sequestered within these aggregates (Figure 31) [180]. Testing the effects of TACC3 depletion, WB analysis showed the total abundance of chTOG was unaffected in either SK-N-SHs or NHDFs (Figure 32A-B). However, IF imaging and quantification showed that chTOG accumulated in the nucleus in TACC3-depleted cells (Figure 32C-F), similar to reported effects of Alp7 deletion in yeast [240, 241]. While these cells are relatively flat and well-suited to single-plane widefield imaging, we confirmed the nuclear accumulation of chTOG in TACC3-depleted cells using confocal microscopy and maximum projection z-stacks (Figure 33, Video S2). These approaches revealed that TACC3 regulates the cytoplasmic localization of chTOG, with loss of TACC3 resulting in its nuclear localization while dominant-negative TACC3 sequestered chTOG in the cytoplasm.

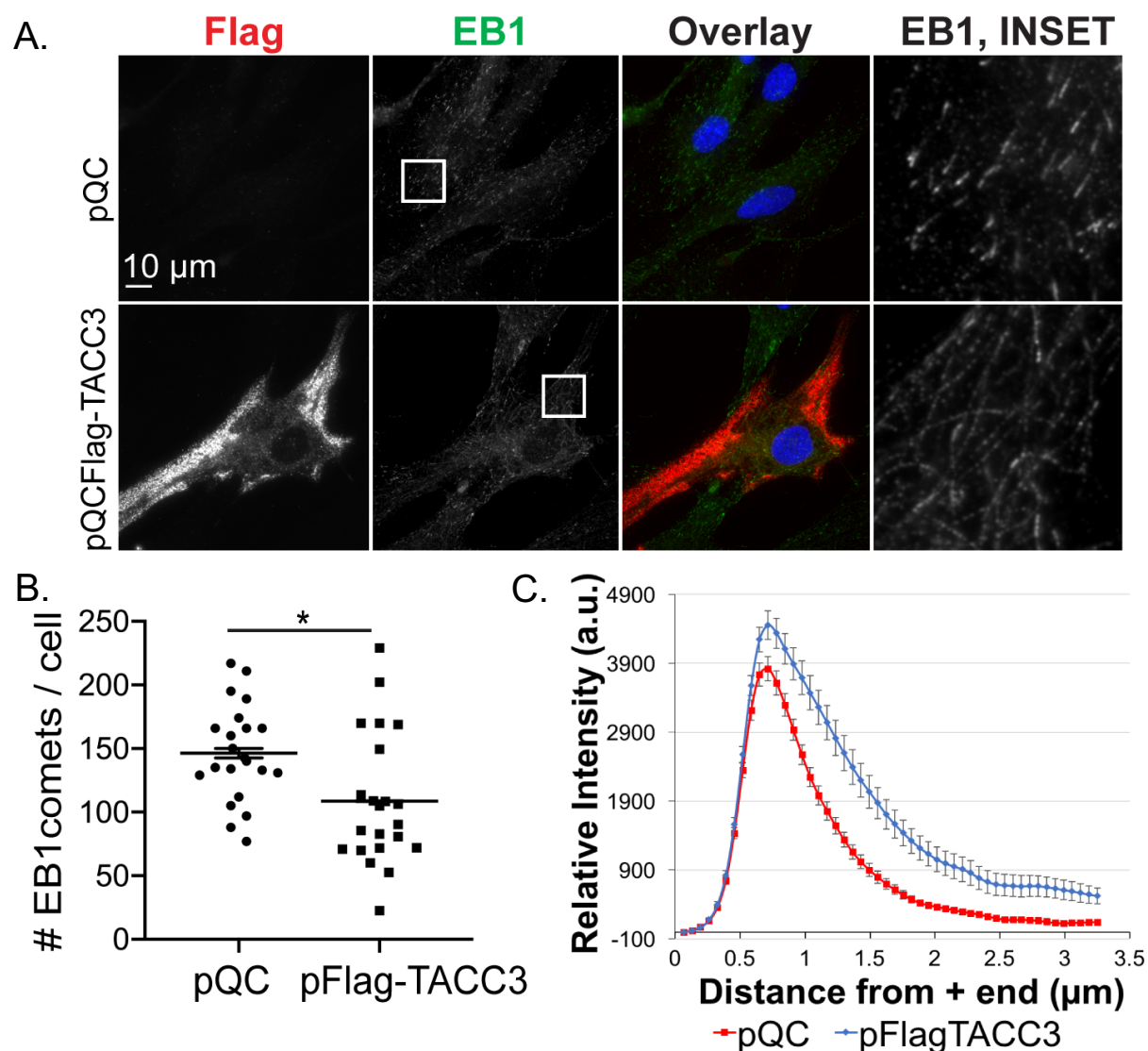


**Figure 29** Expression of dominant-negative TACC3 suppresses MT dynamics. NHDFs were electroporated with pQCXIP (pQC) or pQCXIP-FLAG-TACC3 (pQCFlagTACC3) (A) NHDFs were fixed and stained for FLAG (red) and EB1 (green) along with Hoechst. Inset shows zooms of EB1 comets. Representative images are shown of results derived from 3 independent experiments. (B) Average number of EB1 comets per cell for NHDFs as in A. Total number of EB1 comets were counted in 20 cells per condition over 2 biological replicates; error bars = SEM; \* $p < 0.05$ ; unpaired two-tailed t-test. (C) Line-scan analysis measuring EB1 intensity distribution from the MT plus-end in control and FLAG-TACC3-expressing cells. 250 line-scans were analyzed over 10 cells per condition; error bars denote SEM.

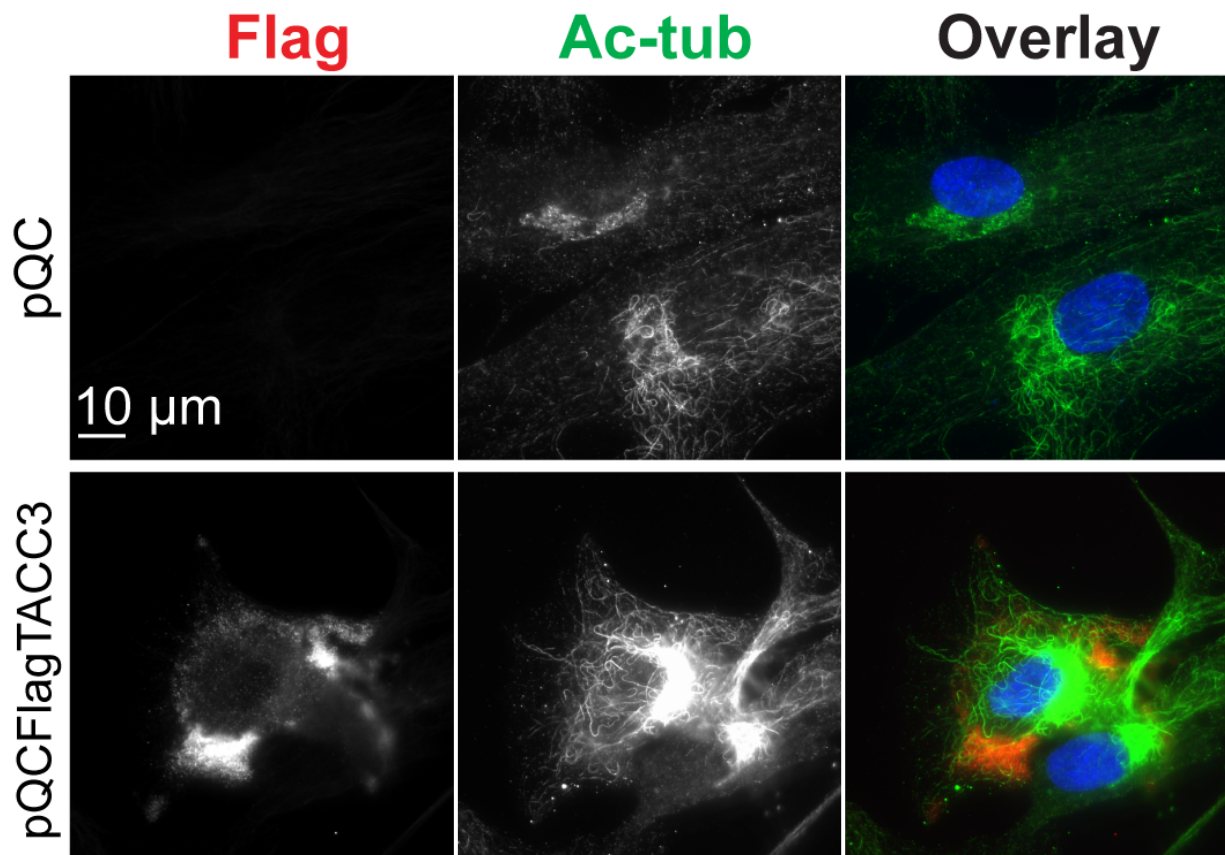


**Figure 30** Dominant-negative TACC3 expression upregulates acetylated MTs in NHDFs. NHDFs were electroporated with pQCXIP (pQC) or pQCXIP-FLAG-TACC3 (pQCFlagTACC3). NHDFs were fixed and stained for FLAG (red) and acetylated (Ac) tubulin (green) along with Hoechst. Representative images are shown of results derived from 2 independent experiments.

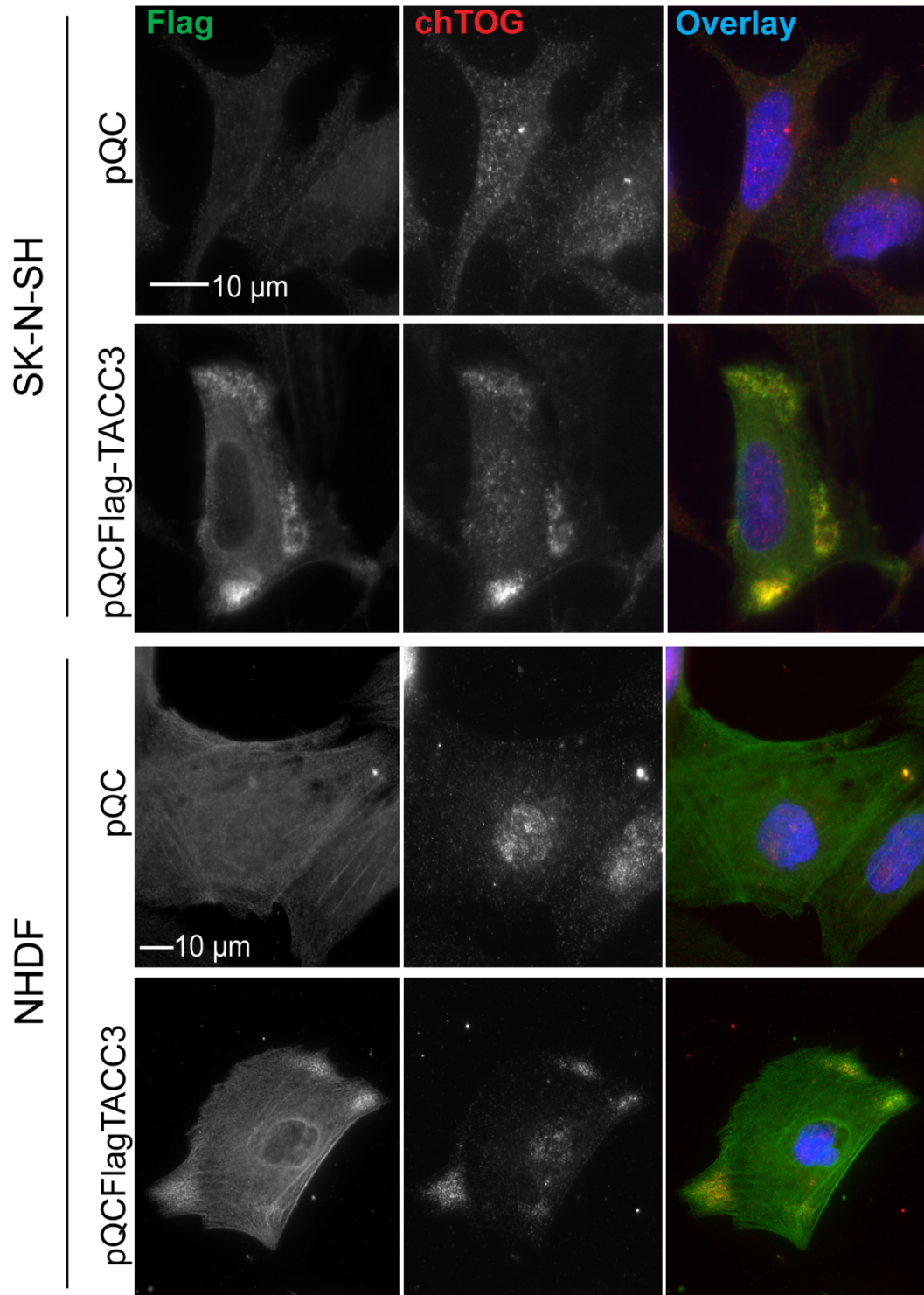


**Figure 31** FLAG-TACC3 sequesters chTOG in cytoplasmic aggregates. SK-N-SHs (top) were transfected and NHDFs (bottom) were electroporated with pQCXIP or pQCXIP-FLAG-TACC3. Fixed cells were stained for FLAG (green) and chTOG (red), and with Hoechst. Representative images are shown of results derived from 3 independent experiments.

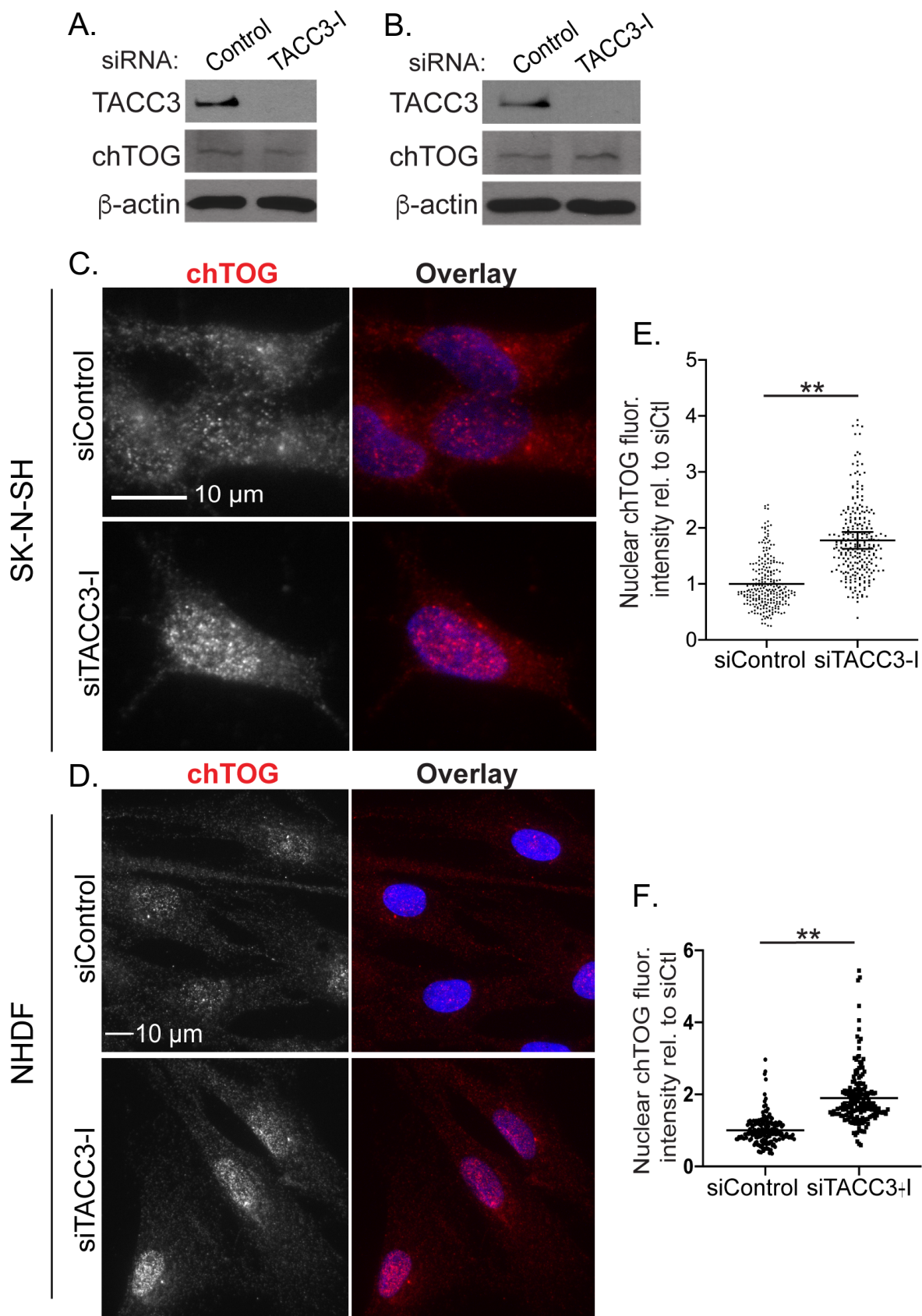


**Figure 32** TACC3 regulates chTOG localization during interphase. (A) SK-N-SHs and (B) NHDFs were treated with control or TACC3 siRNA and analyzed by WB. (C, D) siRNA-treated (C) SK-N-SHs and (D) NHDFs were fixed and stained for chTOG (red) and with Hoechst. (E, F) Average corrected total fluorescence intensity of nuclear chTOG in (E) SK-N-SHs and (F) NHDFs treated with siRNAs. (E)  $\geq 255$  SK-N-SHs and (F)  $\geq 160$  NHDFs per siRNA over 3 biological replicates; error bars = SEM; \*\* $p < 0.01$ ; unpaired two-tailed t-test. All experiments represent 3 independent replicates. Representative images are shown of results derived from 3 independent experiments.

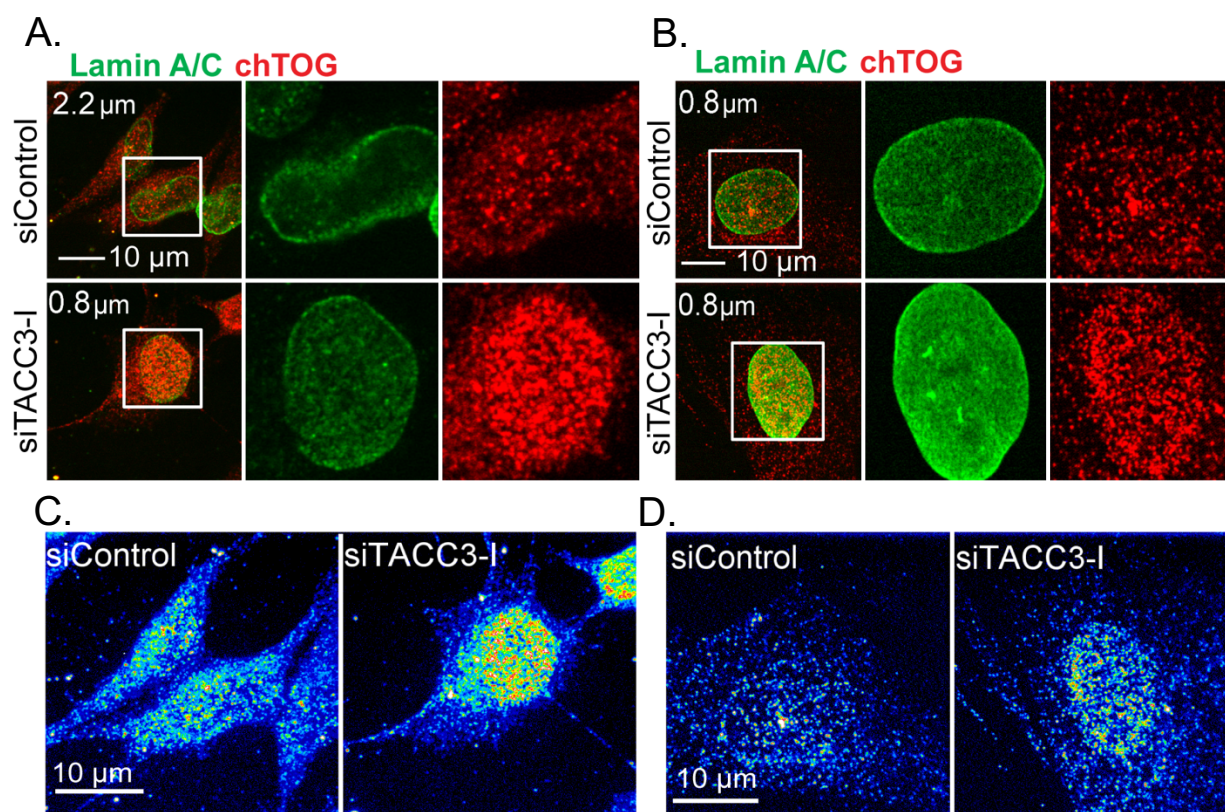


**Figure 33** Confocal microscopy confirms an increase in nuclear chTOG in TACC3-depleted cells. (A) SK-N-SHs or (B) NHDFs were treated with siRNAs, then fixed and stained for lamin A/C (green) and chTOG (red), imaged by confocal microscopy. Stills from Video S2 are shown. (C, D) Maximum intensity projection of chTOG from confocal Z-stack in (C) SK-N-SHs and (D) NHDFs. Color intensity heatmap is shown. Representative images are shown of results derived from 3 independent experiments.

### **TACC3 regulates infection and kinesin-1-based trafficking in SK-N-SHs**

Our data to this point showed that TACC3 perturbations resulted in similar defects in MT plus-end growth and induced acetylated MTs in both SK-N-SHs and NHDFs. Acetylation occurs rapidly and is not exclusive to stable MTs. By contrast, dysregulation of stable de-tyrosinated MT networks and changes in cell morphology only occurred in SK-N-SHs. This suggested that while TACC3 broadly regulates MT dynamics, it has cell-specific functions that control stable MTs in SK-N-SHs and might influence HSV-1 infection. To test this, we treated NHDFs or SK-N-SHs with control or TACC3 siRNAs and then infected them with HSV-1. IF imaging and quantification showed that TACC3 depletion caused a significant decrease in the number of nuclei expressing the viral protein, ICP4 and in the accumulation of VP5-positive viral particles around the nuclei of either NHDFs or SK-N-SHs (Figure 34A-D). While its effects on MT dynamics would make it predictable that TACC3 depletion would affect infection in NHDFs, infection was also impaired in TACC3-depleted SK-N-SHs. Notably, using the same assays EB1 depletion did not affect either ICP4 expression or virus accumulation around the nucleus in SK-N-SHs (Figure 34E-F).

Next, we tested whether effects on HSV-1 infection in SK-N-SHs reflected defects in virus entry or trafficking. We first stained siRNA-treated cells infected with HSV-1 for the viral glycoprotein, gB together with the capsid protein, VP5 (Figure 35, Figure 36). As described earlier, VP5 capsids that do not co-stain for gB represent fused particles. Compared with controls, TACC3 depletion caused an initial reduction in the number of fused particles in the cytosol at 30 min post-infection, but a sizeable number of fused particles were detectable by 60 min (Figure 35, Figure 36). This suggested that TACC3 depletion slowed but did not block HSV-1 entry. To test whether TACC3 also affected the trafficking of HSV-1 particles that eventually enter the cytosol, we

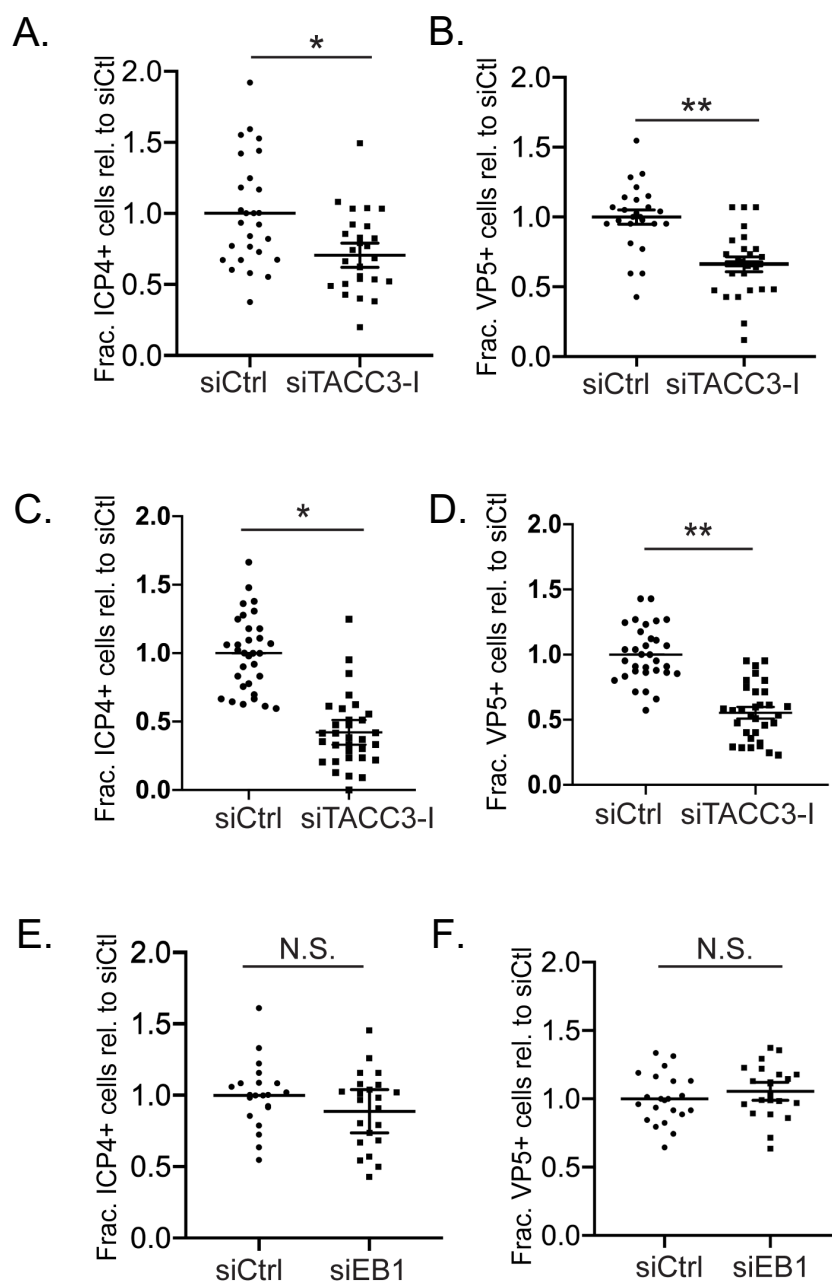


**Figure 34** TACC3 regulates HSV-1 infection in both SK-N-SHs and NHDFs. (A, B) SK-N-SHs and (C, D) NHDFs treated with control or TACC3 siRNA and infected at MOI 20 for 4 hours. Nuclei were stained and assessed for (A, C) ICP4 expression or (B, D) VP5 capsid accumulation.  $\geq 270$  cells per siRNA over 2 biological replicates; error bars = SEM; \* $p < 0.05$ , \*\* $p < 0.01$ ; unpaired two-tailed t-test. (E, F) SK-N-SHs were treated with control or EB1 siRNA (from Figure 7A) and infected with HSV-1, fixed and stained as in A-B. (E) ICP4 expression in the nucleus and (F) VP5 accumulation at the nuclear rim were quantified as above.  $\geq 330$  cells per siRNA over 2 biological replicates; error bars = SEM; N.S. = not significant; two-tailed t-test.

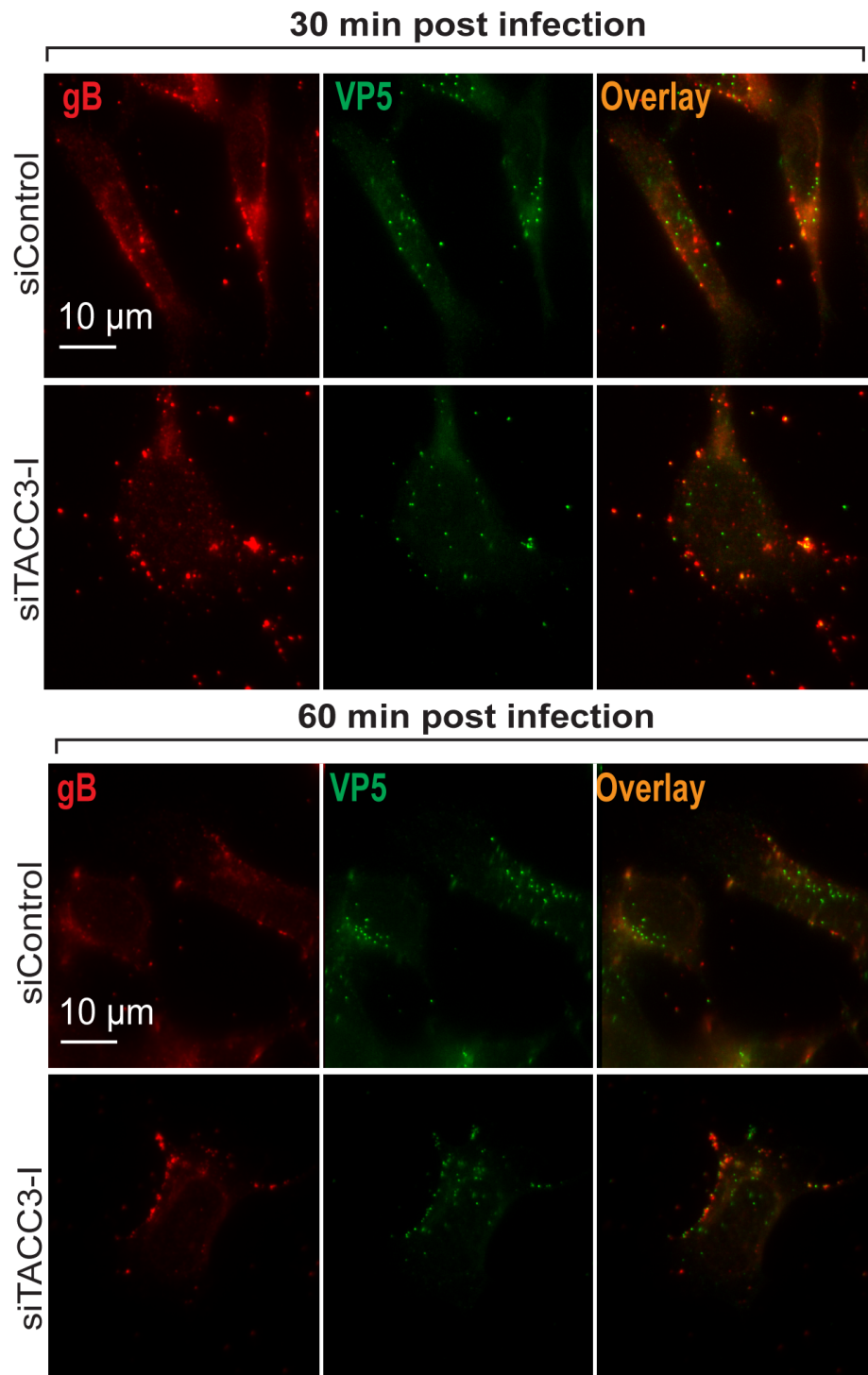


**Figure 35** TACC3 knockdown slows but does not inhibit HSV-1 entry in SK-N-SHs. SK-N-SHs were treated with control or TACC3 siRNA and infected with HSV-1 at MOI 30 for 30 or 60 min. Cells were stained for gB (red) and VP5 (green). Representative images are shown of results derived from 3 independent experiments.

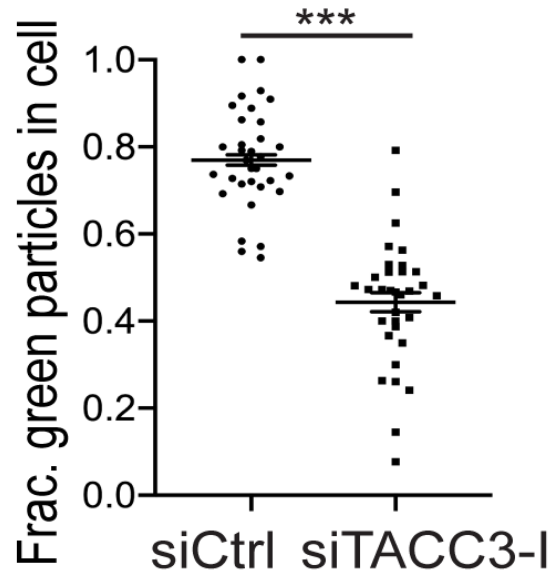


**Figure 36** Quantification of fused HSV-1 particles in TACC3-depleted cells. SK-N-SHs treated and stained as in Figure 35, fixed at 30 min post infection. Average fraction of green particles vs green and yellow particles per cell was quantified. 30 cells per siRNA were analyzed over 3 biological replicates; error bars = SEM; \*\*\* $p < 0.005$ ; unpaired two-tailed t-test.

infected siRNA-treated SK-N-SHs with HSV-1 carrying a GFP-tagged virion protein, VP26 [223]. Live cell video microscopy showed that in control siRNA-treated cells, early in the entry process (30 min) virus particles were distributed throughout the cell and exhibited bidirectional short and long-range movements. By 60 min, many particles had reached the nucleus where they dock and become static (Figure 37A, Video S3). Particle tracking further showed that viruses that were still motile exhibited net retrograde movement towards the nucleus (Figure 37B-C). By contrast, in TACC3-depleted cells many virus particles remained at the cell periphery at both 30 and 60 min timepoints, in line with slower entry detected using fixed imaging approaches. Moreover, particle tracking showed that motile viruses exhibited net anterograde movement away from the nucleus (Figure 37B-C), suggesting increased kinesin-based movement in TACC3-depleted cells. In addition, virus particles near the nucleus appeared to be distributed throughout the enlarged de-tyrosinated MT network formed in TACC3-depleted cells. Tubulin de-tyrosination reduces dynein and increases kinesin-1 affinity and motor processivity on MTs [121-124]. As such, the changes in abundance and organization of de-tyrosinated MTs in TACC3-depleted SK-N-SHs might favor kinesin-1 activity and impair the inward transport of virus particles. If this were the case, suppressing kinesin-1 activity should rescue infection in TACC3-depleted cells. To test this, we treated SK-N-SHs with TACC3-I siRNAs, either alone or in combination with siRNAs targeting the kinesin-1 heavy chain isoform, Kif5B (Figure 38A). IF analysis of siRNA-treated cells suggested that TACC3 depletion did not cause gross defects in Kif5B localization, although more subtle effects cannot be ruled out (Figure 38B). Cultures were then infected with HSV-1 and fixed at 4 h.p.i., followed by co-staining with VP5 and gB. IF analysis and quantification showed that in control cells, fused viral particles accumulated at specific regions of the nuclear periphery (Figure

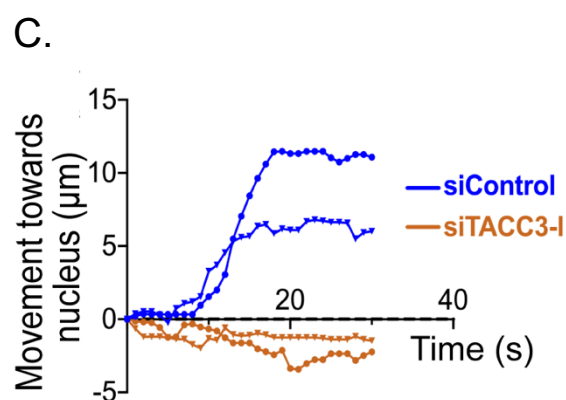
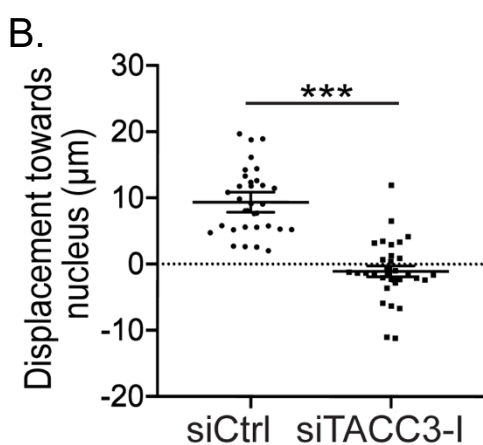
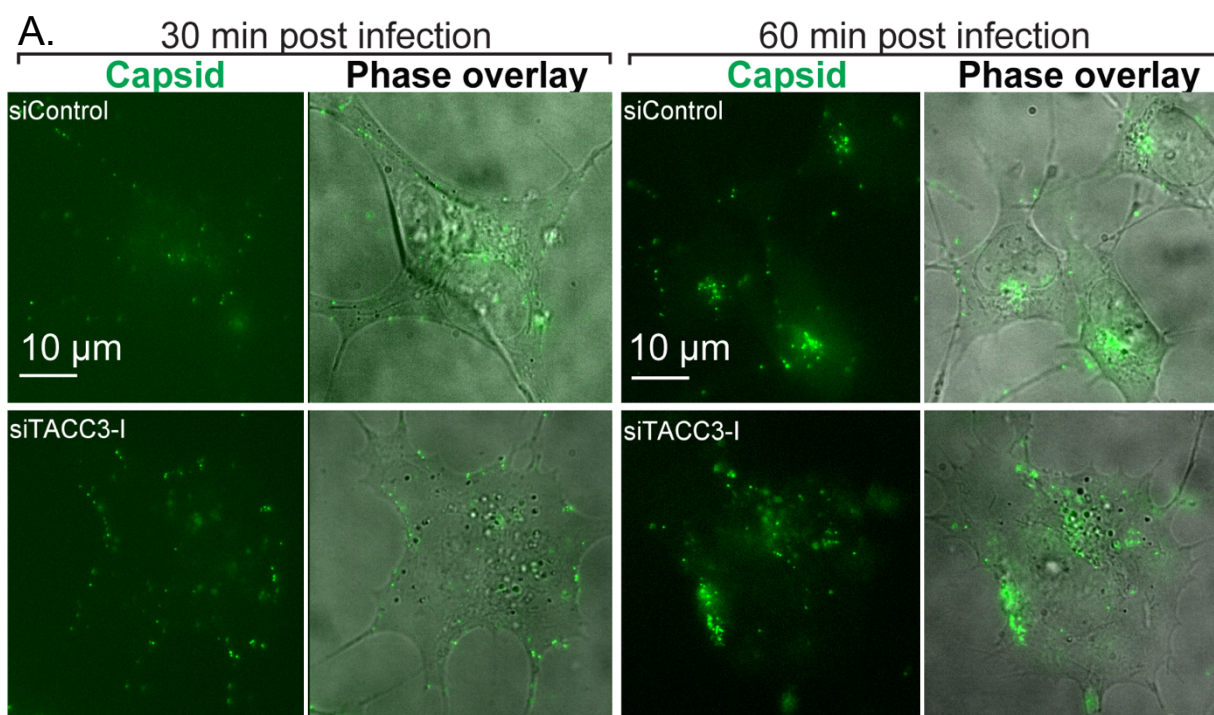


**Figure 37** HSV-1 particles exhibit net anterograde motility during early infection in TACC3-depleted SK-N-SHs. (A) Still images from Video S3 of siRNA treated SK-N-SH infected with HSV-1 K26GFP at MOI 100. Cells were imaged at 30 and 60 min post infection. Phase images show the infected cell. images are shown of results derived from 3 independent experiments. (B) Individual virus particles from cells as in A. were manually tracked for at least 10 seconds. For each track, virus particle displacement relative to the nucleus was quantified. 30 particles per siRNA were analyzed over 3 biological replicates; error bars = SEM; \*\*\* $p < 0.005$ ; unpaired two-tailed t-test. (C) Movement towards the nucleus of two representative particles for each siRNA in A.; blue is siControl- and orange is siTACC3-I-treated cells.

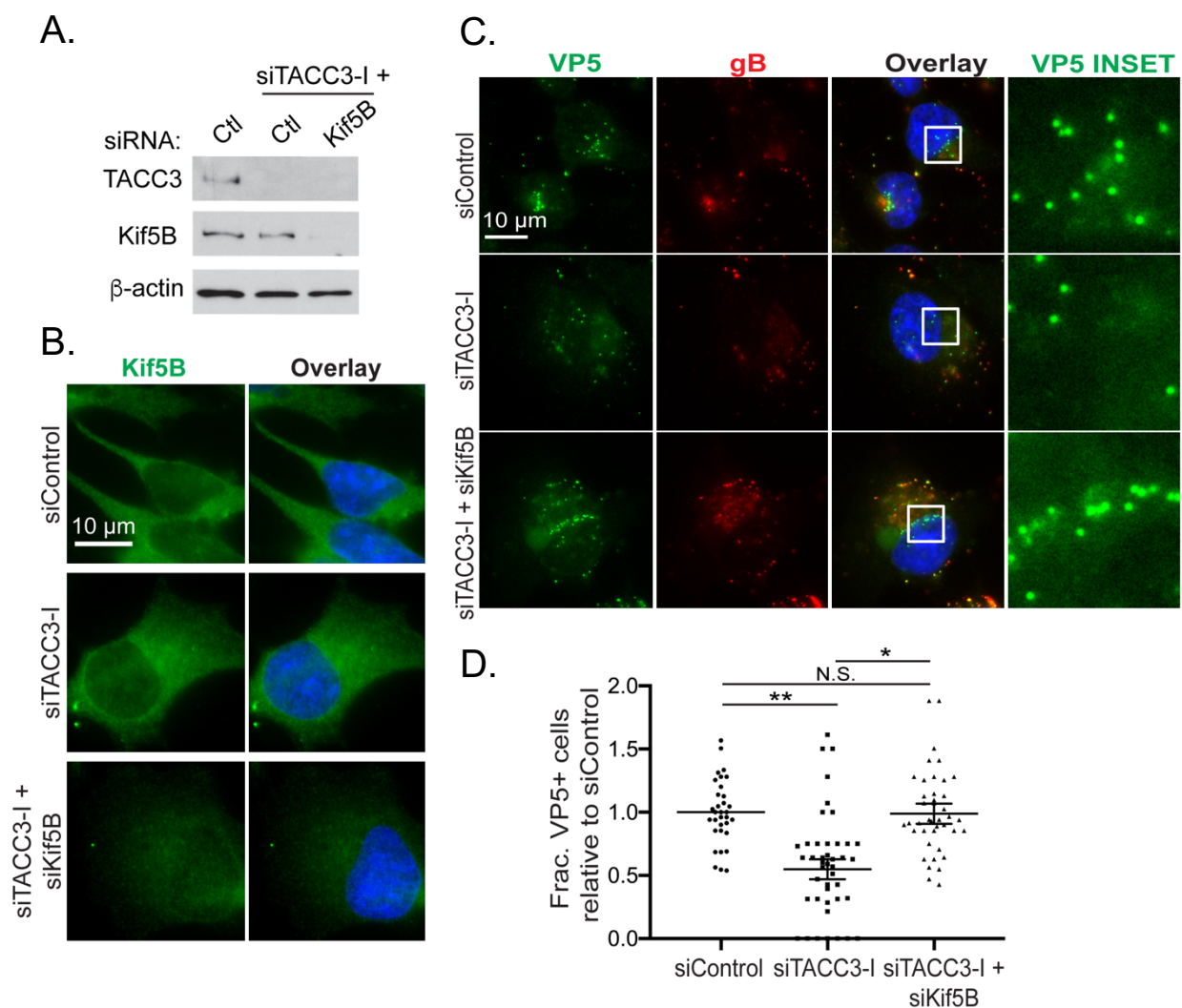


**Figure 38** Kinesin-1 prevents perinuclear accumulation of HSV-1 particles in TACC3-depleted SK-N-SHs. SK-N-SHs were treated with the indicated combination of siRNAs. (A) Cells were analyzed by WB using the indicated antibodies. (B) Cells were fixed and stained for Kif5B (green) along with Hoechst. (C) Cells were infected with HSV-1 at MOI 20 for 4h. Fixed cells were stained for VP5 (green) and gB (red) along with Hoechst. Inset shows zoomed view of VP5 at the perinuclear space. (D) VP5 capsid accumulation at nucleus in SK-N-SHs treated and infected as in C.  $\geq 225$  cells per siRNA over 3 biological replicates; error bars = SEM; \*p < 0.05, \*\*p < 0.01, N.S. = not significant; unpaired two-tailed t-test. All of the experiments represent  $\geq 3$  replicates unless indicated. Representative images are shown of results derived from 3 independent experiments.

38C-D). This pattern of accumulation was reduced in TACC3-depleted cells, but this defect was rescued by Kif5B depletion. We also examined effects on virus movement. siRNA-treated cells were infected with HSV-1 GFP-VP26 virus for 60 min to allow fusion of a significant fraction of virus under all conditions, followed by live cell video microscopy. Time lapse imaging and particle tracking revealed that in control siRNA-treated cells virus particles exhibited net retrograde movements and accumulated around the nuclear periphery (Figure 39, Video S4). While TACC3 depletion again impaired virus movement and translocation to the nucleus, these defects were rescued in TACC3-I siRNA-treated cells by depleting Kif5B (Figure 39, Video S4). These findings suggested that TACC3 regulates the organization of de-tyrosinated MT networks that control kinesin-1-based trafficking pathways exploited by HSV-1, but which may also impact the trafficking of cellular cargos. To test this, we examined transferrin uptake and localization. Following endocytosis, transferrin-containing endosomes enter the recycling endosomal pathway, whereby endosomes undergo either fast recycling to the plasma membrane or slow recycling to the perinuclear endocytic recycling compartment [254]. Furthermore, transferrin is known to be recycled from perinuclear regions to the cell periphery on de-tyrosinated MTs by kinesin-1 [255].

We first examined the sensitivity of Alexa647-transferrin uptake and sorting to the perinuclear space in nocodazole-treated SK-N-SHs. While overall Alexa647-transferrin intensity was partially decreased at 500nM nocodazole, suggesting dynamic MTs maximize the degree of transferrin uptake, it continued to accumulate at the perinuclear space (Figure 40A-B). By contrast, at 10 $\mu$ M nocodazole both transferrin uptake and sorting to the nuclear periphery were impaired. It is important to note that although images show a very strong reduction in the intensity of transferrin accumulation at this perinuclear region in cells treated with 10 $\mu$ M nocodazole, the presence of

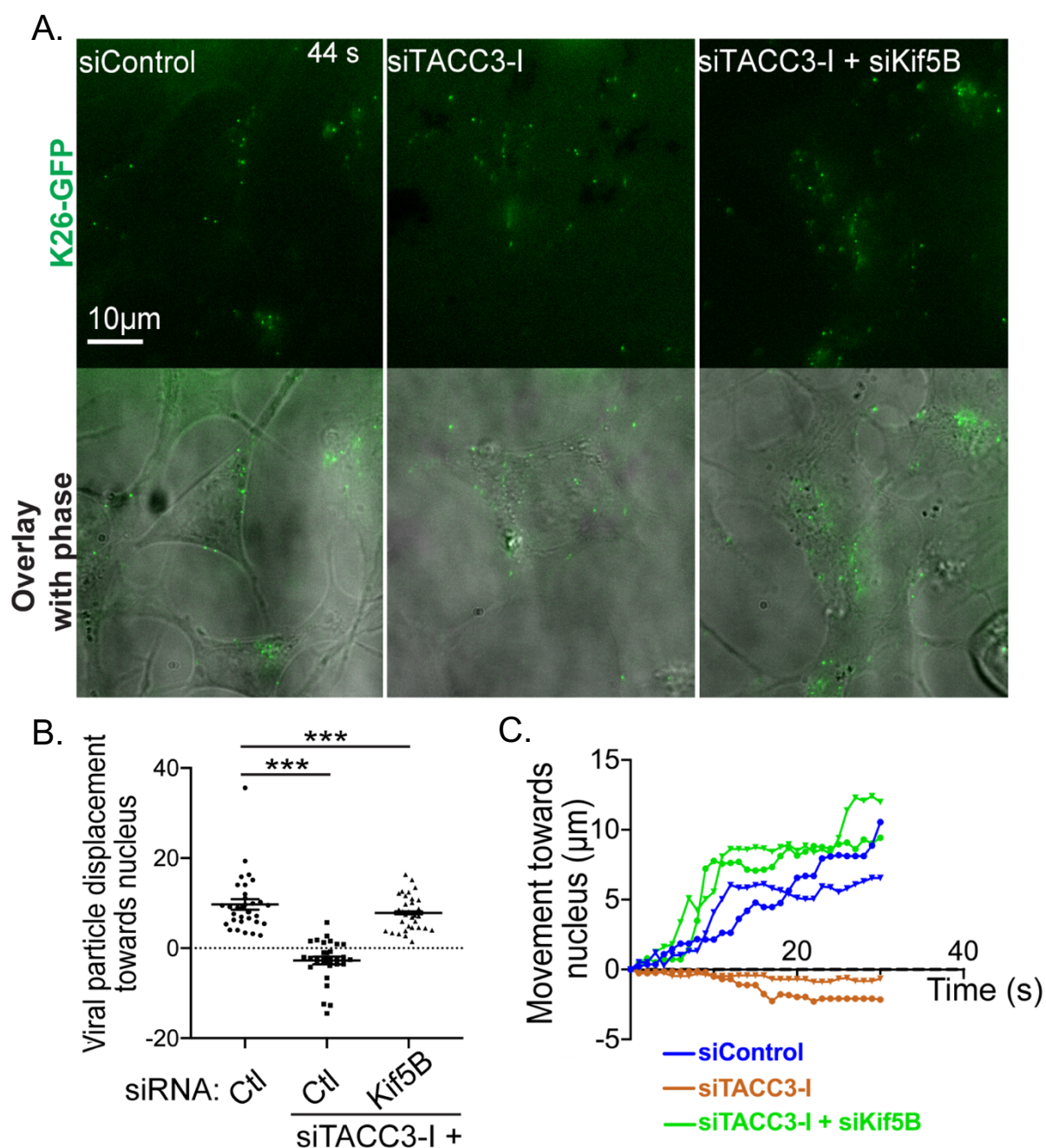


**Figure 39** Co-depletion of TACC3 and kinesin-1 rescues retrograde motility of HSV-1 particles in SK-N-SHs. (A) Still images from Video S4 of siRNA-treated SK-N-SHs infected with HSV-1 K26GFP at MOI 100 and imaged by time-lapse fluorescence microscopy at 60 min post infection to visualize GFP-tagged capsid. Phase images show the infected cell. (B) Individual virus particles from cells as in A. were manually tracked for at least 10 seconds. For each track, virus particle displacement relative to the nucleus was quantified. 30 particles per siRNA were analyzed over 3 biological replicates; error bars = SEM; \*\*\* $p < 0.005$ ; unpaired two-tailed t-test. (C) Movement towards the nucleus of two individual particles as in A. from each siRNA treatment, color-coded as indicated.

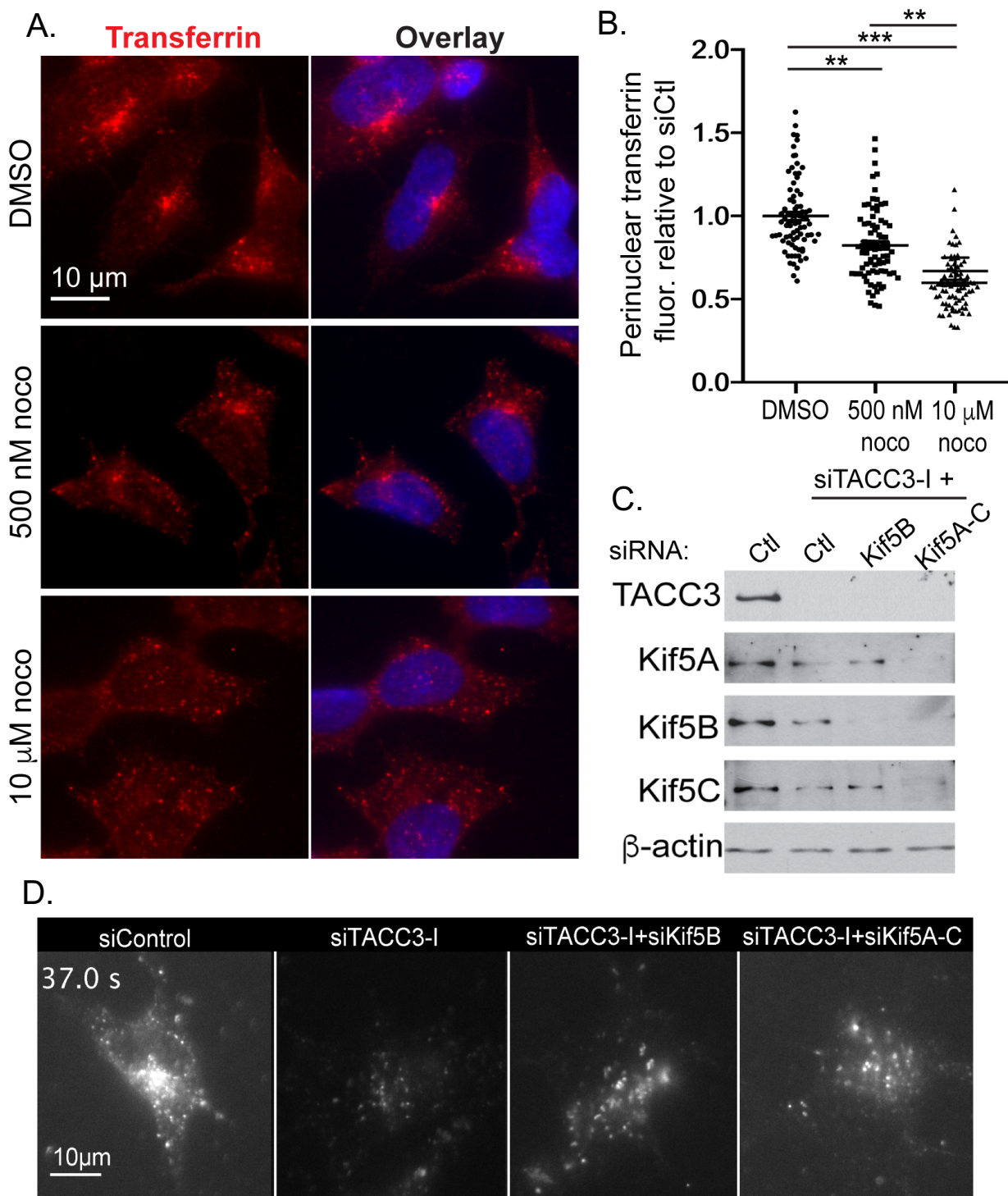


**Figure 40** Kinesin-1 prevents perinuclear accumulation of transferrin in TACC3-depleted SK-N-SHs. (A) SK-N-SHs were treated with DMSO or 10  $\mu$ M nocodazole for 3h or 500 nM nocodazole for 2h. Cells were then incubated with Transferrin-AlexaFluor-647 for 30 minutes and fixed. Nuclei were stained with Hoechst. (B) Average corrected total fluorescence intensity of perinuclear transferrin.  $\geq 80$  cells per siRNA counted over 2 biological replicates; error bars = SEM; \*\*p < 0.01, \*\*\*p < 0.005; unpaired two-tailed t-test. (C) SK-N-SHs were treated with the indicated combination of siRNAs and analyzed by WB. Results shown are representative of 3 independent replicates. (D) siRNA-treated SK-N-SHs were incubated with Transferrin-AlexaFluor-647 for 30 minutes. Still image from Video S5 shows fluorescent transferrin accumulating in control or Kif5B and TACC3 co-depleted cells. Representative images are shown of results derived from 3 independent experiments.

randomly localized and diffuse transferrin-positive vesicles underestimates this effect in quantification approaches.

To examine the effects of TACC3 depletion and the role of kinesin-1, we added Alexa647-transferrin to siRNA-treated SK-N-SHs followed by time-lapse fluorescence microscopy. While Kif5B is the dominant isoform in many cell types, and its depletion rescued HSV-1 infection above, we depleted TACC3 alone or in combination with either Kif5B or all three Kif isoforms (A, B and C) (Figure 40C). Time-lapse imaging showed that in control cells transferrin trafficked along cellular projections into and out of the broader cytoplasmic space, as well as concentrating in specific perinuclear regions (Figure 40D, Video S5). This would be expected for both fast recycling and entry into late endosomal pathways. In TACC3-depleted cells, transferrin uptake appeared reduced and transferrin that was taken into cells did not concentrate at perinuclear regions. However, co-depletion of either Kif5B alone or Kif5A-C largely restored the uptake and accumulation of transferrin at perinuclear regions. This demonstrated that similar to HSV-1, depletion of Kif5B alone was sufficient to rescue defects in transferrin trafficking caused by loss of TACC3. We confirmed these observations by staining fixed cells for de-tyrosinated tubulin, directly imaging and quantifying the accumulation of Alex647-transferrin at perinuclear sites (Figure 41A-B). This further demonstrated how transferrin penetrated deeper into the enlarged de-tyrosinated MT networks to reach the perinuclear space in TACC3-depleted cells when Kif5B was co-depleted (Figure 41A-B). Notably, the perinuclear accumulations of transferrin in TACC3 and Kif5B co-depleted cells were more enlarged than those in control cells. Staining of fixed cells showed that depletion of Kif5B did not reverse the effects of TACC3 depletion on de-tyrosinated

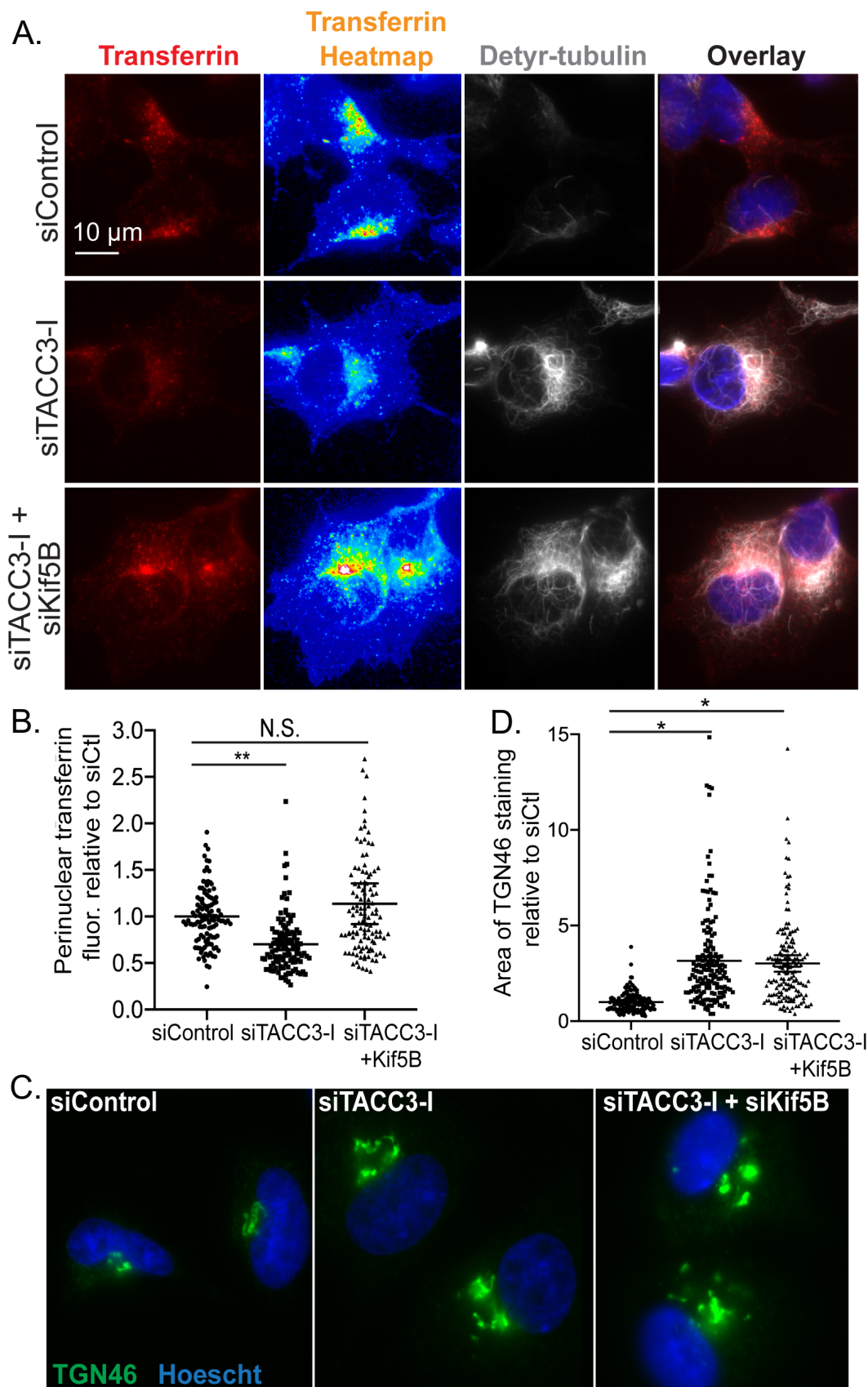


**Figure 41** TACC3 and kinesin-1 co-depletion rescues accumulation of transferrin at perinuclear space in SK-N-SHs. (A) siRNA-treated SK-N-SHs were incubated with Transferrin-AlexaFluor-647 for 30 minutes. SK-N-SHs were then fixed and stained for de-tyrosinated tubulin (Detyr; grey) along with Hoechst. Transferrin-647 shown by color-intensity heat map. Representative images are shown of results derived from 3 independent experiments. (B) Average corrected total fluorescence intensity of perinuclear transferrin.  $\geq 110$  cells per siRNA counted over 3 biological replicates; error bars = SEM; \*\* $p < 0.01$ , N.S. = not significant; unpaired two-tailed t-test. (C) SK-N-SHs treated with the indicated siRNAs were fixed and stained for TGN46 (green) along with Hoechst. Representative images are shown of results derived from 2 independent experiments. (D) Average area of TGN46 staining in SK-N-SHs as in C., relative to siControl.  $\geq 160$  cells per condition over 2 biological replicates; error bars = SEM; \* $p < 0.05$ ; unpaired two-tailed t-test.

MTs or the enlargement of cells (Figure 41A). Moreover, Kif5B depletion did not rescue the effects of TACC3 depletion on Golgi size (Figure 41C-D). This suggested that kinesin-1 did not influence cell shape or Golgi organization that are largely controlled by MTs directly, but played an important role in how cellular and pathogenic cargos reach the perinuclear space in the presence of de-tyrosinated MT networks that are controlled by TACC3.

## Discussion

The importance of EB proteins in regulating MT dynamics is well characterized across many cell systems [126]. In line with our own previous studies [213], EB1 and CLIP170 play critical roles in mediating early HSV-1 infection in human fibroblasts wherein virus transport is mediated by dynamic MT capture. However, neither CLIP170 nor EB1, along with other EB family members, were required for HSV-1 infection in SK-N-SHs. This led us to discover that EB proteins do not detectably affect the formation of de-tyrosinated MT networks and HSV-1 translocation to the nucleus in these cells. It is important to note that these observations do not rule out more subtle roles for EB proteins. However, they reveal how the importance of EB proteins differs across cell types and processes, where other MT regulators can play more dominant roles. Indeed, EB1 and EB3 play distinct and very specialized roles during mitosis and cytomegalovirus infection [45, 256, 257]. Yet, despite our extensive knowledge of EB proteins, much remains to be learned about the contributions of other factors that control MT plus-end dynamics. Despite recent evidence that TACC3 exhibits autonomous +TIP activity, our understanding of how and when it functions outside of mitosis is limited. In *Xenopus* embryos, XTACC3 regulates the recruitment of XMAP215 (chTOG) to MT plus-ends to control filament dynamics and axon

elongation [192]. Similar functions are suggested in yeast, where Alp7 (TACC3) also regulates the cytoplasmic and nuclear localization of Alp14 (TOG) [240, 241]. Our findings show that TACC3 similarly controls chTOG localization and promotes MT plus-end growth in human fibroblasts and neuronal cells. Perturbing TACC3 activity did not affect the initial regrowth of MTs yet it significantly reduced the levels of EB1 comets and altered CLIP170 tracking behavior. This is reminiscent of its functions in mitotic spindle formation and suggests that TACC3 predominantly acts to promote MT polymerization in the cytosol after nucleation, where growing MT ends are then tracked by other +TIPs such as EB1. Once at MT plus-ends, however, the functional importance of EB1 varies with cell type and context.

Although TACC3 regulates MT dynamics in both cell types tested we find that it also has cell-specific functions. Unlike NHDFs that harbor a high proportion of dynamic MTs, perturbing TACC3 functionality in SH-N-SHs resulted in the formation of extensive stable, de-tyrosinated networks accompanied by changes in cell morphology. Kif5B co-depletion did not reverse the effects of TACC3 knockdown on de-tyrosinated MTs, nor did it rescue changes in cell or Golgi morphology that are predominantly controlled by MT filaments themselves. By contrast, defects in HSV-1 and transferrin uptake and localization to the perinuclear space were rescued by co-depletion of Kif5B, suggesting that improper organization of de-tyrosinated MTs disrupts cargo sorting pathways by biasing MT-based transport toward outward-directed motors. This adds support to prior studies suggesting that kinesin-1 has a higher affinity for, or activity on de-tyrosinated MTs [121-123], including in the transport of transferrin [255]. Moreover, our findings suggest that a critical function of TACC3 is to regulate the balance of dynamic and stable MTs in interphase cells, which impacts cell shape and motor-based transport of cargos.

## **CHAPTER 4: Human Cytomegalovirus Exploits TACC3 to Control Microtubule Dynamics and Late Stages of Infection**

This chapter appeared as the published article: Furey C, Astar H, Walsh D. 2021. *J Virol* 95(18): e00821-00821. doi: 10.1128/JVI.00821-21.

The video included in the results section can be found in Supplementary Files.

### **Introduction**

During infection, human cytomegalovirus (HCMV) reconfigures its host cell in a number of ways. One of the most striking changes is the formation of a viral assembly compartment (AC), a large perinuclear structure composed of reorganized host secretory vesicles recruited to the Golgi that becomes the center for virion maturation and envelopment [46, 47, 57, 65, 66, 68, 258-261]. To achieve this extensive cellular reorganization the virus exploits the host microtubule (MT) transport network. While studies using MT depolymerizing or stabilizing agents, and those examining associated motor proteins, have established the importance of MTs in forming the AC and in transporting virus particles [52, 65, 69, 70, 262, 263], the underlying mechanisms by which HCMV actively controls MT networks is less well-defined. Using live cell imaging approaches we recently revealed the surprisingly dynamic nature of the AC and its ability to act not just as a virion maturation site, but also as a Golgi-derived MT organizing center (MTOC) that controls both its own structure as well as the positioning and organization of the host nucleus [44, 45].

While the centrosome is often the functionally dominant site of nucleation in many contexts and is often referred to as “the” MTOC, there are in fact several sites including the Golgi at which MTs can form [78, 264]. MTs consist of  $\alpha$ - and  $\beta$ -tubulin heterodimers that form polarized filaments. Minus-end anchoring at an MTOC seeds the formation of a new MT filament which subsequently grows out into the cytoplasm through the addition of new  $\alpha/\beta$ -tubulin subunits to its

more dynamic plus-end. The dynamic behavior of MT filaments is regulated in large part by a group of highly specialized microtubule-associated proteins known as plus-end tracking proteins, or “+TIPs” [126]. +TIPs locally influence MT plus-end growth, stabilization and depolymerization (catastrophe), as well as regulating interactions with other proteins that enable MT filaments to engage targets. This targeting includes capturing cargos for transport by motor proteins or engaging cellular structures, such as organelles, chromosomes or peripheral actin to control processes such as cell polarization or division [106]. Among the most extensively studied +TIPs are the End-Binding proteins EB1, EB2, and EB3 [126]. EB proteins independently recognize and bind the plus-ends of MTs, which are distinguishable by the transient GTP state of new tubulin subunits before they are rapidly hydrolyzed to a GDP state as they become part of the growing filament [126]. EB proteins not only recognize but also directly influence the dynamics and function of MT plus-ends. Beyond their direct effects on MTs, most other +TIPs require binding to an EB protein in order to be recruited to MT plus-ends and for this reason, the EB proteins are oftentimes viewed as the master regulators of the broader +TIP family [126, 128]. While +TIPs have been extensively studied in a range of biological contexts, recent work is also beginning to uncover their roles in viral infection [200]. As discussed in more detail later, a number of viruses have recently been found to either passively or actively exploit EB proteins and associated +TIPs to mediate their capture and transport to the nucleus during early stages of infection, but less is known about their roles at later stages [265].

An exception to this is HCMV. As its protracted replication cycle progresses, HCMV increases the expression of all three EB family members concurrent with the formation of the AC [45]. Notably, HCMV reduces the MT nucleating activity of the centrosome that is located at the core of the AC and instead, increases MT nucleation from Golgi sites that lie throughout the AC

[45]. Effectively, the AC becomes an enormous Golgi-based MTOC that greatly increases both dynamic and acetylated MT subsets in infected cells, and each subset serves a different function during infection. HCMV specifically exploits EB3 to form MT arrays that are mechanically strengthened by acetylation [108, 109, 265] and which enable the AC to exert such force on the nucleus that despite its size, it undergoes rotational movements [45]. This rotational movement is symptomatic of mechanical pulling by AC-derived acetylated MTs and motors on the nuclear surface that enables the virus to create intranuclear polarity that includes segregation of host and viral DNA [44, 69]. By contrast, EB1 regulates dynamic microtubules that are involved in maintaining the structure of the AC and trafficking of new virus particles once they exit into the cytosol [45].

While the EB proteins have been extensively studied there are other, EB independent +TIPs that remain less well understood, particularly in the context of viral infection. Amongst these, transforming acidic coiled-coil protein 3 (TACC3) also recognizes MT plus-ends and recruits the MT polymerase, chTOG to promote MT growth; in fact, TACC3 and chTOG build the plus-ends that EB proteins then recognize and further regulate [160, 173, 184, 192, 233, 266]. While their activities have been most extensively studied in the context of their original discovery in mitotic spindle formation during mitosis [150, 172, 180, 185, 188, 234, 240, 241], it is now established that TACC3 also regulates MT growth in the cytoplasm of interphase cells in humans, yeast, and xenopus [161, 162, 165, 190-192, 240, 242, 267]. Until recently these TACC3 activities were less well characterized in human cell systems, but we recently showed that loss of TACC3 function impairs dynamic MT growth resulting in the formation of non-dynamic, or more stable MT arrays in both neuronal SK-N-SH cells and primary normal human

dermal fibroblasts (NHDFs) [267]. This in turn affects the motor-based trafficking and sorting of cellular cargos such as endosomes as well as incoming Herpes Simplex Virus type 1 (HSV-1) particles attempting to reach the nucleus [267]. But beyond this general impact on cargo sorting, whether viruses actively exploit EB-independent +TIPs to control MT behavior and promote virus replication remains unknown. Here, we show that HCMV specifically increases cytoplasmic TACC3 abundance as infection progresses in order to recruit chTOG into the cytoplasm from initial sites of MT nucleation in the AC. This enhances the ability of the AC to generate and sustain the growth of dynamic MT arrays extending throughout the cytoplasm. Blocking HCMV-induced increases in TACC3 expression causes mis-localization of chTOG and impairs MT growth, resulting in defects in both Rab-positive early and late endosome organization at the AC and defects in the trafficking and spread of progeny virions.

## **Results**

### **HCMV regulates TACC3 abundance and chTOG localization at mid-to-late stages of infection**

To determine if HCMV infection affects either TACC3 or chTOG, the primary components of the EB-independent plus-end tracking and MT polymerization machinery, we infected primary NHDFs with strain TB40/E and analyzed whole cell lysates taken at various times post-infection. WB analysis revealed that TACC3 levels increased over four-fold by mid stages of infection and remained elevated through later stages (Figure 42). In contrast, levels of TACC3's interacting partner chTOG did not change significantly over the course of infection (Figure 42). To independently confirm these findings, we used immunofluorescence (IF) to examine both the levels and intracellular localization of TACC3 and chTOG at different infection timepoints.

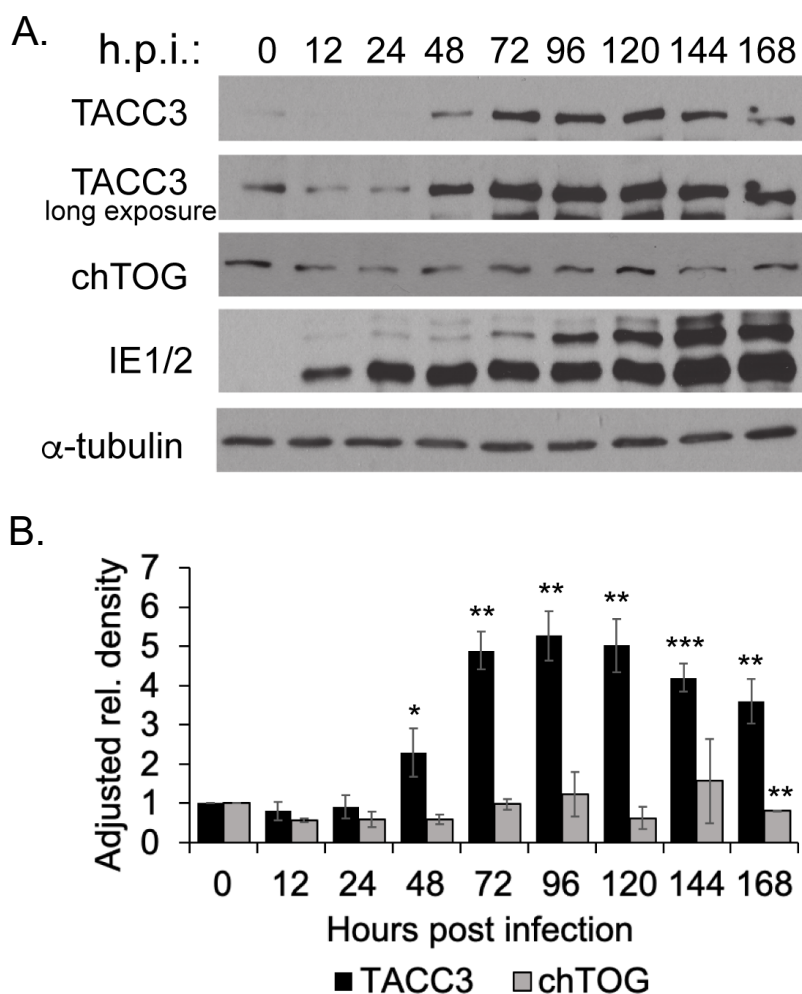


**Figure 42** HCMV increases TACC3 expression as infection progresses. (A) Growth-arrested NHDFs were infected with TB40/E at MOI 1 for the indicated times. Cell lysates were analyzed by WB. Short and long exposures of TACC3 blots are shown to illustrate differences in expression levels in early versus late stages of infection. (B) Average adjusted relative densities (AU) of TACC3 and chTOG were quantified.  $n = 3$  biological replicates; error bars = SEM;  $p < 0.05$ ,  $p < 0.01$ ,  $p < 0.005$ ; unpaired 2-tailed t test.

HCMV-infected cells were fixed at 0, 24, 72, and 120 h.p.i. to span early, middle and later stages of infection. In agreement with WB results, there was a large increase in TACC3 levels at both middle and late infection timepoints, with TACC3 localizing diffusely within the cytoplasm at all stages examined (Figure 43). While shorter exposures required for linear comparisons across all samples and to accurately visualize the localization of TACC3 at later stages of infection meant that TACC3 was not visible in samples from uninfected cells and at earlier stages of infection, longer exposures illustrate the normal levels of TACC3 in the cytoplasm in these samples (Figure 43). We further confirmed the specificity of this TACC3 antibody staining by treating HCMV-infected cells with either control non-targeting or TACC3-targeting siRNAs (Figure 44).

In both mock and early-stage infected NHDFs, chTOG localized to puncta within the nucleus, to the centrosome, and diffusely throughout the cytoplasm (Figure 45). At later timepoints, coincident with the increase in cytoplasmic TACC3, chTOG staining increased and exhibited a notably diffuse pattern throughout the AC region and cytoplasm (Figure 45, Figure 46). Within the AC itself, chTOG co-localized with the primary MT nucleation factor  $\gamma$ -tubulin, both of which strongly labeled the centrosome as a bright punctate structure near the center of the AC as well as more diffusely labeling non-centrosomal sites throughout the broader AC structure [45] (Figure 46). This is in line with findings that chTOG functions in minus-end stabilization and MT nucleation [163, 164, 172], and the staining patterns observed here are in line with the notion that these proteins function at both centrosomal and Golgi-based nucleation sites within the AC [45]. Again, the specificity of the chTOG staining was confirmed in infected cells treated with either control non-targeting or chTOG-targeting siRNAs (Figure 47). Unfortunately, at late timepoints in methanol-fixed cells viral replication factories within the nucleus often create a nonspecific background which interfered with our ability to accurately quantify any loss of chTOG

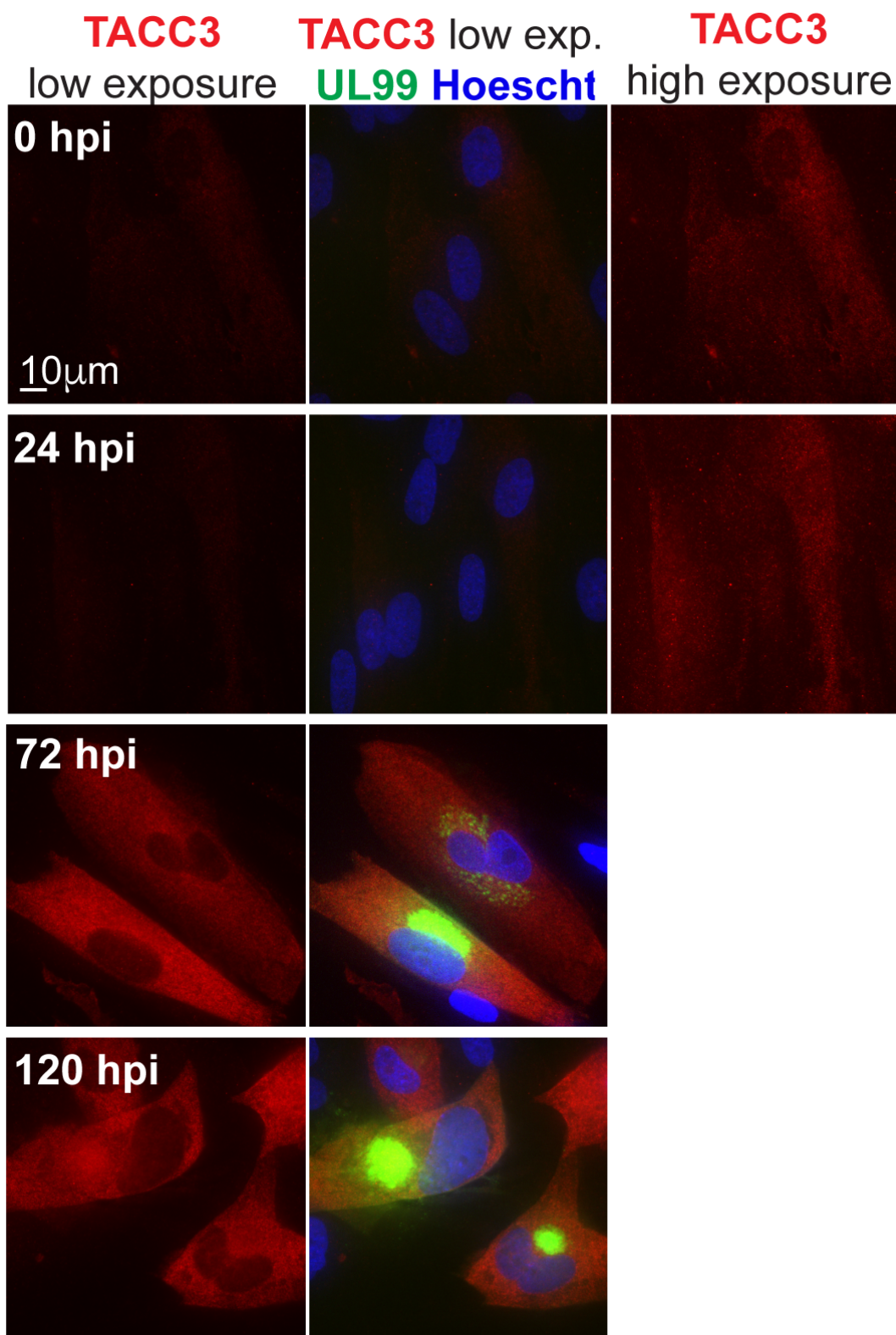


**Figure 43** TACC3 levels increase within the cytoplasm during late HCMV infection. NHDFs were infected with TB40/E-UL99-mCherry at MOI 1 for the indicated times. Cells were fixed in formaldehyde and stained for TACC3 (red). Nuclei were stained using Hoechst (blue). UL99-mCherry was imaged directly, false-colored to green for optimal contrast. Higher exposures are shown for mock and early timepoints to visualize the lower levels of TACC3 in these samples compared to those at later stages of infection. Representative images are shown of results derived from 3 independent experiments.

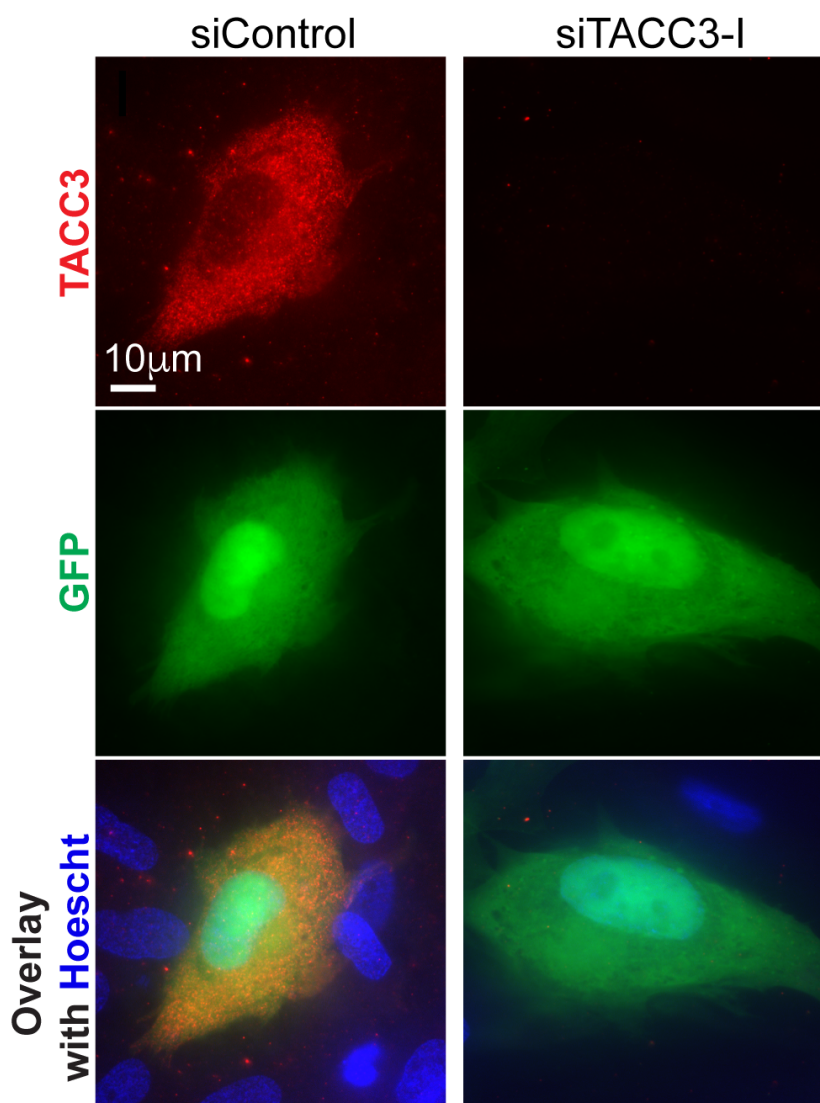


**Figure 44** TACC3 immunofluorescence staining is specific. NHDFs were infected with TB40/E-eGFP at MOI 1. At 5 h.p.i. cells were treated with control nontargeting or TACC3-targeting siRNA. Cells were fixed in formaldehyde at 5 d.p.i. and then stained for TACC3 (red) and with Hoechst. GFP expression shows infected cell. Representative images are shown of results derived from 3 independent experiments.

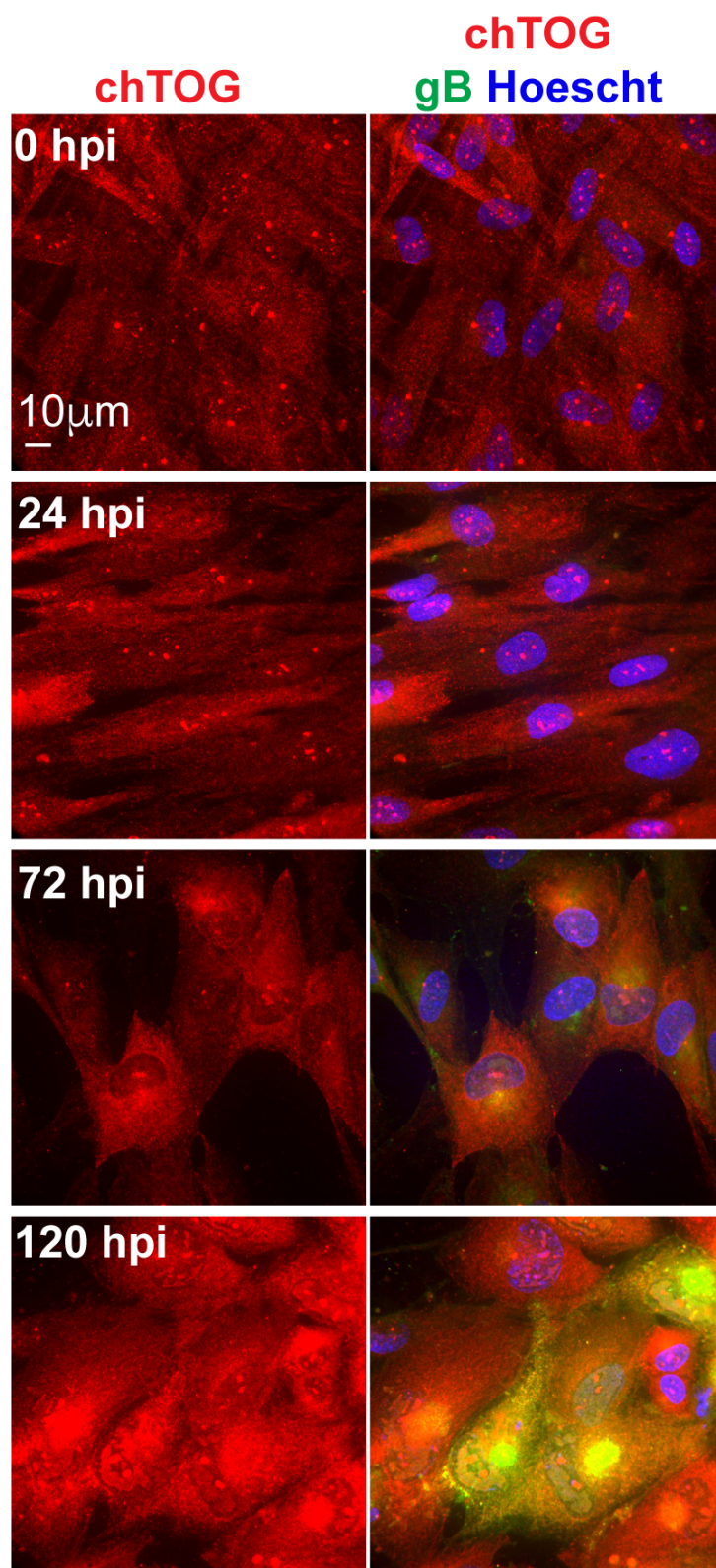


**Figure 45** chTOG accumulates in the cytoplasm as HCMV infection progresses. NHDFs were infected with TB40/E-eGFP at MOI 1 and were fixed in methanol at the indicated times. Cells were stained for chTOG (red), gB (green) and with Hoechst. Representative images are shown of results derived from 3 independent experiments.

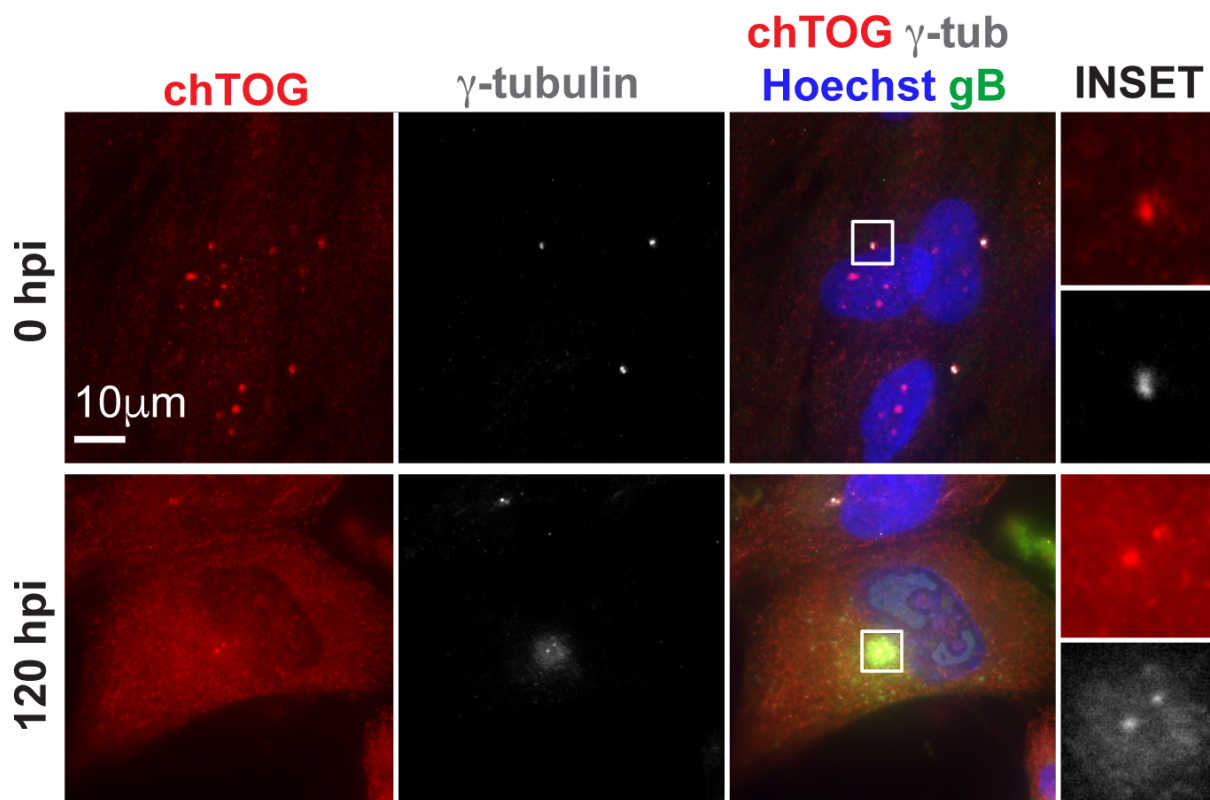


**Figure 46** chTOG localizes diffusely throughout AC and colocalizes with centrosomal markers during HCMV infection. NHDFs were infected with TB40/E-eGFP at MOI 1 and were fixed in methanol at the indicated times. Cells were stained for chTOG (red), gB (green),  $\gamma$ -tubulin (grey), and with Hoechst. Inset shows enlarged view of chTOG and  $\gamma$ -tubulin colocalizing at the centrosome and throughout AC in infected cells. Note that chTOG is found at both  $\gamma$ -tubulin-positive sites and throughout the cytoplasm, in line with its dual roles in MT nucleation and subsequent polymerization/growth. Images are representative of predominant phenotype.

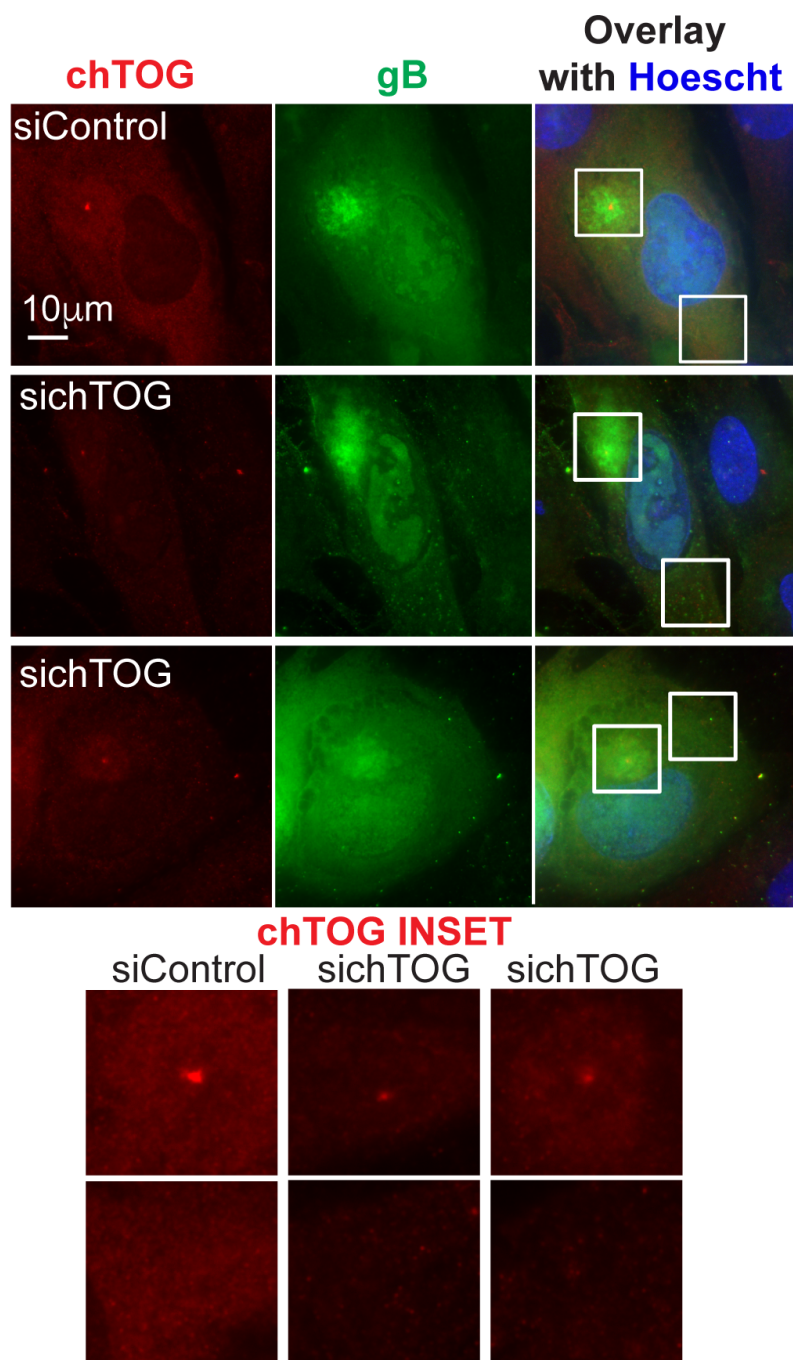


**Figure 47** RNAi treatment depletes cytoplasmic chTOG but leaves residual chTOG at the AC and centrosome. NHDFs infected with TB40/E-eGFP at MOI 1 were treated with control non-targeting or chTOG-targeting siRNA at 5 h.p.i. Cells were fixed in methanol at 5 d.p.i. and then stained for chTOG (red), gB (green), and with Hoechst. Because phenotypes vary moderately in cells depleted of chTOG, examples of both phenotypes observed are shown. Inset (below) shows enlarged view of chTOG levels at the AC and in the cytoplasm, showing residual stable chTOG protein that can remain at sites of MT nucleation in the AC and at the centrosome. Representative images are shown of results derived from 3 independent experiments.

from the nucleus that might accompany these increases in cytoplasmic chTOG. However, the fact that WB analysis shows that the total abundance of chTOG does not increase significantly (Figure 42) combined with our detection of increased chTOG in the cytoplasm as infection progresses aligns with our prior work in uninfected NHDFs wherein experimental overexpression of TACC3 leads to a redistribution of nuclear pools of chTOG to the cytoplasm [267]. This suggests that HCMV-induced increases in TACC3 levels might function to enable the virus to recruit and regulate the cytoplasmic distribution of chTOG, which we explore again later.

Having determined that HCMV increased TACC3 levels and altered chTOG localization, we next sought to determine whether these proteins were of functional importance to infection. To do this, we first examined the effects of siRNA-mediated TACC3 depletion on a single cycle of HCMV replication. To specifically prevent the increase in TACC3 at later stages without affecting earlier stages of infection, we infected NHDFs with TB40/E and applied either control or one of two independent TACC3 siRNAs at 5 hours post-infection (h.p.i.). At 168 h.p.i. cell lysates were collected for WB analysis and supernatants were used for viral titering. WB analysis confirmed that both TACC3 siRNAs efficiently prevented the increase in TACC3 induced by HCMV, with TACC3 siRNA#2 being moderately less effective than TACC3 siRNA#1 (Figure 48A). WB analysis also confirmed that the establishment of infection was not affected under these conditions, with no detectable effect of TACC3 knockdown on levels of HCMV immediate early proteins IE1 and IE2, early viral DNA polymerase protein UL44, or late viral tegument protein pp28 in comparison to control siRNA-treated NHDFs (Figure 48A). We also found no significant effect of TACC3 depletion on single-cycle production and release of infectious virus into supernatants at 168 h.p.i. (Figure 48B). However, HCMV is largely cell-associated and mechanisms of cell-cell spread are distinct from release of virus into culture supernatants. To assess whether TACC3

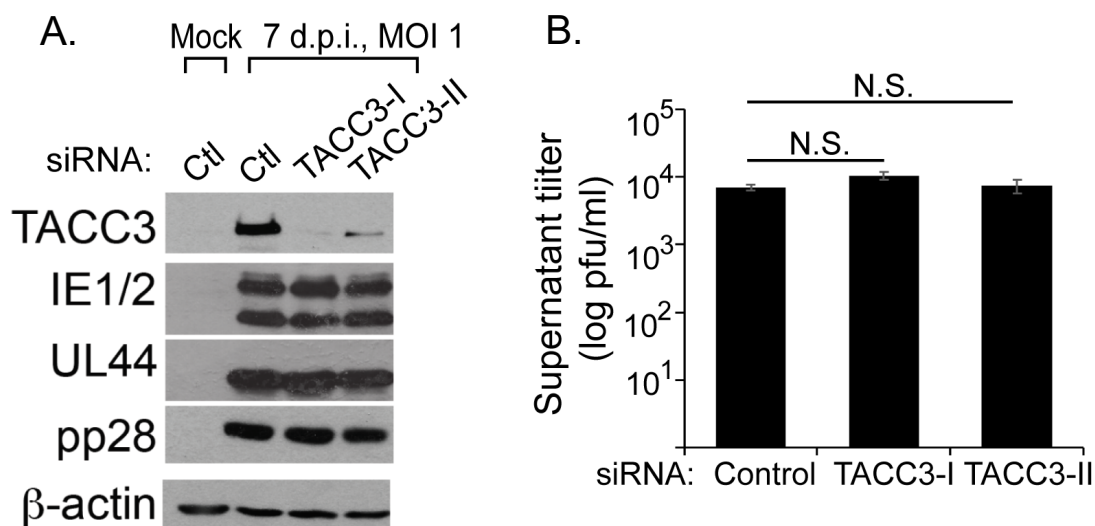


**Figure 48** RNAi-mediated depletion of TACC3 does not affect establishment of HCMV infection in NHDFs. (A) NHDFs were mock-infected or infected with TB40/E at MOI 1. At 5 h.p.i. cells were treated with control non-targeting or one of two TACC3-targeting siRNAs (I or II). Cell lysates were collected at 7 d.p.i. and analyzed by WB with the indicated antibodies. (B) NHDFs were treated as in A. Cell supernatants were collected at 7 d.p.i. and titrated on NHDFs.  $n = 3$ ; error bars = SEM; N.S., not significant; unpaired two-tailed t test. All of the experiments represent 3 biological replicates.

depletion affected virus spread, we performed multi-cycle spreading assays by infecting NHDFs at low MOI with a strain of TB40/E that expresses GFP and again applied either control or TACC3 siRNAs at 5 h.p.i.. At 14 days post infection (d.p.i.) wide-field fluorescent microscopy was used to determine plaque sizes as an initial readout for effects on virus spread (Figure 49A). Quantification of plaque sizes showed that TACC3 depletion caused a significant reduction in viral spread compared with control siRNA-treated cultures (Figure 49A-B). Complementing plaque size measurements, cell lysates and supernatants were collected at 14 d.p.i. WB analysis showed continued depletion of TACC3 up to 14 d.p.i. and reduced levels of IE1/2 in TACC3-depleted cells, reflecting a defect in overall viral protein accumulation due to reduced virus spread (Figure 49C). In line with plaque size and WB analyses, TACC3 depletion reduced the levels of infectious virus released into supernatants by more than 10-fold during multicycle spreading assays (Figure 49D).

In order to confirm that these defects in plaque size were due to TACC3 depletion and not an off-target effect of siRNAs, we attempted to rescue TACC3 levels following knockdown by transducing cells with a TACC3-expressing retroviral vector [267]. However, while we have successfully used this approach to restore TACC3 expression in uninfected cells previously [267], WB analysis revealed that this approach could not restore TACC3 levels to those observed in HCMV-infected cells and only worked at very low efficiency (Figure 49E). We were similarly unable to express a dominant-negative form of TACC3 [267] to levels sufficient to act as dominant negative in HCMV-infected cells.

While the extent to which HCMV upregulates TACC3 expression posed technical challenges to using either rescue or dominant-negative approaches, it is important to point out that we have extensively characterized the TACC3 siRNAs that we use here and have confirmed their

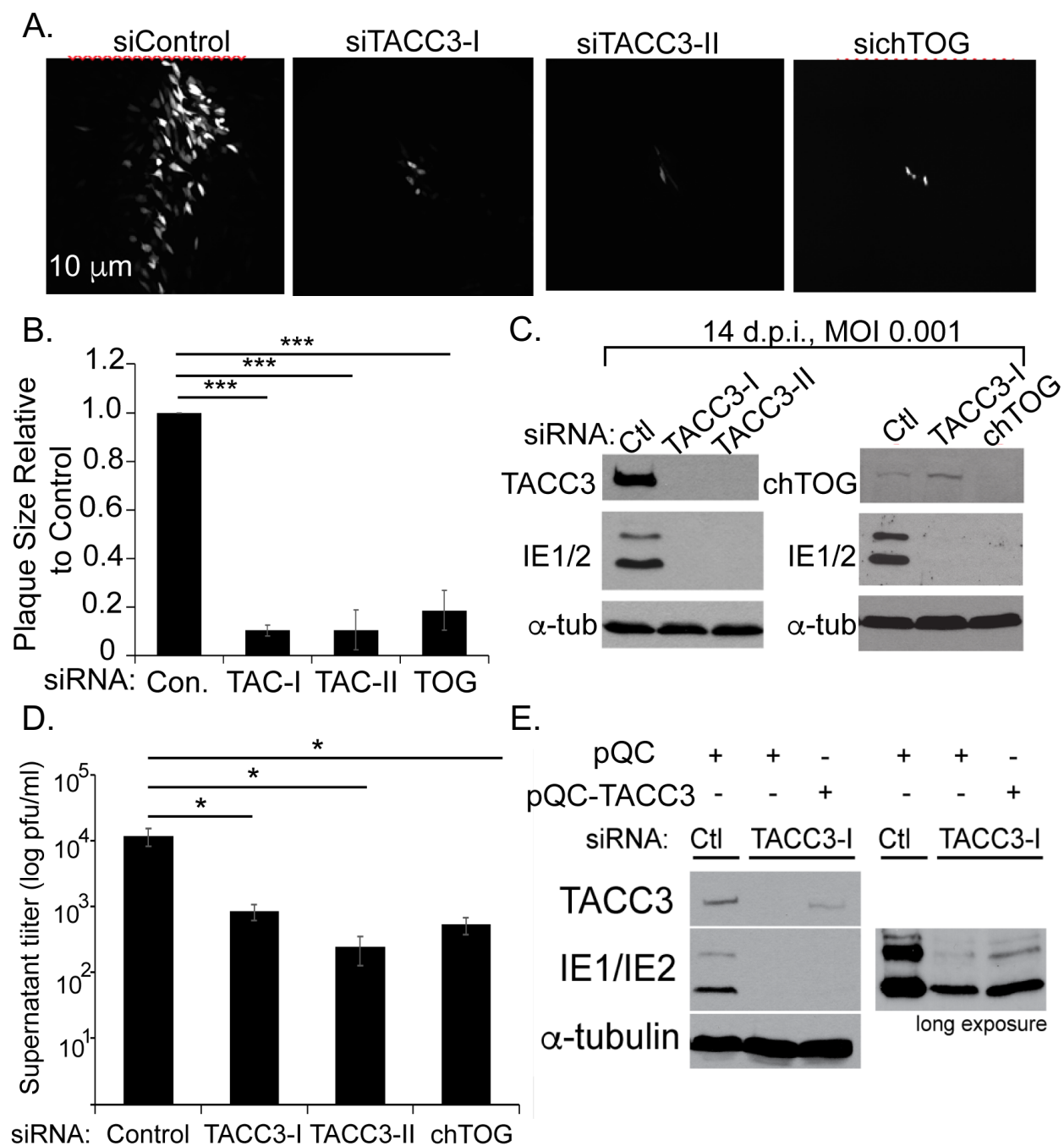


**Figure 49** TACC3 and chTOG are required for efficient HCMV spread. (A) NHDFs were infected with TB40/E-eGFP at MOI 0.001 for 14 days. At 5 h.p.i. cells were treated with control, TACC3 (I or II), or chTOG siRNA. At 14 d.p.i. plaques were imaged by fluorescence microscopy. Representative plaque images are shown. (B) Plaque sizes in A. were measured.  $n = 3$  (>30 plaques); error bars = SEM; \*\*\* $p < 0.0005$ , unpaired two-tailed t test. (C) Cells treated as in A. were lysed at 14 d.p.i. and analyzed by WB. IE1/2 levels are reduced because of reduced HCMV spread in TACC3- or chTOG-depleted cells. (D) Supernatants from cells treated as in A. were collected at 14 d.p.i. and plaque-forming infectious virus was titrated on NHDFs.  $n = 3$ ; error bars = SEM; \* $p < 0.05$ , unpaired two-tailed t test. (E) TACC3 rescue approaches are inefficient in HCMV-infected cells. NHDFs were infected with TB40E at MOI 0.001 and then treated with control non-targeting or TACC3-targeting siRNA at 5 h.p.i. At 24 h.p.i., cells were transduced with pQCXIP or pQCXIP-TACC3 retroviral vectors. Cells were lysed at 14 d.p.i. and analyzed by WB. Long exposure of IE1/2 suggests modest rescue of infection in cells transduced with pQCXIP-TACC3. However, it is important to consider that there is only a small subpopulation of cells infected in these spreading assays yet the level of TACC3 expression in control siRNA-treated cells (lane 1) are higher than the levels produced by retroviral transduction of the whole population (lane 3). As such, rescue efficiency is in fact very low compared to the levels of TACC3 expression in individual infected cells. All of the experiments represent 3 replicates.

specificity in uninfected cells [267]. Similar to uninfected cells [267], we find that both TACC3 siRNAs exhibit the same modest differences in depletion efficiency in HCMV-infected cells and do not affect viral gene expression (Figure 48A). Furthermore, the functional phenotypes that we observe in HCMV-infected cells below are in line with predicted functions of TACC3. However, as an alternative method of confirming that the effects we observe are indeed a reflection of TACC3's function in regulating MT dynamics, we performed the same spreading assays in NHDFs depleted of TACC3's partner, the polymerase chTOG. Results showed that depletion of chTOG resulted in similar defects in HCMV replication and spread as those observed in TACC3-depleted cells (Figure 49A-D). Together with the timing of their accumulation in the cytoplasm, these results suggest that TACC3 and chTOG play a role in late HCMV infection that is required for efficient virus spread.

### **TACC3 and chTOG regulate MT dynamics in HCMV-infected cells**

While increases in TACC3 levels correlated with chTOG accumulation in the cytoplasm (Figure 43, Figure 45), we next tested whether TACC3 was indeed exploited by HCMV to regulate chTOG localization. To do this, we used siRNA-mediated depletion approaches described above that specifically prevent TACC3 upregulation by HCMV without affecting early infection or viral gene expression (Figure 48). We then analyzed how preventing HCMV from increasing TACC3 levels impacted chTOG localization at later stages of infection. IF analysis showed that in control non-targeting siRNA-treated cells, chTOG localized to the bright punctate centrosome at the core of the AC as well as diffusely throughout the AC (Figure 50A), as shown earlier (Figure 46, Figure 47). chTOG was also broadly distributed through the cytoplasm in control siRNA-treated cells, as would be expected for its role as a MT polymerase recruited by TACC3 to promote MT plus-end

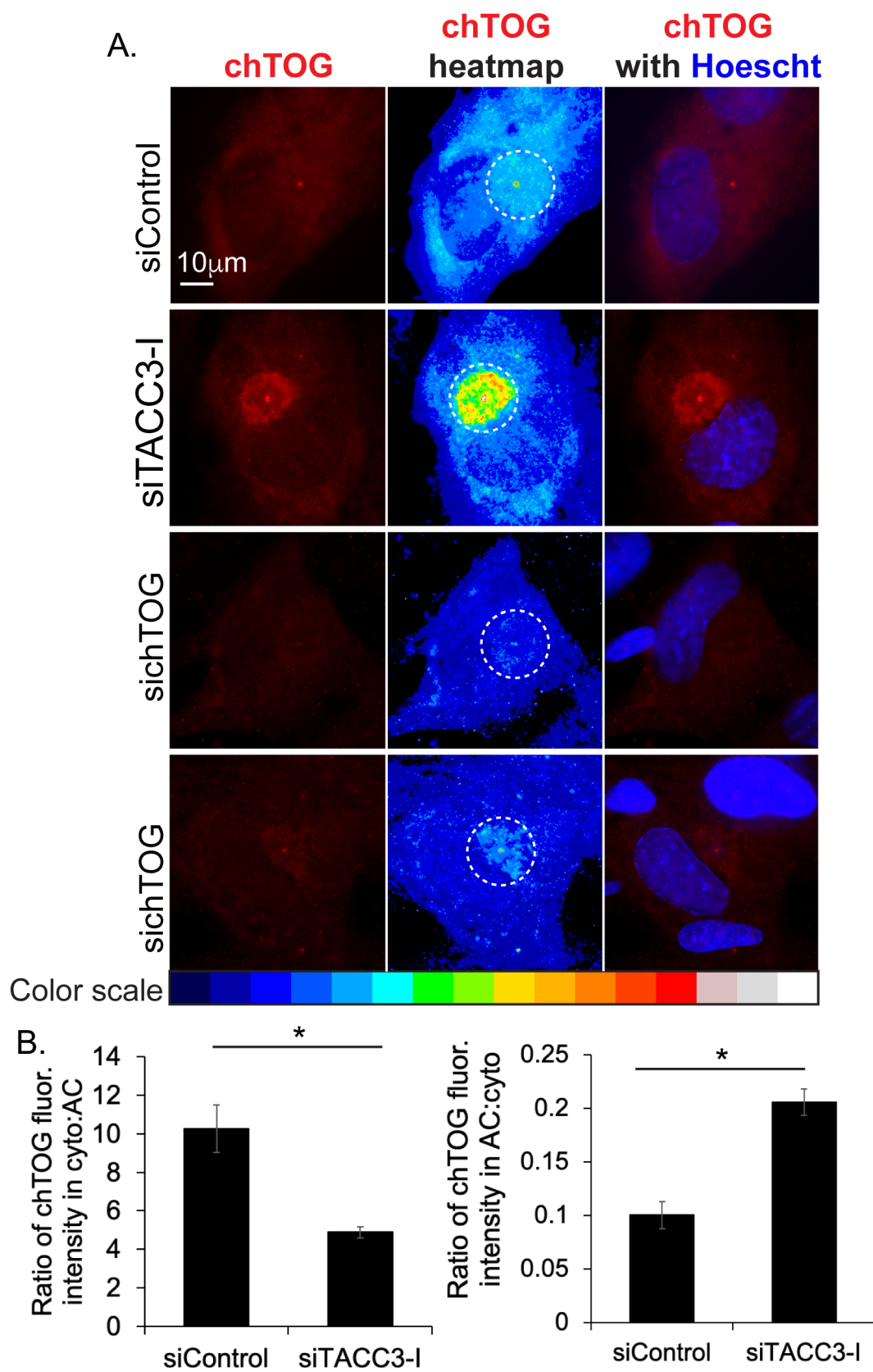


**Figure 50** TACC3 controls chTOG localization in HCMV-infected cells. NHDFs were infected with TB40/E at MOI 1. At 5 h.p.i. cells were treated with control, TACC3, or chTOG siRNAs. Cells were fixed in methanol at 5 d.p.i. and stained for chTOG (red) and with Hoechst (blue). (A) chTOG localization and staining intensity are shown by color-intensity heatmap (center panels). The AC area is circled by dashed white line. Representative cells are shown and in the case of chTOG depletion where phenotypes vary moderately, examples of both phenotypes are shown. In some instances, residual chTOG can be seen at the centrosome and AC in chTOG-depleted cells. (B) Average corrected total fluorescence intensity of chTOG, shown as either a ratio of cytoplasmic chTOG to AC chTOG to illustrate loss of chTOG from the cytoplasmic pool (left) or as ratio of AC chTOG to cytoplasmic chTOG to show accumulation of chTOG in the AC (right).  $n = 3$  (75 cells per siRNA); error bars = SEM; \* $p < 0.05$ , unpaired two-tailed t test. Representative images are shown of results derived from 3 independent experiments.

formation (Figure 50A). By contrast, in TACC3-depleted NHDFs, chTOG staining declined in the cytoplasm and was enriched within the AC and at the centrosome (Figure 50A-B). This distribution pattern is in line with chTOG's requirement for TACC3 to efficiently associate with growing MT plus-ends in the cytoplasm [150, 160, 172, 173, 180, 184, 188, 192, 233, 241, 266]. This antibody staining of chTOG at the AC was specific as it was lost, or greatly diminished in HCMV-infected cells treated with siRNAs to chTOG itself (Figure 47, Figure 50A). Notably, many chTOG siRNA-treated cells exhibited residual chTOG staining at the centrosome and AC, suggesting that chTOG protein may be more stable at sites of MT nucleation than in the broader cytoplasmic environment (Figure 47, Figure 50A). Regardless, this data showed that under normal infection conditions HCMV-induced increases in TACC3 levels function to assist chTOG in leaving nucleation sites that are present throughout the AC, which likely plays an important role in sustaining the growth of new MTs as they extend into the cytoplasm.

To test whether loss of TACC3 or chTOG affected MT dynamics during infection, HCMV-infected NHDFs were treated with control non-targeting, TACC3, or chTOG siRNAs and then fixed and stained for EB1. EB1 proteins recognize the transient GTP-tubulin cap that is present on growing MTs and their accumulation at the plus-ends of growing MTs results in a comet-like staining pattern that is indicative of MT growth rates [126]. In control-siRNA treated cells, many relatively short EB1 comets were observed emanating from the AC region and throughout infected cells, indicative of rapid EB1 turnover at fast-growing dynamic MT plus-ends (Figure 51A-B). In the cytoplasm of either TACC3 and chTOG-depleted cells, EB1 comets were more sparse and those that formed were more elongated (Figure 51A-B). This pattern is indicative of a combination of fewer and less dynamically growing MTs, resulting in longer EB1 residence times [45, 126, 267]. Focusing our IF analysis specifically on EB1 comets in the plane of the AC and centrosome,

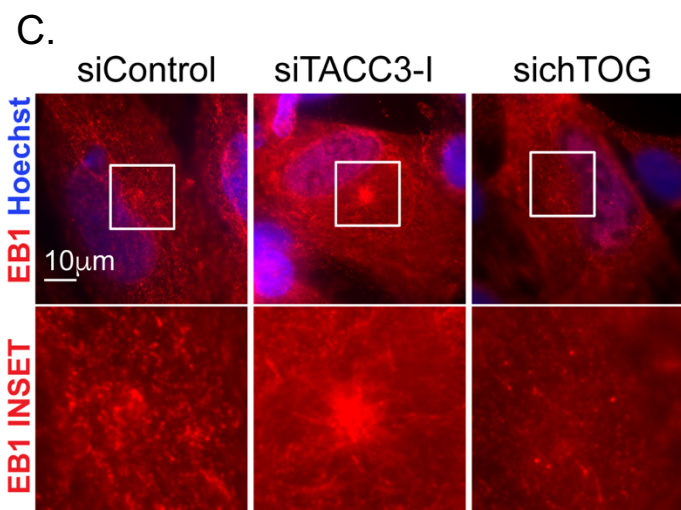
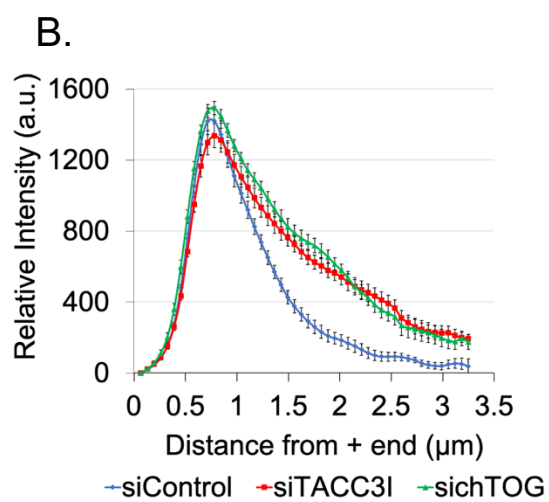
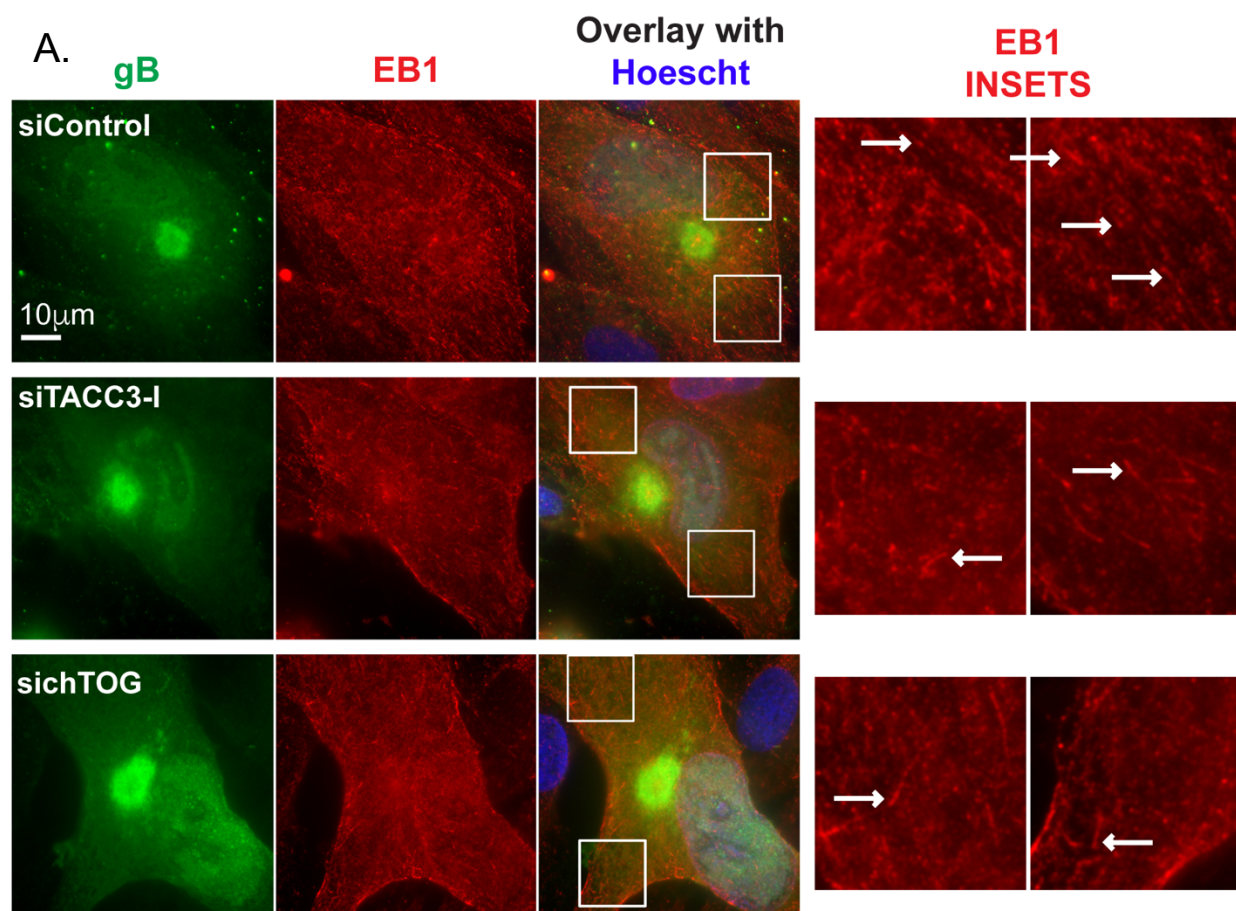


**Figure 51** TACC3 and chTOG regulate MT dynamics in HCMV-infected cells. (A-C) NHDFs were infected with TB40/E at MOI 1. At 5 h.p.i. cells were treated with control, TACC3, or chTOG siRNAs. Cells were fixed in methanol at 5 d.p.i. and stained for gB (green), EB1 (red) and with Hoechst to stain the nucleus. (A) Representative images of EB1 staining patterns are shown. Insets show enlarged view of EB1 comets illustrating regions where comets are more elongated and regions where comets are sparse in TACC3 or chTOG depleted cells. Arrows point to examples of short comets in control cells and elongated comets in TACC3 and chTOG depleted cells. (B) Line-scan analysis measuring EB1 intensity distribution from the MT plus-end in cells from A. 250 linescans were analyzed over 10 cells per condition; error bars denote SEM. (C) Cells were imaged for EB1 in the focal plane of nucleation sites of the centrosome and AC. Inset shows enlarged view that illustrates EB1 comet numbers and staining patterns at nucleation sites under each condition. Representative images are shown of results derived from 3 independent experiments.

we found low levels of EB1 at these regions in control siRNA-treated cells (Figure 51C). This occurs when EB1 rapidly tracks with fast-growing MTs away from nucleation sites out into the broader cytoplasmic environment. By contrast, in TACC3-depleted cells we observed higher levels of EB1 staining at the AC region and EB1 comets appeared elongated compared to control cells (Figure 51C). The high levels of EB1 at the AC suggest an initially high level of MT nucleation at the AC where increased levels of chTOG accumulate when TACC3 is depleted (Figure 50A, Figure 51C). However, the elongated nature of these EB1 comets also indicate slower polymerization of these new MTs as they grow out into the cytosolic space that is lacking chTOG to sustain their growth (Figure 51C and illustrated in Figure 52). In chTOG-depleted cells we observed lower levels of EB1 staining at the AC even compared to control siRNA-treated cells (Figure 51C). This phenotype is in line with the importance of chTOG's presence at the AC to efficiently nucleate new MTs, while the elongated EB1 comets observed in peripheral regions of chTOG-depleted cells (Figure 51A-B) reflect the requirement for chTOG to also sustain persistent MT growth in the cytoplasm. Overall, the amount of EB1 and the nature of EB1 comet lengths, and thus the levels of dynamic MT growth, emanating from the AC or in the cytoplasm directly correlated with the amount of chTOG present at each site in control, TACC3, and chTOG-depleted cells respectively (Figure 50 and Figure 51). It is important to note that extensive MT networks persist in either TACC3 or chTOG-depleted cells (Figure 53), and that changes in the number and plus-end tracking behaviors of EB1 simply reflect changes in MT dynamics or growth rates, and not a complete loss of MT networks. MT filaments would still form under these various conditions due to residual TACC3 or chTOG in depleted cells, the activity of other MT regulators, and because of the natural ability of tubulin heterodimers to spontaneously assemble into filaments that is simply enhanced by TACC3 and chTOG [126]. Taken together, our data shows that chTOG

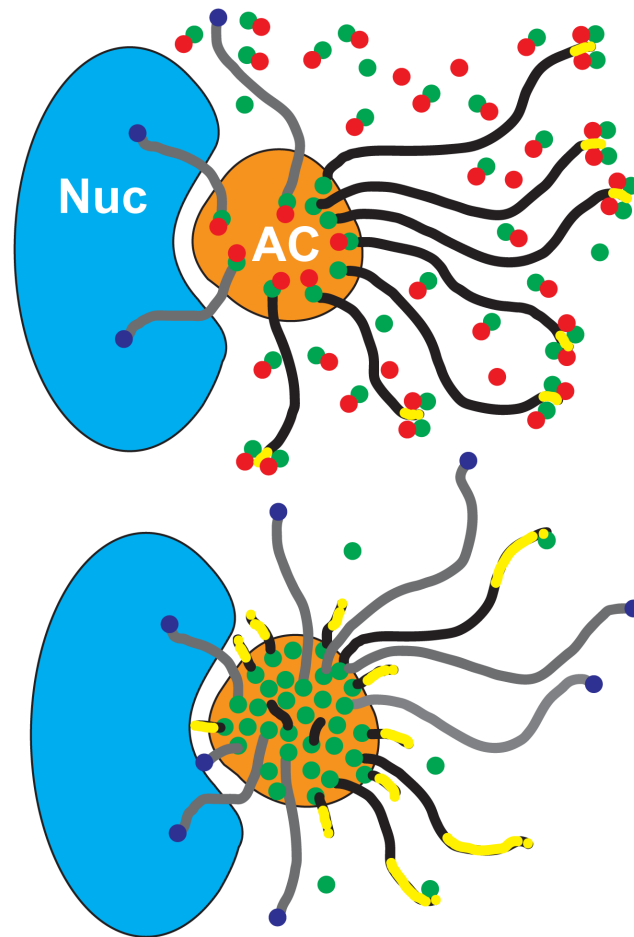


**Figure 52** Model for how TACC3 regulates chTOG localization and enables the AC to increase MT dynamics. (Top) Under normal infection conditions, TACC3 (red) is highly expressed and distributed in both the AC and cytoplasm as it tracks with newly formed and growing MT filaments, recruiting chTOG (green) to ensure persistent dynamic MT growth. The GTP-tubulin tips that are tracked by EB1 are short-lived as MT filaments rapidly grow, resulting in shorter EB1 comets (yellow). Distinct from dynamic MTs, other factors regulate formation of stable, acetylated filaments (gray, blue cap). Nuc = Nucleus. AC = Assembly Compartment. (Bottom) Loss of TACC3 activity results in a failure to recruit chTOG from the AC into the cytosol. This results in accumulation of chTOG at MT nucleation sites throughout the AC, as seen in TACC3-depleted cells in Figure 50. As a result, MT nucleation is efficient but subsequent growth of MTs into the cytoplasm is less efficient; notably, without TACC3, chTOG retains a low level of plus-end polymerization activity (depicted) while spontaneous tubulin multimerization and other factors sustain overall MT mass. However, loss of TACC3 impairs overall polymerization efficiency resulting in a mix of MTs; those that are not growing efficiently, particularly further out in the cytosol (no EB1 staining) and those that are slowergrowing wherein GTP-tubulin is slower to hydrolyze, resulting in longer plus-ends and EB1 residence times that manifest as longer EB1 comet staining patterns. Loss of dynamic growth also results in acetylation of more MT filaments (gray, blue cap) in cells lacking TACC3 activity (see Figure 53 and Figure 54).

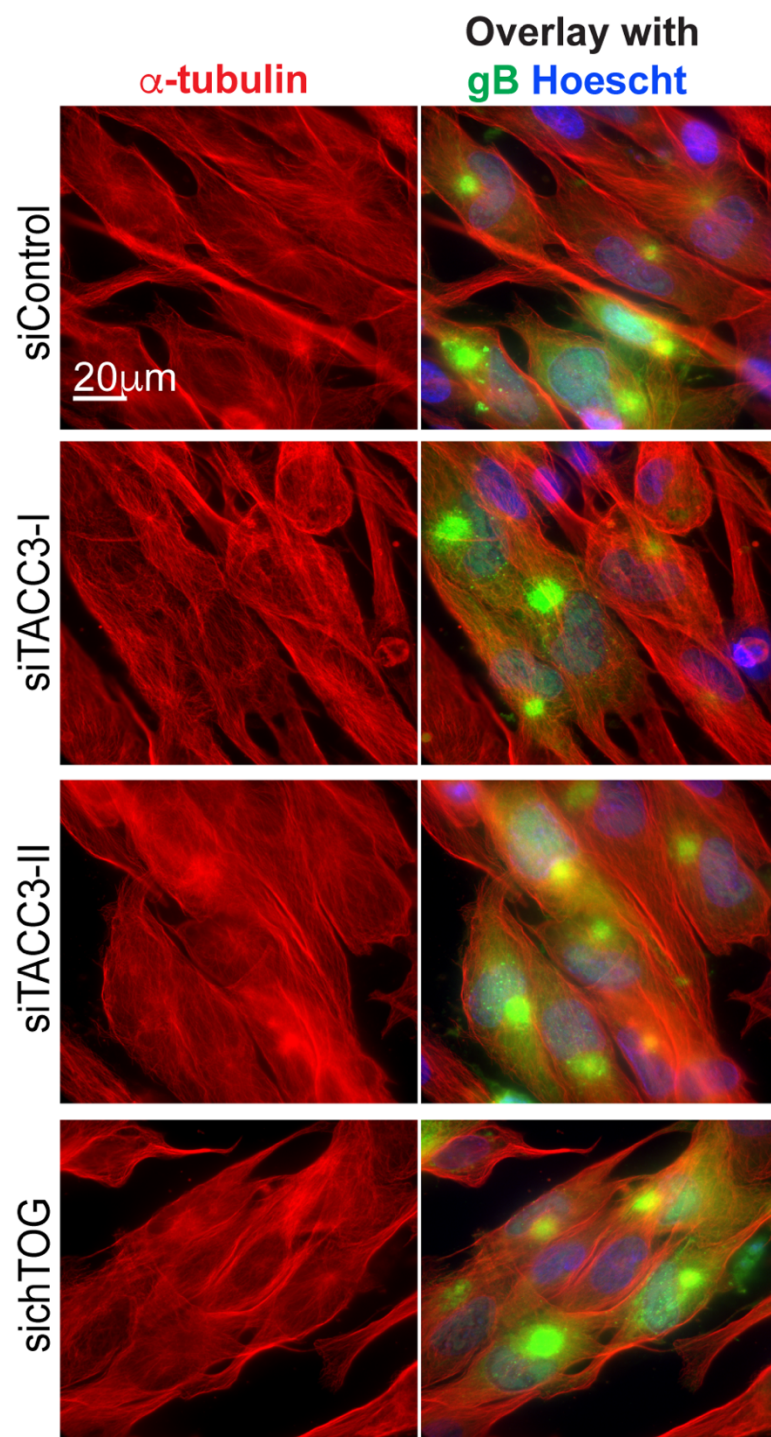


**Figure 53** Depletion of TACC3 or chTOG does not eliminate microtubule networks. NHDFs were infected with TB40/E at MOI 1. At 5 h.p.i. cells were treated with control, TACC3, or chTOG siRNA. Cells were fixed in methanol at 5 d.p.i. Cells were stained for gB (green), total tubulin (red), and with Hoechst. Images are representative of predominant phenotype.

assists in the nucleation of new MTs at the AC while TACC3 then ensures that chTOG is further recruited to the plus-ends of these growing MT filaments to sustain their growth in the cytoplasm, maximizing the dynamic behavior of MTs in infected cells (Figure 52).

To independently test this, we examined effects of TACC3 or chTOG depletion on the levels of acetylated MTs. Post-translational modifications such as acetylation largely accumulate on longer-lived, stable MT filaments and do not accumulate to significant levels on dynamic MT filaments [106]. Interestingly, HCMV increases the formation of both dynamic and acetylated MT subsets, with the latter being regulated by EB3 to control nuclear positioning [45]. By contrast, EB1 regulates the formation of dynamic MT arrays that contribute to AC structure [45]. Notably, depletion of EB1 disrupts dynamic MT growth and as a result, causes an increase in acetylated MTs that emanate from the AC [45]. IF analysis revealed that HCMV-infected cells depleted of TACC3 or chTOG had significantly higher levels of acetylated MTs in comparison to control siRNA-treated cells at 120 h.p.i. (Figure 54, Figure 55). This increase in acetylated MTs is in line with EB1 staining patterns observed above, which cumulatively suggest that TACC3 or chTOG depletion reduces MT dynamics in infected cells at late stages of infection. Moreover, these results are in line with the broader notion that TACC3 and chTOG create the dynamic MT plus-ends that EB1 proteins then operate upon, establishing TACC3 upregulation as a key strategy for HCMV to promote the formation of dynamic MT subsets at later stages of infection.

### **TACC3 and chTOG regulate AC organization and virus trafficking at late stages of infection**

To determine how defects in MT dynamics caused by loss of TACC3 or chTOG might impact later stages of infection, we next examined effects on the localization of specific Rab proteins. Various

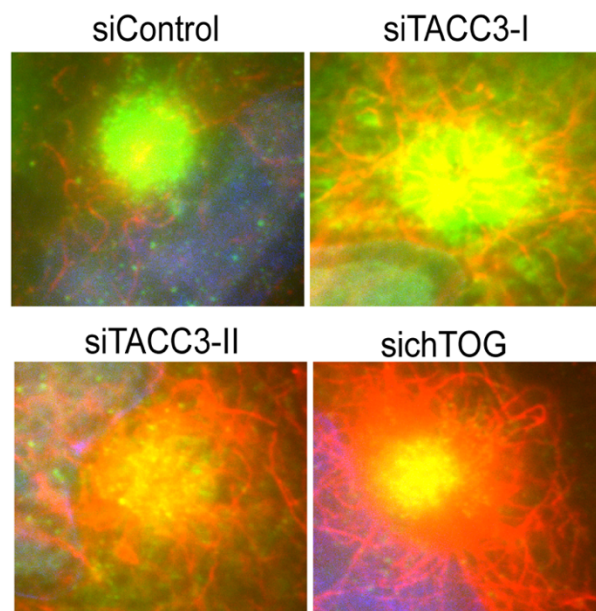
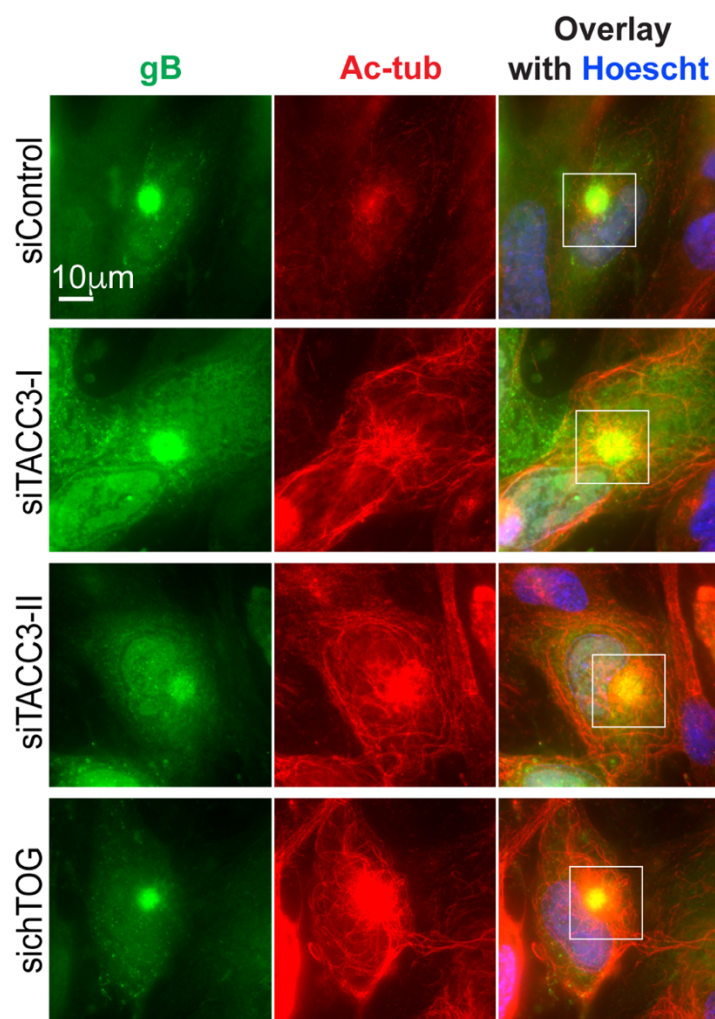


**Figure 54** Loss of TACC3 or chTOG activity results in increased levels of acetylated MTs. NHDFs were infected with TB40/E at MOI 1. At 5 h.p.i. cells were treated with control, TACC3, or chTOG siRNA. Cells were fixed in methanol at 5 d.p.i. Cells were stained for gB (green), acetylated tubulin (red), and with Hoechst. Inset shows enlarged view of acetylated MTs at the AC illustrating the levels of acetylated MT subsets under normal conditions, and increases caused by loss of TACC3 or chTOG. Representative images are shown of results derived from 3 independent experiments.

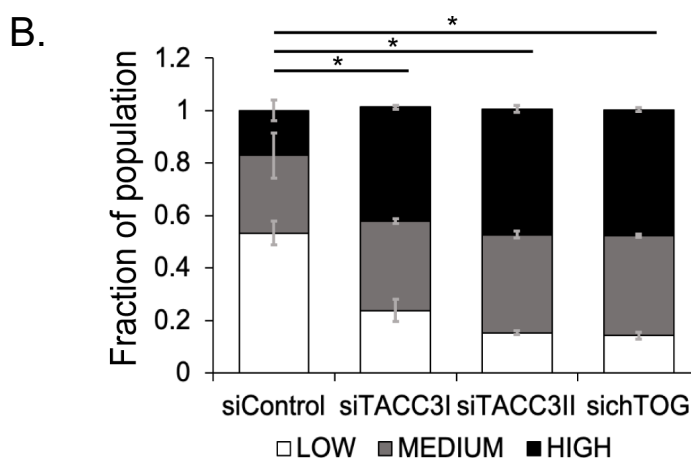
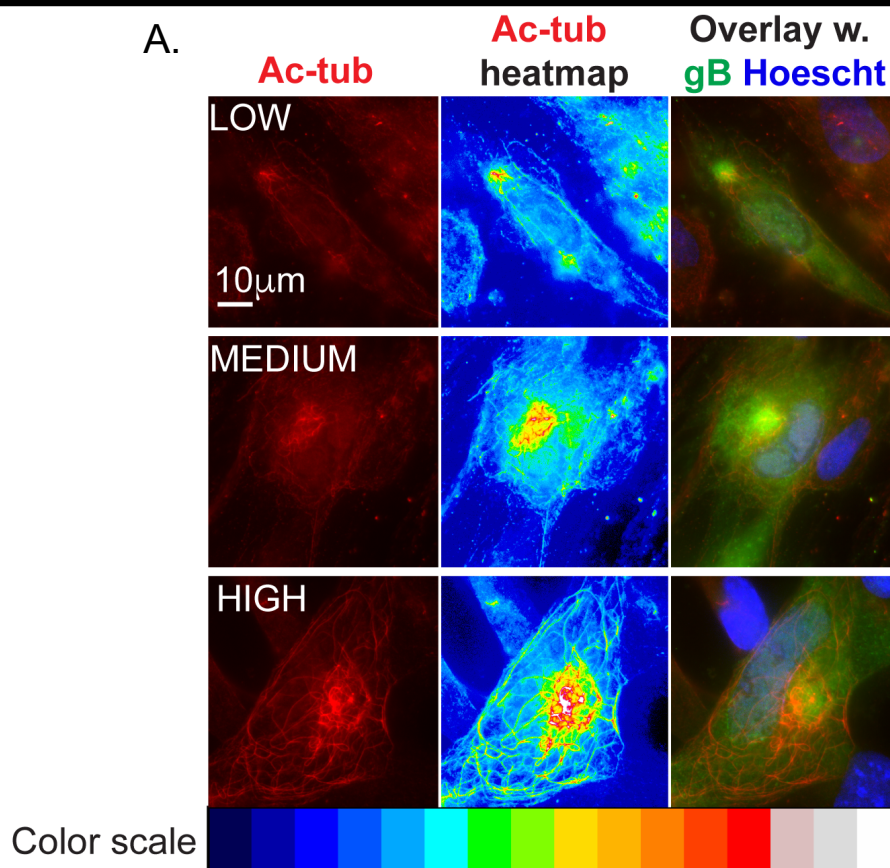


**Figure 55** Categorization of changes in acetylated MTs caused by loss of TACC3 or chTOG. (A) NHDFs were infected with TB40/E at MOI 1 and treated with control nontargeting siRNA at 5 h.p.i. Cells fixed in methanol at 5 d.p.i. were stained for acetylated-tubulin (red), gB (green), and Hoechst. Acetylated-tubulin staining intensity is shown by color-intensity heatmap. Examples are shown of representative cells classified as having low, medium, or high AcMT levels for quantification in Figure 54. (B) NHDFs were infected with TB40/E at MOI 1, treated with the indicated siRNAs at 5 h.p.i., and fixed in methanol at 5 d.p.i. Cells were stained for gB, acetylated tubulin, and with Hoechst. See representative images in Figure 54. Quantification shows average fraction of infected cells with low, medium or high levels of AcMT networks;  $\geq 220$  cells per siRNA over 3 biological replicates; error bars = SEMs; statistical significance shown for fraction of population with high acetylated MTs, \*  $p < 0.05$ ; unpaired 2-tailed t test.

Rab-positive secretory vesicles accumulate in an organized manner to form the AC and are thought to contribute to the ordered tegumentation, envelopment and egress of new virus particles [47, 67, 258, 259]. We therefore examined the localization patterns of Rab5 to label clathrin-coated vesicles and early endosomes, and Rab7 to label late endosomes. IF imaging revealed that in cells depleted of TACC3 or chTOG there were marked differences in the localization of Rab5 and Rab7 in relation to each other within the AC and surrounding regions, compared to cells treated with control non-targeting siRNA. In control cells, Rab5 localized partially at the AC core as well as in puncta that likely represent peripheral vesicles in the outer layers of the AC, while Rab7 localized diffusely in the AC core (Figure 56). Notably, Rab7 antibodies exhibited non-specific cross-reactivity with nuclear replication compartments whose size and organization varies (Figure 56, Figure 57A), but this did not affect our ability to distinguish Rab7-positive cytoplasmic structures. By contrast, in cells depleted of TACC3 or chTOG there seemed to be a reversal of these localization patterns, with Rab5 labeling the AC core more specifically while Rab7 labeling became more diffuse at the core and more peripherally localized (Figure 56). This suggests that TACC3 and chTOG play an important role in sustaining the dynamic growth of MT populations that regulate the proper organization of secretory vesicles in and around the AC.

Exploring this further, we examined the localization of Rab5 or Rab7 relative to the AC and egressing virus particles, labeled with anti-gB antibody. Again, a similar reversal of Rab5 or Rab7 staining patterns relative to the bright gB-positive AC core was observed in cells depleted of TACC3 or chTOG, relative to control siRNA-treated cells (Figure 57, Figure 58). Although gB antibodies also stain nuclear replication compartments, for egressing virus particles we focused our imaging on cells wherein infection had progressed to the point where gB-positive particles were clearly evident throughout the cytoplasm, a phase which is often accompanied by a less

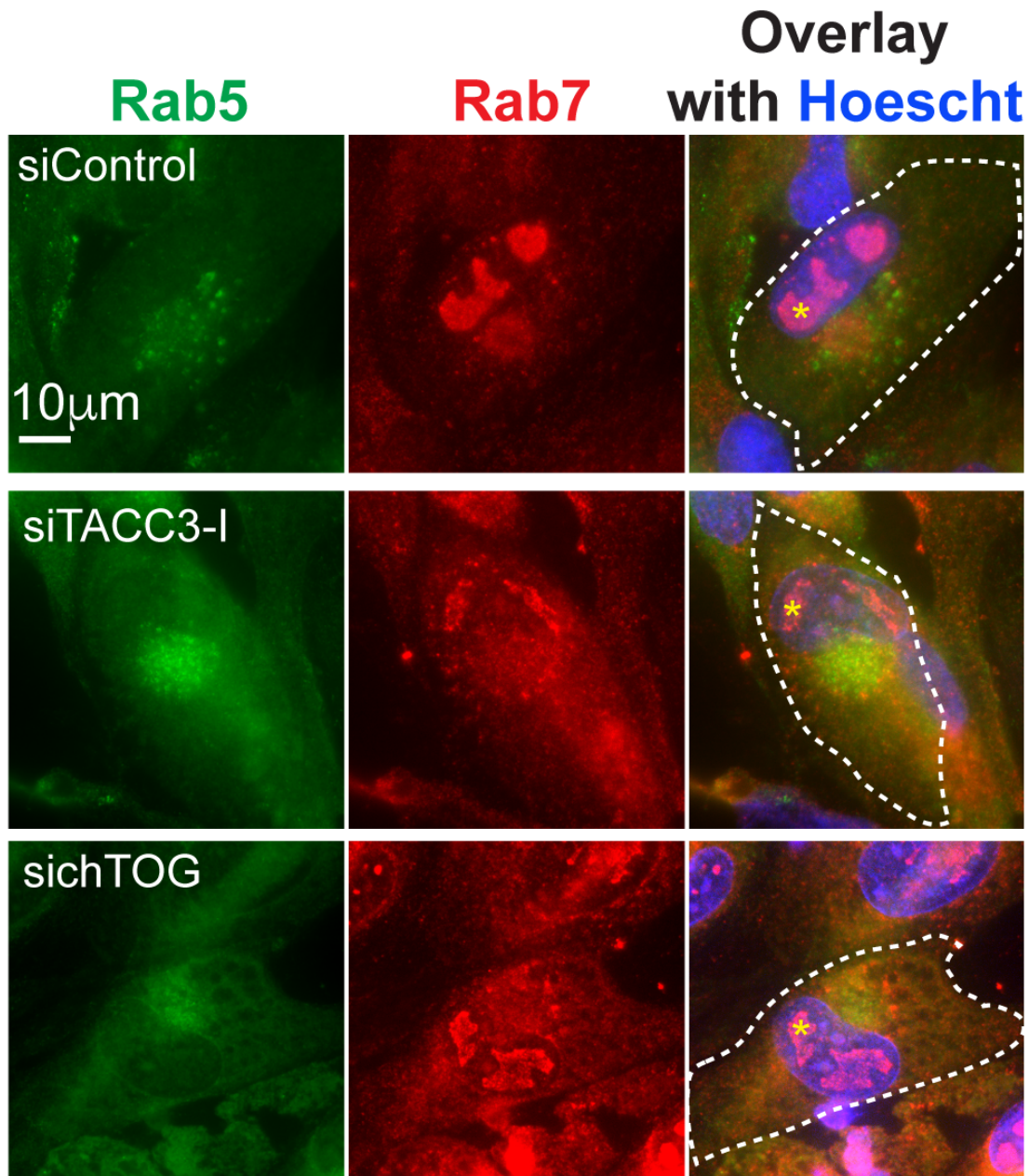


**Figure 56** TACC3 and chTOG coordinate the organized recruitment of endosomal vesicles to the AC. NHDFs were infected with TB40/E at MOI 1. At 5 h.p.i. cells were treated with control, TACC3, or chTOG siRNAs. Cells were fixed in methanol at 5 d.p.i. Cells were stained for Rab5 (green), Rab7 (red), and with Hoechst. Cell cytoplasm is outlined with white dashed line. Examples of non-specific cross-reactivity of Rab7 antibody with nuclear replication compartments are indicated by yellow asterisks in overlay panel. Representative images are shown of results derived from 3 independent experiments.

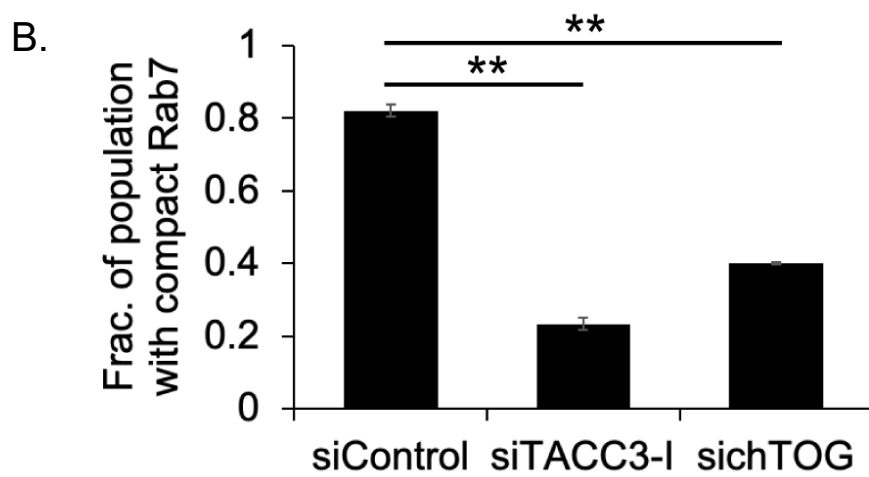
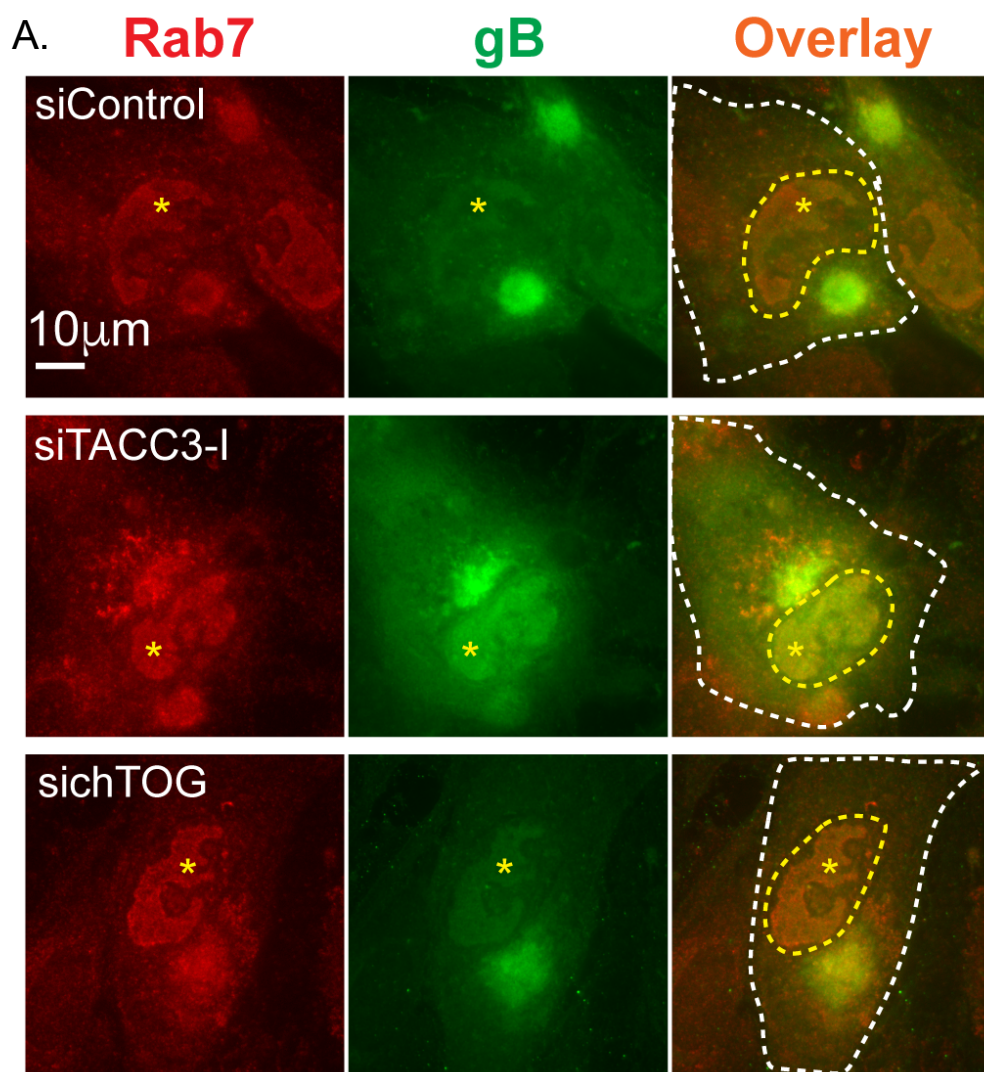


**Figure 57** Rab7 localization at the AC is disrupted by TACC3 or chTOG depletion. NHDFs were infected with TB40/E at MOI 1. At 5 h.p.i. cells were treated with control, TACC3, or chTOG siRNAs. Cells were fixed in methanol at 5 d.p.i. (A) Cells were stained for Rab7 (red) and gB (green). Cell cytoplasm is outlined with white dashed line, nucleus is outlined with yellow dashed line, and examples of non-specific staining of nuclear replication compartments is indicated by yellow asterisks. Analysis focused on Rab-specific staining in the cytoplasm. (B) Fraction of cells with Rab7 staining at AC core as shown for control cells in A.  $\geq 90$  cells per siRNA over 2 biological replicates; error bars = SEMs;  $**p < 0.01$ ; unpaired 2-tailed t test. Representative images are shown of results derived from 2 independent experiments.

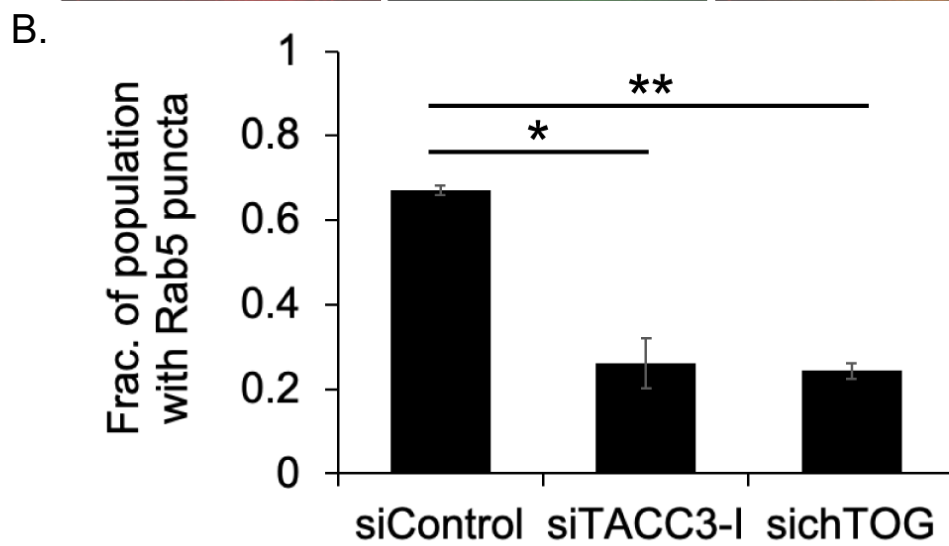
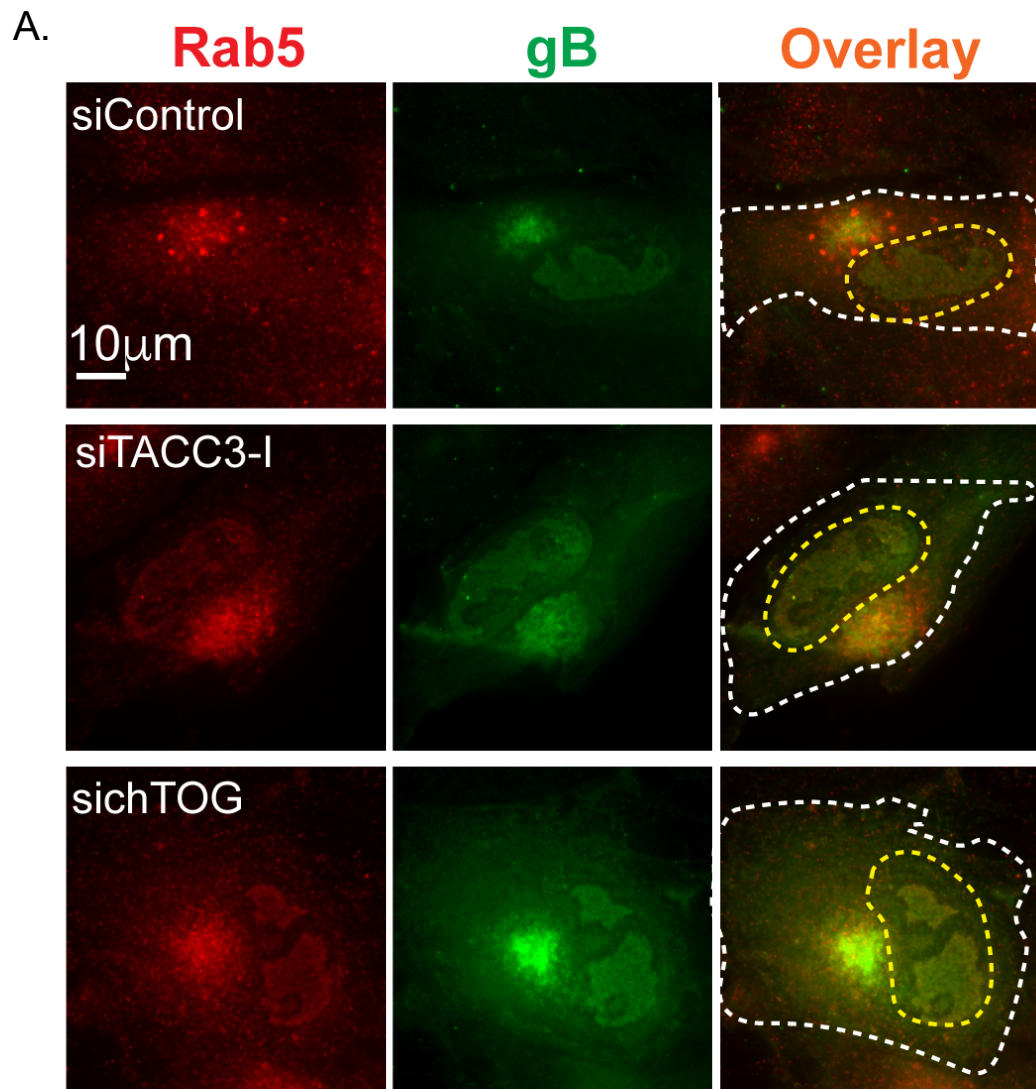


**Figure 58** Rab5 localization at the AC is disrupted by TACC3 or chTOG depletion. NHDFs were infected with TB40/E at MOI 1. At 5 h.p.i. cells were treated with control, TACC3, or chTOG siRNAs. Cells were fixed in methanol at 5 d.p.i. (A) Cells were stained for Rab5 (red) and gB (green). Cell cytoplasm is outlined with white dashed line, nucleus is outlined with yellow dashed line. (B) Fraction of cells with Rab5 staining in puncta throughout AC as shown for control cells in A.  $\geq 90$  cells per siRNA over 2 biological replicates; error bars = SEMs; \* $p < 0.05$ , \*\* $p < 0.01$ ; unpaired 2-tailed t test. Representative images are shown of results derived from 2 independent experiments.

structured AC that also sometimes detaches and migrates from the nuclear “pinch” that the AC initially generates [45] (Figure 59, Figure 60). IF analysis showed that small gB-positive puncta that represent egressing viral particles and small virus-containing vesicles colocalized with Rab5 or Rab7 in the cytoplasm of control siRNA-treated cells. However, in TACC3- or chTOG-depleted cells much larger Rab5- or Rab7-positive vesicles formed that contained gB and appear to contain viral particles (Figure 59, Figure 60), reflecting increased formation of what are likely to be multi-vesicular bodies (MVBs). Together these findings suggest that loss of TACC3 or chTOG function results in defects in secretory vesicle organization that may impact virion egress from the AC.

To test this, we next examined the effects of targeting TACC3 or chTOG using live cell imaging. NHDFs were infected with a strain of TB40/E that expresses a GFP-tagged form of the tegument protein UL99, which labels both the AC itself and individual viral particles [45, 268]. Cells were then treated with control non-targeting, TACC3 or chTOG siRNAs at 5 h.p.i. and live-cell fluorescence microscopy was performed at 120 h.p.i. (Figure 61, Video S6). Imaging revealed similar phenotypes in both TACC3 and chTOG-depleted cells that aligned with our fixed imaging of Rab-positive vesicles. In comparison to control cells, in cells depleted of TACC3 or chTOG there was an increase in large vesicles or MVBs in the cytoplasm that were UL99-positive. In addition, while many fast-moving viral particles were observed in the cytoplasm of control siRNA-treated cells, imaging revealed both a reduction in the number and overall motility of viral particles in the cytoplasm of TACC3- or chTOG-depleted cells (Figure 61, Video S6). Combined, our data shows that TACC3 and chTOG are required for efficient release of virus particles into the cytosol for trafficking, which likely explains defects in virus spread that were observed in our earlier multicycle spreading assays.

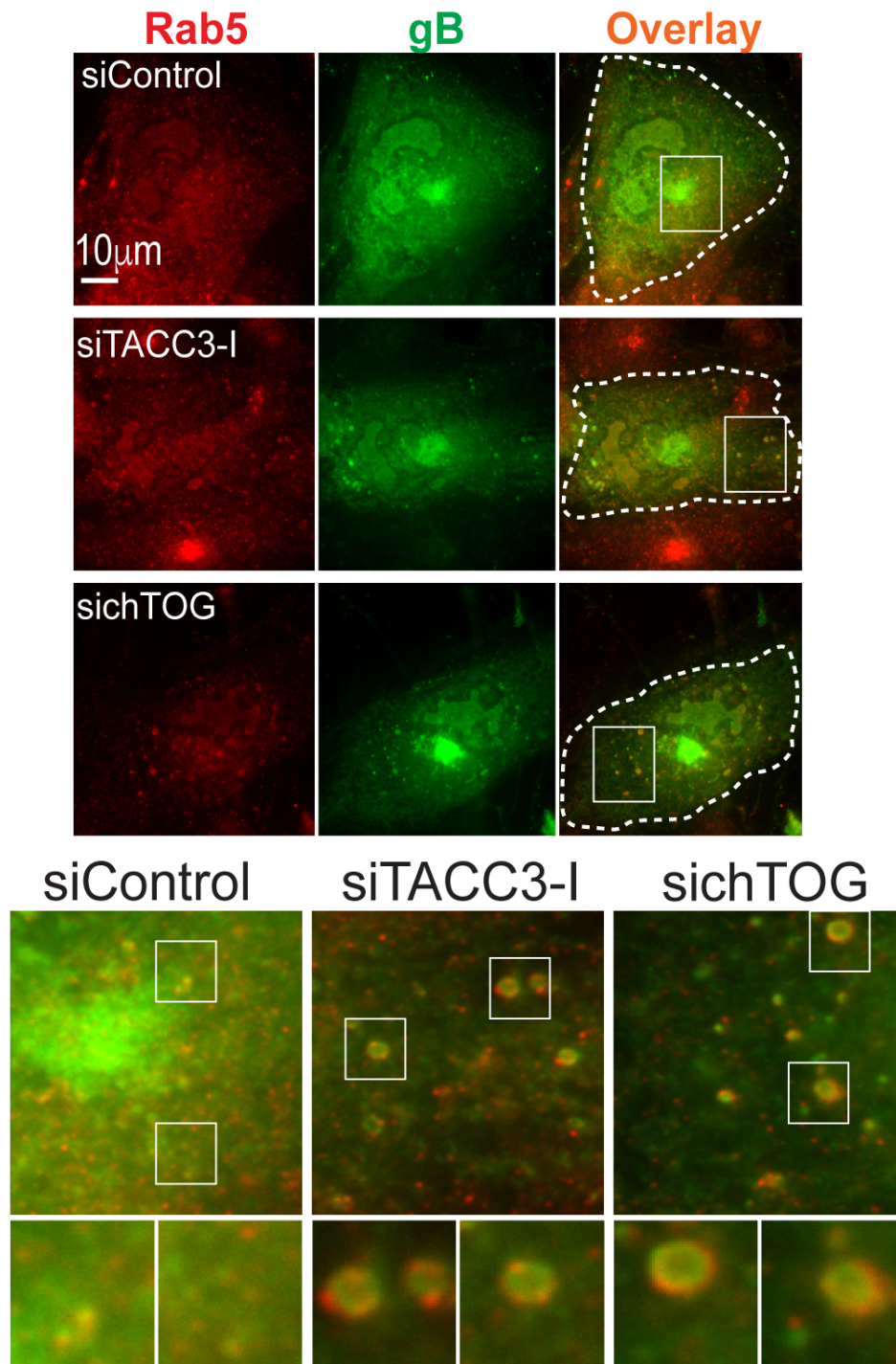


**Figure 59** Loss of TACC3 or chTOG results in formation of MVBs which are Rab5-positive. NHDFs were infected with TB40/E at MOI 1. At 5 h.p.i. cells were treated with control, TACC3, or chTOG siRNA. Cells were fixed in methanol at 5 d.p.i. and then stained for Rab5 (red) together with gB (green). Cell cytoplasm is outlined with white dashed line. Insets (bottom) show examples of large vesicular structures (MVBs) that stain for gB in TACC3 or chTOG siRNA-treated, and not in control non-targeting siRNA-treated cells. Representative images are shown of results derived from 3 independent experiments.

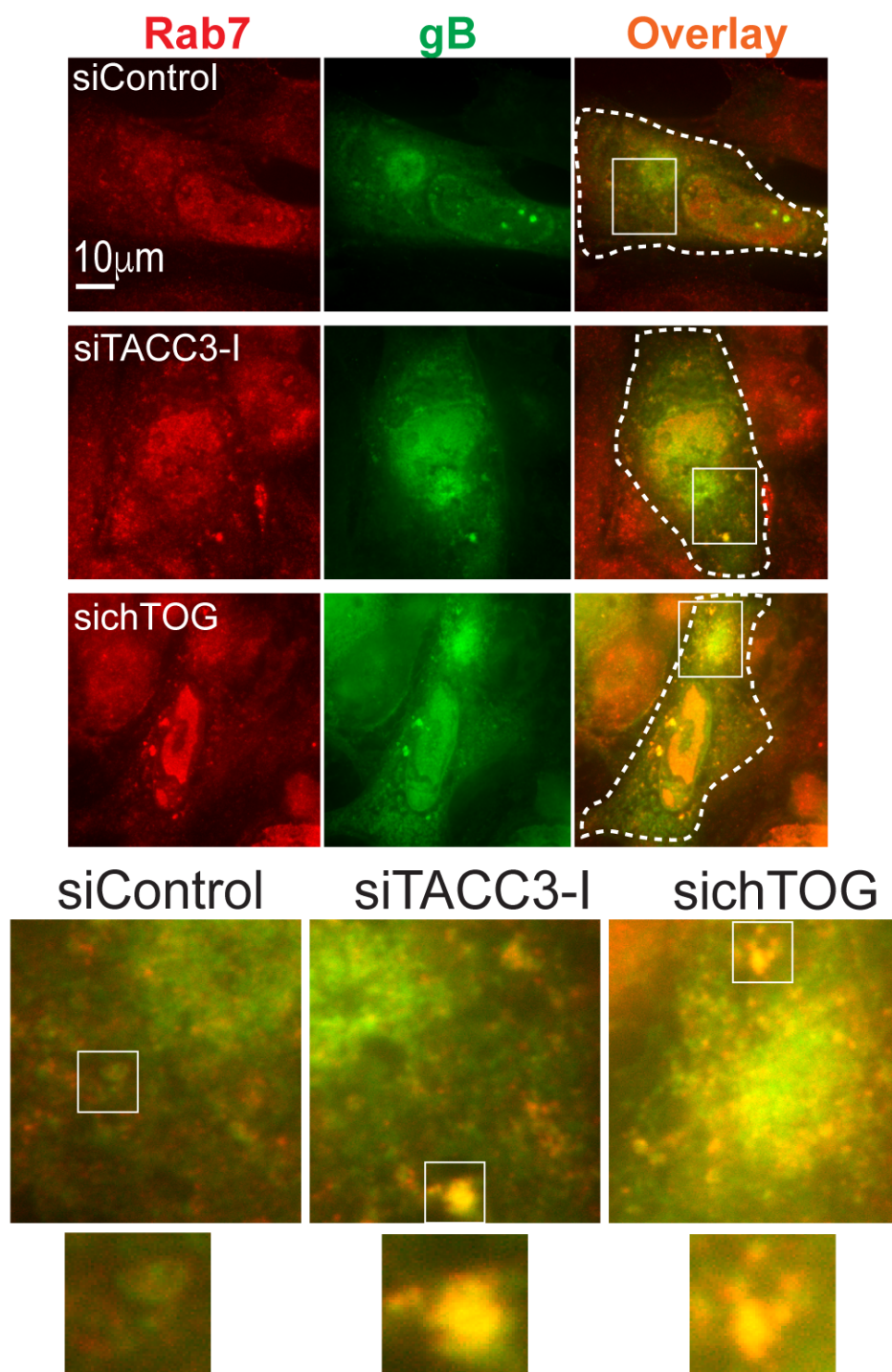


**Figure 60** MVBs that form in TACC3- or chTOG-depleted cells are Rab7-positive. NHDFs were infected with TB40/E at MOI 1. At 5 h.p.i. cells were treated with control, TACC3, or chTOG siRNA. Cells were fixed in methanol at 5 d.p.i. and then stained for Rab7 (red) together with gB (green). Cell cytoplasm is outlined with white dashed line. Insets (bottom) show examples of large vesicular structures (MVBs) that stain for gB in TACC3 or chTOG siRNA-treated, and not in control non-targeting siRNA-treated cells. Representative images are shown of results derived from 3 independent experiments.

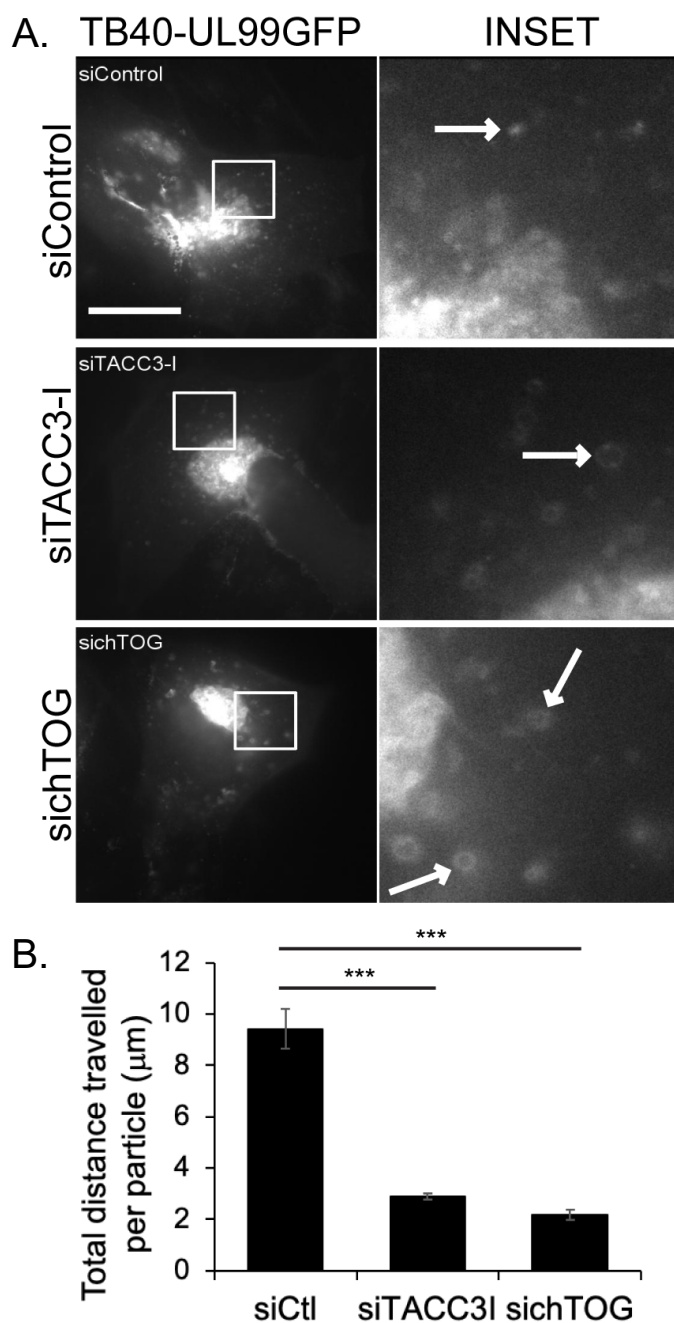


**Figure 61** Depletion of TACC3 or chTOG causes defects in virus trafficking. NHDFs were infected with TB40/EUL99-eGFP at MOI 1. At 5 h.p.i. cells were treated with control, TACC3, or chTOG siRNA. At 5 d.p.i. live cells were imaged by time-lapse fluorescence microscopy. (A) Representative still images from Video S6 are shown. Insets show examples of MVBs (white arrows) and egressing viral particles whose motility can be seen in Video S6. (B) Total distance travelled over 20s per particle ( $\mu\text{m}$ ) was averaged across 10 particles per cell.  $n=10$ ; error bars = SEMs;  $p < 0.005$ ; unpaired 2-tailed t test. Representative images are shown of results derived from 3 independent experiments.

## Discussion

While the importance of MTs during various stages of infection is well established through the study of motors or by grossly perturbing MTs themselves through the use of MT depolymerization and stabilizing agents, such as nocodazole or taxol, the underlying mechanisms by which viruses actively control the dynamic behavior of MT arrays remain less well defined. In particular, an understanding of how viruses co-opt the activity of the host's highly specialized +TIP network to control plus-end activities that include MT growth, stabilization and collapse, as well as capturing cargos for transport, has only recently begun to emerge.

As early as cell attachment and viral entry, Kaposi's Sarcoma associated Herpesvirus (KSHV) has been found to activate a wide range of cell signaling pathways whose downstream targets include RhoA activation of Diaphanous-2 (Dia-2), a +TIP that regulates both MT and actin dynamics, and induces the formation of stable MT networks that facilitate early stages of infection [269]. Early after fusion into the cytosol, Human Immunodeficiency Virus type 1 (HIV-1) particles bind a range of +TIPs directly [209, 211, 270]. Interestingly, engagement of +TIPs by HIV-1 particles activates their MT stabilization activities to create long-lived filaments that enhance retrograde transport to the nucleus, but also serves to regulate HIV-1 core stability, or uncoating. In the case of HIV-1, EB1 plays a critical but indirect role in these processes by delivering other +TIPs to sites of viral entry at the cell periphery, while viral particles then engage these +TIPs but not EB1 itself [208, 270]. By contrast, early after entry into primary fibroblasts HSV-1 capsids do not induce MT stabilization but instead engage dynamic MT filaments through a plus-end complex consisting of EB1, the EB1-associated +TIP cytoplasmic linker protein 170 (CLIP170) and Dynactin 1 (DCTN1), which is also a component of the dynein activating adaptor complex, dynactin [213]. This enables the loading of incoming HSV-1 particles onto MT filaments through

a more passive exploitation of cellular cargo capture processes that initiate retrograde transport by dynein. Interestingly, flavivirus internalization involves the formation of unusual tubule structures and EB3 is reported to promote both virus uptake and tubularization [271]. Late in infection the HSV-1 kinase Us3 activates another +TIP family member, Cytoplasmic-linker associated protein 2 (CLASP2) to stabilize MT filaments that facilitate viral egress [216]. By contrast, Vaccinia Virus (VacV) encodes a protein called F11 that inhibits RhoA-Dia signaling to promote MT dynamics [272] but the potential contribution of +TIPs to poxvirus infection has not been extensively studied to date.

With its more protracted replication cycle spanning several days, HCMV appears to have evolved different and perhaps more diverse strategies to exploit +TIPs as part of how it slowly yet extensively remodels the host cell. We recently found that as infection progresses, HCMV increases the expression of all three EB proteins [45]. This occurs in conjunction with formation of the AC, which becomes a large Golgi-based MTOC that increases the formation of both dynamic and acetylated MTs. EB3 specifically regulates the formation of acetylated MT arrays which are mechanically strong and enable the virus to rotate the nucleus and remodel the intranuclear environment [44, 45]. By contrast, EB1 regulates dynamic MT arrays that are formed during infection. Depletion of EB1 results in reduced MT dynamics and an increase in acetylated MT subsets, and therefore, does not affect nuclear rotation. Instead, loss of EB1 results in defects in AC structure and viral egress imaged using TB40/E expressing UL99-GFP [45], similar to phenotypes that we observe here upon TACC3 or chTOG depletion (Figure 61, Video S6). However, the broader effects of loss of EB1 activity on AC organization and infection have not been studied.

TACC proteins are most widely studied for their role in mitotic spindle formation and of limited studies in viral systems, evidence suggests they may be involved in cellular transformation by small DNA tumor viruses due to their roles in mitosis [273, 274]. However, as discussed earlier, it is now clear that TACC proteins also function to regulate MT dynamics in the cytoplasm of interphase cells, with TACC3 in particular functioning to control the cytoplasmic localization and plus-end binding activity of the MT polymerase chTOG. Here, we provide the first example of a virus that actively targets TACC3 to regulate this process, increasing TACC3 expression levels to increase chTOG availability in the cytoplasm to enhance MT growth rates (illustrated in Figure 52). Like EB proteins [45], TACC3 is upregulated yet chTOG is not, demonstrating that HCMV specifically enhances expression of certain plus-end tracking proteins to control MT arrays (Figure 42). Interestingly, EB proteins and TACC3 are the core +TIPs that recognize the MT plus-end. Furthermore, unlike many other +TIPs, TACC3 functions independently of EB proteins and indeed, by recruiting chTOG it creates the polymerizing activity that forms the dynamic filament plus-ends that EB proteins then track and further regulate. In line with this, like in uninfected cells [267], depletion of TACC3 resulted in defects in EB1 comet staining patterns that are indicative of slower MT growth, resulting in increased acetylation of these less dynamic MTs (Figure 51, Figure 54). This suggests that TACC3 and EB1 likely work in concert as a double-pronged strategy used by HCMV to increase MT dynamics. Like EB1 depletion, loss of TACC3 function results in defects in AC organization and virus spread as visualized using a virus expressing GFP-tagged UL99 (Figure 59, Figure 60, Figure 61, Video S6). Extending upon our understanding of their role in later stages of virus replication, here we show that dynamic MTs regulated by TACC3 and chTOG mediate the proper organization of Rab5- and Rab7-positive vesicles in and around the AC (Figure 56, Figure 57, Figure 58). Defects arising from the loss of either protein result in the

formation of larger vesicular structures that stain for gB and contain virus particles (Figure 59, Figure 60), in line with reports of the formation of MVBs during HCMV infection [55, 58, 59, 61, 62, 268, 275-278]. Increased formation of MVBs upon loss of TACC3 or chTOG availability reduced the release and motility of virus particles in the cytoplasm (Figure 61, Video S6). We have shown previously that loss of TACC3 activity also affects dynamic MT capture of incoming HSV-1 particles [267], an early infection process that is also likely to occur during HCMV infection and likely contributes to the defects in virus spread that occur in multicycle spreading assays (Figure 49A-B). However, although it is impossible to disentangle the contribution of early and late phase events in secondary spreading assays, the timing of the TACC3 increase and chTOG redistribution induced by HCMV, combined with the defects in both endosome organization around the AC and virus trafficking in the cytosol that arise at later stages, suggests that TACC3 plays a key role in efficient cell-cell spread through effects at both early and late stages of replication. Beyond the recent focus on emerging roles of EB proteins during virus infection, our findings reveal how HCMV targets the EB-independent plus-end polymerization complex by specifically upregulating TACC3 to control chTOG polymerase availability, and the central importance of this to late-stage processes that contribute to virus spread.

## CHAPTER 5: Discussion

The MT network is responsible for coordinating a number of events during viral infections, though many of the precise mechanisms by which a virus engages and manipulates host MTs remain unknown [200]. With the ability to influence MT behavior and shape the intracellular environment, +TIPs represent a key middle agent between viruses and the host MT network. Studying the role of +TIPs in viral infections can not only further our understanding of virus-MT interactions, but can also shed light on previously overlooked +TIP functions. Indeed, through my studies of the +TIP TACC3 I show that TACC3 controls the balance between dynamic and stable MTs in human interphase cells which in turn facilitates early stages of HSV-1 infection in different cell types and late stages of HCMV infection.

MT networks are organized and regulated in a unique manner across different cell types [279, 280]. These cell-type specific differences can impact how a virus interacts with MTs in a target cell. Such is the case for HSV-1, as my findings demonstrate that HSV-1 utilizes distinct mechanisms to target MTs for intracellular transport in human fibroblasts (NHDFs) and neuroblast-like cells (SK-N-SHs). While HSV-1 particles require dynamic, tyrosinated MTs for transport to the nucleus in NHDFs [213], HSV-1 uses stable, de-tyrosinated MTs to reach nuclei in SK-N-SHs (Figure 8, Figure 11). Beyond the cell-type specific differences in MT subsets used to establish infection, HSV-1 also requires different +TIP interacting partners to successfully engage MTs in either cell type. While HSV-1 particles depend upon the +TIPs EB1, CLIP170, and dynactin for dynamic MT capture and subsequent retrograde transport in NHDFs [213], HSV-1 engages stable MTs and traffics to the nucleus in an EB-independent manner in SK-N-SH cells (Figure 7, Figure 34E-F). Despite HSV-1 having cell-type specific mechanisms for initiating

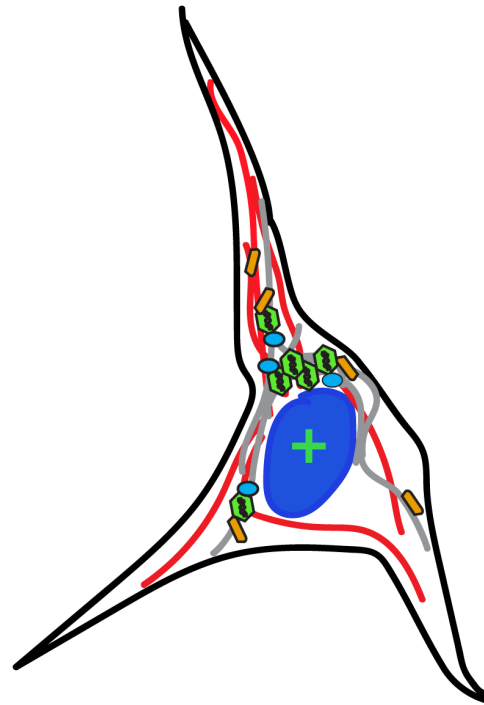
contact with MTs, I found that HSV-1 infection in both cell types relies upon the +TIP TACC3 due to its overarching role in controlling levels and organization of dynamic and stable MT populations.

Prior to my work, TACC3 was primarily studied in the context of mitotic cells, where the protein functions to promote MT spindle elongation by recruiting the MT polymerase chTOG to spindle plus-ends (Figure 5) [183-185, 234]. Despite numerous studies demonstrating the crucial role of TACC3 in regulating mitotic MTs, studies examining TACC3 in interphase cells were limited to yeast, *Drosophila*, and *Xenopus* systems prior to my studies [179, 184, 190, 192, 240-243]. In a singular study of human TACC3 in HeLa interphase cells, disruption of TACC3 levels was found to have no impact on MT dynamics [159]. Importantly, TACC3 exhibits predominantly nuclear localization during interphase in HeLa cells which differs from the cytoplasmic TACC3 localization observed in other cancer cells [180, 281] as well as in the human cell types I use for my studies (Figure 15C). Thus there are limitations to using HeLa cells to determine TACC3 functionality in normal human cells. Here, I provide evidence that TACC3 is in fact central to interphase MT regulation in human cells, with dysregulation of TACC3 resulting in MT growth defects and accumulation of post-translationally-modified stable MTs in NHDFs and SK-N-SHs. Importantly, I find that the predominantly cytoplasmic TACC3 controls interphase MT dynamics by regulating the intracellular localization of chTOG (Figure 32, Figure 33). Depletion of TACC3 results in chTOG sequestration in the nucleus while TACC3 overexpression results in the formation of TACC3-chTOG aggregations in the cytoplasm (Figure 31, Figure 32). In both cases, the loss of free chTOG in the cytoplasm results in stalled MT growth and increased levels of stabilized MTs (Figure 23-Figure 30). These results align with studies done in yeast cells that show

TACC3 homolog Alp7 is required for shuttling of chTOG homolog Alp14 from the nucleus to the cytoplasm during interphase and vice versa during mitosis [179, 190, 240]. This suggests that the regulation of chTOG nucleocytoplasmic localization by TACC3 is an evolutionarily-conserved function, a possibility that further studies in interphase cells of other organisms such as *Xenopus* and *Drosophila* could confirm. In a similar vein, given that mammalian TACC1-3 exhibit tissue-specific expression patterns [189, 282] future experiments to test the effects of altering TACC3 levels in additional primary human cell types could determine whether TACC3 retains its dominant role in regulating chTOG localization in cells that express higher levels of TACC1 or TACC2.

Beyond demonstrating that TACC3 regulates the balance between dynamic and stable MT populations by controlling chTOG localization, my studies also identified TACC3 as a facilitator of HSV-1 infection in NHDFs and SK-N-SHs despite the virus using distinct MT subsets to infect either cell type (Figure 34A-D). In NHDFs the disruption of TACC3 levels results in reduced MT growth and subsequently fewer growing plus-ends for EB1 to bind. Given that HSV-1 transport to the nucleus in NHDFs is dependent upon the EB1/CLIP170/dynactin complex capturing and loading viral particles onto dynamic MTs, the loss of dynamic MTs and EB1 at the cell periphery of NHDFs depleted of TACC3 blocks infection. On the other hand, in SK-N-SHs the de-tyrosinated MT network that HSV-1 particles rely upon for transport becomes enlarged and disorganized in cells depleted of TACC3, leading to disrupted HSV-1 translocation to the nucleus. Importantly, I found that the disruption of HSV-1 transport to the nucleus in TACC3-depleted SK-N-SHs is due to the biasing of de-tyrosinated MTs towards kinesin-based transport which moves cargo in an anterograde manner away from the nucleus (Figure 37, Figure 38, illustrated in Figure 62). Co-depletion of kinesin-1 and TACC3 restores HSV-1 particle transport to the nucleus

NORMAL:



↓ TACC3 ACTIVITY:

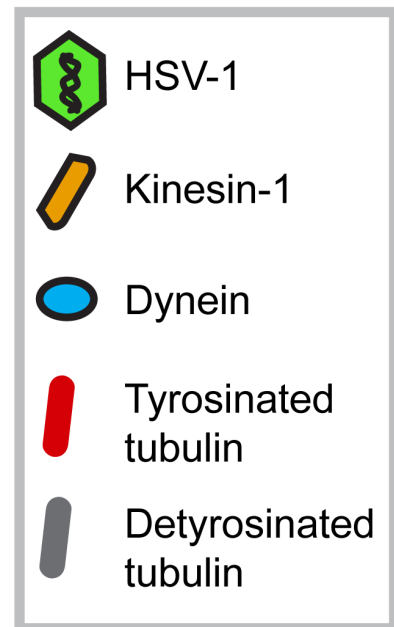
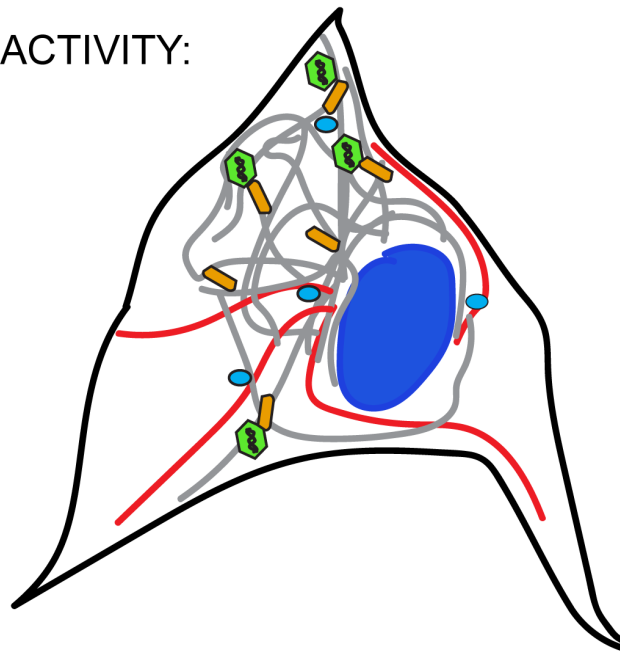


**Figure 62** Model of HSV-1 infection in TACC3-depleted SK-N-SHs. (Top) Under normal conditions, HSV-1 traffics upon the organized de-tyrosinated MT network in SK-N-SHs to reach the perinuclear space. (BOTTOM) In cells depleted of TACC3, loss of dynamic MT growth results in the accumulation of de-tyrosinated MTs which kinesin-1 binds with higher affinity than dynein. Intracellular cargo sorting becomes biased towards kinesin-based transport, resulting in HSV-1 particles being shuttled away from the nucleus on de-tyrosinated MTs.

without affecting the abundance of de-tyrosinated MTs, indicating that under TACC3 depletion conditions kinesin-1 outcompetes other cellular motors for access to de-tyrosinated MTs (Figure 39). Similar patterns emerged when I examined internalized transferrin trafficking in SK-N-SHs, with TACC3 depletion resulting in impaired transport of transferrin to the perinuclear space and kinesin-1/TACC3 co-depletion restoring this localization (Figure 39-41). These results are in accord with a previous study that found kinesin-1 transports recycling transferrin to the cell surface on de-tyrosinated MTs, along with other studies that demonstrate the preferred binding of kinesin-1 to de-tyrosinated MTs [121, 122, 283]. I also found that TACC3 depletion affects size and morphology of the *trans-Golgi* network in SK-N-SHs, with the Golgi expanding away from the perinuclear space in TACC3-depleted cells (Figure 19C). Given that the Golgi depends upon dynein motor activity for maintaining its shape and organization, it is possible that the biasing of de-tyrosinated MTs towards kinesin motor activity also enables kinesin to outcompete dynein for access to Golgi membranes resulting in the expansion phenotype [120-122, 125]. This hypothesis could be tested in a similar manner as discussed for HSV-1 and transferrin, using co-depletion of kinesin-1 and TACC3 to determine if Golgi expansion would be reversed. My studies regarding the intracellular trafficking of HSV-1 and transferrin demonstrate that the abundance of post-translationally modified MTs and proteins such as TACC3 that regulate their abundance have a significant impact on motor-based cargo sorting pathways.

The MT network plays a role in more than just transporting viruses within the host cell. Though MT-dependent trafficking of viral particles to the nucleus is an essential step in early stages of herpesvirus infections, late stages of infection also depend upon MTs for coordination of the intracellular environment to facilitate virion assembly and maturation. This is particularly true

for HCMV which dramatically remodels the host cell during infection through the formation of the AC, alteration of nuclear shape, and reorganization of the intranuclear environment [44, 45, 47]. Previous studies from our lab found that HCMV upregulates EB1 to promote dynamic MTs which maintain AC structural integrity and EB3 to promote nucleation of AC-derived MTs which become acetylated and coordinate the remodeling of the nucleus [45]. EB1 in particular has been implicated in other viral infections as well, including HSV-1 which requires EB1 for intracellular trafficking in fibroblasts and HIV-1 which requires EB1 to initiate MT stabilization via interacting protein Kif4 during early stages of infection [208]. Through my studies I provide the first example of a virus actively targeting TACC3 during infection with HCMV specifically upregulating TACC3 but not its binding partner chTOG during infection in NHDFs, though further studies are warranted to determine if the upregulation of TACC3 is occurring on a transcriptional or post-transcriptional level (Figure 42, Figure 43). RNAi-mediated inhibition of TACC3 upregulation during HCMV infection results in a sequestration of chTOG at the AC (Figure 50), which contrasts with the nuclear sequestration of chTOG seen in uninfected cells depleted of TACC3 (Figure 32). One potential reason for this is that due to the upregulation of TACC3 by HCMV, low levels of TACC3 that remain after siRNA treatment in infected cells are higher than those in siRNA-treated uninfected cells. This would enable the low amounts of remaining cytoplasmic TACC3 to recruit chTOG out of the nucleus where chTOG then gets sequestered within the AC. Previous studies in our lab found that MT nucleating factors such as  $\gamma$ -tubulin, pericentrin, and CDK5RAP2 become enriched at Golgi sites throughout the AC during HCMV infection rather than primarily at the centrosome as in uninfected cells [45]. My findings suggest that chTOG, which plays a role in MT nucleation at the centrosome in uninfected cells [162-164], functions at nucleation sites throughout

the AC during HCMV infection but requires high levels of TACC3 for recruitment to the rest of the cytoplasm to act at the MT plus-end. The upregulation of TACC3 and subsequent recruitment of chTOG to the cytoplasm during HCMV infection is necessary for sustained MT growth (Figure 51). Loss of chTOG from the cytoplasm during infection, facilitated either directly by RNAi or indirectly through TACC3 depletion, results in reduced MT growth and accumulation of MTs that become acetylated (Figure 51, Figure 54, Figure 55B, illustrated in Figure 52). This phenotype is similar to that seen in HCMV-infected cells depleted of EB1 [45], indicating that both TACC3 and EB1 play a part in promoting dynamic MTs during infection. Importantly, our findings add evidence to the model that TACC3 and chTOG act upstream of EB1 to facilitate MT polymerization, with EB1 tracking plus-ends as they are created by the TACC3/chTOG complex (illustrated in Figure 52).

My studies have illustrated the importance of maintaining balance between dynamic and stable MTs, a balance that if disrupted can interfere with cargo trafficking, organization of organelles, and coordination of viral infection. In a model representative of my findings, TACC3 is at the center of this balance, manipulating levels of chTOG in the cytoplasm to drive the MT network towards either dynamic or stalled growth (Figure 63). Through my studies I show one example of a virus, HCMV, hijacking this balance by upregulating TACC3 to promote MT dynamics during late stages of infection. I also show the dependence that HSV-1 has on TACC3 for facilitating intracellular transport during early stages of infection. An interesting question to investigate in future studies is whether other viruses target TACC3 to coordinate the MT network around virus propagation. It would be particularly interesting to examine TACC3 levels and localization in the context of viral infections that induce MT stabilization, such as HIV-1

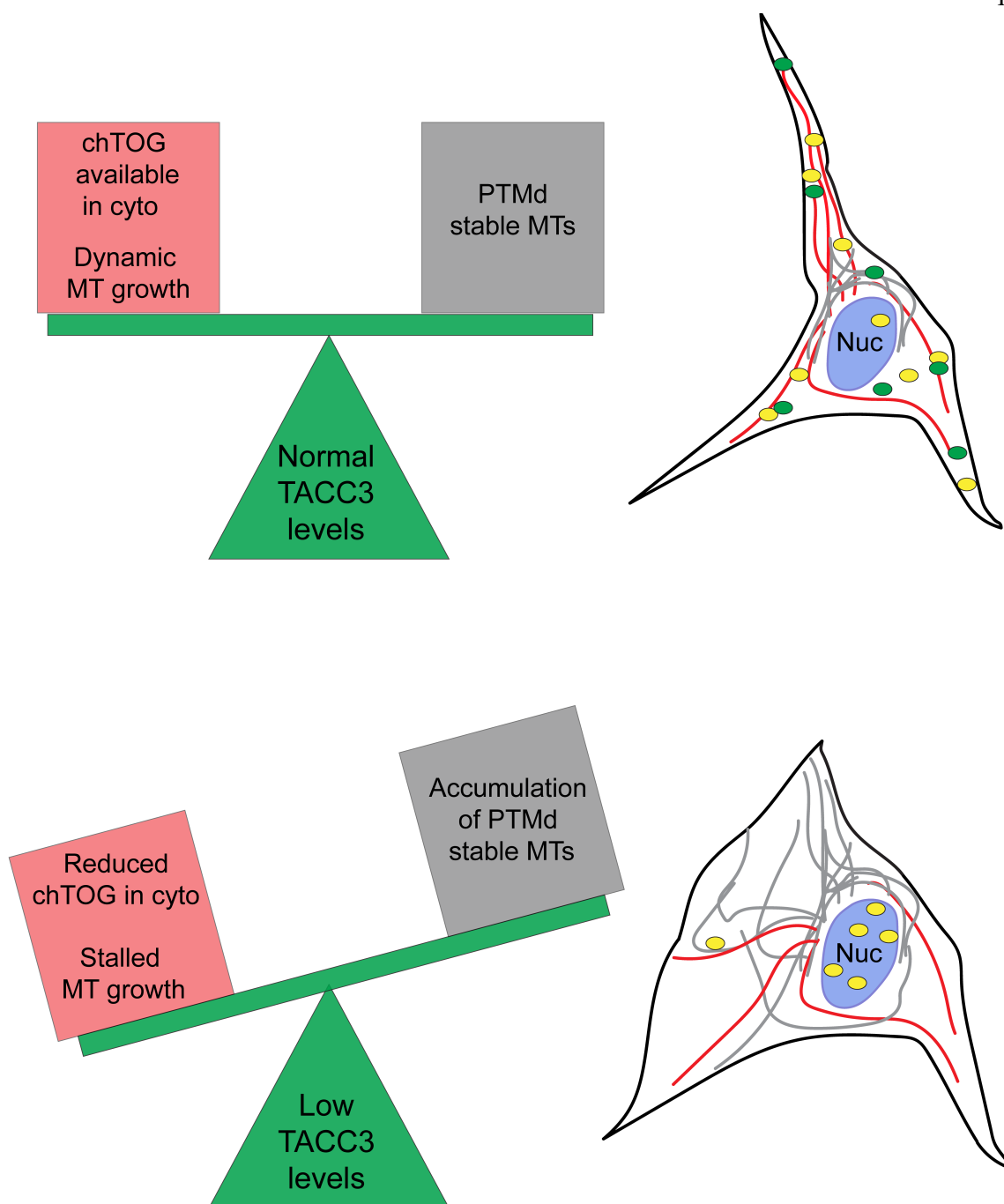


**Figure 63** A simplified model of TACC3 activity. (Top) In human interphase cells, illustrated to the right, there is a balance between dynamic (red) and stable (grey) MT populations. TACC3 (green) maintains this balance by recruiting chTOG (yellow) to the cytoplasm which enables efficient MT growth. Concurrently, stabilized MTs accrue post-translational modifications (PTMs) over time. (Bottom) When TACC3 levels are depleted, chTOG is sequestered in the nucleus causing reduced MT polymerization in the cytoplasm. This skews the balance between MT subsets towards stable, post-translationally modified MTs.

[208, 209, 211], HSV-1 [216], and KSHV [206]. A number of the pathways triggered by these viruses to induce MT stabilization have been characterized, but future studies could examine how these pathways may affect TACC3 or chTOG. Given the forefront role of TACC3 and chTOG in generating dynamic MTs, it is quite possible that these proteins are targeted by viruses in need of dampening dynamics in favor of stabilization. As was the case in these studies, examining TACC3 in the context of viral infection can paint a more complete picture of the protein's biological function in normal cells. Due to its upregulation in several human cancers, TACC3 remains a particularly important cellular factor to understand. The work described here adds to our current knowledge of TACC3 functionality in human cells and lays a foundation for future exploration into the role of TACC3 in both pathogenic and cellular processes.

## References

1. Pellett, P. and B. Roizman, *Herpesviridae In: Knipe D, Howley P, editors. Fields Virology 2*. 2013, Lippincott, Williams & Wilkins.
2. Davison, A.J., et al., *The order Herpesvirales*. Archives of virology, 2009. **154**(1): p. 171-177.
3. Davison, A.J., *Evolution of the herpesviruses*. Veterinary Microbiology, 2002. **86**(1): p. 69-88.
4. Looker, K.J., et al., *Global and Regional Estimates of Prevalent and Incident Herpes Simplex Virus Type 1 Infections in 2012*. PLOS ONE, 2015. **10**(10): p. e0140765.
5. Bouley, D.M., et al., *Characterization of herpes simplex virus type-1 infection and herpetic stromal keratitis development in IFN-gamma knockout mice*. The Journal of Immunology, 1995. **155**(8): p. 3964-3971.
6. Bloom, D.C., N.V. Giordani, and D.L. Kwiatkowski, *Epigenetic regulation of latent HSV-1 gene expression*. Biochimica et biophysica acta, 2010. **1799**(3-4): p. 246-256.
7. Antinone, S.E. and G.A. Smith, *Retrograde Axon Transport of Herpes Simplex Virus and Pseudorabies Virus: a Live-Cell Comparative Analysis*. Journal of Virology, 2010. **84**(3): p. 1504-1512.
8. Nicola, A.V., *Herpesvirus Entry into Host Cells Mediated by Endosomal Low pH. Traffic*, 2016. **17**(9): p. 965-975.
9. Nicola, A.V., et al., *Herpes Simplex Virus Type 1 Enters Human Epidermal Keratinocytes, but Not Neurons, via a pH-Dependent Endocytic Pathway*. Journal of Virology, 2005. **79**(12): p. 7609-7616.
10. Madavaraju, K., et al., *Herpes Simplex Virus Cell Entry Mechanisms: An Update*. Front Cell Infect Microbiol, 2020. **10**: p. 617578.
11. Mabit, H., et al., *Intact microtubules support adenovirus and herpes simplex virus infections*. J Virol, 2002. **76**(19): p. 9962-71.
12. Kristensson, K., et al., *Neuritic transport of herpes simplex virus in rat sensory neurons in vitro. Effects of substances interacting with microtubular function and axonal flow [nocodazole, taxol and erythro-9-3-(2-hydroxynonyl)adenine]*. J Gen Virol, 1986. **67** ( Pt 9): p. 2023-8.
13. Copeland, A.M., W.W. Newcomb, and J.C. Brown, *Herpes simplex virus replication: roles of viral proteins and nucleoporins in capsid-nucleus attachment*. Journal of virology, 2009. **83**(4): p. 1660-1668.
14. Padeloup, D., et al., *Herpesvirus capsid association with the nuclear pore complex and viral DNA release involve the nucleoporin CAN/Nup214 and the capsid protein pUL25*. Journal of virology, 2009. **83**(13): p. 6610-6623.
15. Weinheimer, S.P. and S.L. McKnight, *Transcriptional and post-transcriptional controls establish the cascade of herpes simplex virus protein synthesis*. Journal of Molecular Biology, 1987. **195**(4): p. 819-833.
16. Harkness, J.M., M. Kader, and N.A. DeLuca, *Transcription of the herpes simplex virus 1 genome during productive and quiescent infection of neuronal and nonneuronal cells*. Journal of virology, 2014. **88**(12): p. 6847-6861.

17. McElwee, M., et al., *Structure of the herpes simplex virus portal-vertex*. PLOS Biology, 2018. **16**(6): p. e2006191.
18. Newcomb, W.W., et al., *The Primary Enveloped Virion of Herpes Simplex Virus 1: Its Role in Nuclear Egress*. mBio, 2017. **8**(3): p. e00825-17.
19. Hollinshead, M., et al., *Endocytic tubules regulated by Rab GTPases 5 and 11 are used for envelopment of herpes simplex virus*. The EMBO Journal, 2012. **31**(21): p. 4204-4220.
20. Rémillard-Labrosse, G., et al., *Protein Kinase D-Dependent Trafficking of the Large Herpes simplex Virus Type 1 Capsids from the TGN to Plasma Membrane*. Traffic, 2009. **10**(8): p. 1074-1083.
21. Ahmad, I. and D.W. Wilson, *HSV-1 Cytoplasmic Envelopment and Egress*. International Journal of Molecular Sciences, 2020. **21**(17): p. 5969.
22. Miranda-Saksena, M., et al., *Herpes simplex virus utilizes the large secretory vesicle pathway for anterograde transport of tegument and envelope proteins and for viral exocytosis from growth cones of human fetal axons*. Journal of virology, 2009. **83**(7): p. 3187-3199.
23. Johnson, D.C. and J.D. Baines, *Herpesviruses remodel host membranes for virus egress*. Nature Reviews Microbiology, 2011. **9**(5): p. 382-394.
24. Mador, N., et al., *Herpes simplex virus type 1 latency-associated transcripts suppress viral replication and reduce immediate-early gene mRNA levels in a neuronal cell line*. Journal of virology, 1998. **72**(6): p. 5067-5075.
25. Wang, Q.-Y., et al., *Herpesviral latency-associated transcript gene promotes assembly of heterochromatin on viral lytic-gene promoters in latent infection*. Proceedings of the National Academy of Sciences of the United States of America, 2005. **102**(44): p. 16055-16059.
26. Nicoll, M.P., et al., *The HSV-1 Latency-Associated Transcript Functions to Repress Latent Phase Lytic Gene Expression and Suppress Virus Reactivation from Latently Infected Neurons*. PLoS pathogens, 2016. **12**(4): p. e1005539-e1005539.
27. Bloom, D.C., *Chapter Two - Alphaherpesvirus Latency: A Dynamic State of Transcription and Reactivation*, in *Advances in Virus Research*, M. Kielian, K. Maramorosch, and T.C. Mettenleiter, Editors. 2016, Academic Press. p. 53-80.
28. Du, T., G. Zhou, and B. Roizman, *HSV-1 gene expression from reactivated ganglia is disordered and concurrent with suppression of latency-associated transcript and miRNAs*. Proc Natl Acad Sci U S A, 2011. **108**(46): p. 18820-4.
29. Kim, J.Y., et al., *Transient Reversal of Episome Silencing Precedes VP16-Dependent Transcription during Reactivation of Latent HSV-1 in Neurons*. PLOS Pathogens, 2012. **8**(2): p. e1002540.
30. Cliffe, A.R., A.C. Wilson, and F. Goodrum, *Restarting Lytic Gene Transcription at the Onset of Herpes Simplex Virus Reactivation*. Journal of Virology, 2017. **91**(2): p. e01419-16.
31. BenMohamed, L., et al., *Decreased reactivation of a herpes simplex virus type 1 (HSV-1) latency-associated transcript (LAT) mutant using the in vivo mouse UV-B model of induced reactivation*. Journal of neurovirology, 2015. **21**(5): p. 508-517.

32. Hill, J.M., et al., *Quantitation and kinetics of induced HSV-1 ocular shedding*. Current Eye Research, 1986. **5**(3): p. 241-246.
33. Griffiths, P., I. Baraniak, and M. Reeves, *The pathogenesis of human cytomegalovirus*. The Journal of Pathology, 2015. **235**(2): p. 288-297.
34. Chen, S.-J., S.-C. Wang, and Y.-C. Chen, *Antiviral Agents as Therapeutic Strategies Against Cytomegalovirus Infections*. Viruses, 2019. **12**(1): p. 21.
35. Cannon, M.J. and K.F. Davis, *Washing our hands of the congenital cytomegalovirus disease epidemic*. BMC public health, 2005. **5**: p. 70-70.
36. Dollard, S.C., S.D. Grosse, and D.S. Ross, *New estimates of the prevalence of neurological and sensory sequelae and mortality associated with congenital cytomegalovirus infection*. Reviews in Medical Virology, 2007. **17**(5): p. 355-363.
37. Brown, H.L. and M.P. Abernathy, *Cytomegalovirus infection*. Seminars in Perinatology, 1998. **22**(4): p. 260-266.
38. Vanarsdall, A.L. and D.C. Johnson, *Human cytomegalovirus entry into cells*. Current opinion in virology, 2012. **2**(1): p. 37-42.
39. Martinez-Martin, N., et al., *An Unbiased Screen for Human Cytomegalovirus Identifies Neuropilin-2 as a Central Viral Receptor*. Cell, 2018. **174**(5): p. 1158-1171.e19.
40. Li, G., J.P. Kamil, and B. Tsai, *Viral Regulation of Cell Tropism in Human Cytomegalovirus*. Journal of Virology, 2016. **90**(2): p. 626-629.
41. Goodrum, F.D., et al., *Human cytomegalovirus gene expression during infection of primary hematopoietic progenitor cells: A model for latency*. Proceedings of the National Academy of Sciences, 2002. **99**(25): p. 16255-16260.
42. Reeves, M.B., et al., *Latency, chromatin remodeling, and reactivation of human cytomegalovirus in the dendritic cells of healthy carriers*. Proceedings of the National Academy of Sciences of the United States of America, 2005. **102**(11): p. 4140-4145.
43. Wiedbrauk, D.L., *Chapter 37 - Herpes Simplex Virus*, in *Molecular Diagnostics*, W.W. Grody, et al., Editors. 2010, Academic Press: San Diego. p. 453-460.
44. Procter, D.J., et al., *Cytoplasmic control of intranuclear polarity by human cytomegalovirus*. Nature, 2020. **587**(7832): p. 109-114.
45. Procter, D.J., et al., *The HCMV Assembly Compartment Is a Dynamic Golgi-Derived MTOC that Controls Nuclear Rotation and Virus Spread*. Developmental Cell, 2018. **45**(1): p. 83-100.e7.
46. Das, S., A. Vasanji, and P.E. Pellett, *Three-Dimensional Structure of the Human Cytomegalovirus Cytoplasmic Virion Assembly Complex Includes a Reoriented Secretory Apparatus*. Journal of Virology, 2007. **81**(21): p. 11861-11869.
47. Alwine, J.C., *The human cytomegalovirus assembly compartment: a masterpiece of viral manipulation of cellular processes that facilitates assembly and egress*. PLoS pathogens, 2012. **8**(9): p. e1002878-e1002878.
48. Ryckman, B.J., et al., *Human Cytomegalovirus Entry into Epithelial and Endothelial Cells Depends on Genes UL128 to UL150 and Occurs by Endocytosis and Low-pH Fusion*. Journal of Virology, 2006. **80**(2): p. 710-722.
49. Sinzger, C., *Entry route of HCMV into endothelial cells*. Journal of Clinical Virology, 2008. **41**(3): p. 174-179.

50. Hetzenecker, S., A. Helenius, and M.A. Krzyzaniak, *HCMV Induces Macropinocytosis for Host Cell Entry in Fibroblasts*. *Traffic*, 2016. **17**(4): p. 351-368.
51. Compton, T., R.R. Nepomuceno, and D.M. Nowlin, *Human cytomegalovirus penetrates host cells by PH-independent fusion at the cell surface*. *Virology*, 1992. **191**(1): p. 387-395.
52. Ogawa-Goto, K., et al., *Microtubule Network Facilitates Nuclear Targeting of Human Cytomegalovirus Capsid*. *Journal of Virology*, 2003. **77**(15): p. 8541-8547.
53. Hong, Y., et al., *STING facilitates nuclear import of herpesvirus genome during infection*. *Proceedings of the National Academy of Sciences*, 2021. **118**(33): p. e2108631118.
54. Goldberg, M.D., et al., *Human Cytomegalovirus UL97 Kinase and Nonkinase Functions Mediate Viral Cytoplasmic Secondary Envelopment*. *Journal of Virology*, 2011. **85**(7): p. 3375-3384.
55. Homman-Loudiyi, M., et al., *Envelopment of Human Cytomegalovirus Occurs by Budding into Golgi-Derived Vacuole Compartments Positive for gB, Rab 3, Trans-Golgi Network 46, and Mannosidase II*. *Journal of Virology*, 2003. **77**(5): p. 3191-3203.
56. Cappadona, I., et al., *Human Cytomegalovirus pUL47 Modulates Tegumentation and Capsid Accumulation at the Viral Assembly Complex*. *Journal of Virology*, 2015. **89**(14): p. 7314-7328.
57. Cepeda, V., M. Esteban, and A. Fraile-Ramos, *Human cytomegalovirus final envelopment on membranes containing both trans-Golgi network and endosomal markers*. *Cellular Microbiology*, 2010. **12**(3): p. 386-404.
58. Read, C., et al., *Regulation of Human Cytomegalovirus Secondary Envelopment by a C-Terminal Tetralysine Motif in pUL71*. *J Virol*, 2019. **93**(13).
59. Flomm, F.J., et al., *Intermittent bulk release of human cytomegalovirus through multivesicular bodies*. *bioRxiv*, 2021: p. 2020.12.31.424954.
60. Taisne, C., et al., *Human cytomegalovirus hijacks the autophagic machinery and LC3 homologs in order to optimize cytoplasmic envelopment of mature infectious particles*. *Scientific Reports*, 2019. **9**(1): p. 4560.
61. Momtaz, S., et al., *Cell Type-Specific Biogenesis of Novel Vesicles Containing Viral Products in Human Cytomegalovirus Infection*. *Journal of Virology*, 2021. **95**(11): p. e02358-20.
62. Schauflinger, M., et al., *The Tegument Protein UL71 of Human Cytomegalovirus Is Involved in Late Envelopment and Affects Multivesicular Bodies*. *Journal of Virology*, 2011. **85**(8): p. 3821-3832.
63. Fraile-Ramos, A., et al., *Localization of HCMV UL33 and US27 in endocytic compartments and viral membranes*. *Traffic*, 2002. **3**(3): p. 218-232.
64. Severi, B., M. Landini, and E. Govoni, *Human cytomegalovirus morphogenesis: an ultrastructural study of the late cytoplasmic phases*. *Archives of virology*, 1988. **98**(1): p. 51-64.
65. Sanchez, V., et al., *Accumulation of virion tegument and envelope proteins in a stable cytoplasmic compartment during human cytomegalovirus replication: characterization of a potential site of virus assembly*. *Journal of virology*, 2000. **74**(2): p. 975-986.

66. Rebmann, G.M., et al., *Phosphorylation of Golgi Peripheral Membrane Protein Grasp65 Is an Integral Step in the Formation of the Human Cytomegalovirus Cytoplasmic Assembly Compartment*. *mBio*, 2016. **7**(5): p. e01554-16.
67. Lučin, P., et al., *Cytomegaloviruses Exploit Recycling Rab Proteins in the Sequential Establishment of the Assembly Compartment*. *Frontiers in cell and developmental biology*, 2018. **6**: p. 165-165.
68. Das, S. and P.E. Pellett, *Spatial Relationships between Markers for Secretory and Endosomal Machinery in Human Cytomegalovirus-Infected Cells versus Those in Uninfected Cells*. *Journal of Virology*, 2011. **85**(12): p. 5864-5879.
69. Buchkovich, N.J., T.G. Maguire, and J.C. Alwine, *The Role of the ER Chaperone BiP, SUN-Domain Proteins and Dynein in Altering Nuclear Morphology during Human Cytomegalovirus Infection*. *Journal of Virology*, 2010.
70. Indran, S.V., M.E. Ballestas, and W.J. Britt, *Bicaudal D1-dependent trafficking of human cytomegalovirus tegument protein pp150 in virus-infected cells*. *Journal of virology*, 2010. **84**(7): p. 3162-3177.
71. Desai, A. and T.J. Mitchison, *MICROTUBULE POLYMERIZATION DYNAMICS*. *Annual Review of Cell and Developmental Biology*, 1997. **13**(1): p. 83-117.
72. Tilney, L.G., et al., *Microtubules: evidence for 13 protofilaments*. *J Cell Biol*, 1973. **59**(2 Pt 1): p. 267-75.
73. Bryan, J. and L. Wilson, *Are cytoplasmic microtubules heteropolymers?* *Proceedings of the National Academy of Sciences of the United States of America*, 1971. **68**(8): p. 1762-1766.
74. Osborn, M. and K. Weber, *Cytoplasmic microtubules in tissue culture cells appear to grow from an organizing structure towards the plasma membrane*. *Proc Natl Acad Sci U S A*, 1976. **73**(3): p. 867-71.
75. Bergen, L.G., R. Kuriyama, and G.G. Borisy, *Polarity of microtubules nucleated by centrosomes and chromosomes of Chinese hamster ovary cells in vitro*. *J Cell Biol*, 1980. **84**(1): p. 151-9.
76. Chabin-Brion, K., et al., *The Golgi complex is a microtubule-organizing organelle*. *Mol Biol Cell*, 2001. **12**(7): p. 2047-60.
77. Wu, J. and A. Akhmanova, *Microtubule-Organizing Centers*. *Annu Rev Cell Dev Biol*, 2017. **33**: p. 51-75.
78. Petry, S. and R.D. Vale, *Microtubule nucleation at the centrosome and beyond*. *Nature Cell Biology*, 2015. **17**(9): p. 1089-1093.
79. Efimov, A., et al., *Asymmetric CLASP-dependent nucleation of noncentrosomal microtubules at the trans-Golgi network*. *Developmental cell*, 2007. **12**(6): p. 917-930.
80. Yvon, A.M. and P. Wadsworth, *Non-centrosomal microtubule formation and measurement of minus end microtubule dynamics in A498 cells*. *J Cell Sci*, 1997. **110** ( Pt **19**): p. 2391-401.
81. Komarova, Y.A., I.A. Vorobjev, and G.G. Borisy, *Life cycle of MTs: persistent growth in the cell interior, asymmetric transition frequencies and effects of the cell boundary*. *J Cell Sci*, 2002. **115**(Pt 17): p. 3527-39.
82. Mitchison, T. and M. Kirschner, *Dynamic instability of microtubule growth*. *Nature*, 1984. **312**(5991): p. 237-242.

83. Kerssemakers, J.W.J., et al., *Assembly dynamics of microtubules at molecular resolution*. Nature, 2006. **442**(7103): p. 709-712.
84. Mitchison, T., *Localization of an exchangeable GTP binding site at the plus end of microtubules*. Science, 1993. **261**(5124): p. 1044-1047.
85. Knossow, M., et al., *The Mechanism of Tubulin Assembly into Microtubules: Insights from Structural Studies*. iScience, 2020. **23**(9): p. 101511.
86. Nogales, E., et al., *High-Resolution Model of the Microtubule*. Cell, 1999. **96**(1): p. 79-88.
87. Manka, S.W. and C.A. Moores, *Microtubule structure by cryo-EM: snapshots of dynamic instability*. Essays in biochemistry, 2018. **62**(6): p. 737-751.
88. Alushin, G.M., et al., *High-resolution microtubule structures reveal the structural transitions in  $\alpha$ -tubulin upon GTP hydrolysis*. Cell, 2014. **157**(5): p. 1117-1129.
89. Piedra, F.-A., et al., *GDP-to-GTP exchange on the microtubule end can contribute to the frequency of catastrophe*. Molecular biology of the cell, 2016. **27**(22): p. 3515-3525.
90. Dimitrov, A., et al., *Detection of GTP-Tubulin Conformation in Vivo Reveals a Role for GTP Remnants in Microtubule Rescues*. Science, 2008. **322**(5906): p. 1353-1356.
91. Tropini, C., et al., *Islands Containing Slowly Hydrolyzable GTP Analogs Promote Microtubule Rescues*. PLOS ONE, 2012. **7**(1): p. e30103.
92. Aumeier, C., et al., *Self-repair promotes microtubule rescue*. Nature Cell Biology, 2016. **18**(10): p. 1054-1064.
93. Gardner, M.K., M. Zanic, and J. Howard, *Microtubule catastrophe and rescue*. Current Opinion in Cell Biology, 2013. **25**(1): p. 14-22.
94. Schulze, E. and M. Kirschner, *Dynamic and stable populations of microtubules in cells*. The Journal of cell biology, 1987. **104**(2): p. 277-288.
95. Wen, Y., et al., *EB1 and APC bind to mDia to stabilize microtubules downstream of Rho and promote cell migration*. Nature Cell Biology, 2004. **6**(9): p. 820-830.
96. Sun, D., C.L. Leung, and R.K. Liem, *Characterization of the microtubule binding domain of microtubule actin crosslinking factor (MACF): identification of a novel group of microtubule associated proteins*. Journal of Cell Science, 2001. **114**(1): p. 161-172.
97. Gundersen, G.G., *Evolutionary conservation of microtubule-capture mechanisms*. Nature Reviews Molecular Cell Biology, 2002. **3**(4): p. 296-304.
98. Mimori-Kiyosue, Y., et al., *CLASP1 and CLASP2 bind to EB1 and regulate microtubule plus-end dynamics at the cell cortex*. J Cell Biol, 2005. **168**(1): p. 141-53.
99. Gundersen, G.G., E.R. Gomes, and Y. Wen, *Cortical control of microtubule stability and polarization*. Current Opinion in Cell Biology, 2004. **16**(1): p. 106-112.
100. Webster, D.R., et al., *Differential turnover of tyrosinated and detyrosinated microtubules*. Proc Natl Acad Sci U S A, 1987. **84**(24): p. 9040-4.
101. Wallin, M. and E. Strömberg, *Cold-Stable and Cold-Adapted Microtubules*, in *International Review of Cytology*, K.W. Jeon and J. Jarvik, Editors. 1995, Academic Press. p. 1-31.
102. Song, Y. and S.T. Brady, *Post-translational modifications of tubulin: pathways to functional diversity of microtubules*. Trends in Cell Biology, 2015. **25**(3): p. 125-136.
103. Kreis, T.E., *Microtubules containing detyrosinated tubulin are less dynamic*. EMBO J, 1987. **6**(9): p. 2597-606.

104. Kirschner, M. and T. Mitchison, *Beyond self-assembly: from microtubules to morphogenesis*. Cell, 1986. **45**(3): p. 329-42.
105. Khawaja, S., G.G. Gundersen, and J.C. Bulinski, *Enhanced stability of microtubules enriched in detyrosinated tubulin is not a direct function of detyrosination level*. J Cell Biol, 1988. **106**(1): p. 141-9.
106. Janke, C. and J.C. Bulinski, *Post-translational regulation of the microtubule cytoskeleton: mechanisms and functions*. Nat Rev Mol Cell Biol, 2011. **12**(12): p. 773-86.
107. Peris, L., et al., *Motor-dependent microtubule disassembly driven by tubulin tyrosination*. Journal of Cell Biology, 2009. **185**(7): p. 1159-1166.
108. Portran, D., et al., *Tubulin acetylation protects long-lived microtubules against mechanical ageing*. Nature cell biology, 2017. **19**(4): p. 391-398.
109. Xu, Z., et al., *Microtubules acquire resistance from mechanical breakage through intraluminal acetylation*. Science (New York, N.Y.), 2017. **356**(6335): p. 328-332.
110. Kapitein, Lukas C. and Casper C. Hoogenraad, *Building the Neuronal Microtubule Cytoskeleton*. Neuron, 2015. **87**(3): p. 492-506.
111. Barisic, M., et al., *Mitosis. Microtubule detyrosination guides chromosomes during mitosis*. Science (New York, N.Y.), 2015. **348**(6236): p. 799-803.
112. Akhmanova, A. and M.O. Steinmetz, *Microtubule minus-end regulation at a glance*. Journal of Cell Science, 2019. **132**(11).
113. Murphy, S.M., L. Urbani, and T. Stearns, *The Mammalian  $\gamma$ -Tubulin Complex Contains Homologues of the Yeast Spindle Pole Body Components Spc97p and Spc98p*. Journal of Cell Biology, 1998. **141**(3): p. 663-674.
114. Guillet, V., et al., *Crystal structure of  $\gamma$ -tubulin complex protein GCP4 provides insight into microtubule nucleation*. Nature structural & molecular biology, 2011. **18**(8): p. 915.
115. Song, J.-G., et al., *Mechanism of how augmin directly targets the  $\gamma$ -tubulin ring complex to microtubules*. Journal of Cell Biology, 2018. **217**(7): p. 2417-2428.
116. Tovey, Corinne A. and Paul T. Conduit, *Microtubule nucleation by  $\gamma$ -tubulin complexes and beyond*. Essays in Biochemistry, 2018. **62**(6): p. 765-780.
117. Semenova, I., et al., *Regulation of microtubule-based transport by MAP4*. Molecular Biology of the Cell, 2014. **25**(20): p. 3119-3132.
118. Monroy, B.Y., et al., *Competition between microtubule-associated proteins directs motor transport*. Nature Communications, 2018. **9**(1): p. 1487.
119. King, S.J. and T.A. Schroer, *Dynactin increases the processivity of the cytoplasmic dynein motor*. Nature Cell Biology, 2000. **2**(1): p. 20-24.
120. Reed, N.A., et al., *Microtubule Acetylation Promotes Kinesin-1 Binding and Transport*. Current Biology, 2006. **16**(21): p. 2166-2172.
121. Liao, G. and G.G. Gundersen, *Kinesin Is a Candidate for Cross-bridging Microtubules and Intermediate Filaments: SELECTIVE BINDING OF KINESIN TO DETYROSINATED TUBULIN AND VIMENTIN*. Journal of Biological Chemistry, 1998. **273**(16): p. 9797-9803.
122. Dunn, S., et al., *Differential trafficking of Kif5c on tyrosinated and detyrosinated microtubules in live cells*. Journal of Cell Science, 2008. **121**(7): p. 1085.
123. Cai, D., et al., *Single Molecule Imaging Reveals Differences in Microtubule Track Selection Between Kinesin Motors*. PLOS Biology, 2009. **7**(10): p. e1000216.

124. McKenney, R.J., et al., *Tyrosination of  $\alpha$ -tubulin controls the initiation of processive dynein-dynactin motility*. The EMBO journal, 2016. **35**(11): p. 1175-1185.
125. Nirschl, J.J., et al., *alpha-Tubulin Tyrosination and CLIP-170 Phosphorylation Regulate the Initiation of Dynein-Driven Transport in Neurons*. Cell Rep, 2016. **14**(11): p. 2637-52.
126. Akhmanova, A. and M.O. Steinmetz, *Control of microtubule organization and dynamics: two ends in the limelight*. Nat Rev Mol Cell Biol, 2015. **16**(12): p. 711-26.
127. Bieling, P., et al., *CLIP-170 tracks growing microtubule ends by dynamically recognizing composite EB1/tubulin-binding sites*. Journal of Cell Biology, 2008. **183**(7): p. 1223-1233.
128. Honnappa, S., et al., *An EB1-binding motif acts as a microtubule tip localization signal*. Cell, 2009. **138**(2): p. 366-76.
129. Maurer, S.P., et al., *EBs recognize a nucleotide-dependent structural cap at growing microtubule ends*. Cell, 2012. **149**(2): p. 371-82.
130. Roth, D., et al., *Spatial positioning of EB family proteins at microtubule tips involves distinct nucleotide-dependent binding properties*. Journal of Cell Science, 2018. **132**(4).
131. Su, L.-K. and Y. Qi, *Characterization of Human MAPRE Genes and Their Proteins*. Genomics, 2001. **71**(2): p. 142-149.
132. Komarova, Y., et al., *Mammalian end binding proteins control persistent microtubule growth*. J Cell Biol, 2009. **184**(5): p. 691-706.
133. Bu, W. and L.-K. Su, *Regulation of microtubule assembly by human EB1 family proteins*. Oncogene, 2001. **20**(25): p. 3185-3192.
134. Schwartz, K., K. Richards, and D. Botstein, *BIMI Encodes a Microtubule-binding Protein in Yeast*. Molecular Biology of the Cell, 1997. **8**(12): p. 2677-2691.
135. Beinbauer, J.D., et al., *Mal3, the Fission Yeast Homologue of the Human APC-interacting Protein EB-1 Is Required for Microtubule Integrity and the Maintenance of Cell Form*. Journal of Cell Biology, 1997. **139**(3): p. 717-728.
136. Rogers, S.L., et al., *Drosophila EB1 is important for proper assembly, dynamics, and positioning of the mitotic spindle*. The Journal of cell biology, 2002. **158**(5): p. 873-884.
137. Molines, A.T., et al., *EB1 contributes to microtubule bundling and organization, along with root growth, in Arabidopsis thaliana*. Biology open, 2018. **7**(8): p. bio030510.
138. Straube, A. and A. Merdes, *EB3 Regulates Microtubule Dynamics at the Cell Cortex and Is Required for Myoblast Elongation and Fusion*. Current Biology, 2007. **17**(15): p. 1318-1325.
139. Schröder, J.M., et al., *EB1 and EB3 promote cilia biogenesis by several centrosome-related mechanisms*. Journal of Cell Science, 2011. **124**(15): p. 2539-2551.
140. Zhang, R., et al., *Mechanistic Origin of Microtubule Dynamic Instability and Its Modulation by EB Proteins*. Cell, 2015. **162**(4): p. 849-59.
141. Vitre, B., et al., *EB1 regulates microtubule dynamics and tubulin sheet closure in vitro*. Nature Cell Biology, 2008. **10**(4): p. 415-421.
142. Yang, C., et al., *EB1 and EB3 regulate microtubule minus end organization and Golgi morphology*. Journal of Cell Biology, 2017. **216**(10): p. 3179-3198.
143. Dixit, R., et al., *Microtubule plus-end tracking by CLIP-170 requires EB1*. Proc Natl Acad Sci U S A, 2009. **106**(2): p. 492-7.

144. Lansbergen, G., et al., *Conformational changes in CLIP-170 regulate its binding to microtubules and dynactin localization*. J Cell Biol, 2004. **166**(7): p. 1003-14.
145. Duellberg, C., et al., *Reconstitution of a hierarchical +TIP interaction network controlling microtubule end tracking of dynein*. Nat Cell Biol, 2014. **16**(8): p. 804-11.
146. Moughamian, A.J., et al., *Ordered recruitment of dynactin to the microtubule plus-end is required for efficient initiation of retrograde axonal transport*. J Neurosci, 2013. **33**(32): p. 13190-203.
147. Lee, T., et al., *MCAK associates with EBI*. Oncogene, 2008. **27**(17): p. 2494-2500.
148. Maurer, Sebastian P., et al., *EBI Accelerates Two Conformational Transitions Important for Microtubule Maturation and Dynamics*. Current Biology, 2014. **24**(4): p. 372-384.
149. Gard, D.L., B.E. Becker, and S. Josh Romney, *MAPping the eukaryotic tree of life: structure, function, and evolution of the MAP215/Dis1 family of microtubule-associated proteins*. Int Rev Cytol, 2004. **239**: p. 179-272.
150. Charrasse, S., et al., *The TOGp protein is a new human microtubule-associated protein homologous to the Xenopus XMAP215*. Journal of Cell Science, 1998. **111**(10): p. 1371-1383.
151. Whittington, A.T., et al., *MORI is essential for organizing cortical microtubules in plants*. Nature, 2001. **411**(6837): p. 610-613.
152. Brittle, A.L. and H. Ohkura, *Mini spindles, the XMAP215 homologue, suppresses pausing of interphase microtubules in Drosophila*. The EMBO Journal, 2005. **24**(7): p. 1387-1396.
153. Charrasse, S., et al., *Characterization of the cDNA and Pattern of Expression of a New Gene Over-Expressed in Human Hepatomas and Colonic Tumors*. European Journal of Biochemistry, 1995. **234**(2): p. 406-413.
154. Gergely, F., V.M. Draviam, and J.W. Raff, *The ch-TOG/XMAP215 protein is essential for spindle pole organization in human somatic cells*. Genes & Development, 2003. **17**(3): p. 336-341.
155. Cassimeris, L. and J. Morabito, *TOGp, the Human Homolog of XMAP215/Dis1, Is Required for Centrosome Integrity, Spindle Pole Organization, and Bipolar Spindle Assembly*. Molecular Biology of the Cell, 2004. **15**(4): p. 1580-1590.
156. Rieder, C.L., *Formation of the astral mitotic spindle: ultrastructural basis for the centrosome-kinetochore interaction*. Electron Microsc Rev, 1990. **3**(2): p. 269-300.
157. Wang, P.J. and T.C. Huffaker, *Stu2p: A Microtubule-Binding Protein that Is an Essential Component of the Yeast Spindle Pole Body*. Journal of Cell Biology, 1997. **139**(5): p. 1271-1280.
158. Garcia, M.A., et al., *Fission yeast ch-TOG/XMAP215 homologue Alp14 connects mitotic spindles with the kinetochore and is a component of the Mad2-dependent spindle checkpoint*. EMBO J, 2001. **20**(13): p. 3389-401.
159. Gutiérrez-Caballero, C., et al., *TACC3-ch-TOG track the growing tips of microtubules independently of clathrin and Aurora-A phosphorylation*. Biology Open, 2015. **4**(2): p. 170-179.
160. Brouhard, G.J., et al., *XMAP215 is a processive microtubule polymerase*. Cell, 2008. **132**(1): p. 79-88.

161. Gard, D.L. and M.W. Kirschner, *A microtubule-associated protein from Xenopus eggs that specifically promotes assembly at the plus-end*. The Journal of Cell Biology, 1987. **105**(5): p. 2203-2215.
162. Flor-Parra, I., A.B. Iglesias-Romero, and F. Chang, *The XMAP215 Ortholog Alp14 Promotes Microtubule Nucleation in Fission Yeast*. Current Biology, 2018. **28**(11): p. 1681-1691.e4.
163. Consolati, T., et al., *Microtubule Nucleation Properties of Single Human gammaTuRCs Explained by Their Cryo-EM Structure*. Dev Cell, 2020. **53**(5): p. 603-617 e8.
164. Thawani, A., R.S. Kadzik, and S. Petry, *XMAP215 is a microtubule nucleation factor that functions synergistically with the  $\gamma$ -tubulin ring complex*. Nat Cell Biol, 2018. **20**(5): p. 575-585.
165. Nakamura, S., et al., *Dissecting the nanoscale distributions and functions of microtubule-end-binding proteins EB1 and ch-TOG in interphase HeLa cells*. PLoS One, 2012. **7**(12): p. e51442.
166. Currie, J.D., et al., *The microtubule lattice and plus-end association of Drosophila Mini spindles is spatially regulated to fine-tune microtubule dynamics*. Molecular Biology of the Cell, 2011. **22**(22): p. 4343-4361.
167. Tournebize, R., et al., *Control of microtubule dynamics by the antagonistic activities of XMAP215 and XKCM1 in Xenopus egg extracts*. Nature Cell Biology, 2000. **2**(1): p. 13-19.
168. van der Vaart, B., et al., *SLAIN2 links microtubule plus end-tracking proteins and controls microtubule growth in interphase*. Journal of Cell Biology, 2011. **193**(6): p. 1083-1099.
169. Bonfils, C., et al., *Kinetic Analysis of Tubulin Assembly in the Presence of the Microtubule-associated Protein TOGp \**. Journal of Biological Chemistry, 2007. **282**(8): p. 5570-5581.
170. Spittle, C., et al., *The Interaction of TOGp with Microtubules and Tubulin \**. Journal of Biological Chemistry, 2000. **275**(27): p. 20748-20753.
171. Kinoshita, K., et al., *Reconstitution of Physiological Microtubule Dynamics Using Purified Components*. Science, 2001. **294**(5545): p. 1340-1343.
172. Lee, M.J., et al., *Msp1/XMAP215 interacts with the centrosomal protein D-TACC to regulate microtubule behaviour*. Nat Cell Biol, 2001. **3**(7): p. 643-9.
173. Peset, I. and I. Vernos, *The TACC proteins: TACC-ling microtubule dynamics and centrosome function*. Trends Cell Biol, 2008. **18**(8): p. 379-88.
174. Conte, N., et al., *TACC1-chTOG-Aurora A protein complex in breast cancer*. Oncogene, 2003. **22**(50): p. 8102-16.
175. Still, I.H., P. Vince, and J.K. Cowell, *The third member of the transforming acidic coiled coil-containing gene family, TACC3, maps in 4p16, close to translocation breakpoints in multiple myeloma, and is upregulated in various cancer cell lines*. Genomics, 1999. **58**(2): p. 165-70.
176. Still, I.H., et al., *Structure-function evolution of the transforming acidic coiled coil genes revealed by analysis of phylogenetically diverse organisms*. BMC Evol Biol, 2004. **4**: p. 16.

177. Lucaj, C.M., et al., *Xenopus TACC1 is a microtubule plus-end tracking protein that can regulate microtubule dynamics during embryonic development*. Cytoskeleton, 2015. **72**(5): p. 225-234.
178. Evsikov, A.V., et al., *Systems biology of the 2-cell mouse embryo*. Cytogenet Genome Res, 2004. **105**(2-4): p. 240-50.
179. Sato, M., et al., *Interdependency of fission yeast Alp14/TOG and coiled coil protein Alp7 in microtubule localization and bipolar spindle formation*. Mol Biol Cell, 2004. **15**(4): p. 1609-22.
180. Gergely, F., et al., *The TACC domain identifies a family of centrosomal proteins that can interact with microtubules*. Proc Natl Acad Sci U S A, 2000. **97**(26): p. 14352-7.
181. Kinoshita, K., et al., *Aurora A phosphorylation of TACC3/maskin is required for centrosome-dependent microtubule assembly in mitosis*. The Journal of cell biology, 2005. **170**(7): p. 1047-1055.
182. Giet, R.g., et al., *Drosophila Aurora A kinase is required to localize D-TACC to centrosomes and to regulate astral microtubules*. Journal of Cell Biology, 2002. **156**(3): p. 437-451.
183. Burgess, S.G., et al., *Aurora-A-Dependent Control of TACC3 Influences the Rate of Mitotic Spindle Assembly*. PLoS genetics, 2015. **11**(7): p. e1005345-e1005345.
184. Hussmann, F., et al., *Alp7/TACC-Alp14/TOG generates long-lived, fast-growing MTs by an unconventional mechanism*. Sci Rep, 2016. **6**: p. 20653.
185. Mortuza, G.B., et al., *XTACC3-XMAP215 association reveals an asymmetric interaction promoting microtubule elongation*. Nat Commun, 2014. **5**: p. 5072.
186. Lin, C.-H., C.-K. Hu, and H.-M. Shih, *Clathrin heavy chain mediates TACC3 targeting to mitotic spindles to ensure spindle stability*. The Journal of cell biology, 2010. **189**(7): p. 1097-1105.
187. Singh, P., et al., *TACC3 Protein Regulates Microtubule Nucleation by Affecting  $\gamma$ -Tubulin Ring Complexes* \*. Journal of Biological Chemistry, 2014. **289**(46): p. 31719-31735.
188. Thakur, H.C., et al., *The centrosomal adaptor TACC3 and the microtubule polymerase chTOG interact via defined C-terminal subdomains in an Aurora-A kinase-independent manner*. J Biol Chem, 2014. **289**(1): p. 74-88.
189. Schuendeln, M.M., et al., *The Centrosomal, Putative Tumor Suppressor Protein TACC2 Is Dispensable for Normal Development, and Deficiency Does Not Lead to Cancer*. Molecular and Cellular Biology, 2004. **24**(14): p. 6403-6409.
190. Sato, M., et al., *Nucleocytoplasmic transport of Alp7/TACC organizes spatiotemporal microtubule formation in fission yeast*. EMBO reports, 2009. **10**(10): p. 1161-1167.
191. Zheng, L., et al., *The fission yeast transforming acidic coiled coil-related protein Mia1p/Alp7p is required for formation and maintenance of persistent microtubule-organizing centers at the nuclear envelope*. Molecular biology of the cell, 2006. **17**(5): p. 2212-2222.
192. Nwagbara, B.U., et al., *TACC3 is a microtubule plus end-tracking protein that promotes axon elongation and also regulates microtubule plus end dynamics in multiple embryonic cell types*. Mol Biol Cell, 2014. **25**(21): p. 3350-62.

193. Rutherford, E.L., et al., *Xenopus TACC2 is a microtubule plus end-tracking protein that can promote microtubule polymerization during embryonic development*. *Molecular biology of the cell*, 2016. **27**(20): p. 3013-3020.
194. Stewart, J.P., et al., *Correlation of TACC3, FGFR3, MMSET and p21 expression with the t(4;14)(p16.3;q32) in multiple myeloma*. *Br J Haematol*, 2004. **126**(1): p. 72-6.
195. Duncan, C.G., et al., *Integrated genomic analyses identify ERFF1 and TACC3 as glioblastoma-targeted genes*. *Oncotarget*, 2010. **1**(4): p. 265-77.
196. Song, H., et al., *Overexpression of TACC3 in Breast Cancer Associates With Poor Prognosis*. *Appl Immunohistochem Mol Morphol*, 2018. **26**(2): p. 113-119.
197. Akbulut, O., et al., *A Highly Potent TACC3 Inhibitor as a Novel Anticancer Drug Candidate*. *Molecular Cancer Therapeutics*, 2020. **19**(6): p. 1243-1254.
198. Campo, L. and E.-K. Breuer, *Inhibition of TACC3 by a small molecule inhibitor in breast cancer*. *Biochemical and Biophysical Research Communications*, 2018. **498**(4): p. 1085-1092.
199. Polson, E.S., et al., *KHS101 disrupts energy metabolism in human glioblastoma cells and reduces tumor growth in mice*. *Science Translational Medicine*, 2018. **10**(454): p. eaar2718.
200. Naghavi, M.H. and D. Walsh, *Microtubule Regulation and Function during Virus Infection*. *J Virol*, 2017. **91**(16).
201. Jouvenet, N., et al., *Transport of African Swine Fever Virus from Assembly Sites to the Plasma Membrane Is Dependent on Microtubules and Conventional Kinesin*. *Journal of Virology*, 2004. **78**(15): p. 7990-8001.
202. Momose, F., et al., *Visualization of microtubule-mediated transport of influenza viral progeny ribonucleoprotein*. *Microbes and Infection*, 2007. **9**(12): p. 1422-1433.
203. Sodeik, B., M.W. Ebersold, and A. Helenius, *Microtubule-mediated transport of incoming herpes simplex virus 1 capsids to the nucleus*. *J Cell Biol*, 1997. **136**(5): p. 1007-21.
204. Sanderson, C.M., M. Hollinshead, and G.L. Smith, *The vaccinia virus A27L protein is needed for the microtubule-dependent transport of intracellular mature virus particles*. *Journal of General Virology*, 2000. **81**(1): p. 47-58.
205. Maginnis, M.S., *Virus-Receptor Interactions: The Key to Cellular Invasion*. *J Mol Biol*, 2018. **430**(17): p. 2590-2611.
206. Naranatt, P.P., et al., *Kaposi's sarcoma-associated herpesvirus modulates microtubule dynamics via RhoA-GTP-dependent signaling and utilizes the dynein motors to deliver its DNA to the nucleus*. *Journal of virology*, 2005. **79**(2): p. 1191-1206.
207. Kumar, B. and B. Chandran, *KSHV Entry and Trafficking in Target Cells-Hijacking of Cell Signal Pathways, Actin and Membrane Dynamics*. *Viruses*, 2016. **8**(11): p. 305.
208. Sabo, Y., et al., *HIV-1 induces the formation of stable microtubules to enhance early infection*. *Cell host & microbe*, 2013. **14**(5): p. 535-546.
209. Mitra, S., et al., *HIV-1 Exploits CLASP2 To Induce Microtubule Stabilization and Facilitate Virus Trafficking to the Nucleus*. *J Virol*, 2020. **94**(14).
210. Fernandez, J., et al., *Microtubule-associated proteins 1 (MAP1) promote human immunodeficiency virus type 1 (HIV-1) intracytoplasmic routing to the nucleus*. *Journal of Biological Chemistry*, 2015. **290**(8): p. 4631-4646.

211. Delaney, M.K., et al., *Distinct functions of diaphanous-related formins regulate HIV-1 uncoating and transport*. Proceedings of the National Academy of Sciences, 2017. **114**(33): p. E6932.
212. Roohvand, F., et al., *Initiation of Hepatitis C Virus Infection Requires the Dynamic Microtubule Network: ROLE OF THE VIRAL NUCLEOCAPSID PROTEIN \**. Journal of Biological Chemistry, 2009. **284**(20): p. 13778-13791.
213. Jovasevic, V., M.H. Naghavi, and D. Walsh, *Microtubule plus end-associated CLIP-170 initiates HSV-1 retrograde transport in primary human cells*. J Cell Biol, 2015. **211**(2): p. 323-37.
214. Döhner, K., et al., *Function of Dynein and Dynactin in Herpes Simplex Virus Capsid Transport*. Molecular Biology of the Cell, 2002. **13**(8): p. 2795-2809.
215. Radtke, K., et al., *Plus- and Minus-End Directed Microtubule Motors Bind Simultaneously to Herpes Simplex Virus Capsids Using Different Inner Tegument Structures*. PLOS Pathogens, 2010. **6**(7): p. e1000991.
216. Naghavi, M.H., G.G. Gundersen, and D. Walsh, *Plus-end tracking proteins, CLASPs, and a viral Akt mimic regulate herpesvirus-induced stable microtubule formation and virus spread*. Proceedings of the National Academy of Sciences of the United States of America, 2013. **110**(45): p. 18268-18273.
217. Novoa, R.R., et al., *Virus factories: associations of cell organelles for viral replication and morphogenesis*. Biol Cell, 2005. **97**(2): p. 147-72.
218. den Boon, J.A., A. Diaz, and P. Ahlquist, *Cytoplasmic viral replication complexes*. Cell Host Microbe, 2010. **8**(1): p. 77-85.
219. Akil, A., et al., *Septin 9 induces lipid droplets growth by a phosphatidylinositol-5-phosphate and microtubule-dependent mechanism hijacked by HCV*. Nature Communications, 2016. **7**(1): p. 12203.
220. Boulant, S., et al., *Hepatitis C Virus Core Protein Induces Lipid Droplet Redistribution in a Microtubule- and Dynein-Dependent Manner*. Traffic, 2008. **9**(8): p. 1268-1282.
221. Schepis, A., et al., *Vaccinia Virus-Induced Microtubule-Dependent Cellular Rearrangements*. Traffic, 2006. **7**(3): p. 308-323.
222. Mallardo, M., S. Schleich, and J.K. Locker, *Microtubule-dependent Organization of Vaccinia Virus Core-derived Early mRNAs into Distinct Cytoplasmic Structures*. Molecular Biology of the Cell, 2001. **12**(12): p. 3875-3891.
223. Desai, P. and S. Person, *Incorporation of the green fluorescent protein into the herpes simplex virus type 1 capsid*. Journal of virology, 1998. **72**(9): p. 7563-7568.
224. Malikov, V., et al., *HIV-1 capsids bind and exploit the kinesin-1 adaptor FEZ1 for inward movement to the nucleus*. Nature communications, 2015. **6**: p. 6660-6660.
225. Stephens, D.J., *Functional coupling of microtubules to membranes - implications for membrane structure and dynamics*. J Cell Sci, 2012. **125**(Pt 12): p. 2795-804.
226. Akhmanova, A. and M.O. Steinmetz, *Tracking the ends: a dynamic protein network controls the fate of microtubule tips*. Nat Rev Mol Cell Biol, 2008. **9**(4): p. 309-22.
227. Kristofferson, D., T. Mitchison, and M. Kirschner, *Direct observation of steady-state microtubule dynamics*. J Cell Biol, 1986. **102**(3): p. 1007-19.
228. Janosi, I.M., D. Chretien, and H. Flyvbjerg, *Structural microtubule cap: stability, catastrophe, rescue, and third state*. Biophys J, 2002. **83**(3): p. 1317-30.

229. Howard, J. and A.A. Hyman, *Dynamics and mechanics of the microtubule plus end*. Nature, 2003. **422**(6933): p. 753-8.
230. Guesdon, A., et al., *EB1 interacts with outwardly curved and straight regions of the microtubule lattice*. Nat Cell Biol, 2016. **18**(10): p. 1102-8.
231. Lansbergen, G., et al., *CLASPs attach microtubule plus ends to the cell cortex through a complex with LL5beta*. Dev Cell, 2006. **11**(1): p. 21-32.
232. Komarova, Y., et al., *EB1 and EB3 control CLIP dissociation from the ends of growing microtubules*. Mol Biol Cell, 2005. **16**(11): p. 5334-45.
233. Slep, K.C. and R.D. Vale, *Structural basis of microtubule plus end tracking by XMAP215, CLIP-170, and EB1*. Mol Cell, 2007. **27**(6): p. 976-91.
234. Ding, Z.M., et al., *The role of TACC3 in mitotic spindle organization*. Cytoskeleton (Hoboken), 2017. **74**(10): p. 369-378.
235. Nakaseko, Y., et al., *M phase-specific kinetochore proteins in fission yeast: Microtubule-associating Dis1 and Mtc1 display rapid separation and segregation during anaphase*. Current Biology, 2001. **11**(8): p. 537-549.
236. Gunzelmann, J., et al., *The microtubule polymerase Stu2 promotes oligomerization of the  $\gamma$ -TuSC for cytoplasmic microtubule nucleation*. eLife, 2018. **7**: p. e39932.
237. Kume, K., et al., *Role of nucleocytoplasmic transport in interphase microtubule organization in fission yeast*. Biochem Biophys Res Commun, 2018. **503**(2): p. 1160-1167.
238. Chanez, B., et al., *Eribulin targets a ch-TOG-dependent directed migration of cancer cells*. Oncotarget, 2015. **6**(39): p. 41667-41678.
239. Trogden, K.P. and S.L. Rogers, *TOG Proteins Are Spatially Regulated by Rac-GSK3 $\beta$  to Control Interphase Microtubule Dynamics*. PloS one, 2015. **10**(9): p. e0138966-e0138966.
240. Ling, Y.C., A. Vjestica, and S. Oliferenko, *Nucleocytoplasmic shuttling of the TACC protein Mia1p/Alp7p is required for remodeling of microtubule arrays during the cell cycle*. PloS one, 2009. **4**(7): p. e6255-e6255.
241. Sato, M. and T. Toda, *Alp7/TACC is a crucial target in Ran-GTPase-dependent spindle formation in fission yeast*. Nature, 2007. **447**: p. 334.
242. Erdogan, B., et al., *The microtubule plus-end-tracking protein TACC3 promotes persistent axon outgrowth and mediates responses to axon guidance signals during development*. Neural Dev, 2017. **12**(1): p. 3.
243. Long, J.B., et al., *Multiparametric Analysis of CLASP-Interacting Protein Functions during Interphase Microtubule Dynamics*. Molecular and Cellular Biology, 2013. **33**(8): p. 1528.
244. Roizman, B., D.M. Knipe, and R. Whitley, *Herpes simplex viruses*, in *Fields virology*, D.M. Knipe and P.M. Howley, Editors. 2013, Wolters Kluwer/Lippincott Williams & Wilkins Health: Philadelphia, PA. p. 1823-1897.
245. Brady, S., *Axonal Dynamics and Regeneration*, in *Neuroregeneration*, A. Gorio, Editor. 1993, Raven Press: New York. p. 7-36.
246. Baas, P.W. and M.M. Black, *Individual microtubules in the axon consist of domains that differ in both composition and stability*. The Journal of Cell Biology, 1990. **111**(2): p. 495.

247. Song, Y., et al., *Transglutaminase and Polyamination of Tubulin: Posttranslational Modification for Stabilizing Axonal Microtubules*. Neuron, 2013. **78**(1): p. 109-123.
248. Sahenk, Z. and S.T. Brady, *Axonal tubulin and microtubules: Morphologic evidence for stable regions on axonal microtubules*. Cell Motility, 1987. **8**(2): p. 155-164.
249. Rodríguez, J.A., et al., *Release of tyrosine incorporated as a single unit into rat brain protein*. Biochemical and Biophysical Research Communications, 1973. **54**(1): p. 335-340.
250. Hallak, M.E., et al., *Release of tyrosine from tyrosinated tubulin. Some common factors that affect this process and the assembly of tubulin*. FEBS Letters, 1977. **73**(2): p. 147-150.
251. Biedler, J.L., L. Helson, and B.A. Spengler, *Morphology and growth, tumorigenicity, and cytogenetics of human neuroblastoma cells in continuous culture*. Cancer Res, 1973. **33**(11): p. 2643-52.
252. Gordon, J., S. Amini, and M.K. White, *General overview of neuronal cell culture*. Methods in molecular biology (Clifton, N.J.), 2013. **1078**: p. 1-8.
253. Liao, G., T. Nagasaki, and G.G. Gundersen, *Low concentrations of nocodazole interfere with fibroblast locomotion without significantly affecting microtubule level: implications for the role of dynamic microtubules in cell locomotion*. Journal of Cell Science, 1995. **108**(11): p. 3473.
254. Xie, S., et al., *The endocytic recycling compartment maintains cargo segregation acquired upon exit from the sorting endosome*. Molecular biology of the cell, 2016. **27**(1): p. 108-126.
255. Lin, S.X., G.G. Gundersen, and F.R. Maxfield, *Export from pericentriolar endocytic recycling compartment to cell surface depends on stable, detyrosinated (glu) microtubules and kinesin*. Mol Biol Cell, 2002. **13**(1): p. 96-109.
256. Ban, R., et al., *Mitotic regulation of the stability of microtubule plus-end tracking protein EB3 by ubiquitin ligase SLAH-1 and Aurora mitotic kinases*. J Biol Chem, 2009. **284**(41): p. 28367-81.
257. Ferreira, J.G., et al., *Aurora B spatially regulates EB3 phosphorylation to coordinate daughter cell adhesion with cytokinesis*. The Journal of Cell Biology, 2013. **201**(5): p. 709.
258. Close, W.L., et al., *Infection-Induced Changes Within the Endocytic Recycling Compartment Suggest a Roadmap of Human Cytomegalovirus Egress*. Front Microbiol, 2018. **9**: p. 1888.
259. Das, S., et al., *Identification of human cytomegalovirus genes important for biogenesis of the cytoplasmic virion assembly complex*. J Virol, 2014. **88**(16): p. 9086-99.
260. Seo, J.Y. and W.J. Britt, *Multimerization of tegument protein pp28 within the assembly compartment is required for cytoplasmic envelopment of human cytomegalovirus*. J Virol, 2008. **82**(13): p. 6272-87.
261. Wu, H., et al., *Human Cytomegalovirus Envelope Protein gpUL132 Regulates Infectious Virus Production through Formation of the Viral Assembly Compartment*. mBio, 2020. **11**(5).
262. Cohen, T., et al., *The Microtubule Inhibitor Podofilox Inhibits an Early Entry Step of Human Cytomegalovirus*. Viruses, 2016. **8**(10): p. 295.

263. Clippinger, A.J. and J.C. Alwine, *Dynein mediates the localization and activation of mTOR in normal and human cytomegalovirus-infected cells*. *Genes Dev*, 2012. **26**(18): p. 2015-26.
264. Sanders, A.A. and I. Kaverina, *Nucleation and Dynamics of Golgi-derived Microtubules*. *Front Neurosci*, 2015. **9**: p. 431.
265. Walsh, D. and M.H. Naghavi, *Exploitation of Cytoskeletal Networks during Early Viral Infection*. *Trends Microbiol*, 2019. **27**(1): p. 39-50.
266. Gutierrez-Caballero, C., et al., *TACC3-ch-TOG track the growing tips of microtubules independently of clathrin and Aurora-A phosphorylation*. *Biol Open*, 2015. **4**(2): p. 170-9.
267. Furey, C., V. Jovasevic, and D. Walsh, *TACC3 Regulates Microtubule Plus-End Dynamics and Cargo Transport in Interphase Cells*. *Cell Reports*, 2020. **30**(1): p. 269-283.e6.
268. Moorman, N.J., et al., *A targeted spatial-temporal proteomics approach implicates multiple cellular trafficking pathways in human cytomegalovirus virion maturation*. *Mol Cell Proteomics*, 2010. **9**(5): p. 851-60.
269. Raghu, H., et al., *Lipid rafts of primary endothelial cells are essential for Kaposi's sarcoma-associated herpesvirus/human herpesvirus 8-induced phosphatidylinositol 3-kinase and RhoA-GTPases critical for microtubule dynamics and nuclear delivery of viral DNA but dispensable for binding and entry*. *J Virol*, 2007. **81**(15): p. 7941-59.
270. Santos da Silva, E., et al., *HIV-1 capsids mimic a microtubule regulator to coordinate early stages of infection*. *Embo j*, 2020. **39**(20): p. e104870.
271. Hackett, B.A. and S. Cherry, *Flavivirus internalization is regulated by a size-dependent endocytic pathway*. *Proc Natl Acad Sci U S A*, 2018. **115**(16): p. 4246-4251.
272. Arakawa, Y., J.V. Cordeiro, and M. Way, *F11L-mediated inhibition of RhoA-mDia signaling stimulates microtubule dynamics during vaccinia virus infection*. *Cell Host Microbe*, 2007. **1**(3): p. 213-26.
273. Tei, S., et al., *Simian virus 40 large T antigen targets the microtubule-stabilizing protein TACC2*. *J Cell Sci*, 2009. **122**(Pt 17): p. 3190-8.
274. Yim, E.K., et al., *Anticancer effects on TACC3 by treatment of paclitaxel in HPV-18 positive cervical carcinoma cells*. *Oncol Rep*, 2009. **21**(2): p. 549-57.
275. Tandon, R., D.P. AuCoin, and E.S. Mocarski, *Human cytomegalovirus exploits ESCRT machinery in the process of virion maturation*. *J Virol*, 2009. **83**(20): p. 10797-807.
276. Turner, D.L., et al., *The host exosome pathway underpins biogenesis of the human cytomegalovirus virion*. *Elife*, 2020. **9**.
277. Tooze, J., et al., *Progeny vaccinia and human cytomegalovirus particles utilize early endosomal cisternae for their envelopes*. *Eur J Cell Biol*, 1993. **60**(1): p. 163-78.
278. Bughio, F., et al., *Human Cytomegalovirus *UL135* and *UL136* Genes Are Required for Postentry Tropism in Endothelial Cells*. *Journal of Virology*, 2015. **89**(13): p. 6536-6550.
279. Meiring, J.C.M., B.I. Shneyer, and A. Akhmanova, *Generation and regulation of microtubule network asymmetry to drive cell polarity*. *Current Opinion in Cell Biology*, 2020. **62**: p. 86-95.

280. Goodson, H.V. and E.M. Jonasson, *Microtubules and Microtubule-Associated Proteins*. Cold Spring Harb Perspect Biol, 2018. **10**(6).
281. Briggs, H., et al., *The cell cycle state defines TACC3 as a regulator gene in glioblastoma*. bioRxiv, 2020: p. 2020.10.20.346643.
282. Lauffart, B., et al., *Temporal and spatial expression of TACC1 in the mouse and human*. Developmental Dynamics, 2006. **235**(6): p. 1638-1647.
283. Lin, S.X., G.G. Gundersen, and F.R. Maxfield, *Export from Pericentriolar Endocytic Recycling Compartment to Cell Surface Depends on Stable, Detyrosinated (Glu) Microtubules and Kinesin*. Molecular Biology of the Cell, 2001. **13**(1): p. 96-109.